

2011

Characterization of PA-11 Flexible Liner Aging in the Laboratory and in Field Environments Throughout the World

Arthur Jaeton Mitman Glover
College of William & Mary - Arts & Sciences

Follow this and additional works at: <https://scholarworks.wm.edu/etd>



Part of the [Petroleum Engineering Commons](#), and the [Polymer Chemistry Commons](#)

Recommended Citation

Glover, Arthur Jaeton Mitman, "Characterization of PA-11 Flexible Liner Aging in the Laboratory and in Field Environments Throughout the World" (2011). *Dissertations, Theses, and Masters Projects*. Paper 1539623345.

<https://dx.doi.org/doi:10.21220/s2-rxc2-pc30>

This Dissertation is brought to you for free and open access by the Theses, Dissertations, & Master Projects at W&M ScholarWorks. It has been accepted for inclusion in Dissertations, Theses, and Masters Projects by an authorized administrator of W&M ScholarWorks. For more information, please contact scholarworks@wm.edu.

**Characterization of PA-11 Flexible Pipe Liner Aging in the Laboratory and in
Field Environments Throughout the World**

Arthur Jaeton Mitman Glover

Tappahannock, Virginia

**Master of Science, The College of William and Mary, 2009
Bachelor of Science, The College of William and Mary, 2006**

**A Dissertation presented to the Graduate Faculty
of the College of William and Mary in Candidacy for the Degree of
Doctor of Philosophy**

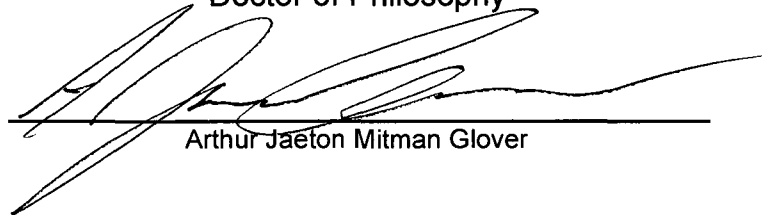
Department of Applied Science

**The College of William and Mary
January, 2011**

APPROVAL PAGE


This Dissertation is submitted in partial fulfillment of
the requirements for the degree of

Doctor of Philosophy




Arthur Jaeton Mitman Glover


Approved by the Committee, December, 2010



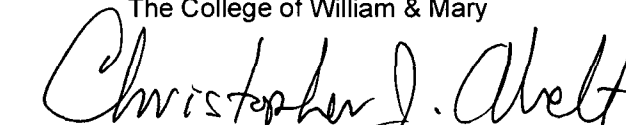
Committee Chair
Professor David Kranbuehl, Applied Science
The College of William & Mary



Professor Mark Hinders, Applied Science
The College of William & Mary



Professor Hannes Schniepp, Applied Science
The College of William & Mary



Professor Christopher Abelt, Chemistry
The College of William & Mary

ABSTRACT PAGE

Polyamide-11 (PA11) is a polymer of the Nylon family whose monomer is obtained from the castor bean, a renewable resource. It is widely used in offshore oil and gas production as a non-rigid flexible pipe liner, allowing for oil and gas transport from the wellhead to floating platforms for processing. The degradation of PA11 over time may lead to the pipe's failure, with possibly catastrophic results which include loss of life. Until now, the characterization of the degradative process has been limited to laboratory studies of the effects of water and temperature on the rate and degree of hydrolysis. In this dissertation, a more exact model than those proposed in the literature thus far is defined and used to quantify the effects of temperature on the rate and degree of PA11 hydrolysis. This is performed using accelerated aging experiments in the lab which are evaluated by a primary means of molecular weight determination, size exclusion chromatography - multiple angle laser light scattering (SEC-MALLS). The effects of methanol and ethanol, used in the industry to control solid hydrate formation, are then characterized with respect to concentration and temperature, a topic which has not yet been addressed in the literature. Also novel to this work is the discovery of the effects of acetic acid, valeric acid, and 3-cyclopropionic acid on the rate and degree of PA11 hydrolysis. While these acids are present in the offshore oil and gas environment, acetic acid is the most common, and has been identified as a serious factor affecting degradation. The effects of acetic acid on rate and degree of hydrolysis are incorporated into the temperature dependence described above, and adapted to a model well suited for characterizing the degradation of PA11 in the changing temperature environments found in the field. By characterizing coupons removed from PA11 pipes in oil production fields in various parts of the world, the model is tested and used to predict aging of PA11 pipe. The model is shown to be effective at predicting degradation for times greater than ten years, which has never before been described. The effects of annealing coupled with decline in molecular weight on PA11 mechanical properties in accelerated aging experiments versus aging in the field environment is discussed. These contributions to understand and predict the aging of PA11 flexible pipes are central to increasing the safety of offshore oil and gas production, a topic that today is vastly important.

TABLE OF CONTENTS

	Page
ACKNOWLEDGEMENTS	vi
CHAPTER 1: INTRODUCTION	1
CHAPTER 2: EXPERIMENTAL METHODS AND TECHNIQUES	7
SIZE EXCLUSION CHROMATOGRAPHY-MULTIPLE ANGLE LASER LIGHT SCATTERING (SEC-MALLS)	7
INTRINSIC VISCOSITY MEASUREMENTS	17
THERMOGRAVIMETRIC ANALYSIS (TGA)	25
DIFFERENTIAL SCANNING CALORIMETRY (DSC)	28
TENSILE TESTING	32
DETERMINATION OF ORGANIC ACID CONCENTRATION IN PRODUCED WATER BY GAS CHROMATOGRAPHY	39
CHAPTER 3: DEGRADATION OF POLYAMIDE-11 BY HYDROLYSIS, METHANOLYSIS, AND ETHANOLYSIS	48
CHAPTER 4: DEGRADATION OF POLYAMIDE-11 BY ORGANIC ACID CATALYZED HYDROLYSIS	72
CHAPTER 5: COMPARISON OF ACCELERATED AGING OF POLYAMIDE-11 TO LONG-TERM MOLECULAR WEIGHT CHANGES IN THE FIELD	91
CHAPTER 6: CONCLUSIONS	130
REFERENCES	136
VITA	140
APPENDIX A: DATA TABLES FOR CHAPTERS 3, 4, AND 5	141
APPENDIX B: PATENT APPLICATION FOR A METHOD FOR MAKING POLYMER COMPOSITES CONTAINING GRAPHENE SHEETS	160

APPENDIX C: CHANGE IN THE C:O RATIO OF GRAPHENE OXIDE DURING PROCESSING (A SUBMITTED PRE-PRINT)	206
APPENDIX D: <i>IN SITU</i> REDUCTION OF FGS-2 IN POLYMER NANOCOMPOSITES AS A FUNCTION OF CHEMICAL STRUCTURE, TIME, AND TEMPERATURE (A FULL-LENGTH MANUSCRIPT NEARLY READY FOR SUBMISSION)	215

Acknowledgements

The author wishes to thank Professor David Kranbuehl for his unlimited guidance and unwavering support in this work.

Many thanks are also due to Professors Abelt, Schniepp, and Hinders, as their contributions over the course of my graduate studies as well as their guidance during the writing of this dissertation were essential.

I also wish to thank the undergraduate research students in our research lab. Without them, this work could never have been completed in a reasonable time.

Thanks are due to my family, Andrea and Dresden, as their influence and care have made me into the person I am today.

My late father, Loper, deserves thanks as he is the one who sent me on the path of science.

I give thanks to Catherine, for sticking around and keeping me sane during trying times, and for her unwavering support in spite of the many nights and weekends worked.

Finally I thank our funding sources, which include a consortium of the world's top oil producers and PA-11 flexible pipe manufacturers.

Chapter 1: Introduction

High demand for petroleum has led to numerous technological advances that have made economically feasible the retrieval and efficient processing of crude oil from some of the most challenging places on Earth. Deep-water oil fields are now being constructed in areas so extreme that they may be considered true feats of engineering. One example is Royal Dutch Shell's Perdido field in the Gulf of Mexico, which lies almost 2.5 km below the surface [1]. This well had been drilled, and all necessary infrastructure related to transporting oil safely to the surface installed, under the roughly 25 MPa generated by the water above.

Once a well is drilled and the oil retrieval begins, the crude is transferred to the surface for processing and distribution. This is typically effected by flexible risers, whose construction, maintenance, and monitoring involves a great deal of technology. A typical riser pipe consists of multiple layers of material, as shown in Figure 1.1 [2]. This diagram shows a cross-section of flexible pipe as would be seen near a flange. The outer layers (3, 4), are typically steel tape wound around the flexible polymer layer to contain the up to 200 psi pressures and reinforce the liner against radial and axial stress. An outer rubbery layer (5), guards against abrasion. The flexible polyamide below this layer (2) is usually polyamide-11 (PA11), but under some circumstances other polymers, such as polyvinylidene fluoride or polyethylene, may be used.

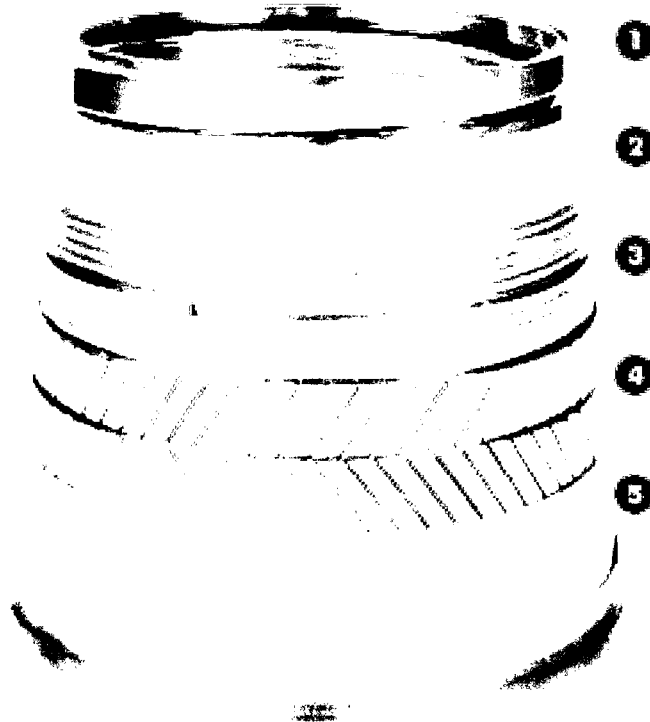


Figure 1.1: Construction of NKT Flexibles' PA11 pipe. Layer 1 is made of steel and protects against abrasion. It also protects against collapse should fluid flow be stopped. Layer 2 is the PA11 liner. Layers 3 and 4 are made of steel tape and reinforce against internal pressure as well as radial and axial stresses. Layer 5 is an outer rubbery layer that guards against abrasion [2].

The inner flexible “z-locked” steel layer (1) provides abrasion protection from pigging tools used in maintenance, and also supports the flexible pipe from collapse under water pressure from the sea’s pressure when oil production is slowed or stopped.

Once the crude oil has been extracted from the well it is transported for initial processing, typically to an offshore platform or a specially designed anchored boat. There the oil is separated from the produced water, which accompanies the crude upon extraction, as well as the natural gas that is also present. The petroleum products are then transported to shore for further refining and distribution.

The safety of offshore oil production is a top priority for oil producers, as mishaps in the typically secluded and often harsh environments may lead to the loss of life as well as irreparable damage to the environment. The recent Deepwater Horizon explosion in the Gulf of Mexico is one such example. Another notable incident, the explosion of the Piper Alpha platform in the North Sea, occurred in 1988 leaving almost 200 dead [3]. Statoil, operating primarily in the North Sea, recently had an injected water (used to maintain pressure in the oil reservoir during extraction) leak in 2008 in their Tordis field [4]. Even once on shore for refining, danger of explosion still exists, as was the case in the 2005 BP Texas City refinery explosion that left 15 dead [5].

According to Rex Tillerson, CEO of Exxon-Mobil Corporation, “Deepwater production, which did not exist prior to 1989, today makes up 15 percent of all non-OPEC production.” He goes on to say that, “By 2030, it will grow to nearly 20 percent.” As we continue to search for oil in increasingly harsh environments, the proper

monitoring and maintenance of appreciable safety margins must be upheld, because according to Tillerson, “If you can’t measure [a safety margin], you can’t manage it” [6].

This dissertation represents work that advances the monitoring, and subsequently the safety, of PA11 flexible pipes in the offshore oil and gas industry by:

- **Creating a model relating the rate and degree of PA11 hydrolysis in water that is the most scientifically accurate and thorough of any model until this point (Chapter 3).**
- **Providing scientifically valuable information regarding the competing kinetic processes of hydrolysis and recombination in the presence of variable temperature and water (Chapters 3 and 5), small alcohols (Chapter 3), and small acids (Chapters 4 and 5).**
- **Demonstrating, for the first time, the effects of methanol and ethanol, used to control hydrate formation, on the aging of PA11 flexible liner (Chapter 3).**
- **Demonstrating that the effects of common small organic acids, such as acetic acid, are far more important than the current focus on the degradative effects of pH of the water or the presence of naphthenic acid in the crude oil (Chapter 4) [7].**

- Predicting for the first time the effects of temperature, water, and acetic acid concentration on the degradation of PA11 flexible pipe liner over the course of years, with results verified by actual field data (Chapter 5).
- Analyzing the role of accelerated aging studies and their value in describing offshore systems regarding both polymer degradation (Chapters 3, 4, 5) and annealing on mechanical tensile properties (Chapter 5).

The appendices first include tabulated data presented in this dissertation, and then detail information on work regarding the use and processing of functionalized graphene sheets (FGS), a precursor to graphene, a relatively new and popular field of study, which I plan to pursue in my postdoctoral work beginning in January.

- Appendix A contains data tables relevant to Chapters 3, 4, and 5.
- Appendix B contains a patent application submitted in June 2009 and June 2010 describing the controlled reduction of FGS during processing.
- Appendix C is a submission to *Polymer Preprints* regarding a talk which I will give at the 2011 American Chemical Society meeting describing the controlled reduction of FGS during nanocomposite processing, and its implications.

- Appendix D is a full-length manuscript detailing the work shown in Appendix C, in the final stages of revision to be submitted for publication.

Chapter 2: Experimental Methods and Techniques

SEC-MALLS

One primary means of determining the weight-average molar mass (MW) of a polymer is MALLS, or Multiple Angle Laser Light Scattering. This light scattering technique, coupled with Size Exclusion Chromatography (SEC), fractionates a dissolved polymer sample based upon chain size and then determines the molecular weight of each fraction, from which an MW of the sample may be calculated.

The purpose of SEC is to separate fractions of a polymer based on hydrodynamic volume, or the time-averaged volume of a given polymer chain in a random coil under the conditions of separation [8]. This separation is conducted by forcing a polymer solution through a High Performance Liquid Chromatography (HPLC) system that contains in-line SEC columns. The columns are packed with small polymer beads whose composition is selected based upon compatibility with the solvent used and the polymers analyzed. Small channels that run through the beads in a convoluted manner perforate the beads [9]. As polymer molecules travel through a column, the small chains pass through the convoluted paths, giving these chains a longer path length through the column as compared to the larger chains which cannot fit through the pores and thus pass directly between the beads, resulting in a shorter path length [9]. As a result, chains with a larger hydrodynamic volume elute prior to small chains.

In the case of the system used in this dissertation, columns HFIP-LG, HFIP-803, and HFIP-805 from Shodex of Japan were used. With packing beads made of a polystyrene-divinyl benzene copolymer, the different model numbers indicate the pore sizes in the beads, which determine how the separation is effected. Column HFIP-803 separates at a 7×10^4 g/mole of polystyrene exclusion limit, column HFIP-805 separates at a 4×10^6 g/mole of polystyrene exclusion limit, and column HFIP-LG is a smaller sacrificial guard column whose purpose is to capture destructive impurities before they reach the larger and more expensive analytical columns [10]. The guard column performs negligible separation.

Multiple-Angle Laser Light Scattering (MALLS) is the technique used that characterizes the separated polymer fractions that result from SEC. The theory deals with Debye scattering as it occurs in dilute polymer solutions. Similar to the Zimm plot, which uses angular scattering data from a range of polymer concentrations and angles to extrapolate to a zero angle and zero concentration, the Debye plot uses the very dilute output of SEC as an approximation to zero concentration, with the zero-angle calculation remaining the same in the case of the Zimm plot [11]. At any given time in our HPLC system, one may consider

$$\frac{Kc}{R_\theta} \approx \frac{1}{M_w} \left[1 + \frac{16\pi^2}{3\lambda^2} \langle r_g^2 \rangle \sin^2\left(\frac{\theta}{2}\right) \right] \quad (2.1)$$

where c – concentration, R_θ – excess Rayleigh ratio (ratio of intensity of scattered light to intensity of incident light at angle θ), $\overline{M_w}$ – weight-averaged molar mass, λ – wavelength of light scattered, $\langle r_g^2 \rangle$ – mean square radius of gyration, θ – detection angle of scattered light, and

$$K = \frac{4\pi^2 n_0^2}{N_A \lambda_0^4} \left(\frac{dn}{dc} \right)^2 \quad (2.2)$$

where n_0 – pure solvent refractive index, N_A – Avogadro's number, and dn/dc – refractive index increment of polymer in the solvent [12].

The light scattering detector used in data collection in this case was the Wyatt¹ miniDAWN, with $\lambda = 690$ nm and $\theta = 45^\circ, 90^\circ, 135^\circ$.

As the miniDAWN provides all scattering information of the polymer solution, one needs the polymer concentration at a given time to satisfy the above equation. Typically, this is carried out by a UV absorbance detector or, in this case, a Wyatt Optilab 803 dynamic refractive index (RI) detector in-line on the chromatography system. With a dn/dc for PA11 in 1,1,1,3,3,3-hexafluoroisopropan-2-ol (HFIP) of 0.253, the signal from the Optilab 803 detection cell could be used to determine the polymer concentration for a given sample of SEC eluent.

Figure 2.1 illustrates the schematic of the SEC-MALLS system.

The HPLC pump is a Waters 515 model at a flow-rate of 0.6 mL/min, and the degassing process is a constant Helium sparge under atmospheric pressure. Tubing was 1/16" O.D. stainless steel.

¹ <http://www.wyatt.com/>

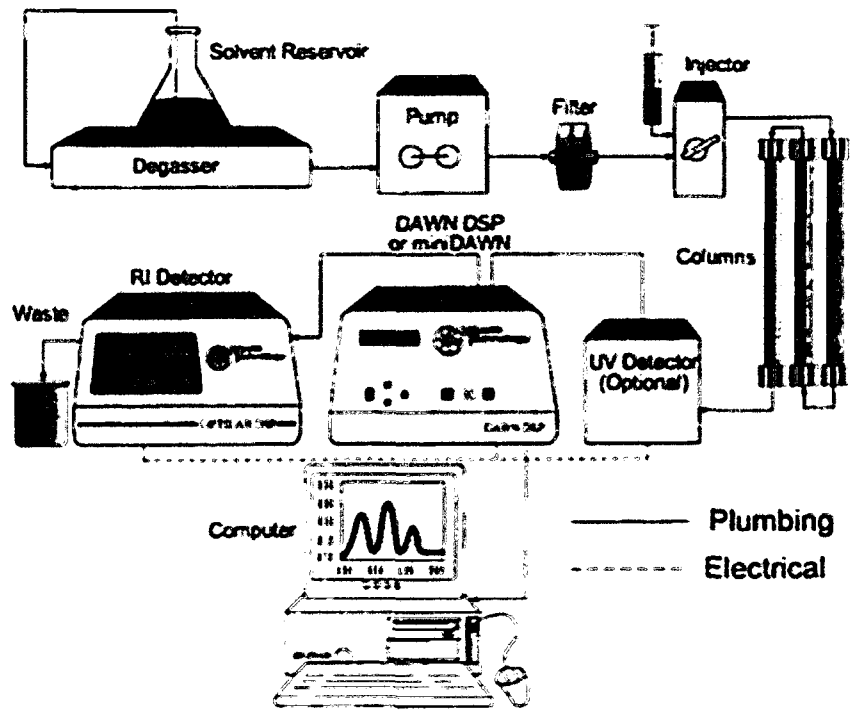


Figure 2.1: SEC-MALLS HPLC system. The system described in this chapter does not include a UV detector. Reproduced from Carraher, Charles E., Jr., *Polymer Chemistry, 6th Ed.* New York: Marcel Dekker, Inc., 2003 [13].

As the Waters 515 is a dual-plunger pump, pressure fluctuations of 5-10 psi are prone to occur due to minute differences between the two plungers. These fluctuations may cause noise in the detected signals, thus some 0.005" I.D. stainless tubing was added post-detector to increase the total pressure of the system to ~500 psi, thereby mitigating the effects of the small fluctuations.

Finally, small pressure fluctuations relating to the temperature change by the lab HVAC system were present, yet of a long enough wavelength to easily subtract from the instrument signals when establishing signal baselines for each run.

Polymer solutions were made at 2 mg/mL in HFIP and the injection volume into the system was 100 μ L. After sample injection, Wyatt Technologies' ASTRA software recorded a chromatogram from the three light scattering angles as well as the concentration information from the RI detector. A typical chromatogram is shown in Figure 2.2. Pre-polymer signal noise is thought to be very small dissolved gas bubbles introduced by the pressure drop that occurs upon sample injection. These bubbles elute before any appreciable polymer is detected, and therefore doesn't affect molar mass. Upon run completion, baselines were defined, the polymer elution times were specified, and a report was generated by ASTRA.

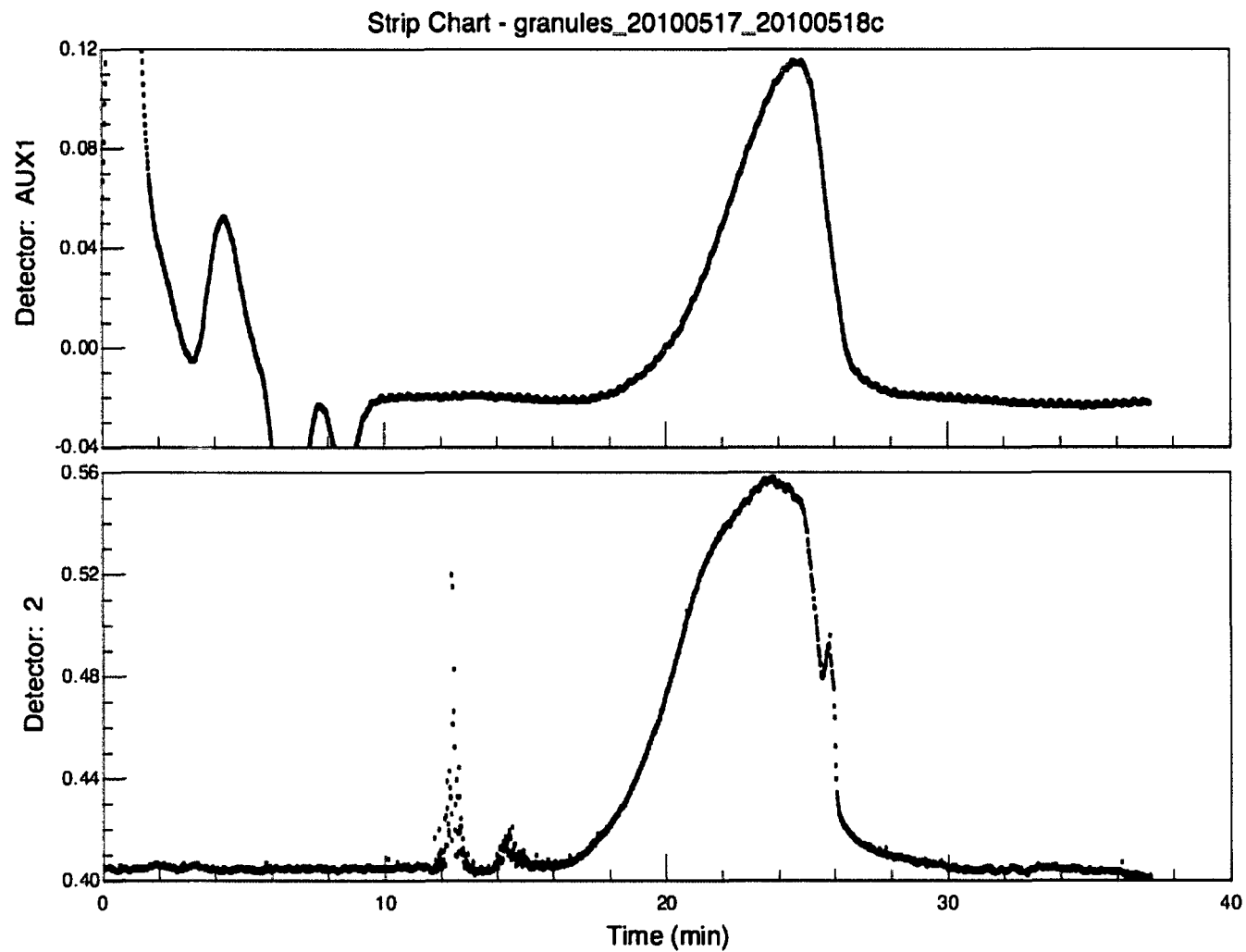


Figure 2.2: Typical output of the SEC-MALLS system, with refractive index (top) and 90° light scattering (bottom) signals.

In order to determine accuracy and precision for this method, as well as verify that the system is properly working, a PA-11 standard is run weekly as well as after any maintenance on the system. This standard, BESNO PA-11 granules, has an independently verified MW of $39\,000 \pm 2\,000$ g/mole. The solution composition information is in Table 2.1, and the SEC-MALLS results of repeated runs are shown in Table 2.2. A plot of molar mass vs. elution time of a typical granules run with an RI detector overlay is shown in Figure 2.3. Note that the decreasing molar mass vs. time relationship as expected by SEC theory is demonstrated.

Table 2.1: Besno PA-11 P40TLOS Granules Standard Solution Information

Density HFIP [14]:	1.6		g/mL
Mass HFIP:	8.066	± 0.001	g
Volume HFIP:	5.041	± 0.001	mL
Mass Polymer:	10.1	± 0.1	mg
Volatile Content:	12.7	± 0.5	%
Corrected Poly. Mass:	8.82	± 0.04	mg
Solution Concentration:	1.75	± 0.01	mg/mL
Injected Mass (100 μ L):	175	± 1	μ g
Independently Verified Molar Mass:	39000	± 2000	g/mole

The standard deviation of the molar masses in Table 2.2 indicates that an uncertainty of ± 2000 g/mole is appropriate. A probable source of error in the MW determination could be due to inhomogeneous sample characteristics, which are amplified due to the very small amounts of sample used to make solutions.

The SEC-MALLS HPLC system is also useful for other HFIP-soluble polymers, given they dissolve readily. For a given polymer system, one must first

determine the dn/dc value prior to determining molar mass results. In order to do so, a solution of the polymer is created in HFIP. The exact concentration is then calculated based on volatile content information from a TGA experiment. Multiple runs are conducted and the average dn/dc necessary to calculate the polymer mass injected is found. Given that, the MW of the polymer sample may be known.

Table 2.2: Besno PA11 P40TLOS granules SEC-MALLS results. Multiple runs were performed to determine instrumental uncertainty.

Run number	Calc. mass dn/dc = 0.253 (μg)	Molar mass at dn/dc = 0.253 (g/mole)	dn/dc to match actual mass (mL/g)	Molar mass at exp'l dn/dc (g/mole)
5-18a	149	36190	0.216	42390
5-18b	167	38700	0.242	40460
5-18c	164	40110	0.238	42640
5-19a	172	36460	0.249	37050
5-20a	162	36980	0.235	39810
Average:	163	37690	0.236	40470
Std. Dev.	9	1669	0.012	2270

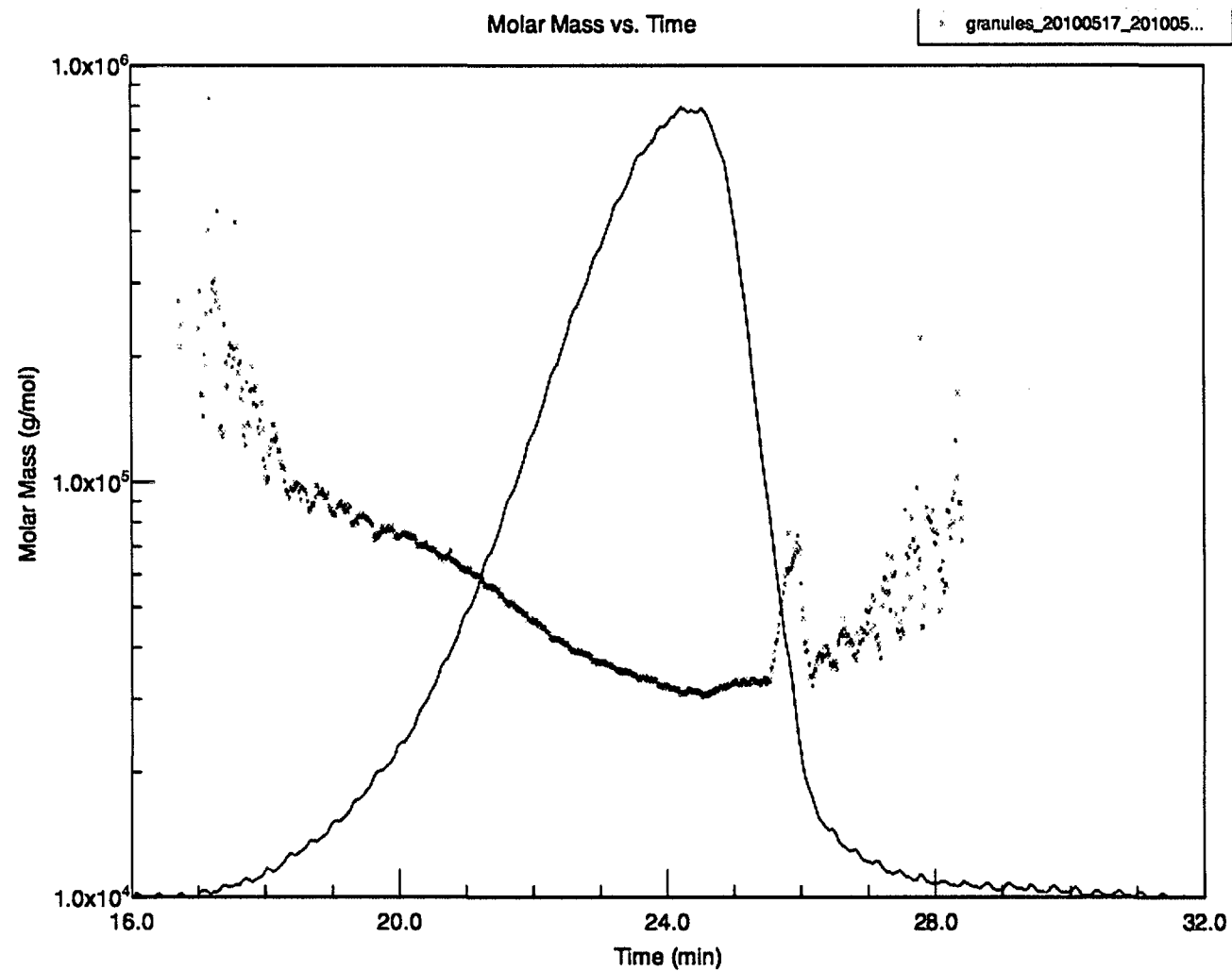


Figure 2.3: SEC-MALLS results. Molar mass vs. time for Besno PA11 P40TLOS granules is shown (dotted line) along with refractive index detector output (solid).

Intrinsic Viscosity Measurements

Another method of characterizing the molecular weight of a polymer is the determination of its intrinsic viscosity. In contrast to MALLS, viscosity measurement is a “secondary method” in that it is not a direct measure of the molar mass of a polymer; instead it must be related through some experimentally defined relationship. The relationship typically employed is given by the Mark-Houwink equation, which, through the use of two solvent/polymer system-specific parameters, relates the intrinsic viscosity of a polymer to its viscosity-average molecular weight [9]. The well-understood theory dealing with the intrinsic flow properties of a polymer necessitates measurement of relative polymer-solvent viscosities at different concentrations and extrapolation of said viscosities to a zero concentration.

Considering the relative viscosity of a polymer to be directly related to the ratio of the time a polymer solution at a given concentration takes to pass through a viscometry capillary tube to the time pure solvent takes to pass through said tube, or:

$$\eta_r = \frac{t}{t_0} \quad (2.3)$$

where η_r – relative viscosity, t – time for a polymer solution to pass through a capillary, and t_0 – time for pure solvent to pass through a capillary [9].

Similarly, the specific viscosity, η_{sp} , is defined as the increase of the viscosity of a solution due to the presence of dissolved polymer [9], or:

$$\eta_{sp} = \eta_r - 1. \quad (2.4)$$

As there is a direct relationship between the concentration of the dissolved polymer and the specific viscosity, one may calculate the reduced specific viscosity (η_{sp}/c) to take this factor into account [9].

Finally, the intrinsic viscosity, $[\eta]$, is defined as the limit of the reduced specific viscosity as the polymer concentration in solution approaches zero [9], or:

$$[\eta] = \lim_{c \rightarrow 0} \left(\frac{\eta_{sp}}{c} \right). \quad (2.5)$$

For industrial purposes, a single solution corrected inherent viscosity (CIV) is determined adapted the already characterized Kraemer relationship. The CIV is defined as [15,16]:

$$CIV = \ln \left(\frac{\eta_r}{C} \right). \quad (2.6)$$

This single solution is to have a concentration of 5 mg/mL. This more efficient method is useful for comparing the viscosity-average molecular weight of PA-11 samples and for detecting changes in molecular weight due to degradation. In Equation 2.6, C is defined as:

$$C = c(1 - p) \quad (2.7)$$

where c is the solution concentration and p is the plasticizer content. The determination of p is described in the following Thermogravimetric Analysis section. Plasticizer may be present at concentrations over 15% in fresh material, and therefore must be taken into account when calculating the true concentration of the polymer and subsequently its CIV [7].

Regarding the single solution viscosity CIV measurement of PA-11, one must select a viscometer for its capillary size based on the flow time for pure solvent. For viscosity measurements, m-cresol is chosen over HFIP (the solvent of choice for HPLC analysis) due to it being orders of magnitude cheaper. Given the viscosity of pure m-cresol at room temperature, size 2 Ubbelodhe viscometers were used to give run times of at least 100 seconds to allow for accurate measurements. As the viscosity of a solution is temperature-dependant, all experiments were conducted in a temperature-controlled oil bath held at 20°C.

Polymer solutions were created by first chopping a sample into small pieces in order to increase surface area to speed dissolution. These samples were then dried at 100-110°C for no less than 1 hour. Solutions were made at nominal concentrations of 5mg/mL, with the exact final concentrations calculated based upon the volatile content of the polymer as determined by thermogravimetric analysis, explained in the next section.

Fresh m-cresol was run through the viscometers at least once for every three polymer solutions tested. The fresh run times, when compared to prior fresh run times, gave information regarding potential contaminants in the viscometers, problems with bath temperature regulation, or impurities in the solvent. Both fresh m-cresol and polymer solutions were run until three subsequent times agreed to within 1% of each other.

Run-time and concentration information was then used to calculate the CIV for a given sample. Typical data is shown in Table 2.3. The slight differences between viscometers lead to differing pure solvent run times, reinforcing the importance

of recording which viscometer one uses for a given measurement. The five standard polymer solutions give outstanding precision. Given a standard deviation of 0.004, one may say that 95% of the time a CIV value is within ± 0.008 of the true value.

While the Mark-Houwink equation relates the intrinsic viscosity of a polymer to its viscosity-average molecular weight, one may consider a two-parameter relationship between the weight-average molecular weight as determined by MALLS experiments and the CIV. As many samples were characterized via both the MALLS and by viscometry, one may determine a relationship between the two quantities by plotting $\ln(\text{MW})$ vs. $\ln(\text{CIV})$ and calculating a least-squares fit line. Figure 2.4 illustrates the least squares fit line, whereas Figure 2.5 shows this line with the actual data by plotting MW vs. CIV. Also included in Figure 2.5 is the pre-2006 line, which includes fewer data points and is constructed using a base-10 log function.

Table 2.3: Besno PA11 P40TLOS granules standard single-solution CIV determination. All viscometers are size 2 Ubbelodhe, m-cresol is 99+% pure, and the volatile content of the samples was 12.7%.

Standard Solution Number	Viscometer Serial Number	Pure Solvent Run Time (s)	Polymer Solution Run Time (s)	Uncorrected Poly. Sol'n Conc. (mg/mL)	Corrected Poly. Sol'n Conc. (mg/mL)	CIV
1	E-591	190	360	5.000	4.365	1.46
2	G-197	181	342	5.000	4.365	1.46
3	E-493	183	344	5.001	4.366	1.45
4	G-197	179	339	5.000	4.365	1.46
5	E-493	179	339	5.000	4.365	1.46
Average:						1.46
Standard Dev.:						0.004

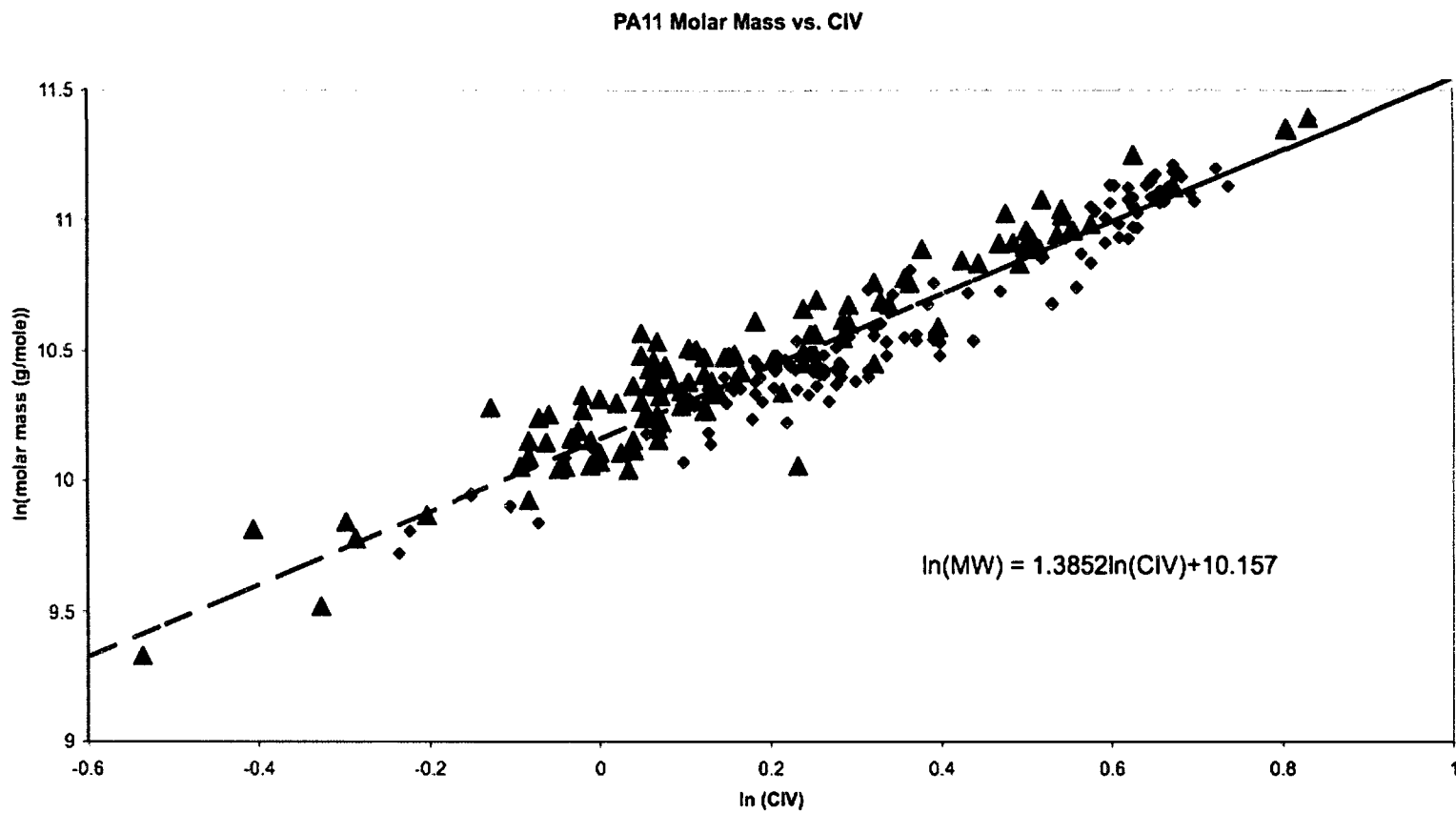


Figure 2.4: A plot $\ln(\text{MW})$ vs. $\ln(\text{CIV})$ for PA11 samples to establish a mathematical relationship between the two types of measurements.

PA11 Molar mass vs. CIV

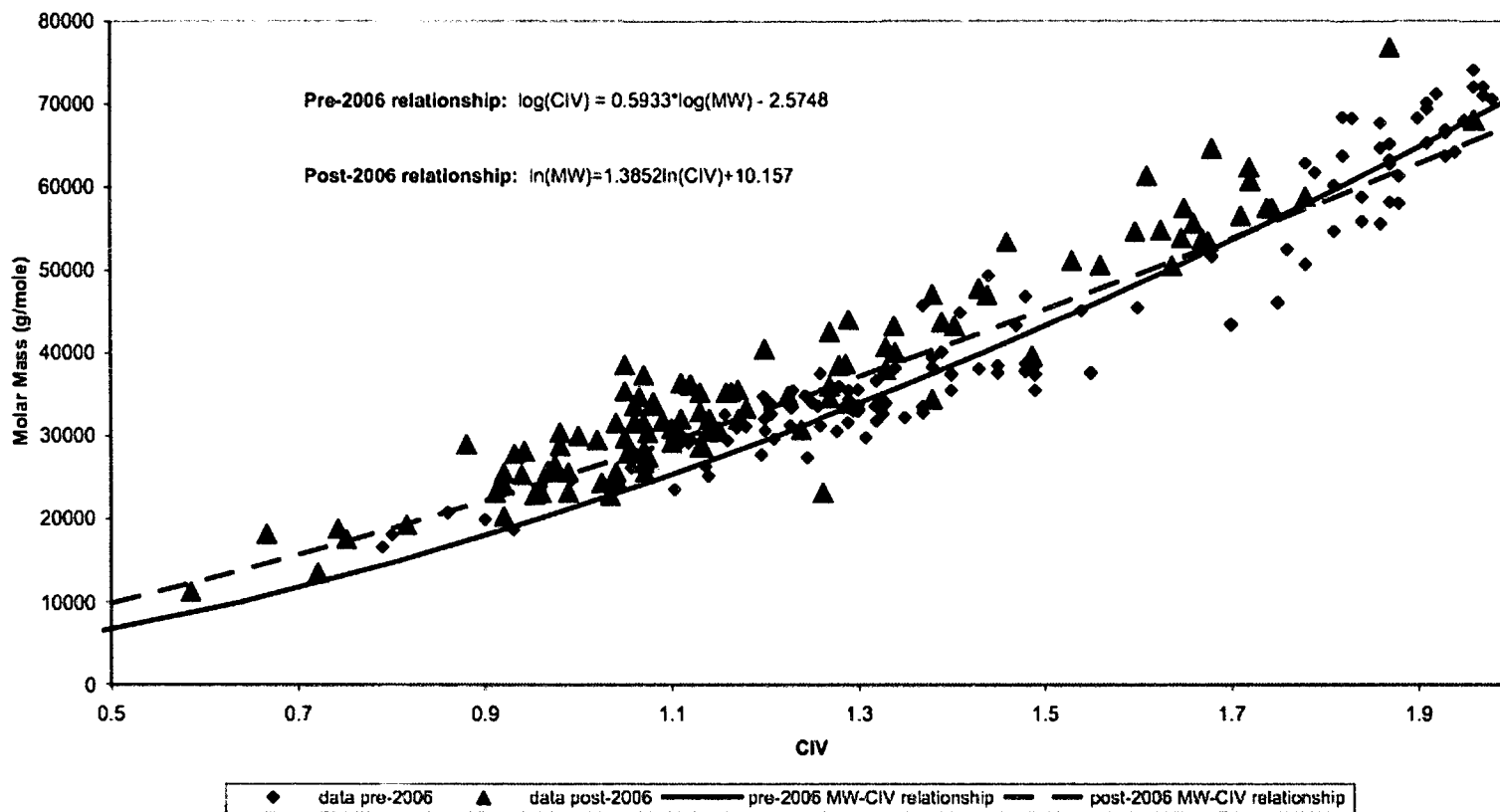


Figure 2.5: Molar mass vs. CIV for measured PA11 samples.

The scatter about the line in Figure 2.5 may be in part attributed to error in the measurements. It also should be considered that these data points were collected from some aging experiments in which organic acids were present, thereby introducing possible modifications of the polymer chains beyond the hydrolysis scheme presented in Chapter 3: PA-11 Aging in Water, Methanol, and Ethanol. These end-group variations, further discussed in Chapter 4: PA-11 Aging in the Presence of Low Concentrations of Small Organic Acids, may modify the flow properties of the polymer of a similar chain length thus giving a different CIV value for a very similar weight-averaged molecular weight. For this reason, one should consider at the very least a MALLS measurement instead of conducting a simpler CIV experiment and converting to a weight-average molecular weight. In other words, the methods are not completely interchangeable.

The CIV for other polymers may as easily be determined given the mathematical and experimental work outlined above and will be treated as the situations appear in subsequent chapters.

Thermogravimetric Analysis (TGA)

Regarding the determination of the corrected inherent viscosity (CIV) of a polymer, the concentration of volatile compounds in the polymer must be determined for calculation of the true polymer concentration in the solution being tested, as this value will be significantly lower than the nominal solution concentration. Failure to take the volatile content into account will result in the understatement of CIV.

Thermogravimetric analysis (TGA) provides a means for one to monitor the mass loss of a material as a function of temperature in a programmable furnace.

The instrument used in these experiments is a model Q500 from TA Instruments², which is capable of mass determination to the nearest microgram, furnace control up to 1000.0°C, and can maintain an inert environment to prevent oxidation of the polymer in the melt state. Such oxidation would lead to the reduction of sample mass through evolution of carbon dioxide and water, and subsequent over-estimation of volatile content. This would propagate through CIV calculations to yield a value higher than is the case.

The first step in the conduction of a TGA experiment is to prepare a slice of sample weighing $20 \text{ mg} \pm 10 \text{ mg}$. It should be no thicker than 1 mm so that the diffusion mechanism does not hinder volatile evolution. This sample is then placed in a pan that has been cleaned via pyrolysis (a Bunsen burner will suffice) and tared by the instrument. The instrument is programmed to:

- 1 – Select N₂ as the purge gas.

² <http://www.tainstruments.com/>

2 – Equilibrate at 105°C and hold for 25 minutes.

3 – Equilibrate at 110°C and hold for 35 minutes.

4 – Equilibrate at 240°C and hold for 120 minutes.

Step (1) is to ensure no oxidation will occur during the experiment. Steps (2) and (3) are to drive away water and low-MW compounds such as water, small alcohols, or small acids. Step (4) removes the plasticizer from the polymer, which vaporizes readily between 200°C and 240°C [7].

Upon completion of the TGA experiment, the bundled TA Universal Analysis software automatically constructs a plot showing the percentage of mass loss vs. time. The user then annotates the plots for convenience based on the information desired. Figure 2.6 shows a typical TGA run on the Rilsan Besno PA-11 P40TLOS granules standard. According to the Figure 2.6, our sample had 1.42% water and 11.6% plasticizer. This is consistent with the published total plasticizer content of 12.7% [7].

As the mass and temperature are precisely known in a TGA experiment, the main source of error is limited to the actual sampling of the polymer. In order to avoid overloading the balance, one must use a relatively small amount of sample, ensuring that it accurately represents the whole of the polymer. It is therefore ideal in the case of a large sample to repeat the experiment multiple times, with sampling that is adequately spatially separated.

Sample: granules
Size: 20.2330 mg
Method: Ramp
Comment: plasticizer

TGA

File: C:\...jaeton\granules 20100517.001
Operator: ajg
Run Date: 2010-05-17 10:25
Instrument: TGA Q500 V6.3 Build 189

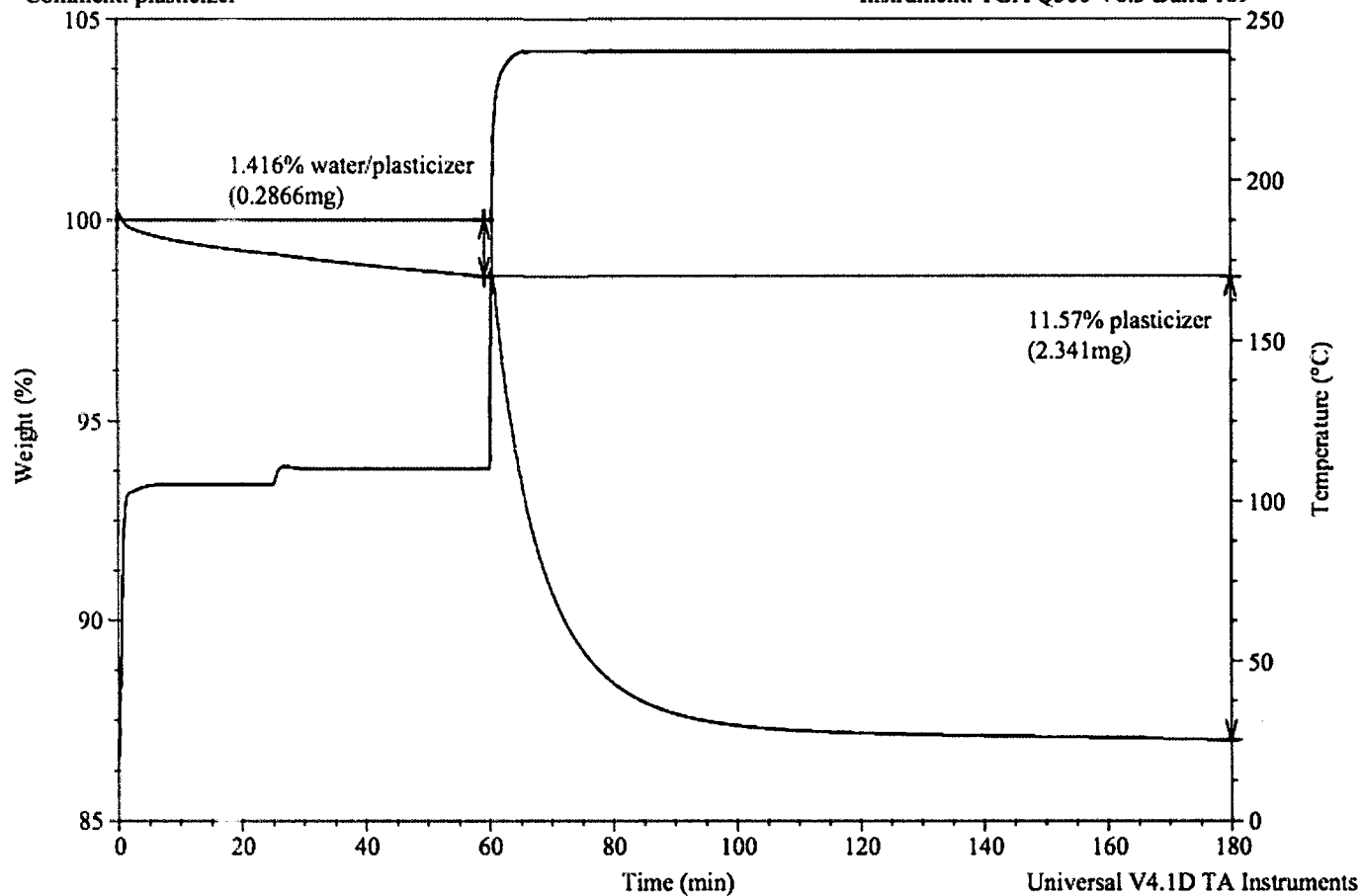


Figure 2.6: TGA experiment showing water and plasticizer content of Besno PA11 P40TLOS granules.

Differential Scanning Calorimetry

A second thermal analysis method is Differential Scanning Calorimetry (DSC.) Calorimetry, the study of enthalpy change as a result of a chemical reaction or a change in physical state, is mainly used in this work to determine the degree of crystallinity in PA11. It is also useful in the determination of glass transition temperatures and how they are affected in copolymers through altering component ratios and/or annealing, and in the characterization of the reduction of carbon nanoparticles in the copolymers in which they are added.

The percent crystallinity of PA11 describes the ratio of crystalline material (as opposed to amorphous) to total sample within this semi-crystalline polymer. This ratio plays a role in the theory of heterogeneous degradation of this polymer system, but more noticeably, it influences the mechanical properties on the macroscopic scale of the polymer system, as shown in Chapter 5 [15]. The means of determining the percent crystallinity using DSC consists of heating the polymer through the temperature at which the crystalline regions melt, and then comparing the amount of heat it takes to melt these regions, in Joules per gram of sample, to the amount of heat it would take for 100% crystalline PA-11 to melt [9].

The conduction of a DSC experiment to determine the percent crystallinity of PA-11 begins with sampling a representative 5-15 mg of polymer, accurately determining its mass, and sealing it in a hermetic aluminum pan by crimping it using a

specialized press. The material is then placed in the instrument, and under a steady flow of nitrogen, subjected to the following method:

- 1 – Jump to 130.00°C.
- 2 – Modulate $\pm 1.00^\circ\text{C}$ every 60 seconds.
- 3 – Ramp $1.00^\circ\text{C}/\text{min}$ to 215.00°C.

Step (1) includes a jump to the temperature near the temperature range of interest so as to maximize efficiency. Step (2) gives complex heat capacity information as a function of temperature and is carried out throughout step (3), which heats the sample at a steady rate through the temperature range of interest.

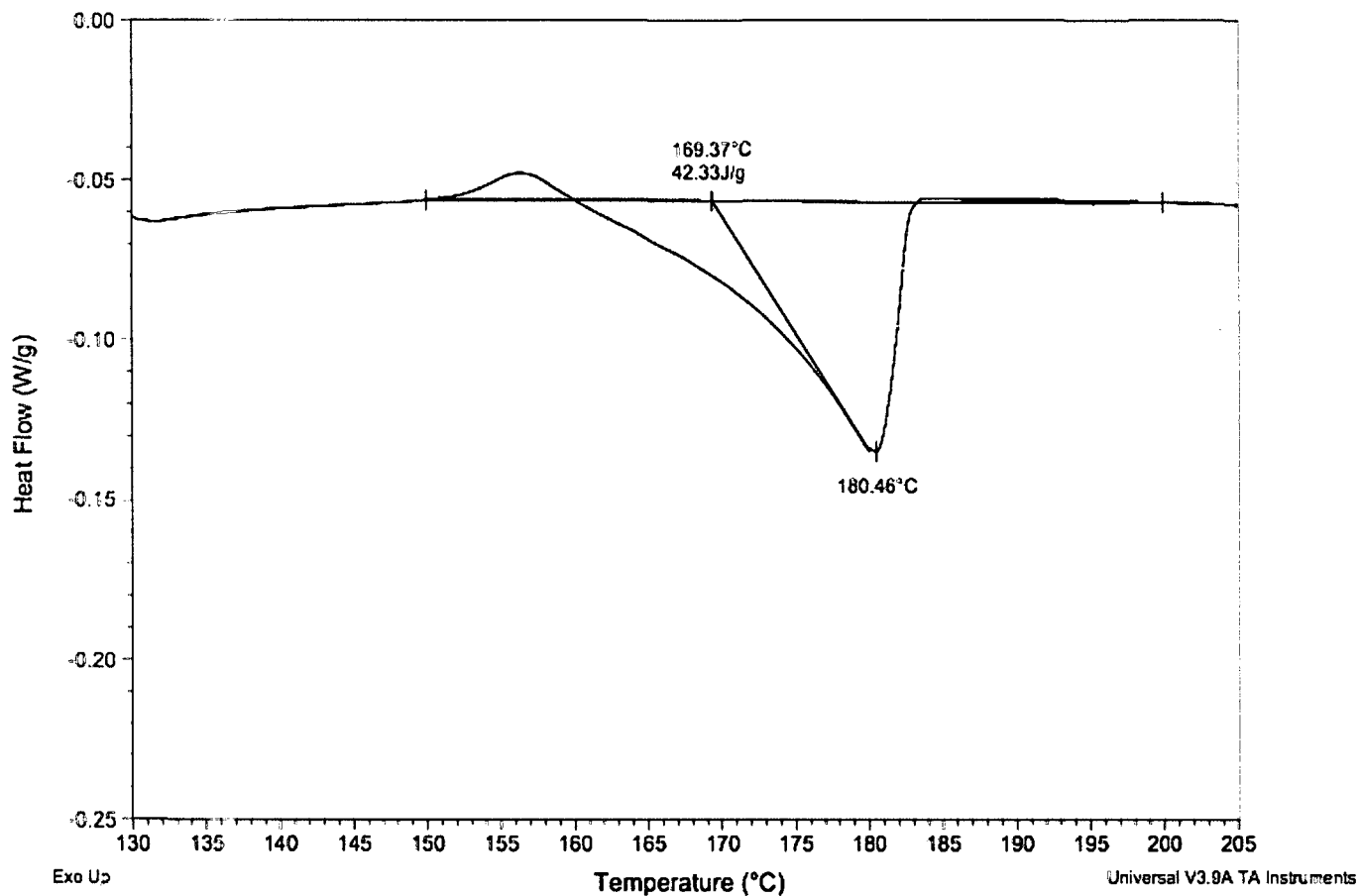
Figure 2.7, a plot of heat flow (in W/g) vs. temperature ($^\circ\text{C}$), shows results typical of a DSC experiment on a Rilsan Besno PA11 P40TLOS granules standard. The endothermic peak is a result of the melting of the crystalline regions. This peak is integrated from 150°C to 200°C and the heat of fusion of the melting process is given. This value is then divided by 190 J/gram, which is the heat of fusion of 100% crystalline PA-11, and multiplied by 100 so as to be a percentage [17].

Table 2.4 shows the results from a series of five runs of the Rilsan Besno PA-11 P40TLOS granules standard. The application of a statistical Q-test to the peak melting temperatures allows one to throw out the 182.40°C value in run 1 with greater than 99% confidence. The resulting precision of the peak melting temperatures indicates the good temperature resolution of the instrument. The heats of fusion also tend to agree, with the standard deviation equivalent to 4% of the magnitude of said quantities.

Sample: granules DSC run 3
Size: 6.4000 mg
Method: kinetic and Tg
Comment: to determine precision

DSC

File: C:\...granules 3 20100517.001
Operator: ajg
Run Date: 17-May-10 15:49
Instrument: 2920 MDSC V2.6A



30

Figure 2.7: DSC plot of Besno PA11 P40TLOS granules standard. Ramp rate is 1°C/min.

Table 2.4: DSC results of five runs of Besno PA11 P40TLOS granules standard to establish instrumental uncertainty. The heat of fusion of 100% crystalline material was taken to be 190 J/g [17].

Run number	Peak Melting Temperature (°C)	Heat of Fusion (J/gram)	Percent Crystallinity (%)
1	182.4	42.3	23.2%
2	180.4	45.6	25.3%
3	180.5	42.3	23.5%
4	180.7	45.8	25.3%
5	180.5	45.1	25.0%
Average:	180.5	44.2	24.4%
Std. Dev.	0.1	1.8	1.0%

Sources of error in these experiments begin with the issue of heterogeneity in a polymer sample. Depending on the dimensions of the sample, the presence of temperature gradients could lead to varying results within a sample. Thus, sampling should be representative of the whole the sample, which may be verified through repeated experiments. Another source of error lies in the determination of the mass of the sample studied, as due to balance limitations, one may know the mass only to 0.1 milligram. This source of error tends to be small, ~1%.

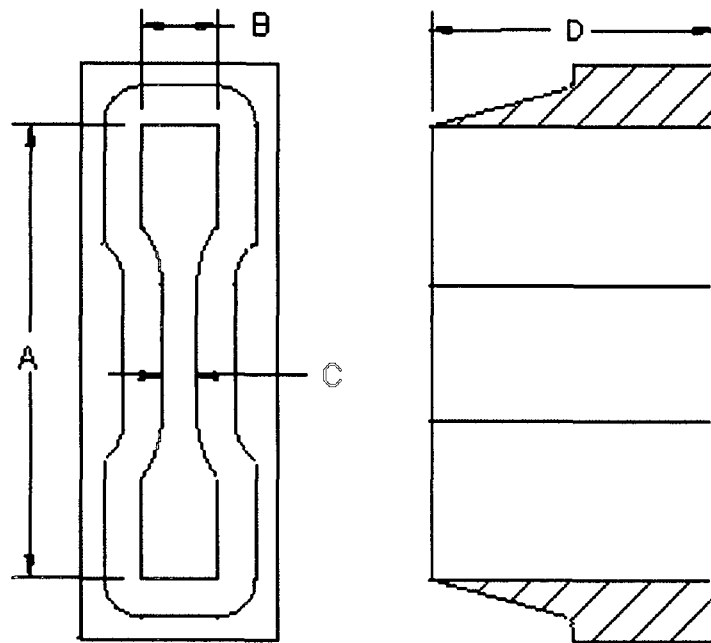
The DSC may also be useful to the polymer chemist in other ways, such studying the cure kinetics of epoxy systems, thus allowing for the tuning of such systems to achieve desired qualities, monitoring effects of composite composition on thermal properties, or even measuring the heats of reduction or oxidation of materials.

Tensile Testing

The tensile test is one means of measuring the macroscopic mechanical properties of a material. Values such as percent elongation, Young's modulus, and maximum stress are quantities that indicate the condition of a polymer to the typical end-user of the polymer products. These quantities are affected by the average molar masses of the polymer chains, the spatial relationship of the chains to each other (degree of crystallinity being an example), and the temperature at which the material is tested.

The shape of a sample to be tested must also be considered, as one should localize the stretching force to an identifiable area of a consistent cross section. Thus, ASTM D-638³ defines the dimensions for the mechanical dies used to punch the tensile samples. The specific die to be used is selected based on the material to be tested and the size of the sample from which the test specimen is to be cut. It should be noted that mechanical samples of different sizes may yield different tensile quantities. For example, this can be due to the introduction of small defects in a brittle sample upon punching of the test specimen. For smaller test dies, these defects may represent larger areas of the samples. Thus one should be considerate of this phenomenon. Throughout work presented in this dissertation, the ASTM D-638-5-IMP test die is used. Figure 2.8 shows its dimensions.

³ <http://www.astm.org/Standards/D638.htm>



D-638-5-IMP

#	Nominal Dimension
A	2.500
B	0.375
C	0.125
D	1.250

*Dimensions are in Inches

Figure 2.8: ASTM tensile test die D-638-5-IMP dimensions

Another factor that influences the measured properties is the speed at which the sample is stretched. A sample stretched more quickly will not allow time for stress-relaxation within the polymer chains, whereas a sample stretched excessively slowly will not give an accurate representation of reaction to stress in typical industrial environments. An industry-wide accepted strain rate of 0.25 inch/minute is employed for all stretched samples in this dissertation.

Our specific tensile test instrument, the MTS 810 by Mechanical Testing Systems⁴, allows one to vary strain rates from zero to more than twelve inches/sec, and is equipped with a load cell capable of measuring stresses up to 5000 lbs. Once the sample is loaded and the instrument is programmed, it runs until the user stops the experiment upon the sample being broken. The instrument samples data at a user-specified interval, and records time, strain, and force in a .txt file. The user then divides the force by the cross-sectional area of the portion of the test sample being strained to yield the pressure in MPa. This pressure is the stress used to make the stress vs. strain plot.

It should be noted that as the sample is stretched, the cross sectional area of the test piece decreases. If one were to continuously calculate a pressure with a given force using the original cross sectional area, one would be calculating the “engineering stress,” as opposed to the “true stress” [18]. This calculation tends to underestimate maximum stress withstood by the material because as the sample is stretched, its cross-sectional area decreases. The true stress is therefore higher. One may correct for this error by assuming the volume of the rectangular section remains constant. Since

⁴ <http://www.mts.com/>

$$V_{\text{initial}} = L_{\text{initial}} \times A_{\text{initial}} \quad (2.8)$$

where volume (V), length (L), and area (A) are all known by measurement before the experiment begins, one may also assume that volume remains constant, or

$$V_{\text{initial}} = V_{\text{time}} \quad (2.9)$$

where V_{time} is the volume at any given time in the experiment. Therefore

$$L_{\text{initial}} \times A_{\text{initial}} = L_{\text{time}} \times A_{\text{time}} \quad (2.10)$$

or

$$A_{\text{time}} = \frac{L_{\text{initial}} \times A_{\text{initial}}}{L_{\text{time}}} \quad (2.11)$$

As the instrument records the strain along with time, L_{time} of the test sample is known throughout the experiment. With the above equation, one may calculate the cross-sectional area at any point in time and therefore be able to calculate the true stress for a test specimen.

Figure 2.8 shows the typical true stress vs. strain curve for fresh plasticized PA-11 with a weight-averaged molar mass of 68 000, determined using SEC-MALLS. The resulting mechanical properties are labeled and tabulated on the plot. Figure 2.9 is the zoomed-in initial linear portion of the curve used to determine the tensile modulus. Table 2.5 shows the results from five runs of this material, to establish precision. Note that the standard deviations for all measured properties are relatively low.

Table 2.5: Unaged commercial PA11 tensile test results. The molar mass was determined by SEC-MALLS to be 68 000 g/mole. The samples were cut with ASTM die size D-638-5-IMP. The strain rate was 0.25 in/min.

Run number	Elongation at Break (%)	Modulus (MPa)	Maximum Stress (MPa)
1	247%	64	115
2	250%	75	108
3	251%	72	107
4	252%	76	125
5	255%	65	141
Average:	251%	70	119
Std. Dev.	3%	6	14

Unlike most of the methods described so far, the tensile test gives a sense of the overall molecular properties of a sample, which may be dependant on many microscopic factors.

**True Stress v. Strain
Plasticized PA-11 Sample 1
July 29, 2010**

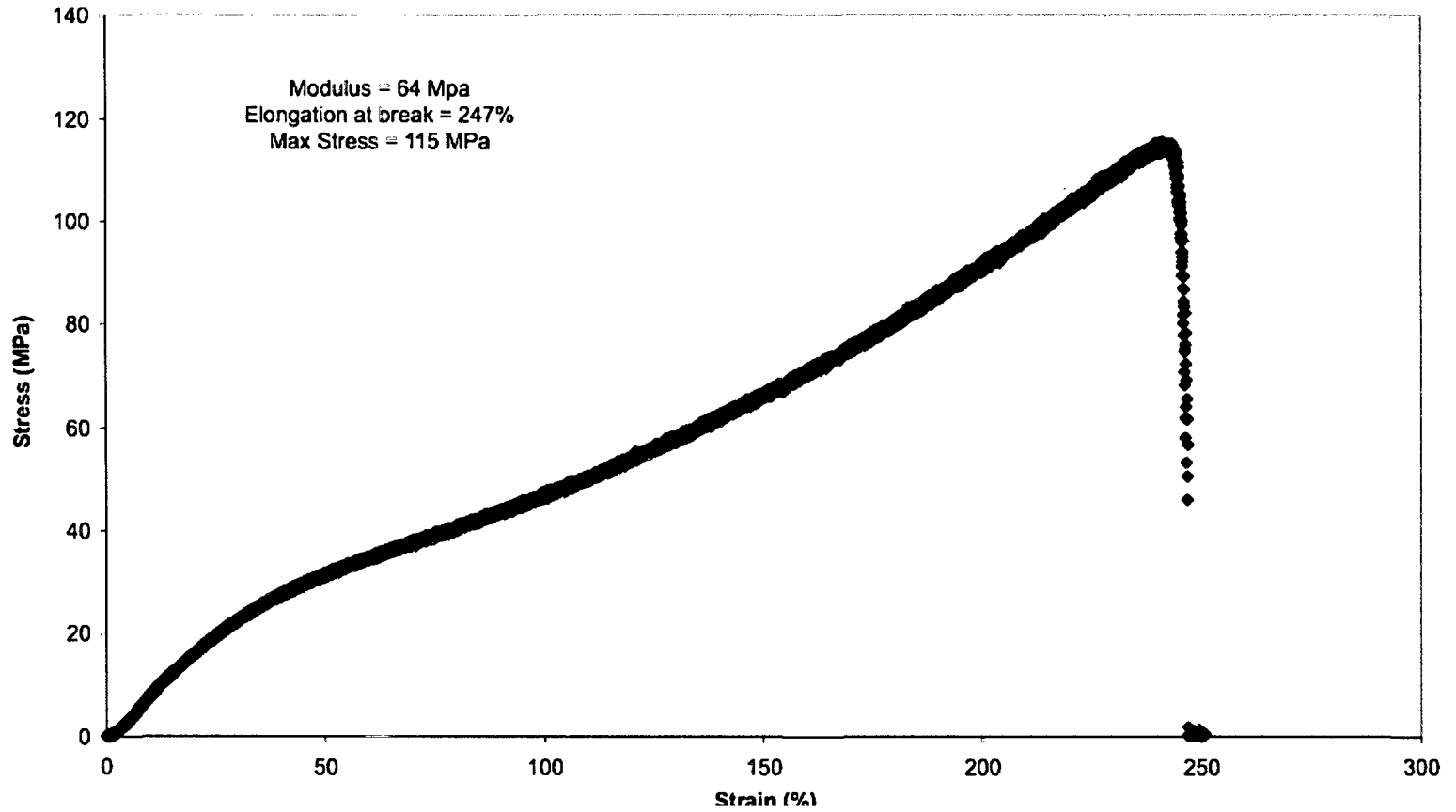


Figure 2-8: True stress vs. strain curve for unaged commercial PA11.

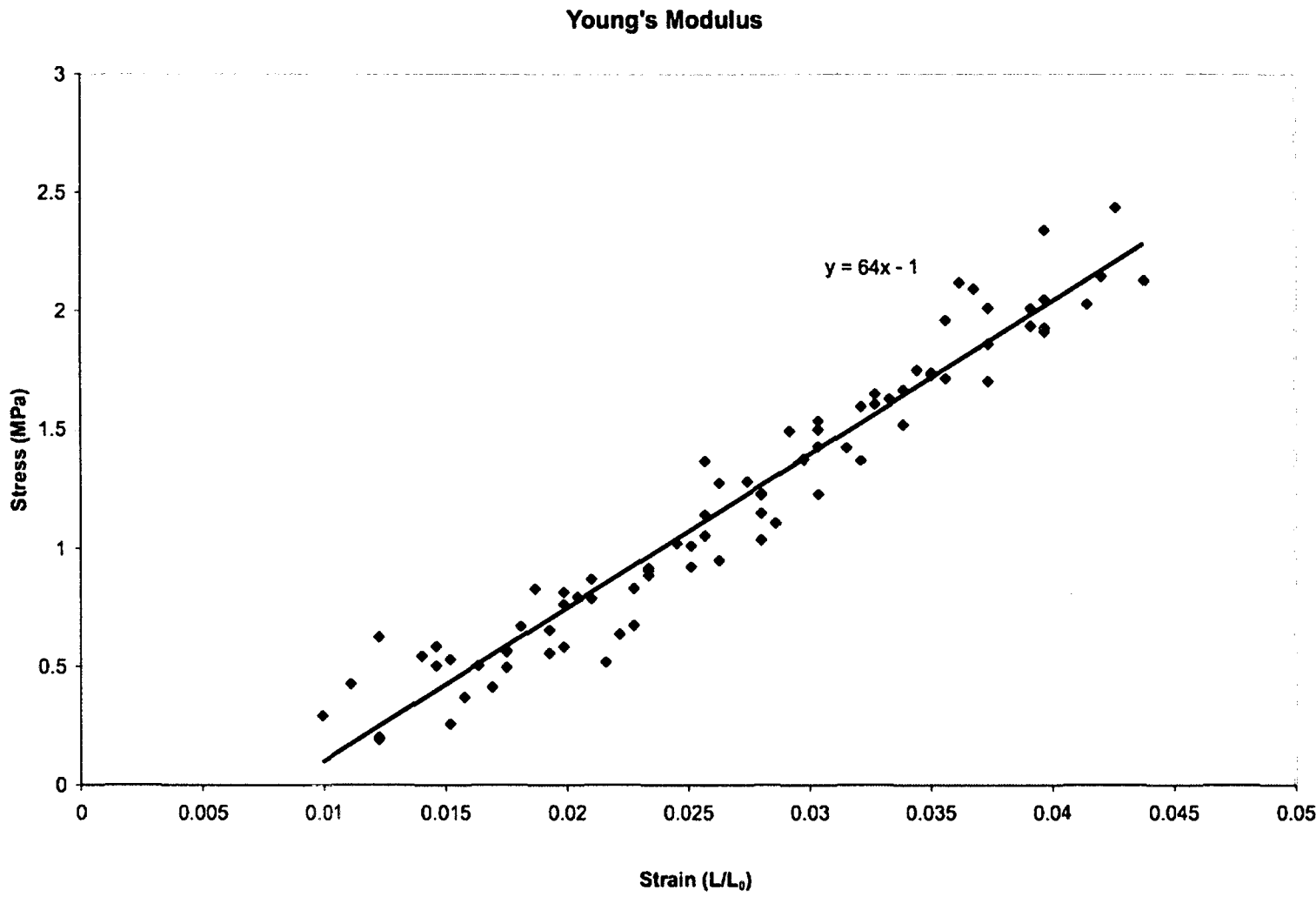


Figure 2-9: Stress vs. strain plot for determination of the modulus of PA11 over the initial linear portion of the curve.

Determination of Organic Acid Concentration in Produced Water by Gas Chromatography

In order to model the lifetime of PA11 in the field, as described in Chapter 5, a detailed temperature history along with organic acid concentration is required. While the field operator must provide the temperature history, the organic acid concentration information may or may not be provided. In the case that the acid information is not known, fluid samples consisting of crude oil still with produced water are shipped to our laboratory from the field and analyzed using gas chromatography (GC). We have developed techniques to quantify acetic acid, 3-propionic acid, butyric acid, and valeric acid.

Experimental Method

An Agilent⁵ model 6890GC was used for acid analysis. The instrument configuration is as follows. The inlet is in splitless mode, at 300°C, using He at 15.0 psi. The capillary column is a 15 m J&W model 122-1013 also operating at 15.0 psi. The detector is a flame ionization detector (FID) maintained at 250°C with a H₂ and air flame.

The oven program was determined by trial-and-error until all analyzed components of a crude oil/production water sample were adequately separated. The final program is as follows:

⁵ <http://www.home.agilent.com/>

1. Initial temp. 29°C.
2. Ramp 5°C/min. to 40°C.
3. Ramp 15°C/min. to 125°C.

Sample preparation involved gravity filtration through Whatman no. 3 qualitative filter papers until the samples were clear. Typically one filtration accomplished this, however a second filtration was sometimes required. The samples were spiked with the internal standard, 1-butanol, to a nominal concentration of 100 ppm. The samples were chromatographed using a 1 µL injection volume. Acid concentration was determined using internal standard response factors as outlined in the following section.

Calibration by the Internal Standard Method

The internal standard method is a means of controlling variations in injection volume due to human limitation [19]. By relating a component peak area representing a known concentration in a stock solution with the internal standard peak area at a known concentration, one may calculate a response factor between the standard and component. The relationship is:

$$\frac{c_r}{c_{st}} = \frac{a_r}{a_{st}} R_f \quad (2.12)$$

where c_r and c_{st} are the concentrations in a known standard solution of reference component r and the internal standard, respectively [19]. The variables a_r and a_{st}

represent the peak areas of component r and the internal standard, respectively [19]. The response factor, R_f , may then be calculated by rearranging Equation (2.12):

$$R_f = \frac{c_r a_{st}}{c_{st} a_r} \quad (2.13)$$

When analyzing a solution of unknown acid concentration, the unknown solution is spiked with a known concentration of internal standard (which obviously must not exist in the sample) and analyzed on the instrument. By rearranging (2.12), one may then calculate the concentration of the unknown component in the solution, as R_f is known from Equation (2.13). Equation (2.14) shows this rearranged form.

$$c_r = \frac{a_r c_{st}}{a_{st}} R_f \quad (2.14)$$

Results

Table 2.5 contains the results of the determinations of R_f for each acid against the internal standard, 1-butanol. The calculations are performed based on Equation (2.13). Figure 2.10 is the chromatogram of the run "ACIDS05d." The large peak eluting at 0.54 minutes is remaining ethanol, which was used to clean the syringe between runs. The asymmetry of the peaks is likely due to uneven volatilization of the acids. The noise after the six-minute mark is due to high-boiling compounds left in the column from prior runs.

Table 2.5: GC determination of the response factors for acetic acid, 3-cyclopropionic acid, butyric acid, and valeric acid with respect to internal standard 1-butanol.

Acid	File name	Acid Elution Time (min)	Internal Std. Elution Time (min)	Acid Conc. (ppm)	Internal Std. Conc. (ppm)	Acid Area (pA*s)	Internal Std. Area (pA*s)	Response Factor (unitless)
Acetic	ACIDS05	1.93	1.54	108	106	12.05	58.03	4.91
	ACIDS05c	2.02	1.53	108	106	9.72	53.13	5.57
	ACIDS05d	1.85	1.53	108	106	9.34	46.06	5.02
	Average:	1.93	1.54					5.17
	Std. Deviation:	0.09	0.01					0.35
3-Propionic	ACIDS05	2.75	1.54	116	106	34.11	58.03	1.86
	ACIDS05c	2.82	1.53	116	106	33.20	53.13	1.75
	ACIDS05d	2.67	1.53	116	106	30.88	46.06	1.63
	Average:	2.75	1.54					1.75
	Std. Deviation:	0.08	0.01					0.11
Butyric	ACIDS05	3.88	1.54	102	106	49.82	58.03	1.12
	ACIDS05c	3.95	1.53	102	106	44.38	53.13	1.15
	ACIDS05d	3.87	1.53	102	106	38.12	46.06	1.16
	Average:	3.90	1.54					1.15
	Std. Deviation:	0.04	0.01					0.02
Valeric	ACIDS05	5.06	1.54	100	106	46.71	58.03	1.17
	ACIDS05c	5.14	1.53	100	106	46.74	53.13	1.07
	ACIDS05d	5.11	1.53	100	106	40.63	46.06	1.07
	Average:	5.11	1.54					1.10
	Std. Deviation:	0.04	0.01					0.06

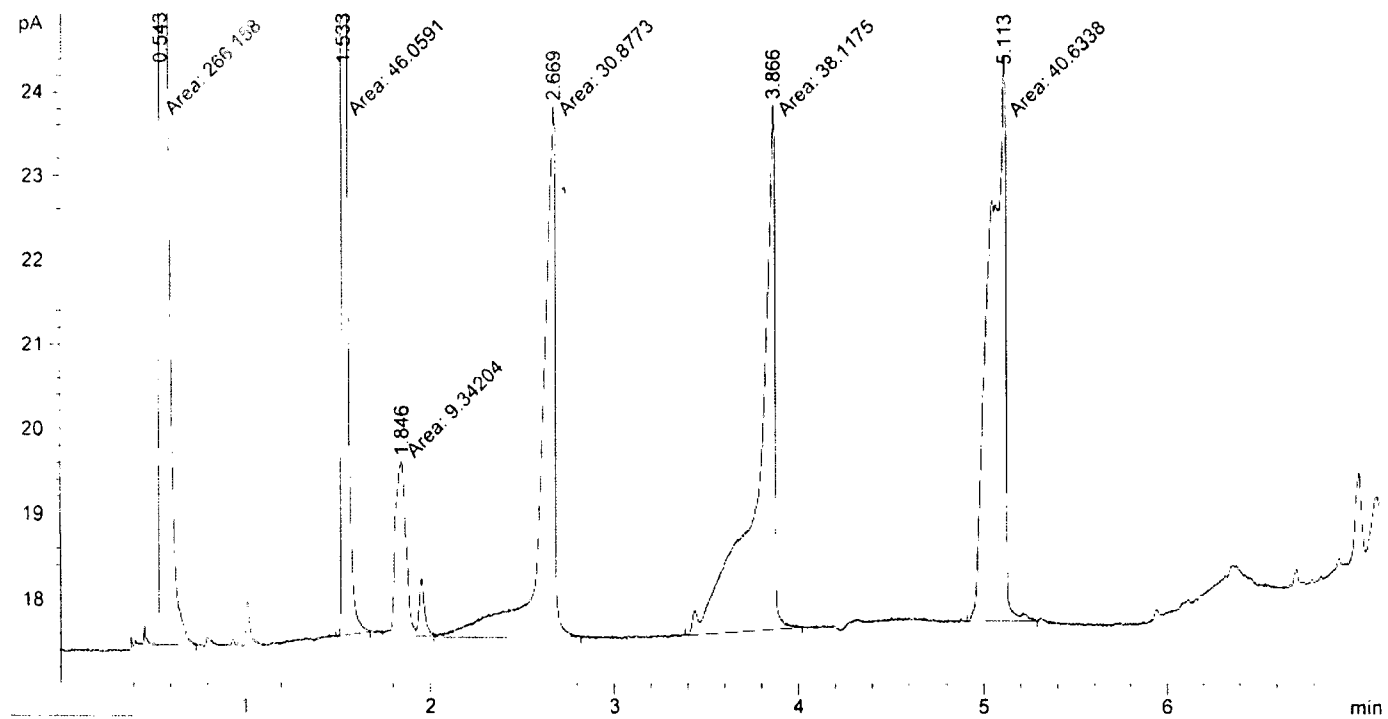


Figure 2.10: GC chromatogram for run "ACIDS05d," used to determine the response factors of small organic acids against the internal standard 1-butanol.

Table 2.6 shows the results of the acid concentrations in a sample from “North Sea Field B.” The calculations are based on Equation (2.14). Figure 2.11 is a chromatogram of the run “RIS305A.” The peaks that are not tabulated in Table 2.6 are unknown and could represent a wide variety of organic molecules due to the fluid coming directly from the field. Table 2.7 compiles the results of the four runs by acid type. Struck through values were not included in average calculations.

One source of error related to acid concentration determination likely stems from contaminants in the column due to its use department-wide. Another source of error is due to volatilization problems of the acids, as is evident due to the large degree of asymmetry of the peaks. As a result, the uncertainties are 30% and 40% for acetic acid and 3-propionic acid, respectively. The concentrations of butyric acid and valeric acid are so low that their uncertainties are each 100%.

Table 2.6: Small organic acid concentration as determined by GC. 1-butanol was the internal standard.

File name	Acid	Internal Std. Elution Time (min)	Acid Elution Time (min)	Internal Std. Conc. (ppm)	Acid Area (pA*s)	Internal Std. Area (pA*s)	Response Factor (unitless)	Acid Conc. (ppm)
RIS305A	acetic	1.58	1.99	109	50.66	27.37	5.17	1043
	3-propionic		2.76		11.42		1.75	80
	butyric		3.90		2.82		1.15	13
	valeric		5.14		0.62		1.10	3
RIS305C	acetic	1.58	1.82	109	37.61	29.91	5.17	708
	3-propionic		2.61		8.71		1.75	56
	butyric		3.82		0.70		1.15	3
	valeric		5.11		0.57		1.10	2
R31219B	acetic	1.75	1.75	116	18.80	8.26	5.17	1364
	3-propionic		2.72		2.08		1.75	51
	butyric		Not Detected		0.00		1.15	0
	valeric		5.21		0.16		1.10	2
R31219D	acetic	1.73	2.01	116	11.98	7.24	5.17	992
	3-propionic		3.14		0.90		1.75	25
	butyric		3.64		0.16		1.15	3
	valeric		5.32		0.67		1.10	12

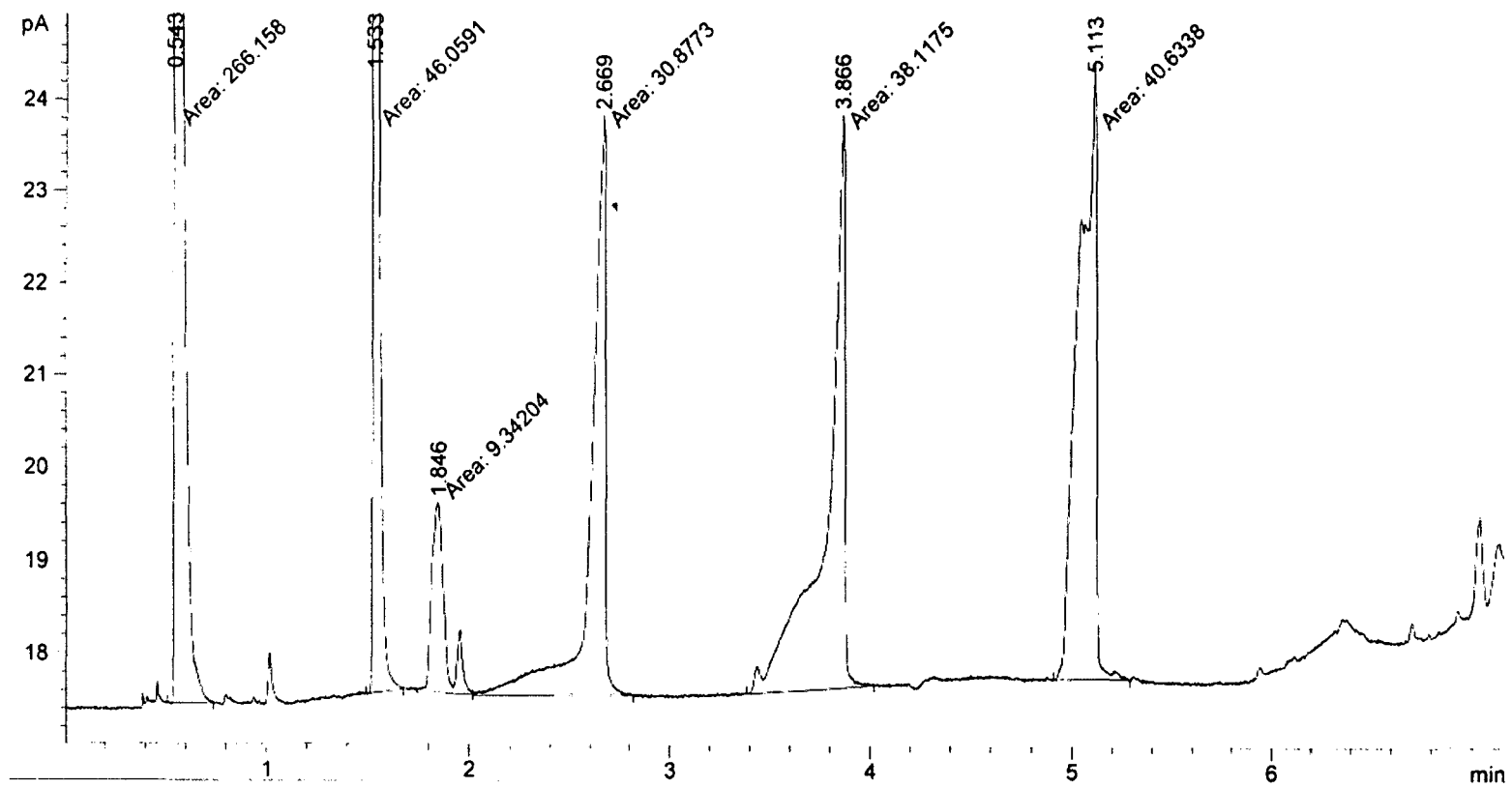


Figure 2.11: GC of North Sea Field B production water to analyze for small organic acids.

Table 2.7: Acid concentration GC results from North Sea Field B.

Acid	Run				Avg. Conc. (ppm)	Std. Dev. (ppm)	Reported Conc. (ppm)
	RIS305A	RIS305C	R31219B	R31219D			
acetic	1043	708	1364	992	1027	269	1000 ± 300
3-propionic	80	56	51	25	53	23	50 ± 20
butyric	13	3	0	3	2	2	2 ± 2
valeric	3	2	2	12	2	1	1 ± 1

Chapter 3: Degradation of Polyamide-11 by Hydrolysis, Methanolysis, and Ethanolysis

Introduction

Polyamide-11 (PA11) is a medium-performance polymer whose monomer, 11-aminoundecanoic acid, is produced from the extract of castor beans [20]. It is polymerized via condensation reaction, and is widely used as the liquid barrier of the flexible pipes connecting floating platforms to wellheads on the seafloor in the offshore oil and gas industry.

A number of qualities have led to its use in this application, including its good resistance to chemical attack and mechanical properties [20]. It has a considerable resistance to creep, and though it is a semi-crystalline material, its flexibility and 400% elongation at break make it an excellent liner in flexible pipes [20].

PA-11 is susceptible to degradation via hydrolysis, the reverse of the condensation polymerization reaction. This addition of water to the amide bond leads to cleavage of the polymer chain and subsequent reduction in average molecular weight. This chain cleavage may proceed to a ductile-brittle transition point on the order of $MW=20\ 000$ g/mole, at which mechanical properties drop sharply, leaving the liner prone to sudden failure [15]. This hydrolysis reaction at the amide bond has been determined to occur in three scenarios: acid catalyzed ($pH<7$), based catalyzed ($pH>7$), and at neutral $pH=7$ [21].

The acid catalyzed scheme begins with protonation of the carbonyl oxygen, opening the carbonyl carbon to attack [22-24]. The next, rate-determining step, is addition of a water molecule to this carbonyl carbon, yielding a tetrahedral intermediate [23]. This intermediate then quickly collapses into an acid and an amine. McClelland arrived at this mechanism through monitoring the exchange of ^{18}O -labeled carbonyl groups at the amide bonds [23].

The base catalyzed mechanism is similar to the acid catalyzed scheme [25-28]. It begins with the rate-determining attack at the carbonyl carbon by a hydroxide ion, which forms a tetrahedral intermediate. As in the case of the acid-catalyzed mechanism, this collapses to make an acid and an amine. This mechanism was also proven by ^{18}O exchange, in work by Bender et al. [27].

The third means of amide hydrolysis, occurring in water at pH=7, has been described theoretically by Dirk Zahn based on simulation results regarding N-methylacetamide [29]. His proposed mechanism begins with participation of two water molecules – one of which adds a hydroxide group to the carbonyl carbon, while another simultaneously protonates the nitrogen at the amide bond. The leftover proton from the hydroxide addition to the carbonyl group joins the water molecule upon protonation of the nitrogen in a manner similar to the Grothuss mechanism [29]. The resulting tetrahedral intermediate dissociates to an acid and an amine, as was the case with the acid and base catalyzed mechanisms.

The pH=7 neutral water hydrolysis has been demonstrated and modeled in the case of PA-11 by Meyer et al., Chaupart et al., and Jacques et al [15,30,31]. Their

findings, including kinetics and modeling schemes, will be treated more thoroughly later on in this chapter, and in Chapter 5.

The question thus becomes whether small alcohols, namely methanol or ethanol, play a role in the degradation of PA-11. In practice, these small alcohols are used to inhibit the formation of hydrates, solids which may restrict oil flow as well as damage oil production equipment, through one of two means [32]. One way is by introducing to the flow line periodic high concentration batch treatment, whereas the other is introducing a low concentration constant flow with the oil. As of yet, no study has been performed on these small alcohols with regard to the degradation of polyamide polymers.

Regarding the addition of methanol to amide bonds, one study was published in 1973 describing the addition of methoxy ion to an amide bond [33]. A basic mechanism for the methanol-catalyzed degradation, or methanolysis, of the amide bond was proposed, beginning with formation of a destabilized tetrahedral intermediate that is effected by the joining of a methoxide ion to the carboxylic carbon of the bond. The scission of the amide bond then occurs through the collapse of this intermediate, leaving an ester and an amine. The dissociation constant of the proton on methanol ($pK_a=15.5$) indicates the availability of methoxide ions in the system, as well as a means of destabilizing the carbonyl bond as described by the acid-catalyzed hydrolysis scheme.

The concept of ethanolysis, or addition of an ethoxide ion to an amide bond, has also been reported in the presence of HCl and heat [34]. Though no specific mechanism is given, one might expect it to proceed in the same manner as methanolysis. This would entail the formation of an ethoxide ion through deprotonation of the ethanol molecule ($pK_a=15.9$), which then attacks the carboxylic carbon upon protonation of the carbonyl

oxygen by the acidic conditions, and concludes with the cleavage of the amide bond upon tetrahedral intermediate collapse.

In this chapter, the hydrolysis of PA11 in pure water is demonstrated and characterized at 70°C, 90°C, 100°C, and 120°C. The effects of the presence of methanol and ethanol in the hydrolytic environment on the rate and overall extent of degradation are explored. The existence of an equilibrium molecular weight, where the rates of hydrolysis and recombination become equal, is observed. It is also shown, that ethanol *does not* seem to affect the rate nor degree of hydrolysis in water solutions. These findings are mathematically treated with fewer assumptions and approximations than in prior methods as measured by the equilibrium molecular weight.

Experimental

Coupons of commercially available PA11 with plasticizer, identical to that used in flexible pipes, were cut into 0.5 cm x 0.5 cm x 0.5 cm cubes and placed into heavy-walled Ace glass pressure tubes. These tubes were then filled with 25mL solutions of deionized water and either methanol to make a weight concentration of 0%, 5%, 10%, and 30%, or ethanol to make a concentration of 30%.

In order to eliminate the effects of the irreversible oxidative process, which would lead to an over-exaggeration of degradative processes, each tube was bubbled with Argon in order to displace the dissolved oxygen present to ppb levels. This meant bubbling each tube for between twenty and thirty minutes in a deoxygenated chamber prior to

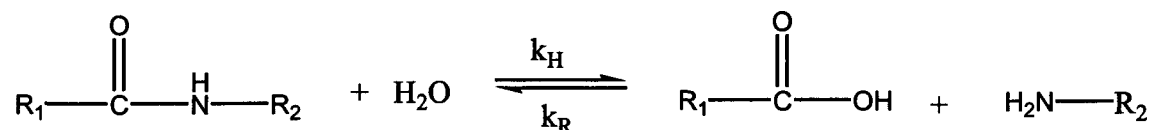
sealing. The oxygen level was monitored at each sampling and found to be below .01 ppm.

The sealed tubes were placed in ovens held at 120°C, 100°C, 90°C, and 70°C. There, they were sampled at intervals selected to yield a good representation of the degradative process. The resealing process was repeated in the same way as the initial setting-up of the tubes. At each sampling point, the oxygen level was measured. Then each tube got a fresh solution, bubbled again in Argon, resealed with a new PTFE O-ring, and placed back in its respective oven. No tube was left out of the ovens for any longer than eight hours.

Thermogravimetric analysis as well as average molecular weight determinations were conducted as described in Chapter 2.

Mathematical Theory

With regard to amide hydrolysis, one may describe the general process by the competing rates of hydrolysis and recombination:



The differential representation of this process is

$$-\frac{d[\pm\text{NH}_2]}{dt} = -\frac{d[-\text{COOH}]}{dt} = k_R[-\text{NH}_2][-\text{COOH}] - k_H[-\text{NHCO}][-\text{H}_2\text{O}]. \quad (3.1)$$

By assuming the water concentration is large and constant, one may incorporate this into k_H , which becomes k'_H . Theoretically, each broken amide bond yields one amine and one acid, or in the case of alcoholysis, one amine and one ester. However, as alcoholysis only appears to occur in the presence of acid or base, we will assume stoichiometric formation of amine and acid. Thus, this equation was previously represented by

$$-\frac{d[\pm\text{NH}_2]}{dt} = -\frac{d[-\text{COOH}]}{dt} = k'_R[-\text{COOH}]^2 - k'_H[-\text{NHCO}] \quad (3.2)$$

where k'_H is now a pseudo first-order rate constant.

Equation (3.1) may then be represented by the generic equation

$$\frac{dx}{dt} = k_1(a_0 - x) - k_{-1}x^2 \quad (3.3)$$

where x represents the amine or acid product concentration at time t , and a_0 represents the initial amide bond concentration [35].

Given equilibrium conditions, $\frac{dx}{dt} = 0$, the equation may be solved for k_{-1} :

$$k_{-1} = \frac{k_1(a_0 - x_e)}{x_e^2} \quad (3.4)$$

where x_e represents the equilibrium product concentration [35]. The substitution of (3.4) into (3.3) and integration yields

$$\frac{x_e}{(2a_0 - x_e)} \ln \left(\frac{a_0 x_e + x(a_0 - x_e)}{a_0(x_e - x)} \right) = k_1 t. \quad (3.5)$$

By definition, this hydrolytic process may be interpreted where

$$x = a_0 - a \quad (3.6)$$

and

$$x_e = a_0 - a'_e. \quad (3.7)$$

This defines the product concentrations in terms of the amide concentrations at time t and at equilibrium.

One may then substitute (3.4) and (3.5) into (3.3) and achieve the result

$$\left(\frac{a_0 - a'_e}{a_0 + a'_e} \right) \ln \left[\frac{a_0^2 - a'_e a}{a_0(a - a'_e)} \right] = k'_H t. \quad (3.8)$$

Likewise, substituting (3.4) and (3.5) into (3.2) gives

$$k'_R = \frac{k'_H a'_e}{(a_0 - a'_e)^2}. \quad (3.9)$$

As this problem involves the changing concentration of amide bonds, a , in the solid state, one may convert from MW to a by assuming MW/M_n , or polydispersity, is the theoretical value of 2 for a condensation reaction [9]. The relationship between Mw and a is defined as:

$$a = \left[\frac{MW}{2 \times 183.29} \right] - 1. \quad (3.10)$$

One may then use (3.8) to determine k'_H and a'_e by altering their values so that the variance between measured data points and points predicted by (3.8) is minimized. It is then possible to calculate k'_R using (3.9).

The results of the above kinetic model may be plotted using the Arrhenius equation to find the activation energies, E_a , of the reactions in pure water, and at various concentrations of alcohols in deionized water.

Results

The aging process is displayed by plotting MW vs. aging time (days) for each concentration of methanol in the case of 120°C (Figure 3.1), 100°C (Figure 3.2), and 90°C (Figure 3.3).

As the degradative process at 70°C takes prohibitively long, on the order of 2000 days, to reach equilibrium, we use the Arrhenius dependence of the systems at 90°C, 100°C, and 120°C to determine the equilibrium molar masses, MW'_e , at 70°C. With the predicted equilibrium MW'_e , the low temperature 70°C data may then be analyzed for the kinetic constants k'_H and k'_R using MW'_e and compared to the experimental data. The resulting 70°C data is shown in Figure 3.4.

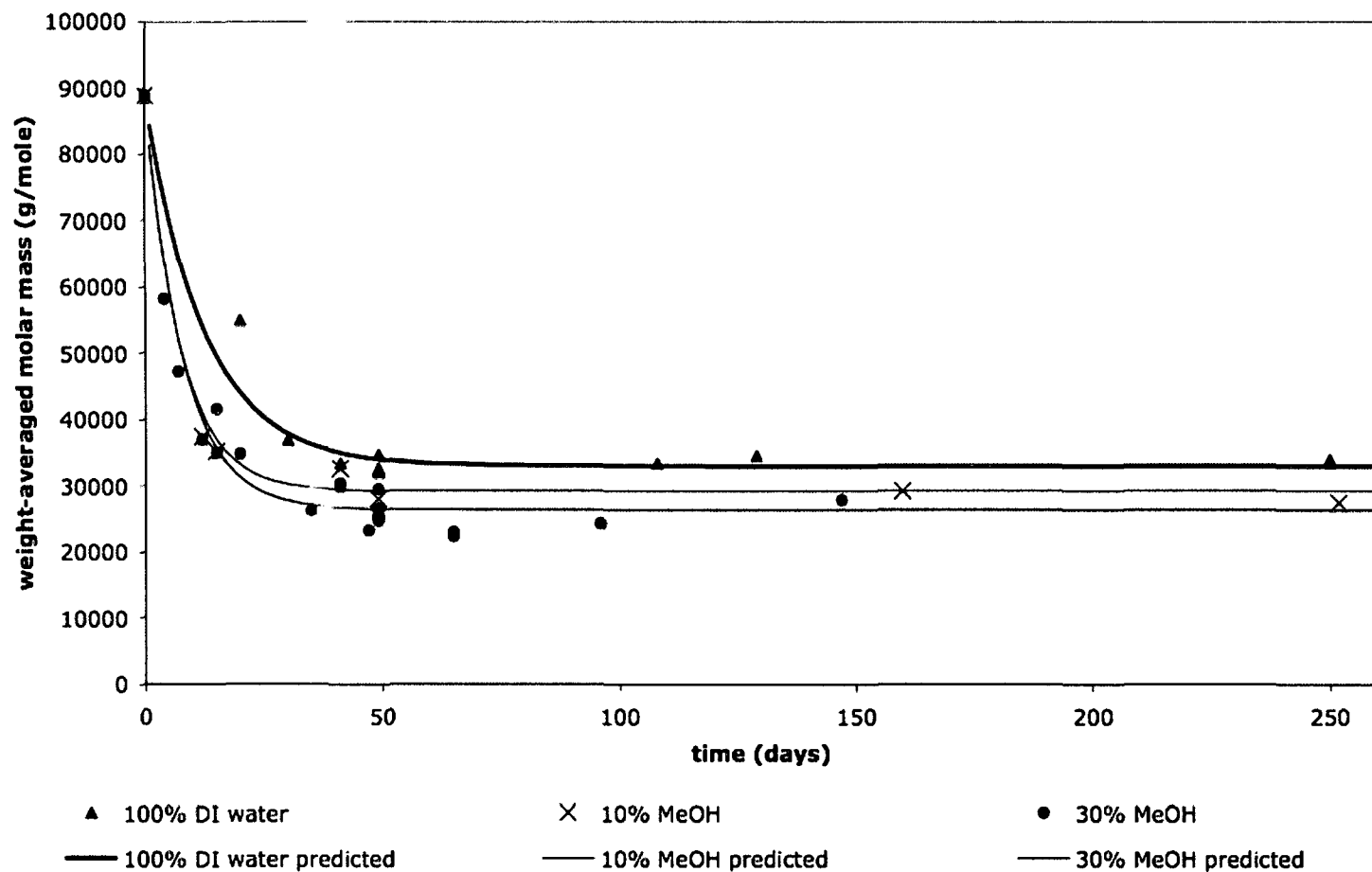
120C, commercial PA11, MW v. ageing time

Figure 3.1: PA11 aging at 120°C in 30% MeOH, 10% MeOH, and 100% DI water. The data was fit by the above-described model.

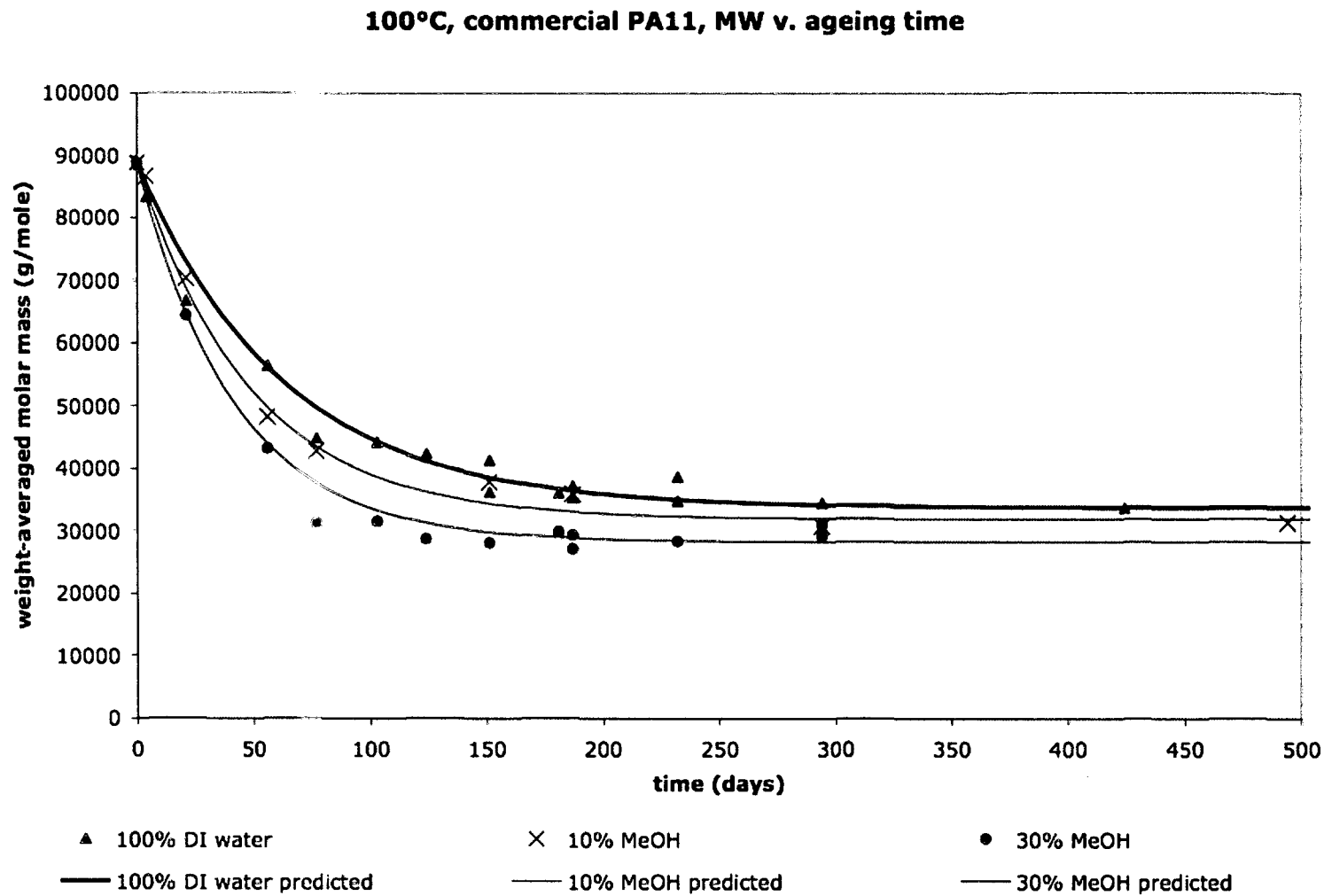


Figure 3.2: PA11 aging at 100°C in 30% MeOH, 10% MeOH, and 100% DI water. The data was fit by the above-described model.

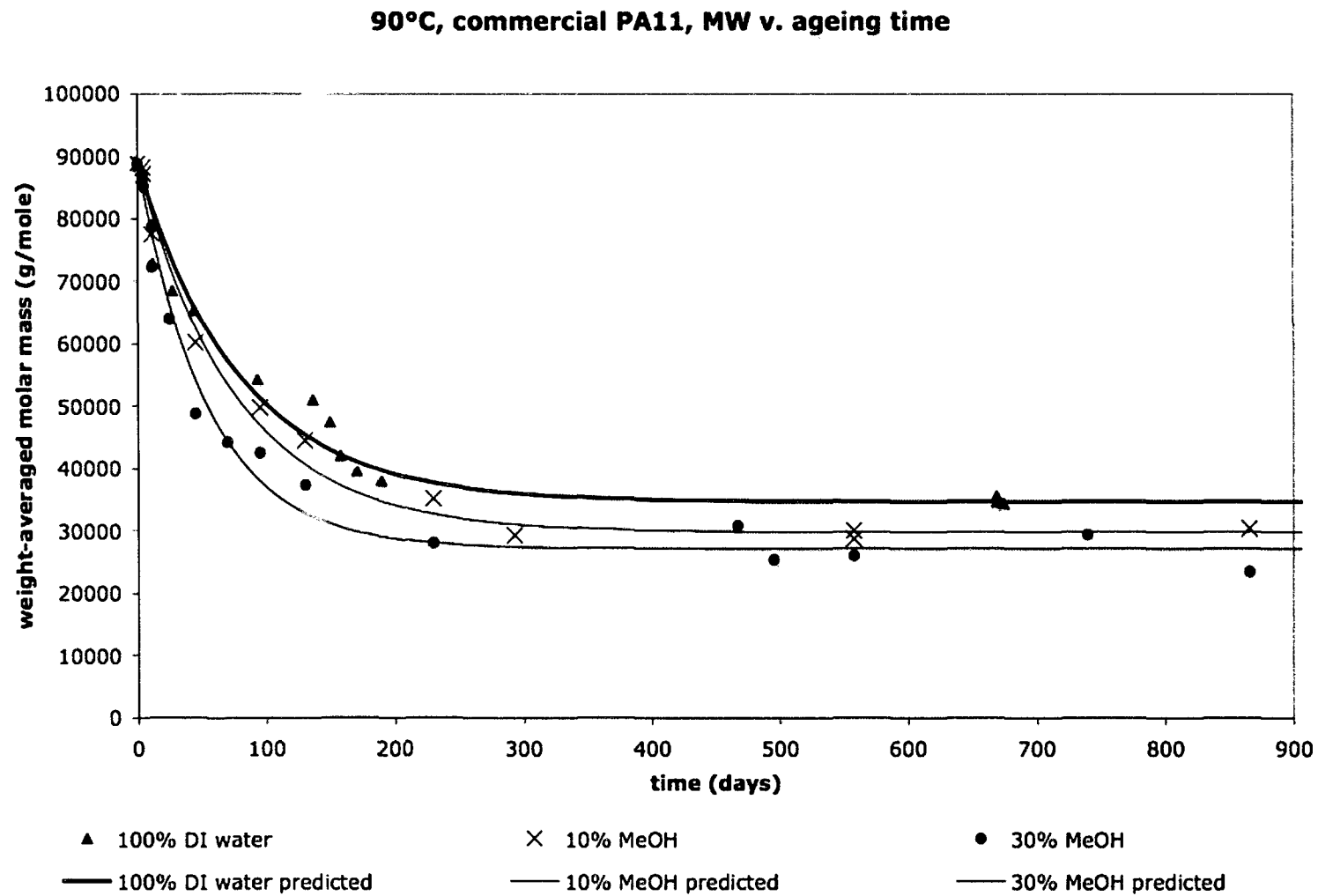


Figure 3.3: PA11 aging at 90°C in 30% MeOH, 10% MeOH, and 100% DI water. The data was fit by the above-described model.

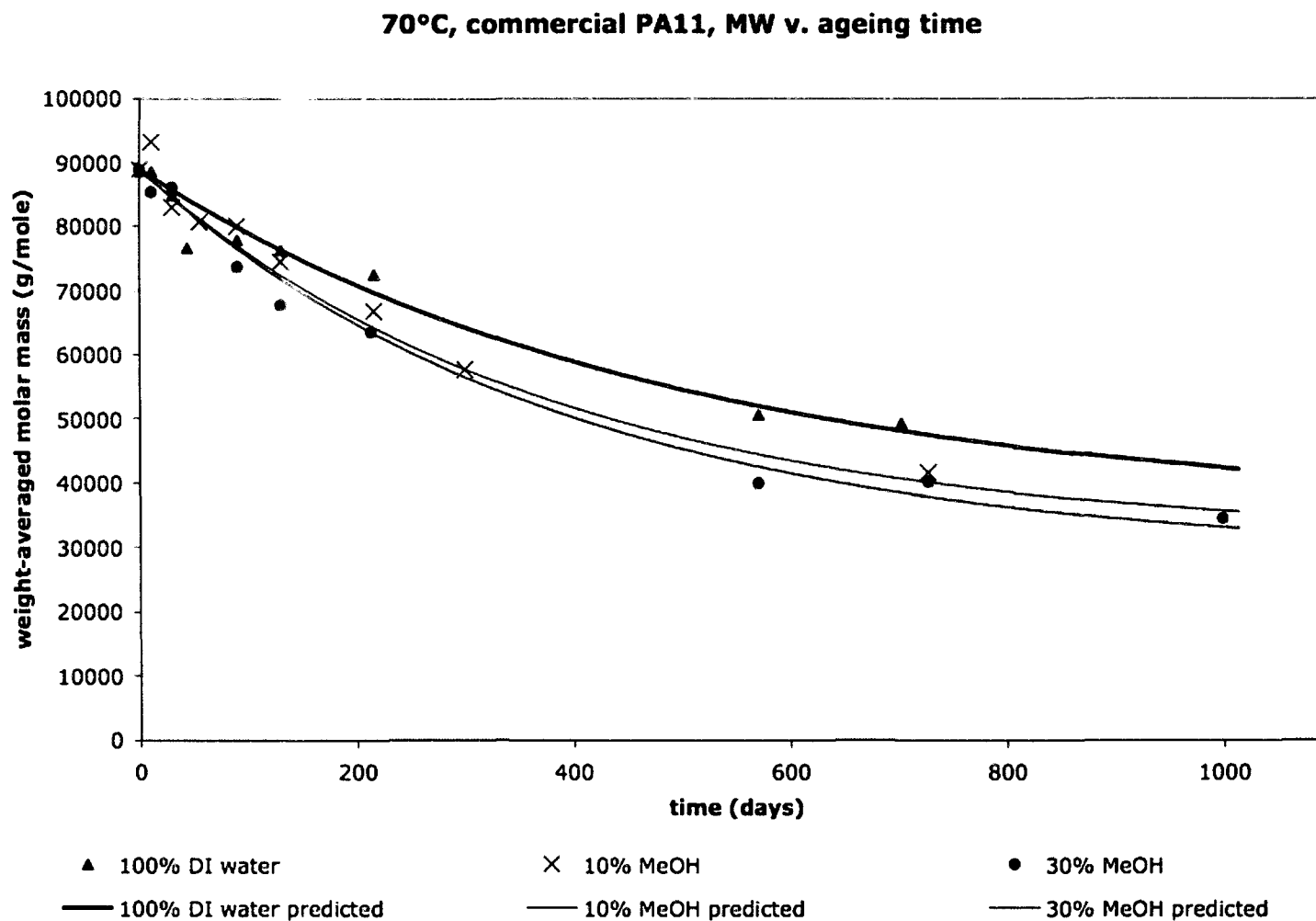


Figure 3.4: PA11 aging at 70°C in 30% MeOH, 10% MeOH, and 100% DI water. The equilibrium molecular weight was determined by the temperature dependence of the 120°C, 100°C, and 90°C data. The rate was determined by fitting the data with the extrapolated MW'e.

The predicted values obtained from a best fit of equation (3.8) to the experimental data shown in the Figures 3.1-3.4 for k'_H , k'_R and MW'_e are shown in Table 3.1 for 120°C, 100°C, 90°C and 70°C. The uncertainties for k'_H and MW'_e in Table 3.1 were estimated based on shifting the values and evaluating the resulting fit visually. The uncertainty for k'_R was estimated by using the uncertainties in k'_H and MW'_e to evaluate its shift based on equation (3.9). The best-fit lines are also displayed in Figures 3.1-3.4.

The Arrhenius plots used to determine the temperature dependencies of the rate constants are shown in Figures 3.5-3.6. The temperature dependence of MW'_e is shown in Figure 3.7. The activation energies are reported in Table 3.2. The uncertainties in the activation energies for k'_H were estimated by altering the slope of the Arrhenius plot based on the uncertainties in k'_H and found to be ± 16 kJ/mole. The same method was used to find the error in the activation energies in k'_R , and was determined to be ± 40 kJ/mole.

Table 3.1: The model fitting parameters k'_H , k'_R , and MW'_e as a function of test fluid and temperature. The 70°C MW'_e was calculated using the temperature dependence of MW'_e at 120°C, 100°C, and 90°C.

	Temp. (°C)	Test Fluid			
		100% DI	30% EtOH	10% MeOH	30% MeOH
k'_H ± 20%	120°C	5.1E-02	5.4E-02	9.2E-02	1.0E-01
	100°C	1.0E-02	1.2E-02	1.5E-02	1.7E-02
	90°C	7.7E-03	8.7E-03	8.7E-03	1.3E-02
	70°C	1.2E-03	1.1E-03	1.7E-03	1.7E-03
k'_R ± 30%	120°C	2.0E-04	1.7E-04	2.7E-04	2.5E-04
	100°C	4.0E-05	5.4E-05	6.6E-05	4.7E-05
	90°C	3.3E-05	3.9E-05	2.7E-05	3.3E-05
	70°C	5.7E-06	7.5E-06	6.5E-06	4.9E-06
MW'_{eOH} ± 8%	120°C	33000	30200	29200	26400
	100°C	33700	35300	34900	28200
	90°C	34600	35500	29700	27100
	70°C*	35700	41300	33100	28500

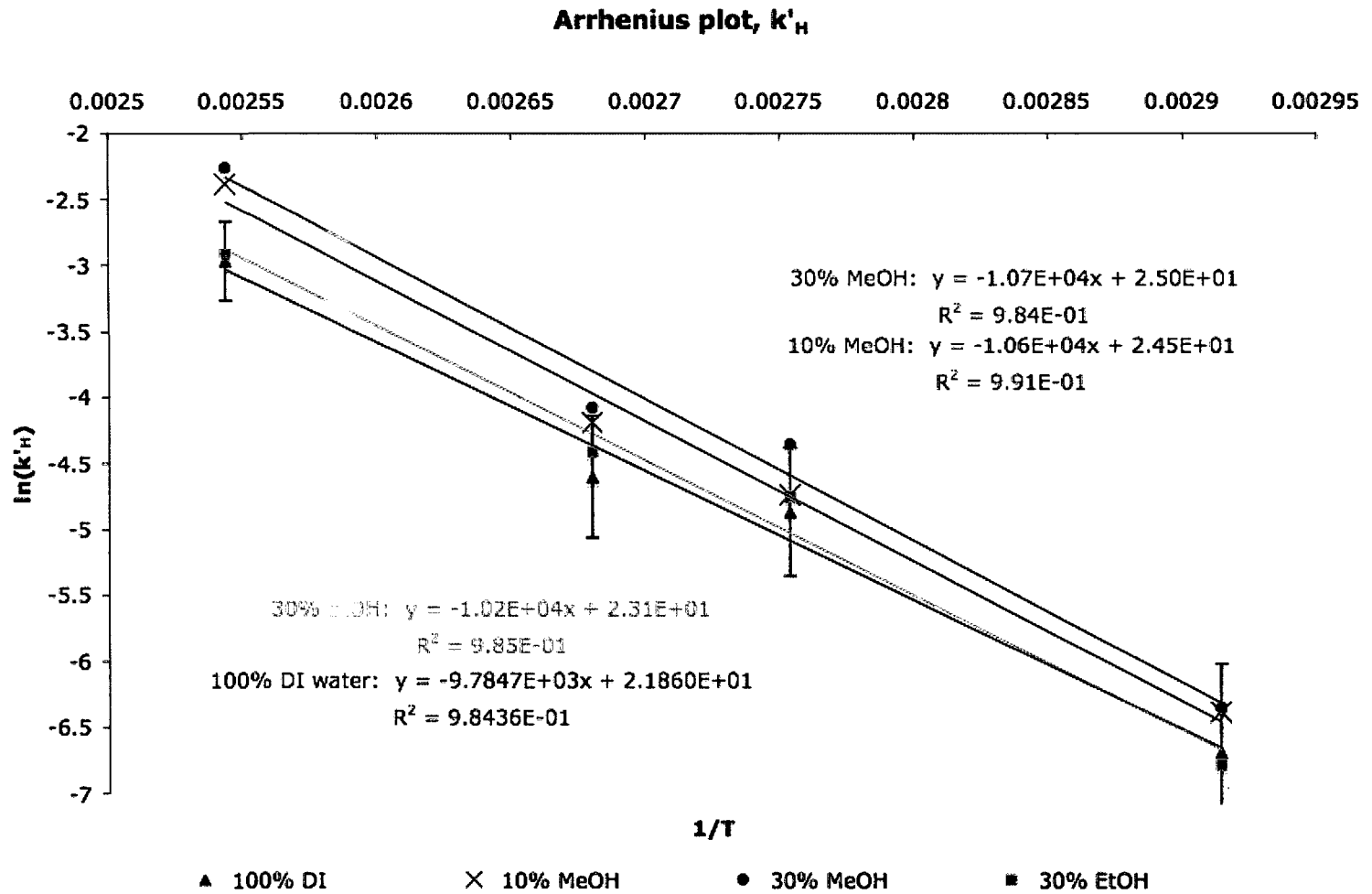


Figure 3.5: Arrhenius plot for k'_H . Error bars representing 10% in either direction are shown for water, but are applicable to the other data points as well.

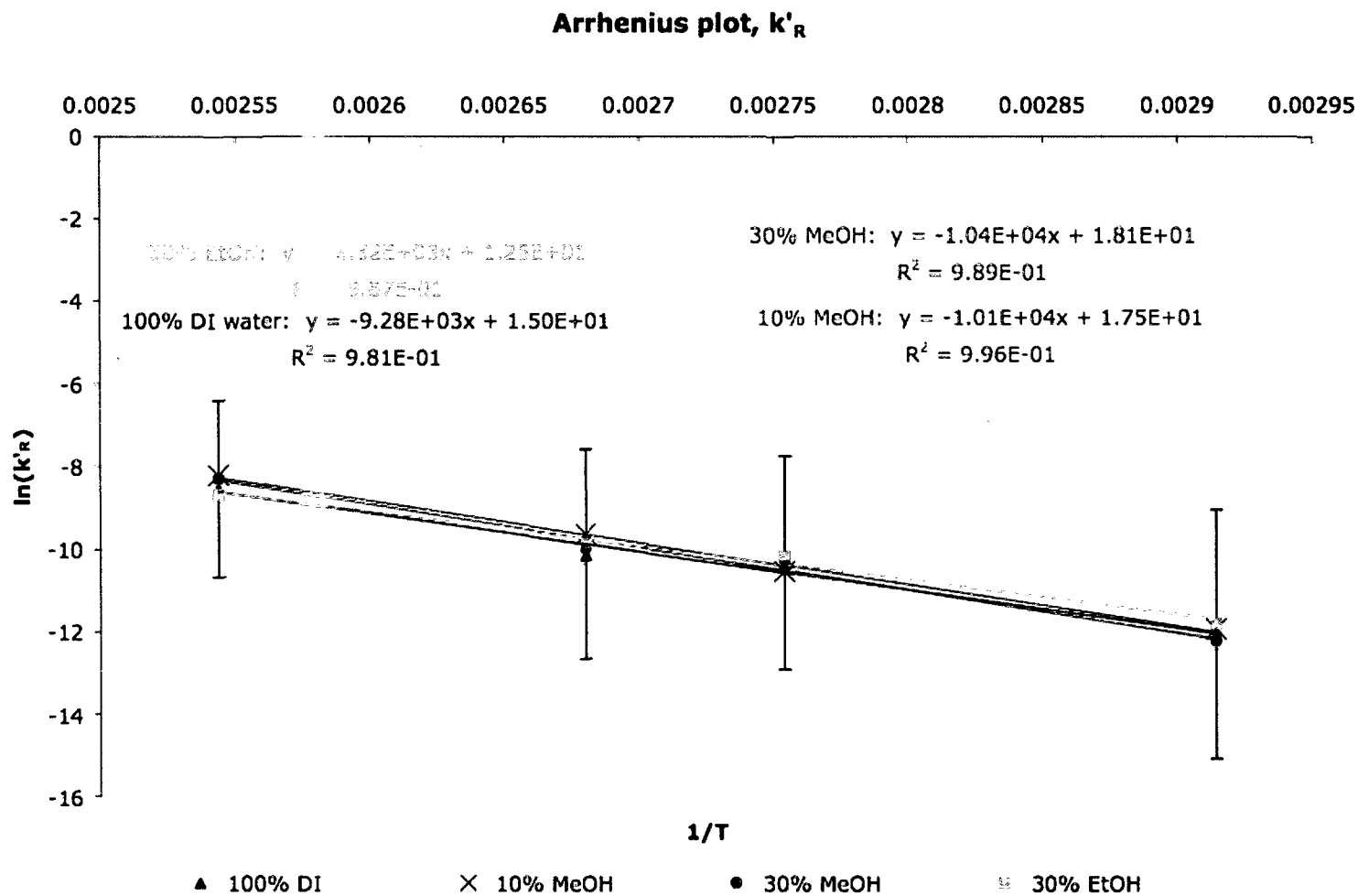


Figure 3.6: Arrhenius plot for k'_R . Error bars representing 25% in either direction are shown for water, but are applicable to the other data points as well.

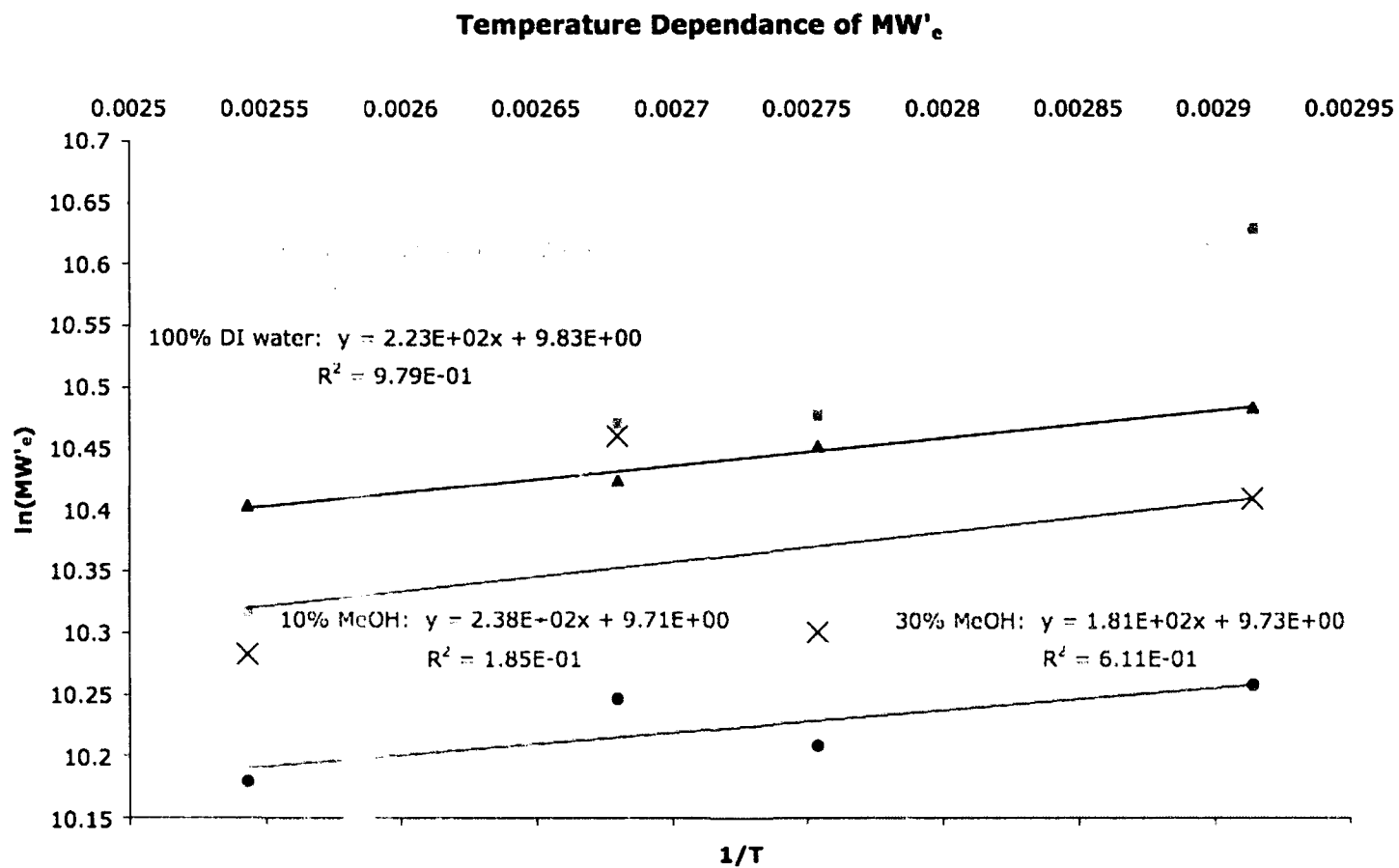


Figure 3.7: A plot of $\ln(MW'_e)$ vs. $1/T$ which illustrates the temperature dependence for MW'_e .

Table 3.2: Activation energies for k'_H and k'_R . The uncertainties were determined by evaluating the effect on the slope of the Arrhenius plot based on the uncertainties in the values of k'_H and k'_R .

Fluid	Ea (kJ/mole)	
	$k'_H \pm 16$	$k'_R \pm 40$
100% DI	81	77
10% MeOH	88	84
30% MeOH	89	86
30% EtOH	85	69

The 30% ethanol data were treated in the same manner. The data for the experimental ethanol runs, along with the model fits, are plotted against the model result for water, in order to demonstrate its lack of effect on either rate of hydrolysis nor the equilibrium value of MW'_e . See Figures 3.8-3.11.

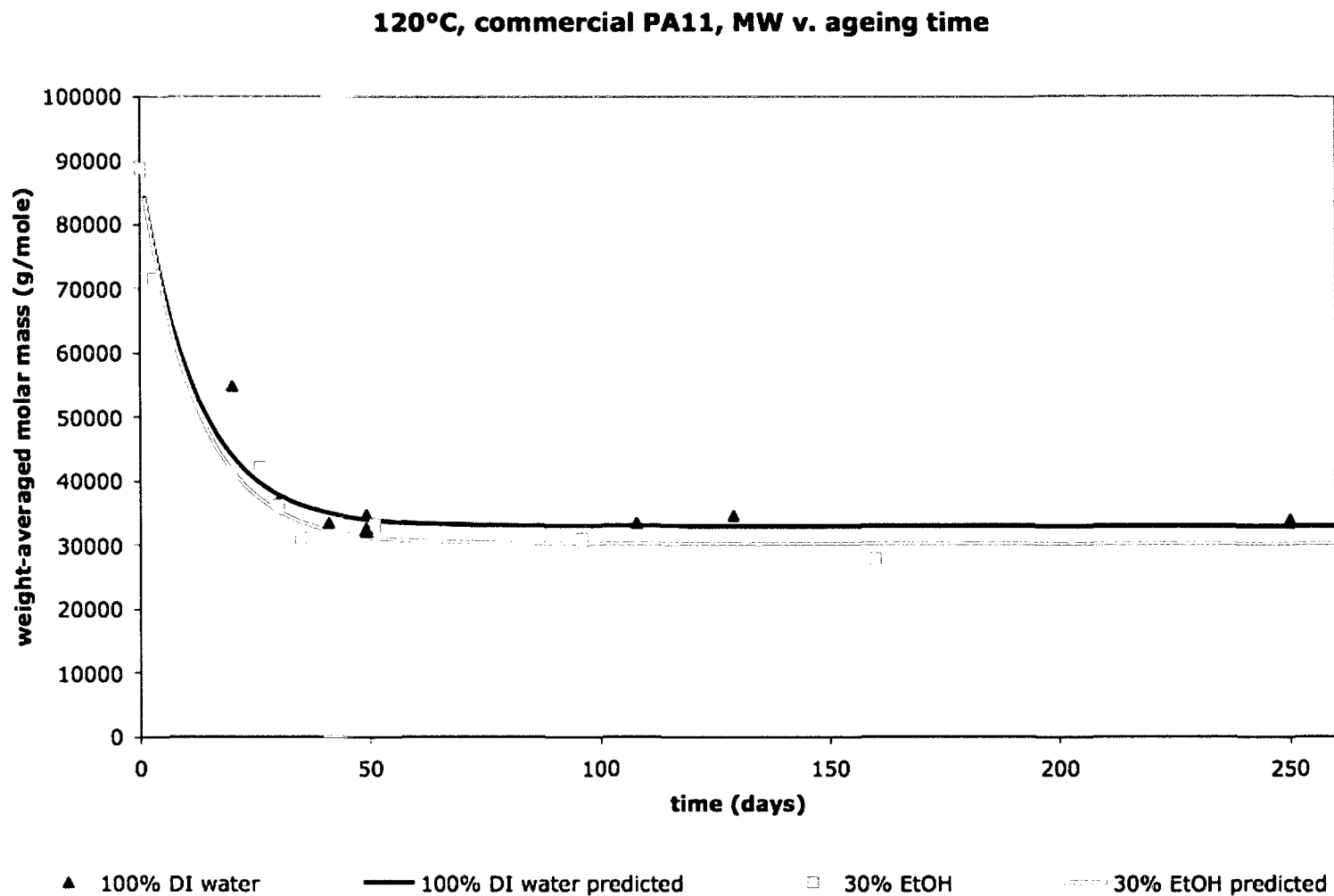


Figure 3.8: PA11 aging at 120°C in 30% EtOH and 100% DI water. The data was fit by the model described in this chapter.

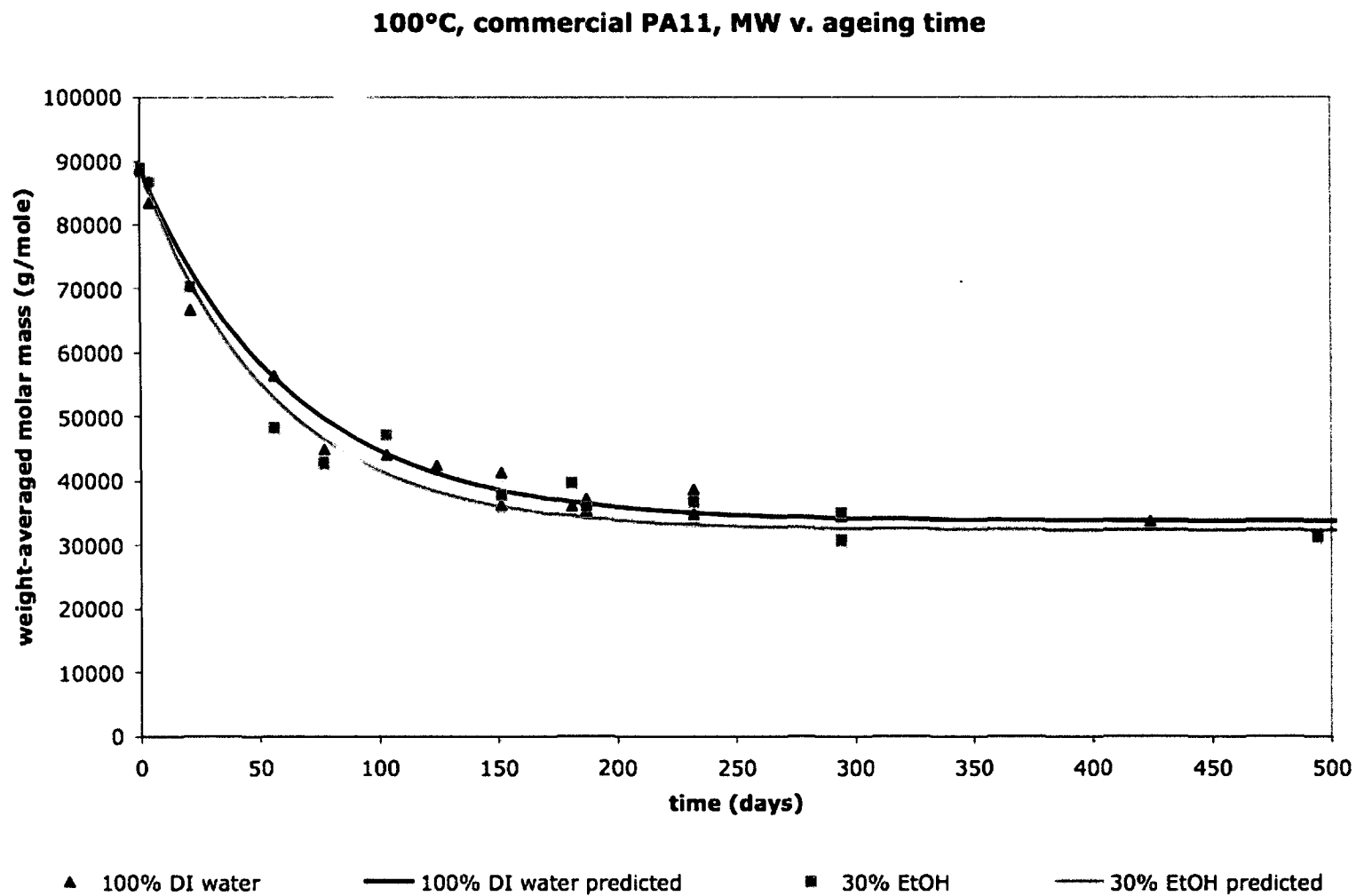


Figure 3.9: PA11 aging at 100°C in 30% EtOH and 100% DI water. The data was fit by the model described in this chapter.

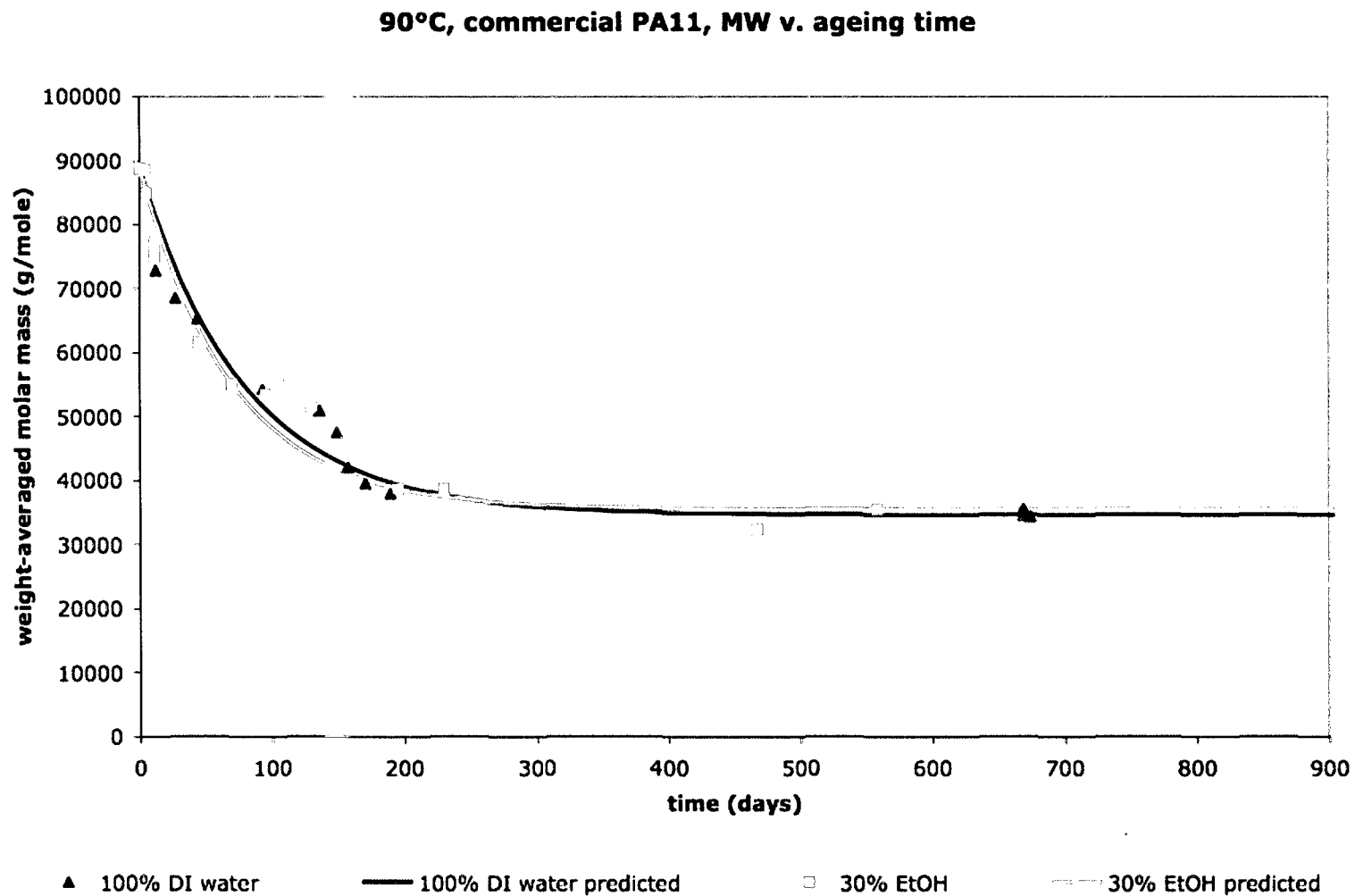


Figure 3.10: PA11 aging at 90°C in 30% EtOH and 100% DI water. The data was fit by the model described in this chapter.

70°C, commercial PA11, MW v. ageing time

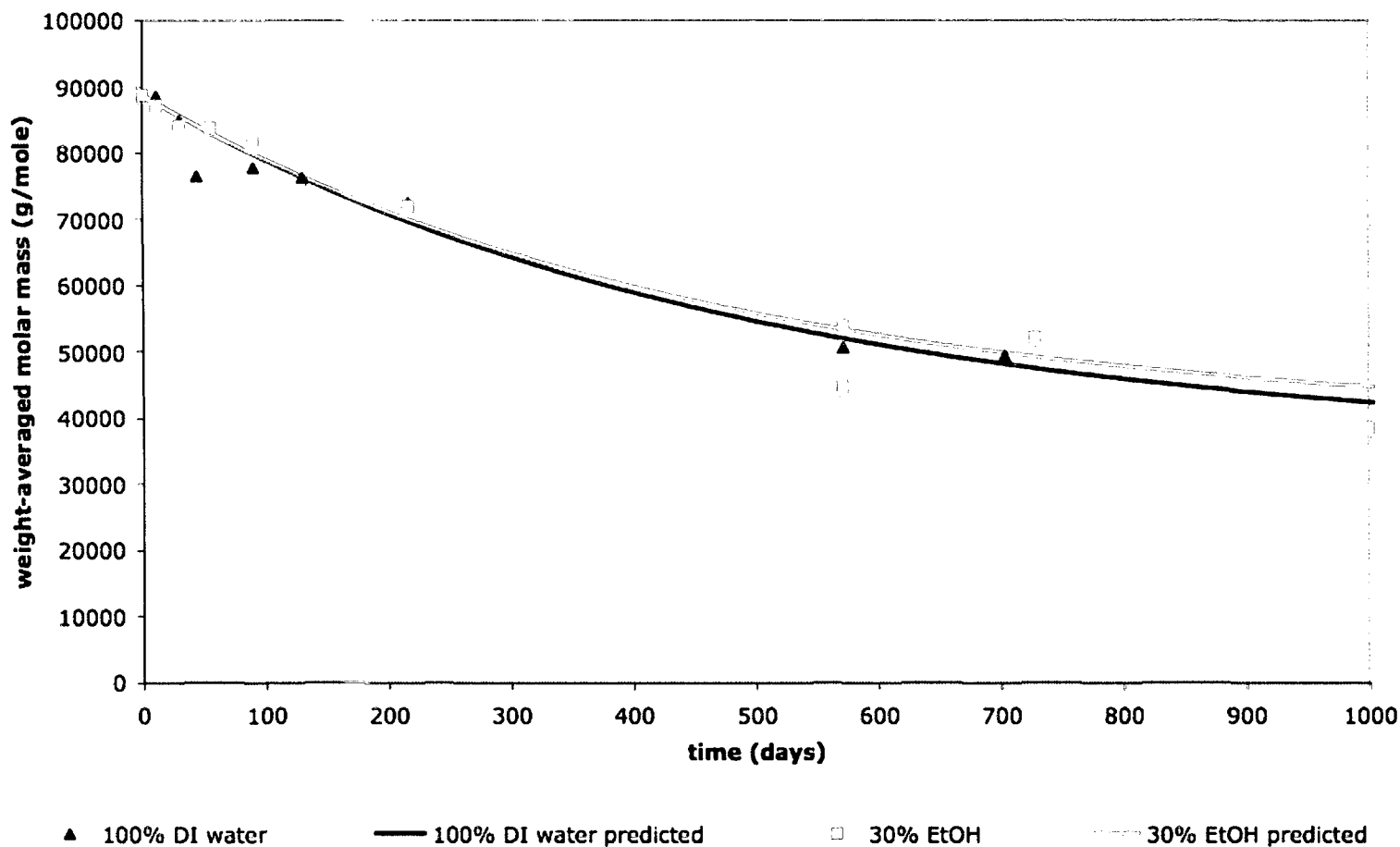


Figure 3.11: PA11 aging at 70°C in 30% EtOH and 100% DI water. Both systems were fitted by first extrapolating the MW_e based on its temperature dependence at 120°C, 100°C, and 90°C, and then optimizing the k_H parameter to best fit the data.

Discussion

The presence of methanol is shown to have a significant effect on the speed and degree to which PA11 degrades, especially at higher temperatures. The activation energies of both k'_H and k'_R are not significantly different for each fluid environment due to the error involved in the molar mass determinations discussed in Chapter 2, along with the errors shown for k'_H and k'_R .

The proposed activation energy for water, 81 ± 16 kJ/mole, is in good agreement with the 87 kJ/mole calculated by Meyer et al. [31]. The uncertainty in their measurement was not specified.

The presence of ethanol, even at 30% by volume, does not affect the degradation process significantly. This result occurs in contrast to the results seen with 30% methanol, even though ethanol is present in the same concentration. This result is more significant considering the fact that ethanol is a slightly stronger base.

One hypothesis is that ethanol, due to either its size or hydrophilic/phobic interactions, may reduce its effective concentration near the carbonyl group to nearly zero. There may also be steric hindrances that occur with regard to the larger ethoxide attaching to the carbonyl carbon, once it is inside of the polymer. In both cases the rate of amide bond cleavage due to the presence of ethanol would be considerably lower than that which occurs due to methanol.

Another example of the different behaviors of ethanol versus methanol occur in the human body. The enzyme alcohol dehydrogenase converts each alcohol into formic acid and acetic acid, respectively. The problem presents itself at this point, where

the readily formed formate then acts on mitochondrial enzymes, with toxic effects on the body. Acetate does not do this.

Conclusions

It is clearly shown that methanol accelerates the degree of degradation of PA11. This has implications in the offshore oil and gas industry, in that the use of methanol in combating hydrate formation should be done with caution. Alone, it does not appear to degrade the PA11 to a point near the ductile-brittle transition. However, according to the literature, when coupled with an acidic environment, the effects of methanolysis may be amplified. Further study to explore the effects of methanol coupled with acidic environments is warranted.

The use of ethanol as a hydrate inhibitor does not appear to have any effect at all on PA11 degradation. Although its effects when coupled with an acidic environment have not been explored, it appears to be much safer for the PA11 liner.

Chapter 5 deals with the presence of small organic acids and how they affect the degradation of PA11. As will be shown, the effects they have on a polymer liner are much greater. Coupled with the use of methanol in a flexible pipe, the degree of degradation could be catastrophic, a serious implication with regard to safe operating procedures for the offshore oil and gas industry.

Chapter 4: Degradation of Polyamide-11 by Organic Acid Catalyzed Hydrolysis

Introduction

The mechanism and kinetics of hydrolytic degradation of polyamide-11 (PA11) in pure water has been proposed and experimentally proven in recent years [15,30,31]. This temperature-dependant process has implications in the offshore oil and gas industry with regard to the lifetime of the polyamide pipe liners employed by oil companies worldwide. As PA11 is a semi-crystalline polymer with an abrupt ductile-brittle transition, pipe liners are prone to sudden failure at low molecular weights. Understanding the effects of small degradative molecules likely encountered by the liners is therefore important. It has already been shown in Chapter 3 that small alcohols decrease equilibrium molecular weight and increase the rate at which the system reaches this molecular weight.

The effects of small carboxylic acids have yet to be adequately explored. It has been shown that carboxylic acids, ranging in size and shape from formic acid to naphthenic acids, are present in various concentrations in crude oil, depending on the geology of the rock and environmental conditions in which the oil was formed [36]. This has been confirmed in cases in industry through GC analysis of extractable acids [37].

It is already known that acids present significant issues with regard to the production of petroleum-based products from offshore operations. Acid-rich oils found

in the North Sea, West Africa, and Venezuela, have already lent problems through the formation of obstructive precipitates [37,38]. It is believed that the acids, especially the naphthenics, form salts at higher pHs which cause hard formations inside of production equipment, thus reducing production and efficiency [37]. It is also known that the presence of naphthenic acids causes corrosion in metallic production equipment [38].

To this point in the literature, the addition of acetate ion to an amide bond has been reported to occur only in the presence of very strong acid [39,40]. In the case of an unspecified amount of nitric acid, limited success was had [39]. However, in the presence of concentrated HCl, the reaction proceeded to completion [40].

In this study, the effects of acetic, 3-cyclopropionic, and valeric, and naphthenic acids at varying concentrations and temperatures on the degradation of PA11 pipe liner are explored and fit to a mathematical model. These acids were chosen to represent a wide range of acids found in crude oils of various locations. Acetic is simple, linear, and water-soluble. Valeric is linear and less hydrophilic. 3-cyclopropionic has a cyclic portion and is hydrophobic. Finally naphthenic acids are a mixture of larger cyclic hydrocarbons that are also hydrophobic. The results in this accelerated aging study are compared with real-world data from actual pipe liners in use throughout the world in Chapter 5.

Experimental

Solutions of acetic acid (Aldrich, 99.8%) and valeric acid (Aldrich, 99%) were prepared in deionized water at concentrations of 600 and 1200 ppm by volume. Solutions of 3-cyclopropionic (Aldrich, 99.5%) and naphthenic acid (Aldrich, CAS 1338-24-5) were added to heavy white mineral oil (Aldrich) at concentrations of 600 and 1200 ppm. The structures of these molecules are shown in Figure 4.1.

Coupons of commercially available PA11 with plasticizer, identical to that used in flexible pipes, were cut into 0.5 cm x 0.5 cm x 0.5 cm cubes and placed into 50 mL heavy-walled Ace glass pressure tubes. To these tubes 15mL of stock acid solution was added. Then, 15mL of mineral oil (for the water-soluble acids) or 15mL of water (for the oil-soluble acids) was added to the tube. Half of the PA11 coupons were held in the oil phase, and half in the water phase using steel cages.

To eliminate the effects of oxidation, which would lead to an over-exaggeration of the degradative process, each tube was bubbled with Argon (99.999%) for between twenty and thirty minutes in a deoxygenated chamber in order to displace the dissolved oxygen to ppb levels. The oxygen level was monitored with an Oakton DO110 series dissolved oxygen meter at the sampling intervals. The limit of detection of the instrument was 10 and it had an uncertainty of ± 10 ppb. Over the course of the experiments, the oxygen levels were maintained between 0 and 50 ppb.

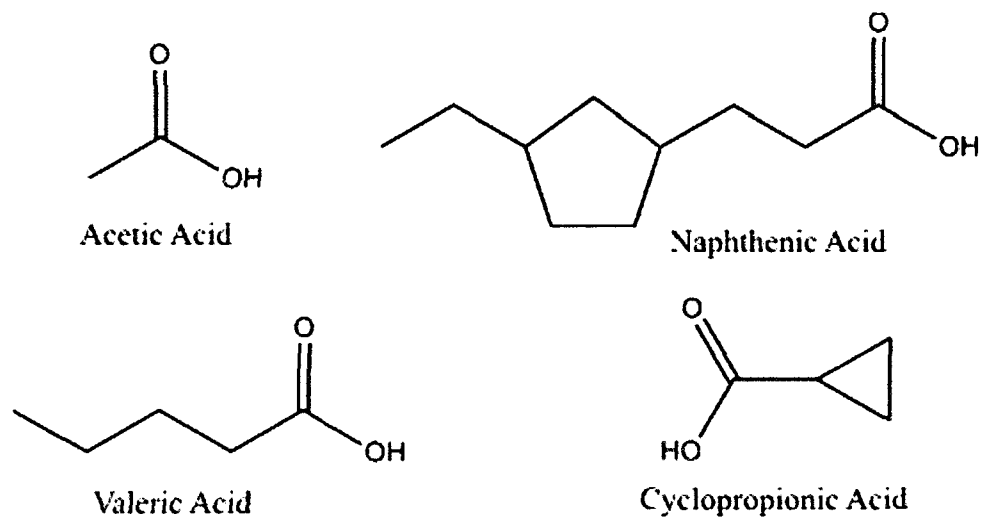


Figure 4.1 – Structures of the small organic acids used in this study.

Once sealed, the tubes were placed in ovens held at 100°C. They were sampled at intervals selected for a good representation of the degradative process. Samples from the oil and water phases were both retrieved. The resealing process was repeated in the same way as the initial setting-up of the tubes. No tube was left out of the ovens for any longer than eight hours.

Thermogravimetric analysis was performed on a portion of each sample to determine the amount of volatile compounds absorbed, as described in Chapter 2. Viscosity and SEC-MALLS experiments were performed to determine the degree of degradation, also as described in Chapter 2.

Mathematical Theory

Similar to the mathematical treatment described in Chapter 3, one may describe the general process as previously shown by the competing rates of hydrolysis and recombination [30,31]. Under the premise of the acid-catalyzed degradation scheme proposed by Schowen et al. [41], one may re-write equation (3.1) as:

$$-\frac{d[-\text{NH}_2]}{dt} = -\frac{d[-\text{COOH}]}{dt} = k_{\text{RAc}}[-\text{NH}_2][-\text{COOH}] - k_{\text{HAc}}[-\text{NHCO}][-\text{H}_2\text{O}] \quad (4.1)$$

where k_{HAc} and k_{RAc} denote the acid-catalyzed rates of hydrolysis and recombination, respectively. By again assuming acid and amine are produced in stoichiometric amounts, and that the concentration of water is large and constant within the polymer matrix, we re-write (4.1) with k_{HAc} becoming the pseudo first order rate constant of hydrolysis,

k'_{HAc} :

$$-\frac{d[-\text{NH}_2]}{dt} = -\frac{d[-\text{COOH}]}{dt} = k'_{\text{RAC}}[-\text{COOH}]^2 - k'_{\text{HAC}}[-\text{NHCO}]. \quad (4.2)$$

The mathematical treatment of this equation is the same as described in Chapter 3, (3.3) - (3.7). This leads to a revised relationship between initial amide bond concentration (a_0), equilibrium amide bond concentration in the acid-catalyzed case (a'_{eAc}), amide bond concentration at time= t (a), and rate of hydrolysis (k'_{HAC}).

$$\left(\frac{a_0 - a'_{\text{eAc}}}{a_0 + a'_{\text{eAc}}} \right) \ln \left[\frac{a_0^2 - a'_{\text{eAc}}a}{a_0(a - a'_{\text{eAc}})} \right] = k'_{\text{HAC}}t. \quad (4.3)$$

The reverse process, amide recombination, is expressed in this scheme as

$$k'_{\text{RAC}} = \frac{k'_{\text{HAC}}a'_{\text{eAc}}}{(a_0 - a'_{\text{eAc}})^2}. \quad (4.4)$$

As in Chapter 3, one may plot the experimental data as amide bond concentration versus time and optimize k'_{HAC} and a'_{eAc} in (4.3) to minimize the variance between experimental points and amide concentration at time= t . k'_{RAC} may then be calculated using (4.4).

Results

It was determined in all cases that samples from the oil and water phases had the same MW within the error of the measurement. An average of the oil and water phases was used for data presentation and analysis.

At 100°C, it is shown that the organic acids studied both accelerate the ageing process and increase the degree to which it occurs. In the cases of all four acid systems, as compared to the water/mineral oil system, significant effects are realized, as seen in Figures 4.2, 4.3, 4.4, and 4.5.

100°C, commercial PA11, Acetic Acid, MW v. ageing time

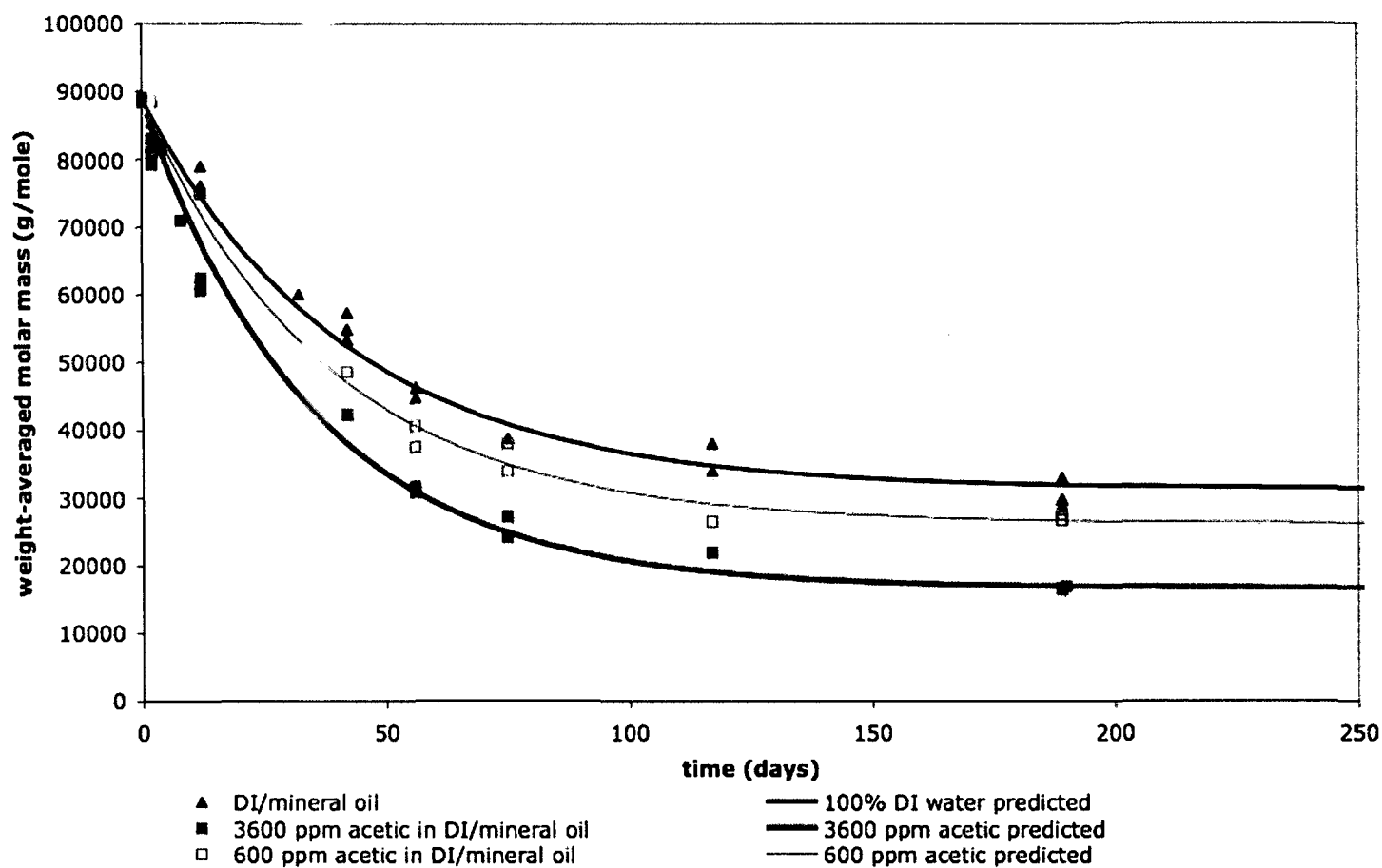


Figure 4.2: The aging of commercial PA11 at 100°C in two concentrations of acetic acid, along with a white mineral oil/deionized water environment. The model described in this chapter was fitted to the

100°C, commercial PA11, Valeric Acid, MW v. ageing time

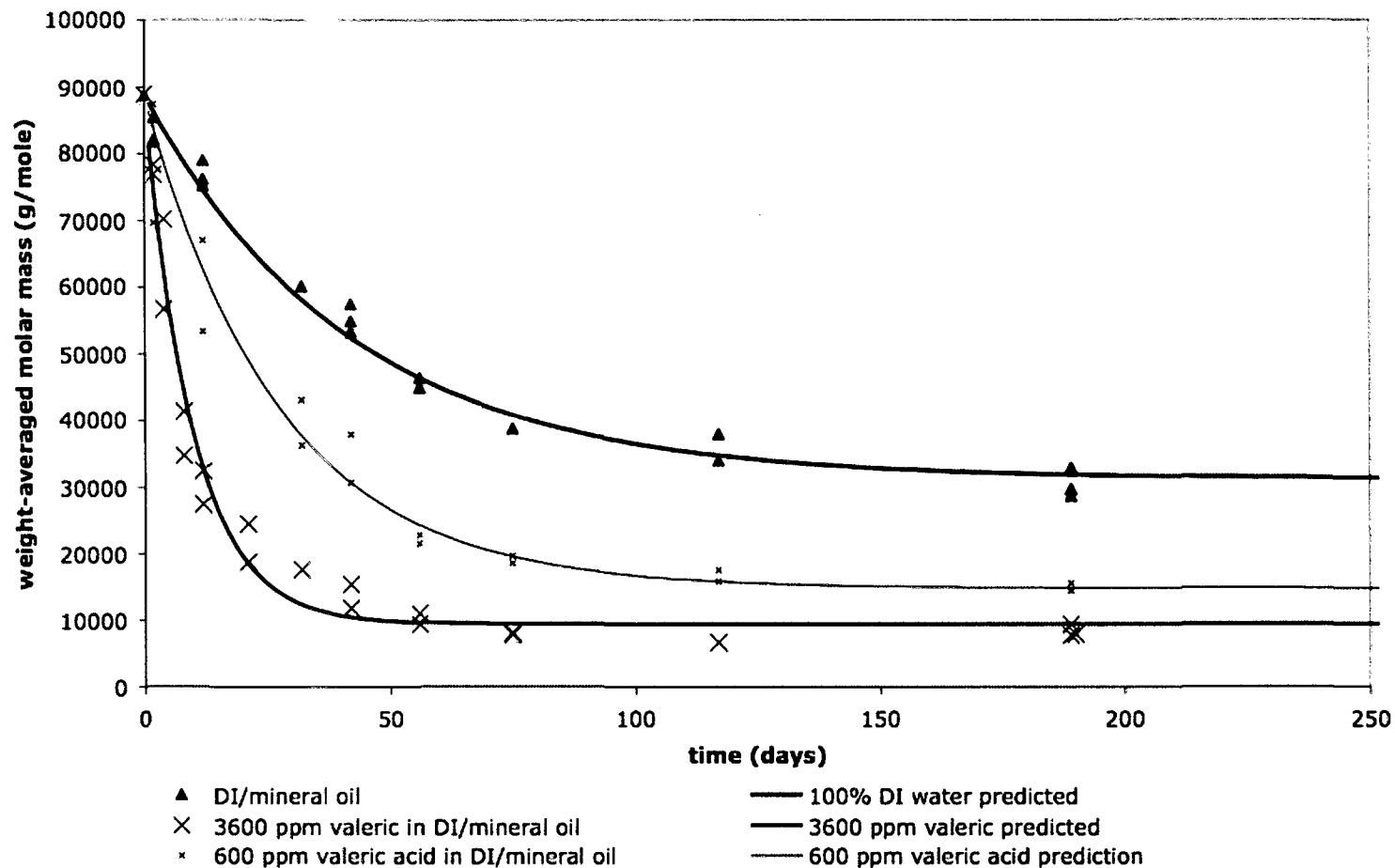


Figure 4.3: The aging of commercial PA11 at 100°C in two concentrations of valeric acid, along with a white mineral oil/deionized water environment. The model described in this chapter was fitted to the data sets.

100°C, commercial PA11, Cyclopropionic Acid, MW v. ageing time

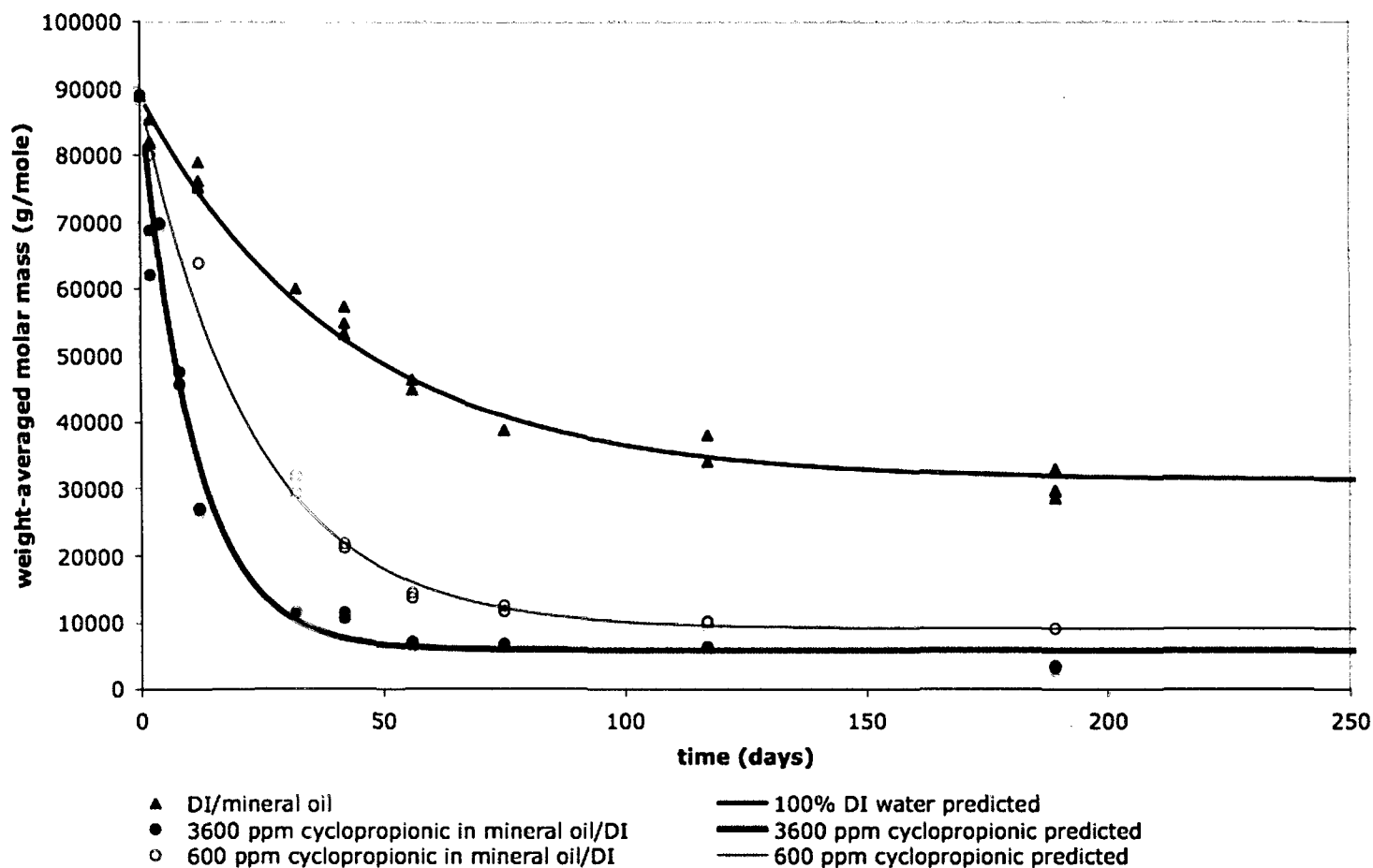


Figure 4.4: The aging of commercial PA11 at 100°C in two concentrations of cyclopropionic acid, along with a white mineral oil/deionized water environment. The model described in this chapter was fitted to the data sets.

100°C, commercial PA11, Naphthenic Acid, MW v. ageing time

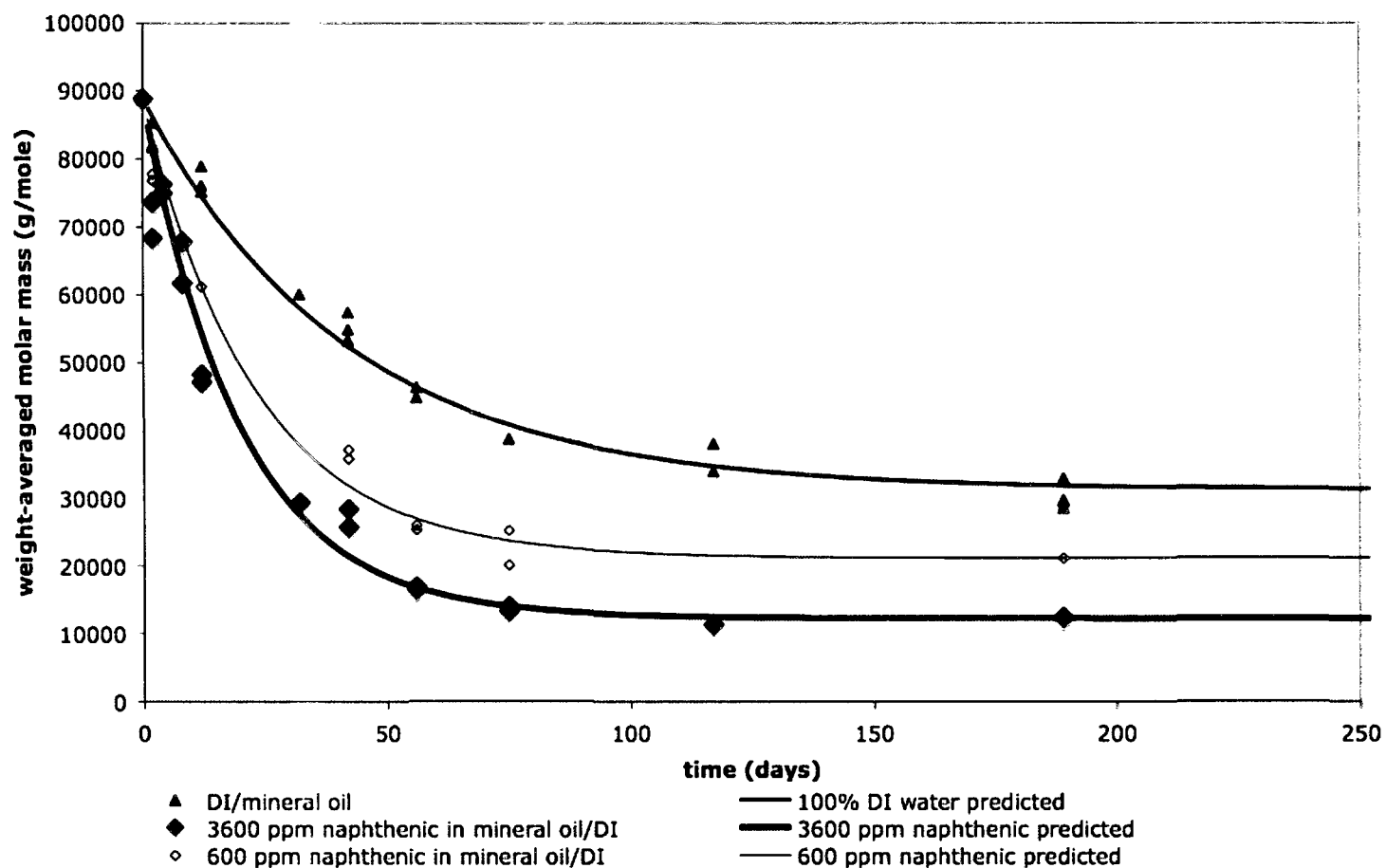


Figure 4.5: The aging of commercial PA11 at 100°C in two concentrations of naphthenic acid, along with a white mineral oil/deionized water environment. The model described in this chapter was fitted to the data sets.

The ageing processes for the various acids may also be compared with each other, as in Figures 4.6 and 4.7.

100°C, commercial PA11, 600 ppm acids, MW v. ageing time

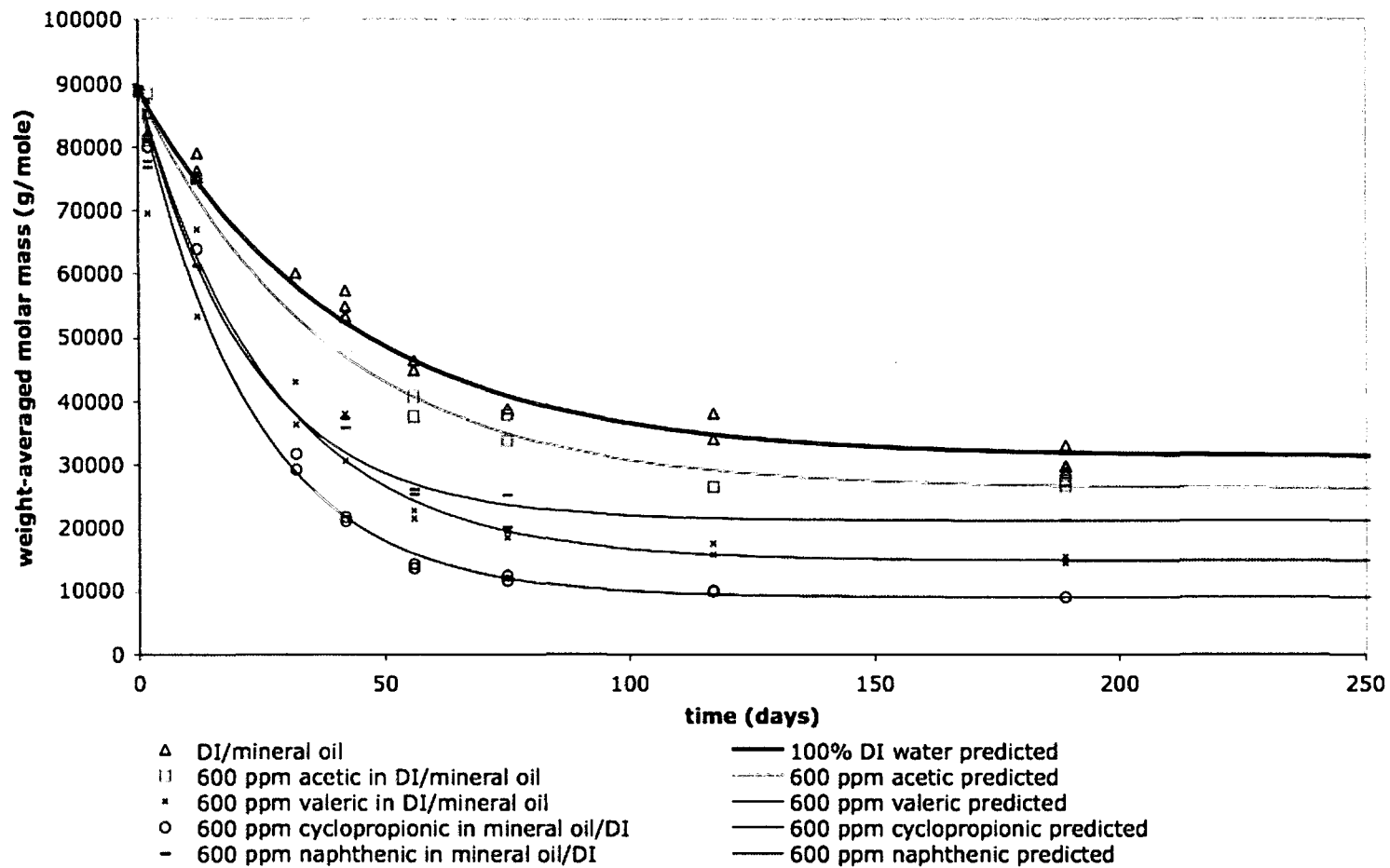


Figure 4.6: The aging of commercial PA11 at 100°C in 600 ppm small carboxylic acid solutions.

100°C, commercial PA11, 3600 ppm acids, MW v. ageing time

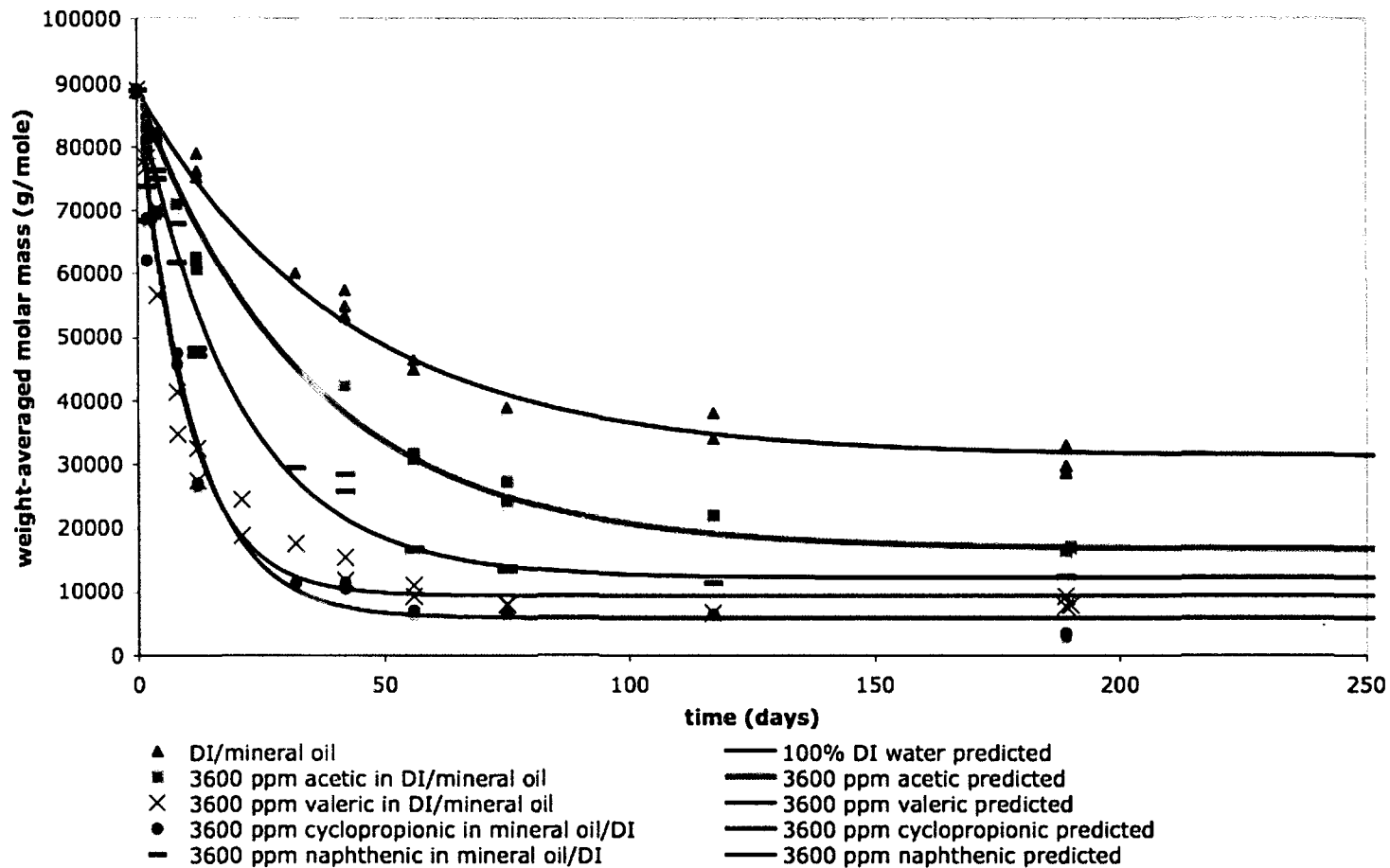


Figure 4.7: The aging of commercial PA11 at 100°C in 3600 ppm small carboxylic acid solutions.

Table 4.1: Rate constants and equilibrium molar masses for small carboxylic acids at 600 and 3600 ppm.

Acid	Concentration	k'_{HAc} $\pm 0.2\text{E-}02$	k'_{RAC} $\pm 1.6\text{E-}5$	MW'_{eAc} (g/mole) $\pm 8\%$
	(ppm) ± 10 ppm			
Water	-	1.6E-02	5.4E-05	31400
Acetic	600	1.9E-02	4.5E-05	26200
	3600	2.4E-02	2.7E-05	16700
Naphthenic	600	3.4E-02	5.6E-05	21200
	3600	4.4E-02	3.2E-05	12200
Valeric	600	3.1E-02	3.0E-05	14800
	3600	9.2E-02	4.8E-05	9400
Cyclopropionic	600	3.9E-02	2.0E-05	9000
	3600	8.6E-02	2.5E-05	5800

The dependence of acid concentration on rate of hydrolysis is shown in Figure 4.8, and equilibrium molar mass vs. acid concentration in Figure 4.9. In Figure 4.8, the lines are forced through the zero-concentration point. The uncertainties in the k'_{HAc} and MW'_{eAc} values make the error in the k'_{RAC} values large, but the values in Table 4.1 show that there is little to no change in the k'_{RAC} , within the uncertainty. This suggests that any effects on k'_{RAC} regarding acid type or concentration are small.

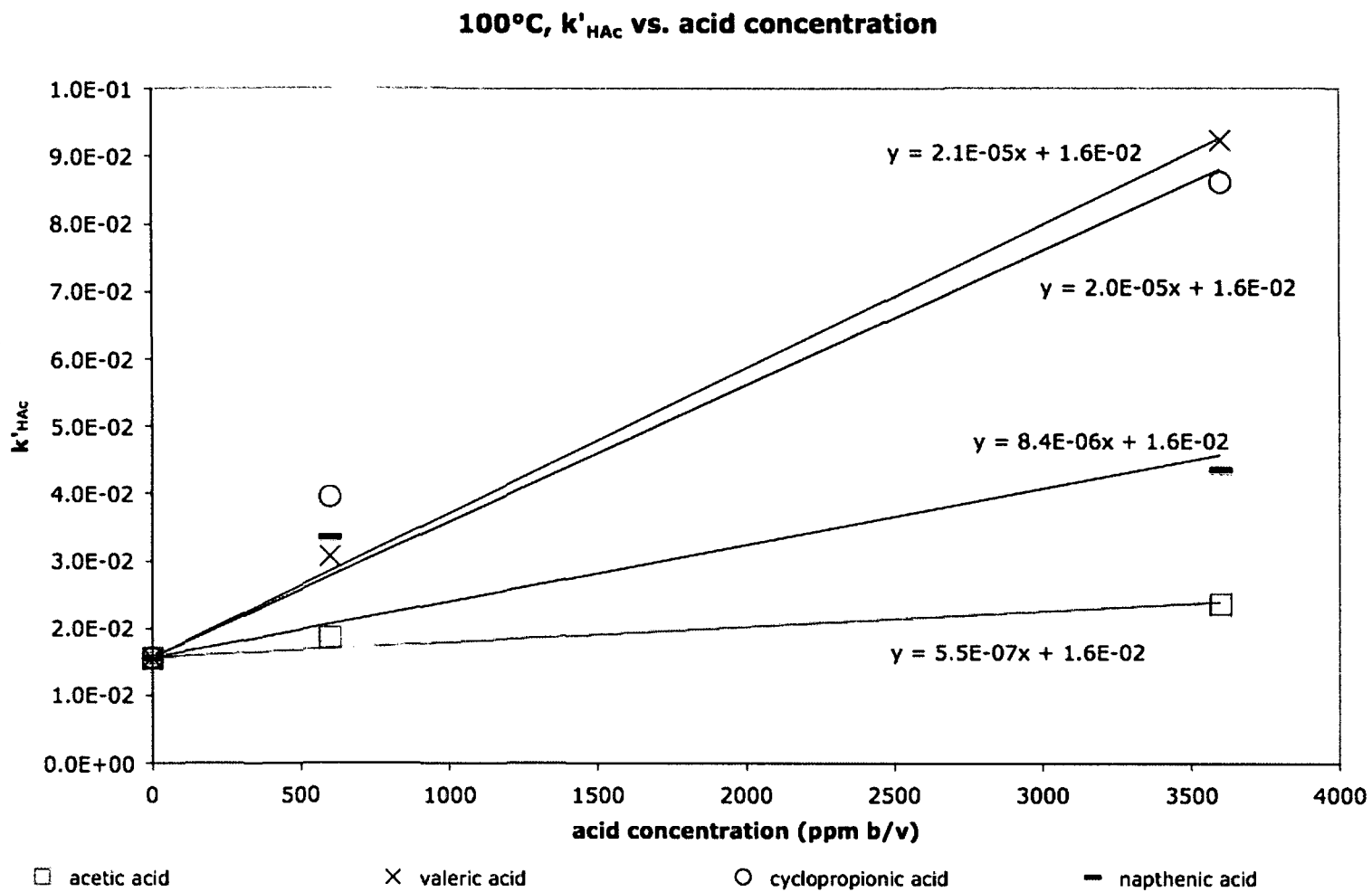


Figure 4.8: The PA11 rate of acid-catalyzed hydrolysis, k'_{HAC} , vs. small carboxylic acid concentration at 100°C.

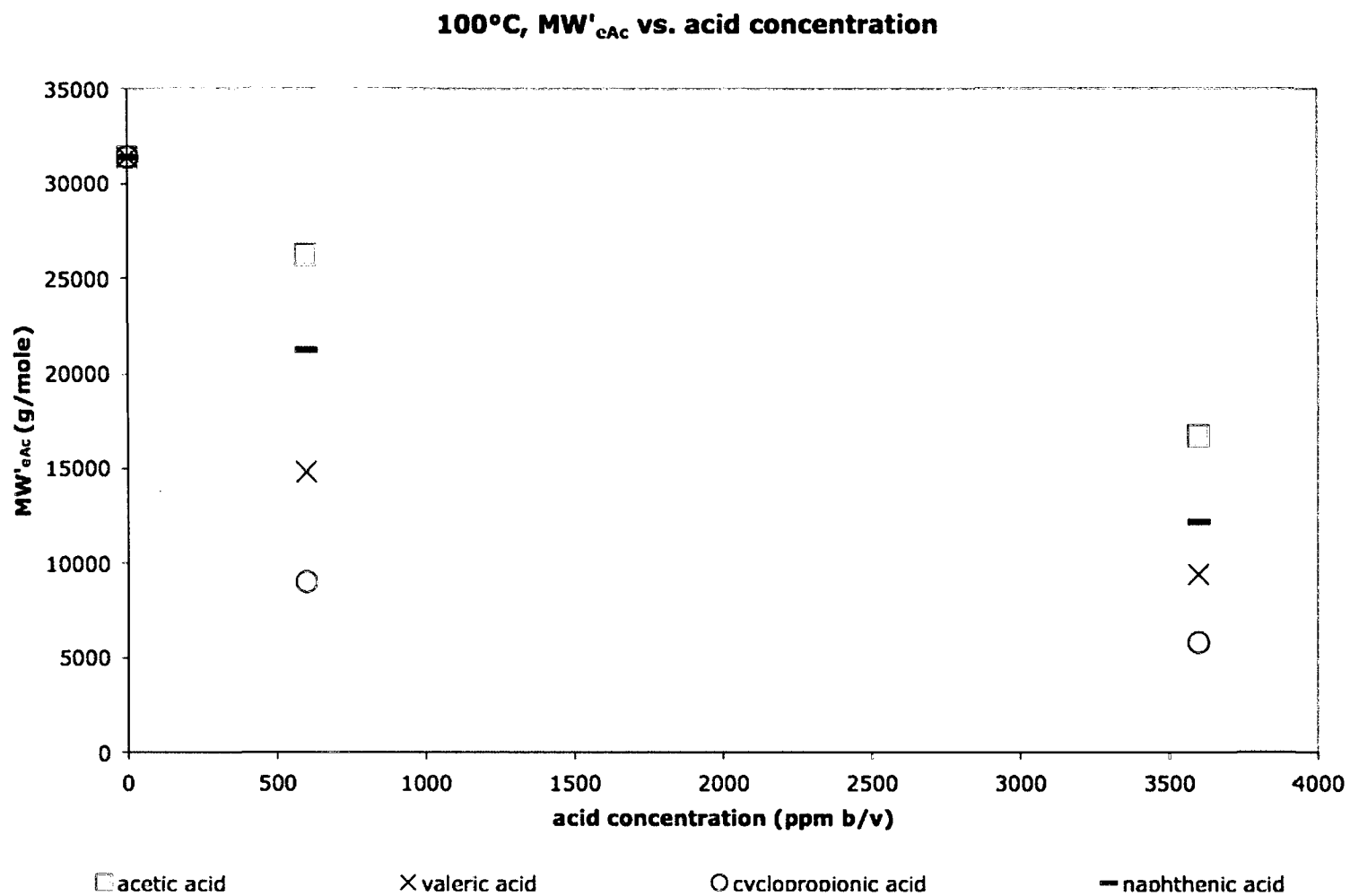


Figure 4.9: The effect of MW'_{eAc} for commercial PA11 as a function of small organic acid concentration at 100°C.

Discussion

It appears that the two phases of the test systems (oil and water) have no bearing on the ability of an acid to degrade the polymer, regardless of the acid's solubility in either water versus oil. This is likely due to acids being transferred from the fluid to the polymer, and subsequently replenished in the depleted testing fluid. This appears to happen even when acid solubility in a given fluid is low. Work by Havre et al. describes the presence of naphthenic acids on both sides of an oil/water interface, and notes that the acid forms micelles in the water phase, and reversed micelles in the oil phase[38]. This supports the finding of equal degrees of degradation in both oil and water phases.

The data shows the degradative processes are catalyzed by the organic acids as proposed previously by lowering the energy barrier of the formation of a tetrahedral intermediate at the amide bond [42]. This intermediate collapses, leaving an acid and an amine. This same process is thought to occur in some enzymes in the human body. Pepsin, for example, has a number of carboxylic acid groups adjacent to the active site that appear to facilitate the addition and removal of amino and acyl groups [42].

Due to the degradative processes yielding an equilibrium molar mass, as opposed to continually declining, it is unlikely that the acids are reacting and "capping" the amine ends of the hydrolyzed chains. If this were the case, one would expect a further decline in equilibrium molar mass, possibly without an equilibrium value, as the amine ends become amidized and removed from the repolymerization kinetic scheme in the model described above.

The data also suggests that there is a concentration dependence on the rate at which the PA-11 degrades. In all cases, k'_H is higher for the 3600 ppm concentrations as compared to the 600 ppm, and all 600 ppm k'_H 's are higher than water. The concentration dependence across the range studied appears to be linear. Equilibrium molecular weight is shown to decline with higher concentrations of acetic, valeric, naphthenic, and cyclopropionic acids, however this relationship is not linear and more work needs to be done to establish a scientifically-based mathematical dependence. This relationship is likely a function of the acid structure, as the acetic acid seems to have a possibly linear dependence throughout the concentration range studied here whereas naphthenic acid, for example, appears to have a higher-order dependence.

Acetic and valeric, the two straight-chain acids, effect the degradation of PA11 to a similar degree. The valeric acid, more hydrophobic, appears to be more detrimental. This may be due to it being more readily absorbed by the PA11. The small, hydrophobic, and cyclic cyclopropionic acid is even more effective at accelerating the rate of hydrolysis when compared to the valeric acid. This suggests that the similar degree of hydrophobicity in a smaller volume allows it to be absorbed even more easily. Finally, the naphthenic acid, though more hydrophobic, is much larger than the other acids and is likely to not be able to enter the polymer matrix due to spatial restrictions.

Conclusion

All of the studied acids yield significant degradative effects when compared to water alone. The effects of the acids are appreciable at low concentrations, according to the drop between zero and 600 ppm in Figure 4.9. According to Chaupart et al, the ductile-brittle transition of PA-11 is slightly above $MW=12\ 000\ g/mole$, as that is the theoretical limit at which the polymer loses all amorphous regions, leaving only the brittle crystalline lamellae [15]. According to this work, PA-11 in the presence of acetic, valeric, and cycloprionic acids is in danger of failure, depending on the temperature and concentration. Though all of these acids are found in the field, acetic is the most common, as is to be shown in Chapter 5. Further study with regard to the dependence of acetic acid-catalyzed degradation will be pursued and compared to multiple real-world examples from the field in Chapter 5.

Chapter 5: Comparison of Accelerated Aging of Polyamide-11 to Long-Term Molecular Weight Changes in the Field

Introduction

The useful lifetime of PA11 in the crude oil and water environments found in the field depends on several factors, primarily temperature but also the concentration of small carboxylic acids, as shown in Chapter 4. In Chapters 3 and 4, it is shown that the kinetics of PA11 aging follow an Arrhenius temperature dependence. By incorporating the temperature-dependant aspects of PA11 aging with the effects of small acid concentration, one has the means to approximate PA11 lifetime in the field. This degree of modeling with respect to PA11 has not yet been performed on aging in the field.

One way in which a specific field environment may be simulated is through replication of ion and acid content in the field in deionized water. The crude oil and production water which flows through a liner in a given sub-sea field may be analyzed for elemental as well as acid type and concentration. Given these ion and acid concentrations, one determines the appropriate amount of commonly available salts and acids to add to the deionized water in which the PA11 is aged. This simulated solution may then be placed into reaction vessels to which PA11, both fresh and pre-aged, is

added. An advantage to this approach is that one may gather more conservative lifetime estimates by increasing the concentrations of components hypothesized to be most destructive.

An alternative to ageing in the simulated solution is to pre-age PA-11, again both fresh and pre-aged, in crude oil and produced water mixtures drawn directly from the fields and shipped to the lab. An advantage to this method is that one may easily test environments from multiple points in an oil field without the costly and time-consuming determination of component analysis and replication of the fluid environments.

In this chapter, the rate and degree of molecular weight change in the lab for multiple field-scenarios is demonstrated and reconciled with basic models for water and small organic acids as described in Chapters 3 and 4. In cases for which liner samples from the field are available for analysis, the results are compared to accelerated aging findings utilized by the exact model.

Modeling

Prior to this work, four publications have been published which model the effects of temperature on the ageing of PA11 in water alone [15,30,31,43]. The first work was published by Serpe and Chaupart, added to a year later by coworkers Chaupart, Serpe, and Verdu, then updated in 2002 by coworkers Jacques et al. [15,30,43]. As the work described in the 1997 publication is build upon in the subsequent 1998 and 2002 publications, these collective findings of these three papers are treated together.

There are three main assumptions made in this modeling scheme, one of which has been removed by the model taken into account in this dissertation. The first assumption is that aging conditions within a solid sample of polymer are homogenous [15,30,43]. This means that there is no diffusion of monomer from the sample as chains are broken. It is also assumed that there is a constant MW maintained in the sample throughout the ageing process. This is valid as the diffusion of water in to the polymer reaches an equilibrium in two to three days [30].

Another assumption is that the effects of crystallinity are neglected [15]. It is proposed that hydrolytic aging is much more likely to occur in amorphous regions in the polymer matrix due to the tight packing and subsequent steric hindrances found in the crystalline regions of the polymer.

It is also determined that acid and amine chain ends formed via amide hydrolysis are increased in stoichiometric ratio over the course of hydrolysis [15,30,43]. This is reasonable with respect to aging, as theoretically this is the only significant outcome of such a process. By extension what this assumption is declaring is that the

polydispersity, or ratio of weight-averaged molar mass to number-averaged molar mass, of PA11 remains near two, the theoretical value for any polycondensation reaction [9].

The concentration of water in the polymer is treated as a constant, as it has been shown in previous literature that the diffusion process is fast relative to hydrolysis reaction, and that the water remains a constant 2-3% in the PA-11, depending on specific conditions within the aging environment, once reaching an equilibrium [43].

Finally, the critical assumption that has been removed by the current model is that the average number of amide bonds within a polymer chain was assumed to not be changing as the degradation proceeded [15,30]. This assumption, that amide bond concentration remains constant with respect to the hydrolytic process, would be expected to over estimate the speed with which the aging process occurs, even though a final equilibrium molar mass is obtainable.

With that, these two papers report an aging model where at time t ,

$$Mn = \frac{\frac{1}{Mn_0} + \frac{1}{Mn_e} + \left(\frac{1}{Mn_e} - \frac{1}{Mn_0} \right) e^{-Kt}}{\frac{1}{Mn_0} + \frac{1}{Mn_e} - \left(\frac{1}{Mn_e} - \frac{1}{Mn_0} \right) e^{-Kt}} \quad (5.1)$$

where Mn is number-average molar mass at time= t , Mn_0 is initial molar mass, Mn_e is equilibrium molar mass, and K is the temperature-dependant rate-determining variable [30]. K is defined as

$$K = 2\sqrt{k_R k_H E_0 W_p} = 2 \frac{k_R}{Mn_e} \quad (5.2)$$

where k_R is the rate of acid and amine recombination, k_H is the rate of hydrolysis, E_0 is the initial concentration of amide bonds (found from the initial molar mass), and W_p is the concentration of water in the polymer matrix. Mn_e may then be re-written as

$$Mn_e = \sqrt{\frac{k_R}{k_H E_0 W_p}} \quad (5.3)$$

and so

$$k_R = \frac{KM_{ne}}{2} \quad (5.4)$$

and [30]

$$k_H = \frac{K}{2Mn_e E_0 W_p}. \quad (5.5)$$

Meyer et al. [31], an independent group whose work pre-dates the final Jacques et al. paper by around six months, describe a hydrolytic process that is arrived at in a similar fashion to the work performed by those in refs. [15], [30], and [42]. Their work stands out in that they employ light scattering, a primary means of determining molar mass as described in Chapter 2, to characterize the hydrolysis of PA11. They also go beyond the pre-dated publications by proving that the same equilibrium molar masses reached via hydrolysis may be obtained through condensation, which dominates in the case when $Mw_0 < Mw_e$. The implications of this fact are important and will be shown when considering real-world field aging systems later in this chapter.

Regarding the derivation of the kinetic equations, their assumptions are the same as those outlined in refs. [15], [30] and [42], yet they go on to stipulate that the presence of plasticizer does not affect the aging process [31]. With that, it is shown that

$$MW_t = MW_e \left(\frac{1 + \frac{MW_0 + MW_e}{MW_0 - MW_e} e^{Jt}}{-1 + \frac{MW_0 + MW_e}{MW_0 - MW_e} e^{Jt}} \right) \quad (5.6)$$

where MW_t is molar mass at time= t , MW_0 is the initial molar mass, and MW_e is the equilibrium molar mass [31]. It is then shown that

$$J = 2\sqrt{k_h k_p [-NHCO-][H_2O]} \quad (5.7)$$

and

$$MW_e = \frac{2\sqrt{MW_0 D}}{\frac{k_h}{k_p} [-NHCO-][H_2O]} \quad (5.8)$$

where k_h is the rate of hydrolysis, k_p is the rate of condensation, D is the density of the polymer, and $[-NHCO-]$ and $[H_2O]$ are the concentrations of amide units and water, respectively [31].

With prior modeling work thus treated, the model proposed in Chapters 3 and 4 is now treated. One significant issue with the model described thus far is the assumption that the initial concentrations of acid and amine are zero. This is acceptable in the constant-temperature cases described to this point, in that for the purposes of data fitting and molar mass predictions, one may calculate the molar mass for any number of times to create a line based on initial molar mass, temperature, and acid concentration. However, when one attempts to begin with a given molar mass that is the product of a prior aging calculation, the incorrect assumption that acid and amine concentrations are zero leads to large errors and that this precludes the possibility of molar mass ever going up through recombination, even under the conditions where $MW_e > MW_0$.

Because the new model does not make the important assumption that amide bond concentration remains constant over the course of aging, it provides more scientifically accurate determinations of k'_H , k'_R , and MW'_e . And, more accurate determinations of temperature dependence and finally activation energies are performed for each scenario. However, our work in Chapters 3 and 4 must be adapted for use in predicting PA11 aging in dynamic conditions when the temperature changes. This is done by adapting the previously described findings to the modeling scheme described by Meyer et al., a model that inherently adjusts the rate of molar mass based upon initial and equilibrium molar masses [31].

To begin, we consider the temperature dependence of k'_H and k'_R with respect to the pH=7 water scenario as described in Chapter 3. Using these two relationships, we may predict the degradation rate and MW versus time in water under field conditions. They are found to be

$$k'_H = 3.12 \times 10^9 e^{\left(\frac{-9.78 \times 10^3}{T}\right)} \quad (5.9)$$

and

$$k'_R = 3.25 \times 10^6 e^{\left(\frac{-9.28 \times 10^3}{T}\right)}. \quad (5.10)$$

Equation (3.9), relating k'_H , k'_R , a_o , and a'_e , may be solved for a'_e using the quadratic equation. Recall, a is the concentration of amide bonds, which is directly proportional to the MW. As the quadratic equation yields two results, the nonphysical one was ignored, leaving

$$a'_e = \frac{2k'_R a_o + k'_H - \sqrt{4k'_H k'_R a_o + k'^2_H}}{2k'_R} \quad (5.11)$$

As Equations (5.9-5.11) give the complete temperature dependence in water with respect to the exact model as described in Chapter 3, this model may be modified to account for the presence of acetic acid. The dependence of k'_{HAc} on the concentration acetic acid at 100°C was demonstrated in Figures 4.8. Using the concentration dependence of acetic acid, and by assuming that it has the same temperature dependence as water, we may calculate a temperature dependent k'_H using equation 5.9, and then modify it using the concentration dependence, as shown in equation 5.12:

$$k'_{HAc} = (5.5 \times 10^{-7}) \times c + k'_H \quad (5.12)$$

where k'_{HAc} is the now temperature *and* acetic acid concentration dependent rate of hydrolysis, c is the concentration of acetic acid in ppm, and k'_H is the temperature-dependent rate of hydrolysis in water.

The rate of recombination, k'_R , has the highest percentage of uncertainty with respect to concentration of acetic acid, whereas the molar mass is known with a much greater degree of certainty. Thus, the results of (5.9) and (5.10) are used in (5.11) to determine the temperature-dependent water equilibrium molar mass. This equilibrium molar mass is then changed according to the concentration of acetic acid using a normalized molar mass vs. concentration relationship, derived from Figure 4.9. That relationship is shown here:

$$MW'_{eAc} = MW'_e \times [(-1.34 \times 10^{-4}) * c + 1.00] \quad (5.13)$$

where MW'_{eAc} is the temperature and acetic acid concentration dependent equilibrium molecular weight and MW'_e is the temperature dependent molecular weight in water.

Given these values for k'_{HAc} and MW'_{eAc} , one may then replace the corresponding parameters in the Meyer et al. equation described in (5.6), where J becomes k'_{HAc} and MW_e becomes MW'_{eAc} . MW_t and MW_0 retain the same meanings. Thus:

$$MW_t = MW_{eAc} \left(\frac{1 + \frac{MW_0 + MW_{eAc}}{MW_0 - MW_{eAc}} e^{k'_{HAc}t}}{-1 + \frac{MW_0 + MW_{eAc}}{MW_0 - MW_{eAc}} e^{k'_{HAc}t}} \right). \quad (5.14)$$

Figure 5.1 shows this updated non-exact model versus the exact model arrived at thus far. It should be noted that although they arrive at the same equilibrium molecular weight, the shapes of the curves are slightly different in that the nonexact model falls more quickly. This is due to the assumption in the derivation of the nonexact model that amide bond concentration remains constant, whereas the kinetics in the exact model take varying amide bond concentration into account. However, the fit is good, especially at small step sizes. Figure 5.2 shows this relationship with 600 ppm acetic acid.

**Exact model and nonexact model comparison
100°C water, 0 ppm acetic acid, $j=k'_{HAC}=.0155$**

100

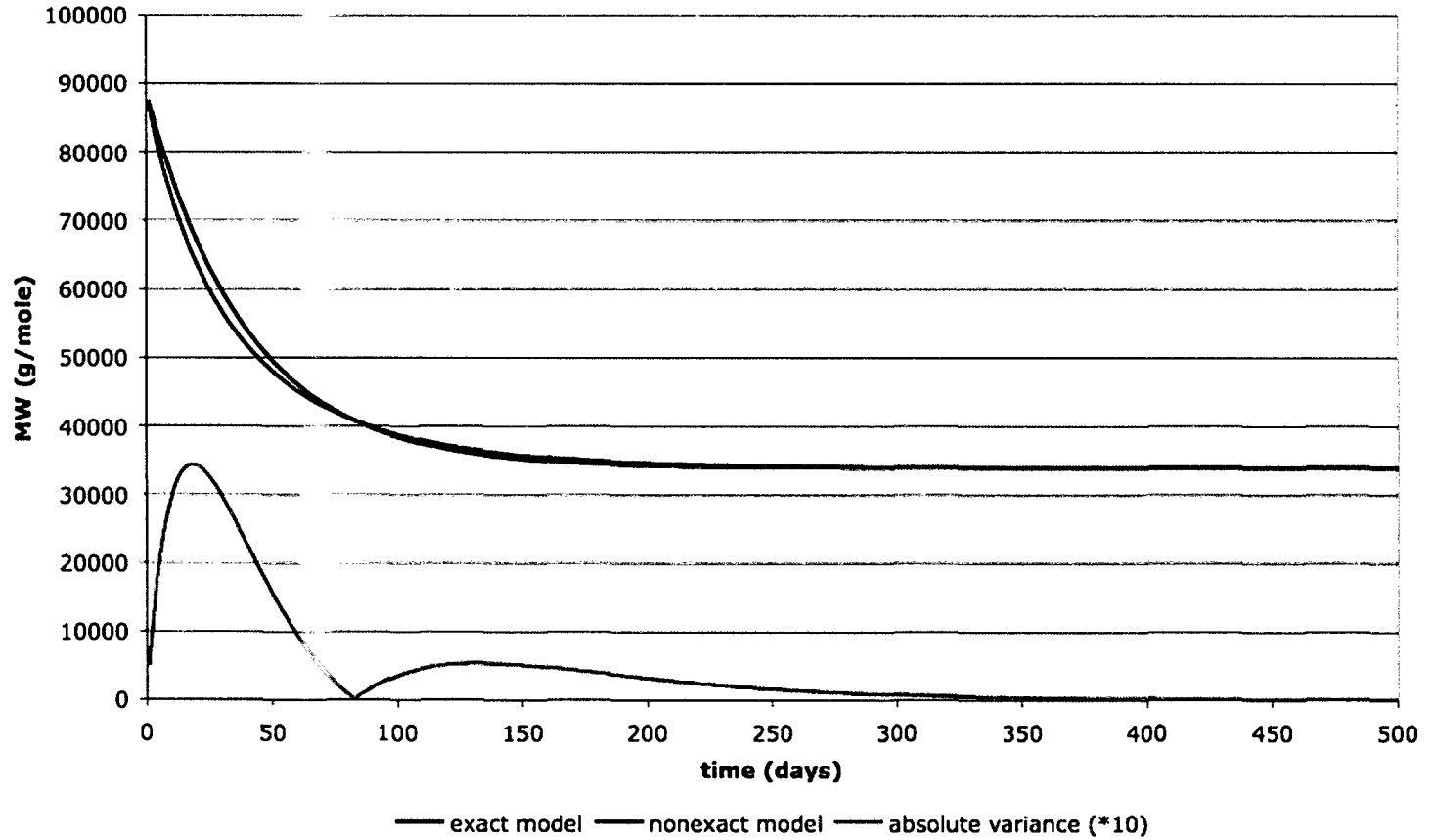


Figure 5.1: A comparison between the exact and non-exact models at 100°C without acetic acid. The absolute variance is the absolute value between the two models multiplied by ten.

**Exact model and nonexact model comparison
100°C water, 600 ppm acetic acid, $j=k'_{\text{HAC}}=0.0158$**

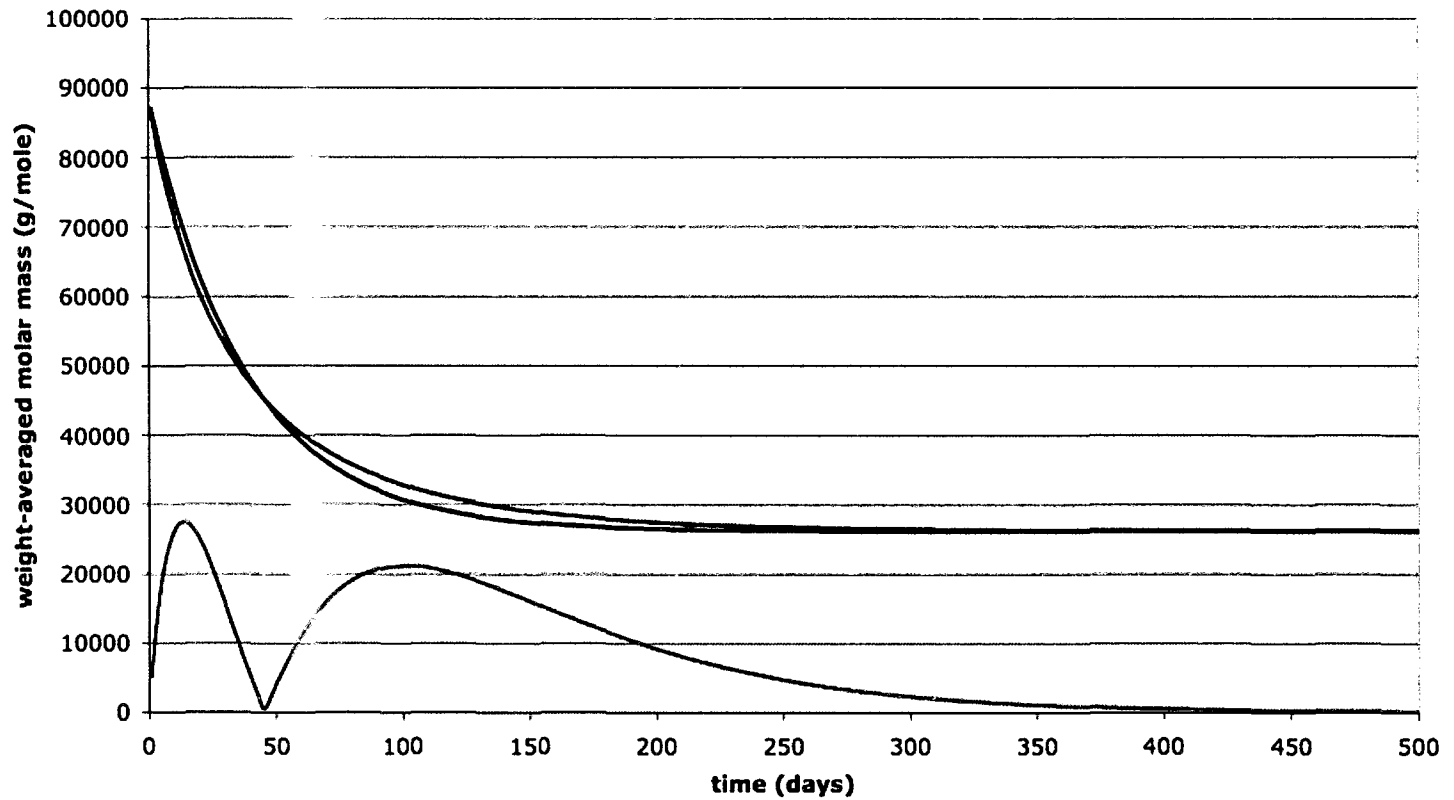


Figure 5.2: A comparison between the exact and non-exact models at 100°C with 600 ppm acetic acid. The absolute variance is the absolute value between the two models multiplied by ten.

Characterizing Offshore Liners with the Model

Case 1: Asian-Pacific Field A:

Asian-Pacific Field A exists off the NW shore of Australia. The acetic acid concentration of this field is negligible. In order to qualify the model described above, the exact temperature history is used along with the measured molar masses of coupons retrieved from the field and analyzed in the lab. Two areas of the riser were studied – the hotter wellhead, which has an average temperature of 120°C, and the cooler topside, which has an average temperature of around 94°C.

This study begins with an analysis of the wellhead coupons. Figure 5.3 plots molar mass vs. time for the model prediction, temperature vs. time, and the coupon measurements from three areas of the sample.

Asian-Pacific Field A, 0 ppm Acetic Acid, Wellhead Prediction

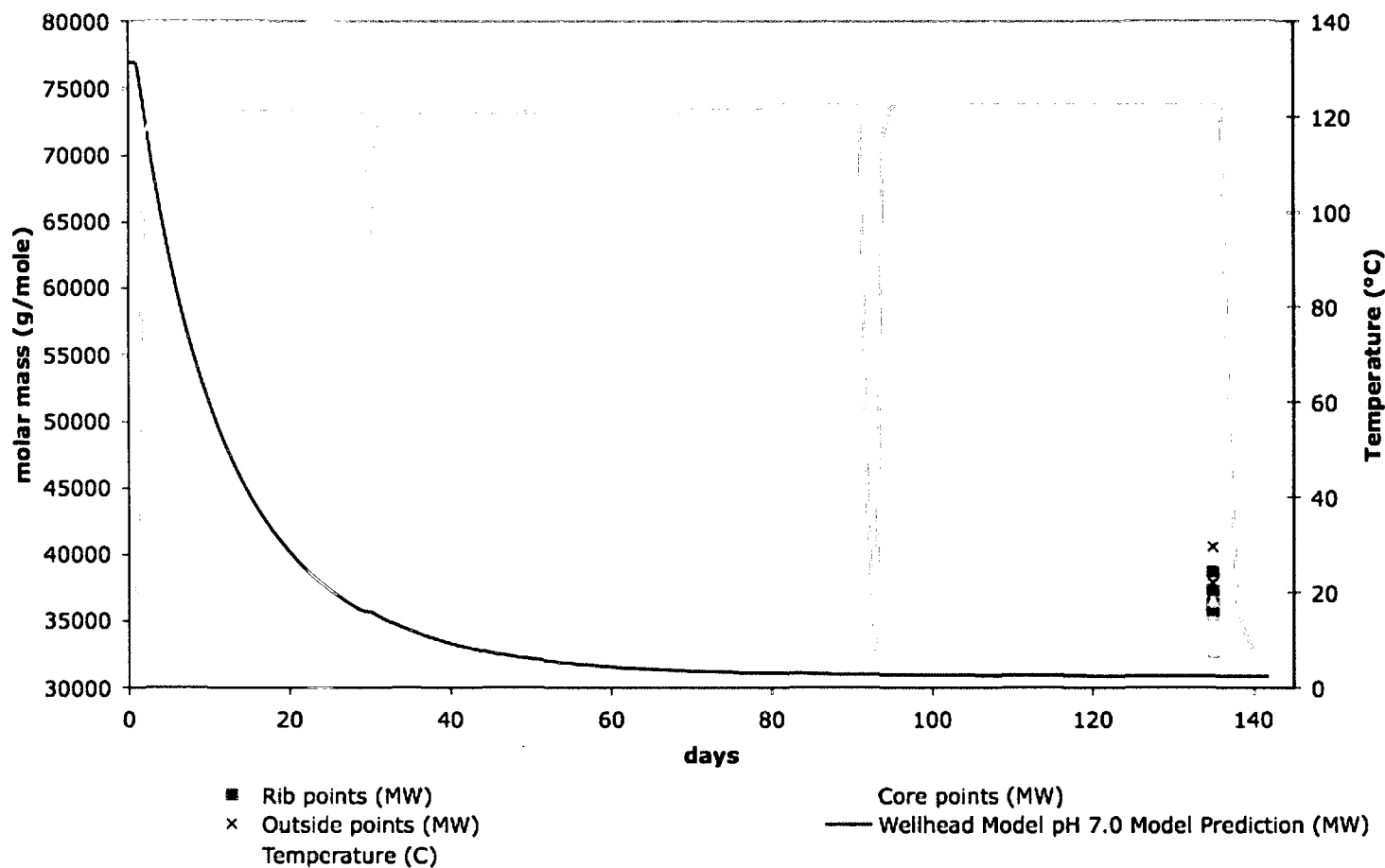


Figure 5.3: Degradation prediction for Asian-Pacific Field A. This field has nominal acetic acid content. Experimental points representing a cross section from a sample of the pipe liner are shown.

We see that the high temperatures lead to an estimated equilibrium molar mass in roughly eighty days, and that the periodic decreases in the temperature are not prolonged enough to allow for any significant re-polymerization of the PA11. The wellhead coupons, analyzed at day 135, have an average molar mass of ~36 000 g/mole. The rib, outside, and core measurement represent a cross-section of the sample of liner tested. This sample was fully submerged in the fluid flow, however, so we would expect the outside edge and rib edge to have the same molar mass, whereas the core of the sample represents a different layer of the material and could be different. This is reflected in the analysis in that the rib/outside samples are higher than the core samples.

The model predictions of the coupon's molecular weight are below the measured values by about twice the expected variation for a MALLS measurement. Given the scatter both above and below the model's predictions for laboratory studies and the field coupon results to be reported next, this is likely due to the temperature being somewhat lower than the 120°C reported in the coupon holder.

Data from the topside of the system was simultaneously taken. These results are shown in Figure 5.4. Two formulations of polymer coupons were aged from day 0 to day 145 (Phase 1). One had an initial molar mass of 85 000 g/mole, and the other an initial mass of 75 000 g/mole. This system was also mostly water with negligible acetic acid content. The molar masses of the coupons follow the model prediction. At around day 50, the samples appear to drop more quickly than the model would predict. As the temperature was steady during the time from the preceding sampling until day 50, we may conclude that the chemical makeup of the flow changed for a short while.

Phase 2 (Figure 5.4) of this topside analysis began around day 160, after the expedited analysis of the Phase 1 coupons by our lab. Samples of three molar masses were added to the flow stream. The first type was fresh PA11 with a molar mass of 83 000 g/mole, the second was leftover material from the Phase 1 study (molar mass was averaged), and the third was material from the wellhead study shown in Figure 5.3. This wellhead material was used in order to give an accelerated look at the equilibrium molar mass of the system; as it started with a low molar mass, it should arrive at its equilibrium more quickly than the fresh and slightly-aged samples.

In the case of the Phase 2 fresh material, the sampled coupons follow the model prediction well until a deviation is seen at around day 270. The molar mass did not significantly decline from this point until the end of Phase 2. The pre-aged Phase 1 topside pieces follow the prediction very closely. The molar mass of the wellhead pieces *increased* over the course of Phase 2, as the equilibrium molar mass is higher at this lower temperature. All samples in Phase 2, except for the fresh material, followed the prediction well. They should have continued to age, and would have likely converged at the predicted value of ~33 000 g/mole.

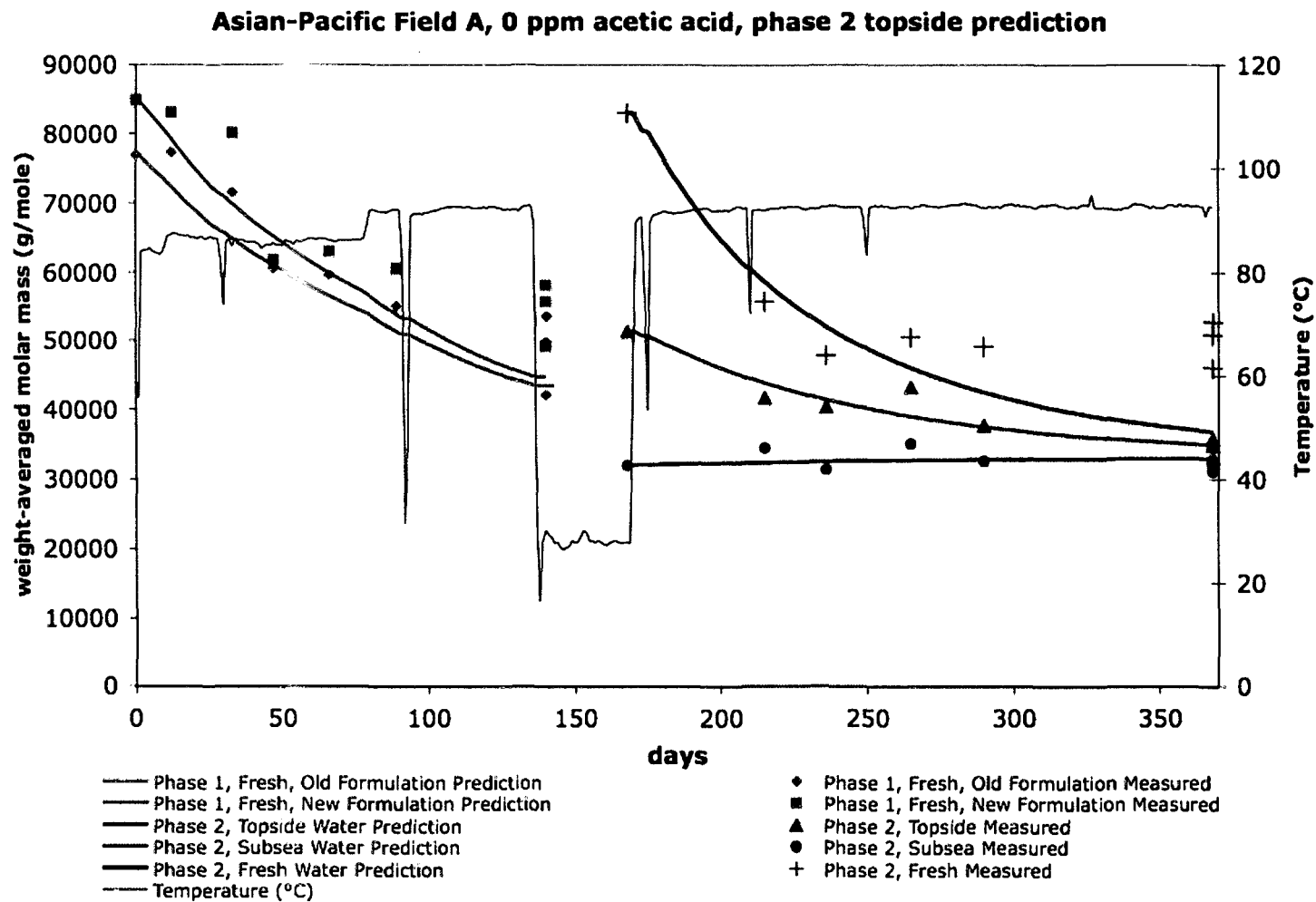


Figure 5.4: Asian-Pacific Field A topside, phase 2. Days 0-150 cover the same time period shown in Figure 5.3 at the wellhead. Fresh PA11, along with samples pre-aged to two different MWs were added at the beginning of phase 2. The MW predictions are shown.

Case 2: North Sea Field A

The North Sea Field A is another field that has a negligible acetic acid concentration. The two risers studied from this field have been monitored since 2000. Over the last ten years, four coupon samplings have been performed, and only until now have they been treated as a whole to give a picture of how the PA11 in that field is doing. On our advice, at each sampling, starting with the second sampling at day ~1500, fresh material was inserted into the space in the coupon holder from which the studied sample was removed. These fresh coupons were studied at future samplings to see if the composition of the field flow was changing and affecting the aging differently than the earlier period.

Riser 1 has an average temperature for the first 1700 days of around 63°C. Different flow rates, corresponding to varying levels of production and/or maintenance on the system yields a lower average temperature (around 54°C) for the time after that. Riser 5 shows a fairly steady history of 63°C, marked by a period of low temperature production from days 1200 to 2200.

Figure 5.5 shows the temperature, model prediction, and actual coupon results for Riser 1. Each sample is denoted by “inside” or “outside,” representing the inner core of the material versus the outer layer. The initial sampling at day 800 shows the coupon material to be lower than the predicted value. This could be due to higher acid concentration early on in the life of the field. The next sampling was accurately predicted by the model. The MW at 3100 days for the coupon that was installed fresh only 600 days prior, however, is lower than its predicted value. As it was the only coupon sampled at that time, it is difficult to say whether this aging was representative of

the rest of the coupons or if a lab error was made. However, every sampling after that shows the model to be pessimistic by 3000-5000 g/mole. This indicates that fluid flow is benign with respect the PA11 liner and suggests the model predictions are conservative, or that the temperature in the coupon holder is slightly lower.

North Sea Field A Riser 1

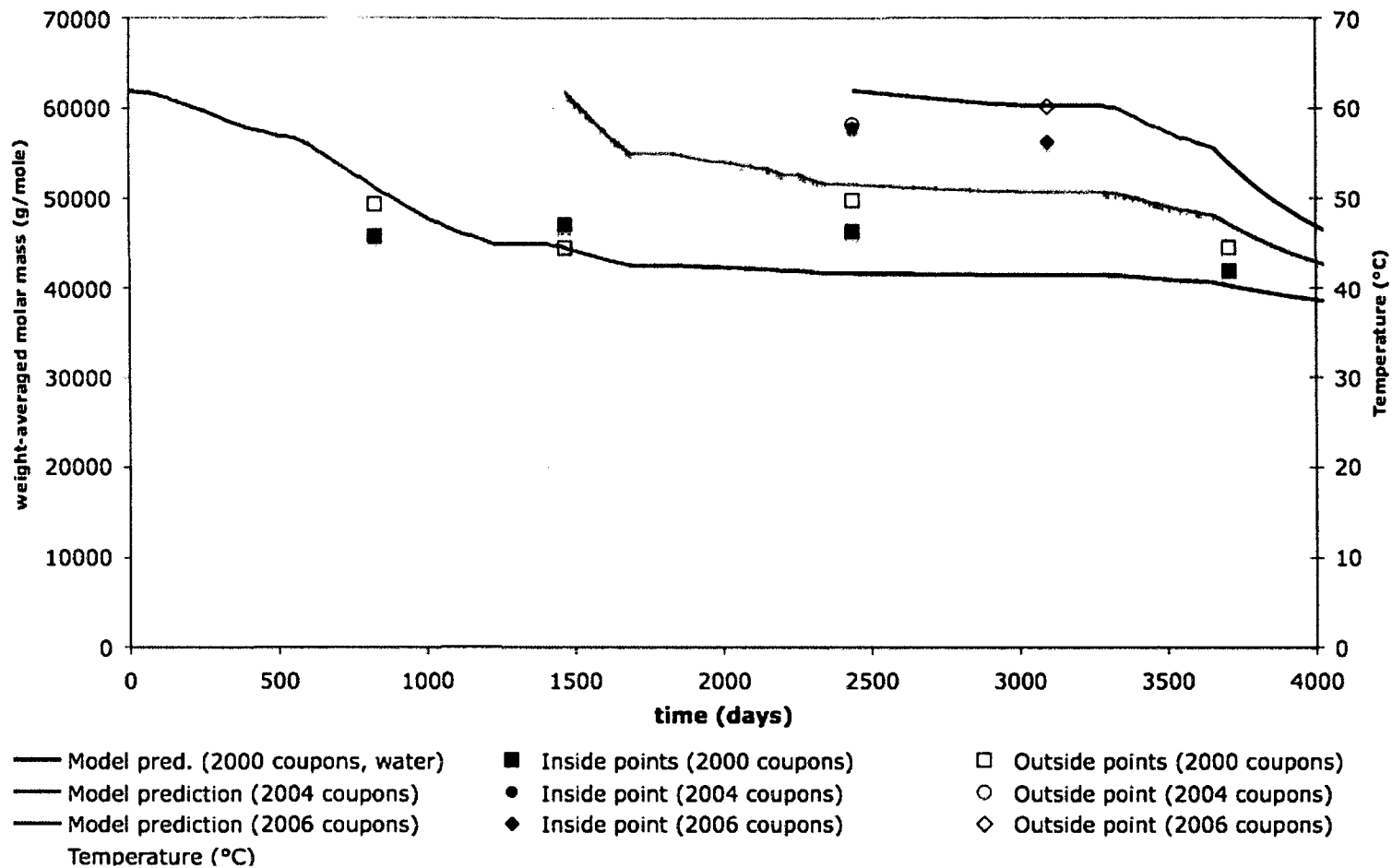


Figure 5.5: North Sea Field A Riser 1, 0 ppm acetic acid. Fresh PA11 coupons were added in 2000, 2004, and 2006.

Figure 5.6 shows the results from the North Sea Field A Riser 5. The overall trends are similar to those seen in Riser 1. The initial MW sampling of the original coupons was slightly lower than the model would have predicted, while the second sampling of MW is in agreement with the model. Subsequent samplings are typically 5000 g/mole above what the model predicts.

Regarding the ability of the kinetic model to predict the molar mass of coupons retrieved from the field, it has been shown that in the cases of negligible acid concentration, the model works well. This is particularly pleasing for aging temperatures well below the temperatures of our accelerated laboratory studies. To this point it has been shown to be typically 0-5000 g/mole pessimistic at a given sampling, however in only two cases, the first pulls of North Sea Field A Risers 1 and 5, has it been above the measured values. This is valuable in that a safety margin appears to be built in to our estimates. These conservative predictions are important in today's offshore oil industry.

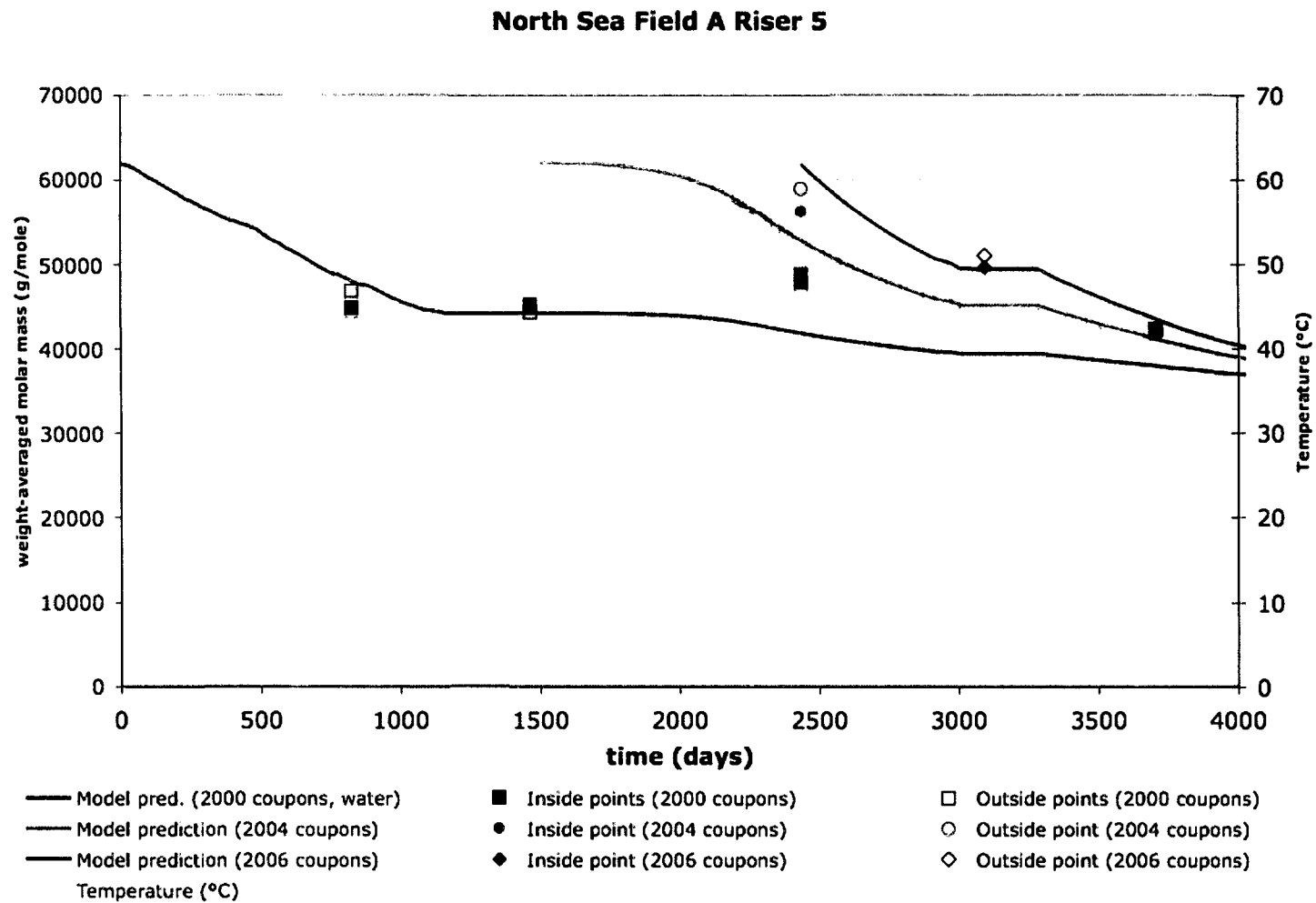


Figure 5.6: North Sea Field A Riser 5. Fresh PA11 coupons were added in 2000, 2004, and 2006. The findings are similar to those in riser 1.

Case 3: Asian-Pacific Field B

A different field in the Asian-Pacific region, Field B, has been characterized in the lab via accelerated aging at high temperature in a fluid consisting of a mixture of salts and organic acids. An outside lab, whose methods are not known, determined the elemental and acid content of the fluid. The main acid component was acetic acid, found to be 337 ppm. These components were added to deionized water in the lab. Transition metals, which could, according to S. Kawaguchi and K. Araki as well as J. Groves and R. Chambers, Jr., catalyze amide hydrolysis, were found only in trace amounts [44,45].

In order to understand the role of acetic acid concentration in this accelerated study, three experiments were conducted. This first contained fresh, unaged commercial PA11 in the salt mix with the prescribed acid concentration. The second contained fresh, unaged commercial PA11 in the salt mix with double the prescribed acid concentration. Finally, a third test environment was created in 100% DI water which contained pre-aged PA-11 that had a starting value of 32 000 g/mole.

The results of the aging study are shown in Figure 5.7. The 337 ppm acetic acid samples aged at a faster rate than the model predicts. This is surprising, as the nonexact ageing model has been shown to decline more quickly than the exact aging model, as seen in Figures 5.1 and 5.2. The 674 ppm acetic acid run also declines at a faster rate than predicted, and also is seen to have lower molar masses at each sampling than the 337 ppm test. As the samples move toward equilibrium, in both cases, they assume molar masses that are 2000-5000 g/mole higher than the predictions, on average.

The pre-aged sample follows the 100% DI prediction fairly closely. The prediction is again 2000-5000 g/mole below the actual data points. It should be noted that in determining the prediction for this run, the initial molar mass was set to the same value as the fresh samples, and then shifted after the line was constructed to the point where the model matched the starting molar mass. This was done in order to produce an accurate MW_e , which changes based on the starting molar masses of the polymers. Should the model have been started with an initial molar mass of 32000, the MW_e would have been around 7000 g/mole. This is due to the model starting with an initial condition of $[-COOH]=[-NH_3]=0$.

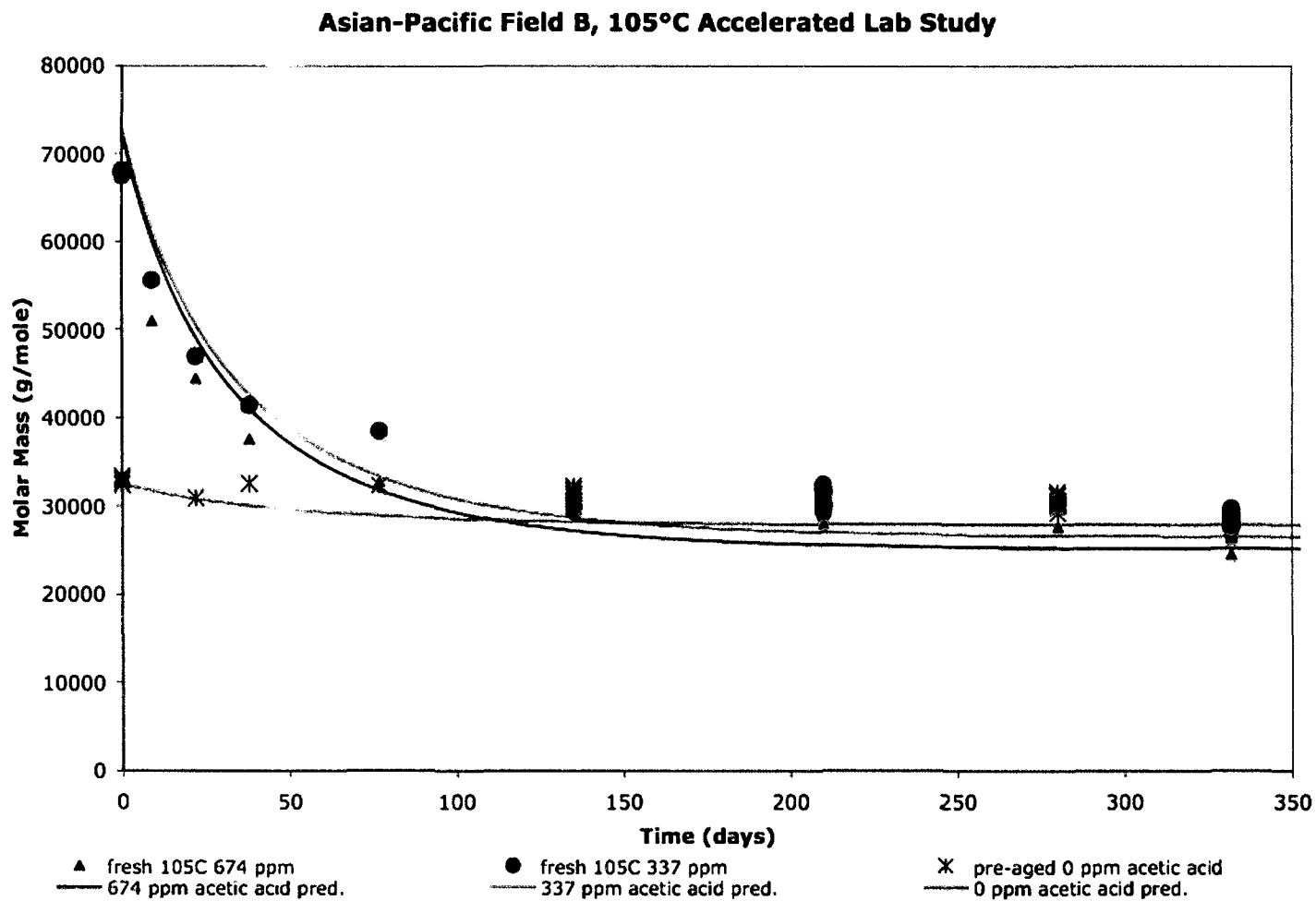


Figure 5.7: Asian-Pacific Field B accelerated lab study results. Field environments were replicated and aged at high temperature to infer what would happen at low temperatures found in the field.

Case 4: North Sea Field B

A fourth case deals with a low-temperature oil field in the North Sea with an appreciable amount of acetic acid. This field has an average temperature of 63°C and has an acetic acid concentration of 1000 ppm as of the day 3700 sampling, measured by me using an oil sample sent to us using gas chromatography, as shown in Chapter 2. Using this acid concentration, which falls within the three concentrations used to establish an concentration dependence in Chapter 4 (0 ppm, 600 ppm, and 3600 ppm), along with the daily temperature data, a lifetime prediction is plotted in Figure 5.8 against the experimental points. Similar to Case 2, this case includes the replacement of aged samples with fresh samples. Thus, fresh pieces of unaged PA11 were placed in the flow lines in 2000, 2005, 2006, and 2008.

Both the core and the outside of the coupons were measured. The outside of the coupons consistently remains higher than the core; this could be due to

The model data for the year 2000 samples shows a consistent under-estimation of 5000-10 000 g/mole of the molar masses of the coupons. This trend is also apparent with the 2005 coupons. However, though still pessimistic for the 2006 and 2008 coupons, the model is not as far off. The error is closer to 2000-5000 g/mole in those cases. This effect is most likely due to varying acid concentration over time in the fluid. As the acid concentration was only evaluated at the last sampling time, it is possible that this was a higher than the average acid concentration than what was present throughout the 3200 days.

North Sea Field B, 1000 ppm acetic acid

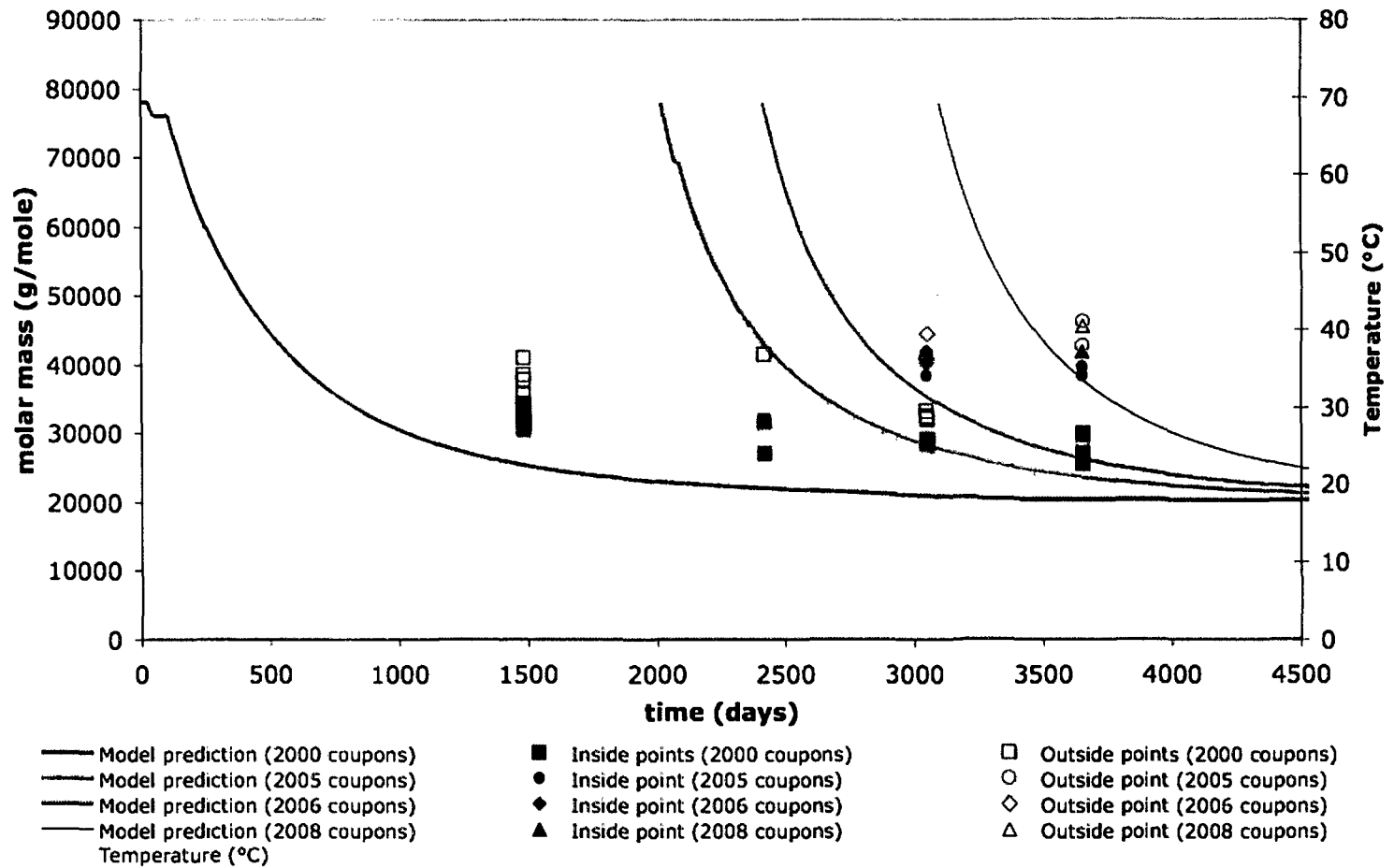


Figure 5.8: North Sea Field B modeled with 1000 ppm acetic acid.

Further evidence of this point is presented in Figure 5.9. In this figure, the acid model is run at 600 ppm acetic acid, instead of the 1000 ppm measured and used in Figure 5.8. These model lines fit the experimental data more closely in all four sets of coupons. Though it is likely that the 1000 ppm evaluation of the acid concentration is correct, it is possible that the average concentration over time was closer to 600 ppm.

North Sea Field B, 600 ppm acetic acid

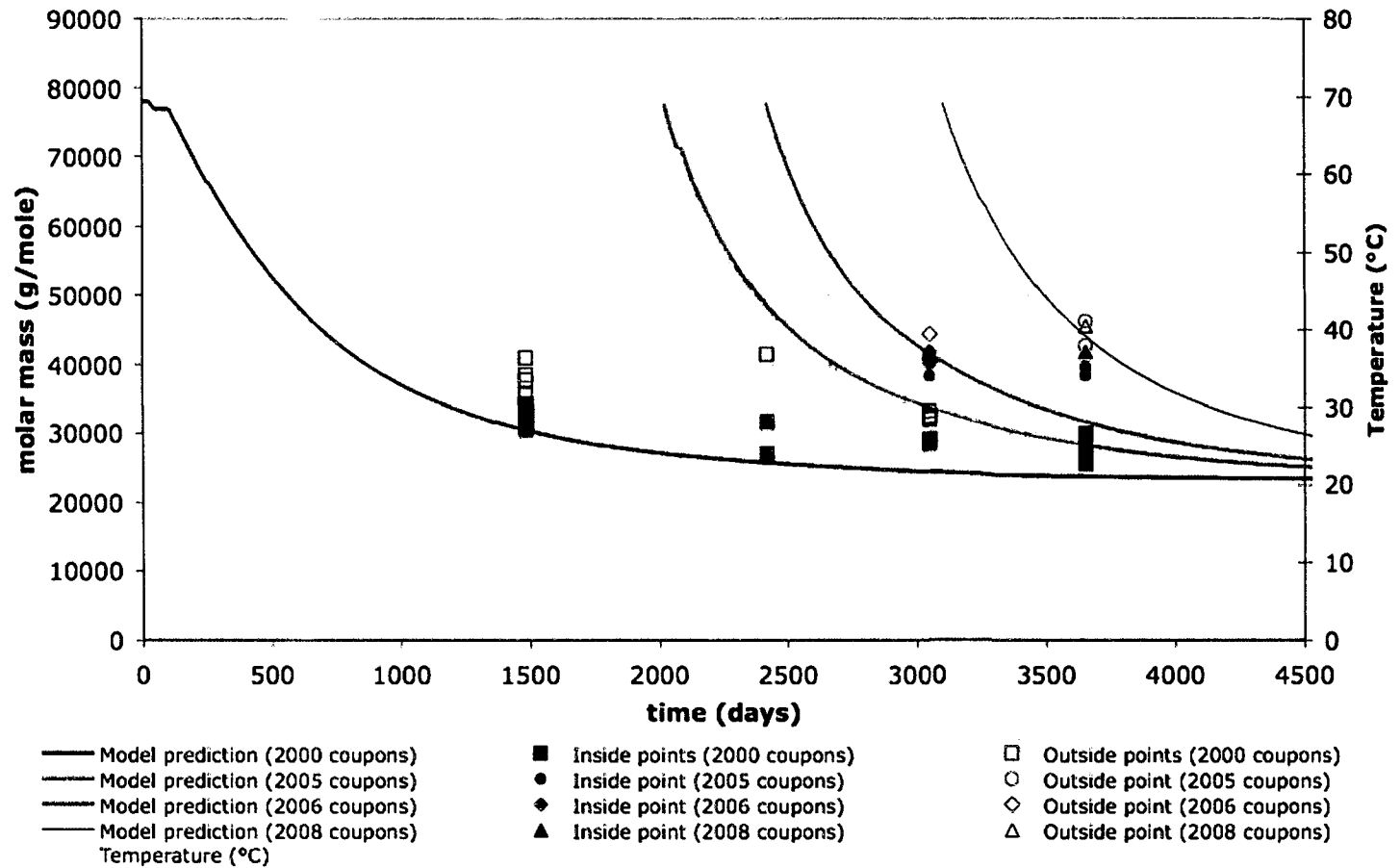


Figure 5.9: North Sea Field B modeled with 600 ppm acetic acid. These modeling results fit the coupon data more closely.

Regarding Accelerated Aging Studies as a Means of Estimating Future Mechanical Properties

The mechanical properties of PA11 are dependent on two variables – crystallinity and molar mass [31,46]. According to work shown by Meyer et al., the percent elongation at break for PA11 aged at 105°C begins to decline at ~35 000 g/mole (MW), and is in danger of failure (defined as less than 50% elongation at break) from 30 000 g/mole (MW) down [31]. Figure 5.10 is a reproduction of these findings by Meyer et al.

Percent Elongation vs. Mw(SEC) 105°C

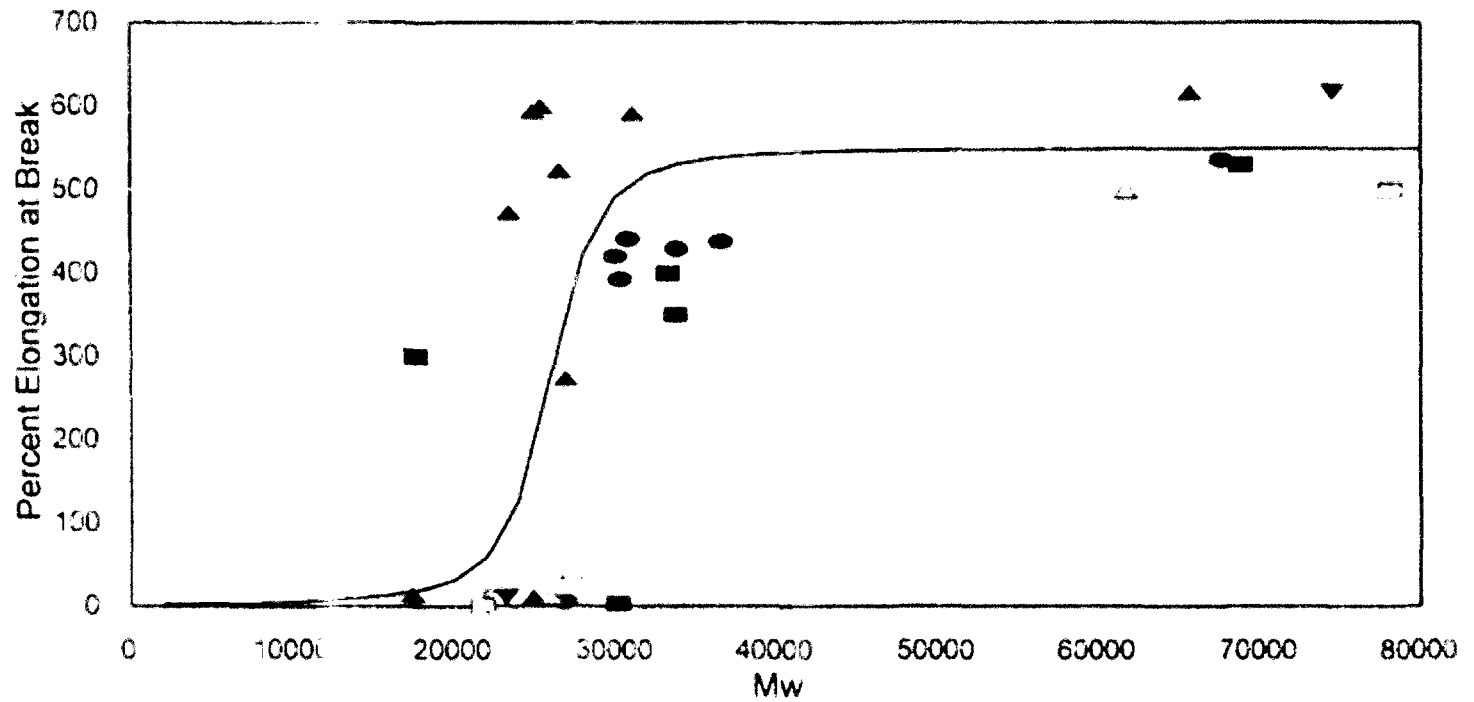


Figure 5.10: Percent Elongation at Break vs. Molar Mass (g/mole) of PA11 aged at 105°C. This Figure illustrates the ductile-brittle transition of PA-11. Reproduced from Meyer et al [31].

Using accelerated aging studies to estimate the weight-average molar mass changes of lower-temperature systems, as in the cases previously described in this chapter, is a helpful technique. This is because aging mechanical samples at high temperatures may accelerate annealing, leading to a sample that overestimates brittleness and underestimates useful lifetimes in the field.

In general, one may estimate that the maximum rate of annealing for a semi-crystalline polymer occurs at the temperature representing the average of T_g and T_m [9]. In this case, the average of 44.5°C and 188°C is 116°C [47]. Typical temperatures used in accelerated aging studies are often very close to this estimated temperature of highest annealing rate. This has the implication that accelerated aging studies to estimate mechanical properties based solely upon their molar masses could underestimate the true elongation at break value of actual risers in the field because the percent crystallinity is higher than would occur at lower aging temperatures.

Case 5: Asian-Pacific Field B Mechanical Study

A section of PA11 flexible liner was obtained from near a flange close to a wellhead of Asian-Pacific Field B. A photograph of a quarter of the assembly as received is shown in Figure 5.11. The outer metal sheath is much thicker than what is typically found, as it was adjacent to a fitting. It was machined into quarters from which mechanical samples were punched and tested as described in Chapter 2.

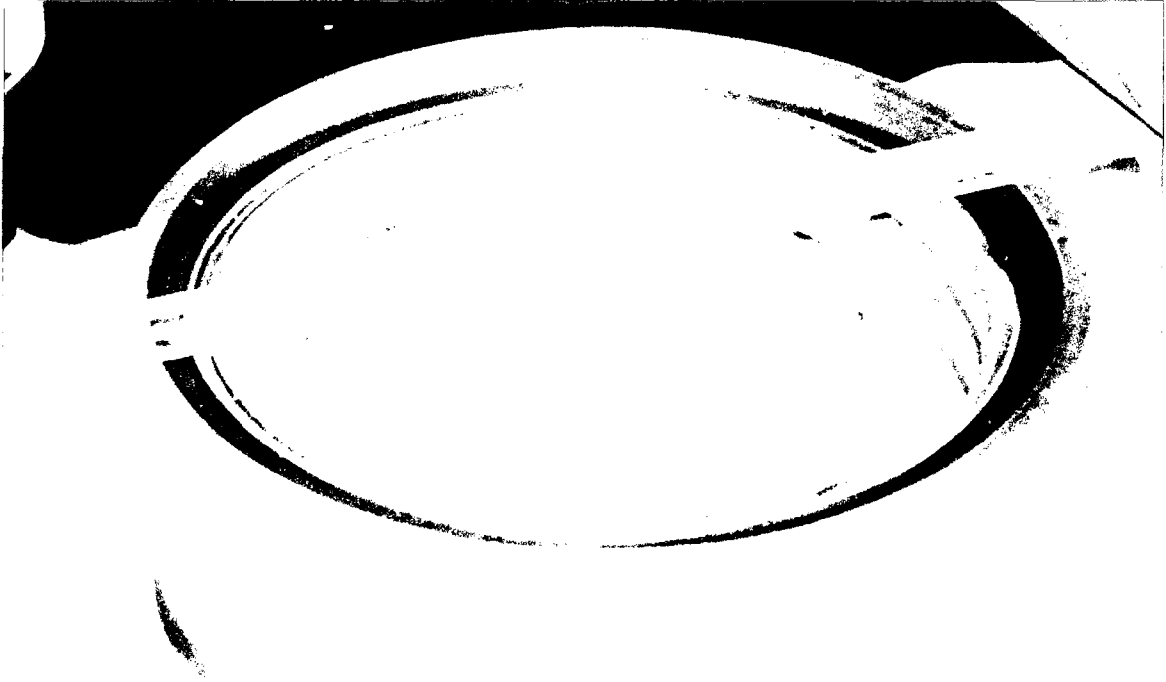


Figure 5.11: PA11 flexible pipe liner from near a wellhead flange as received from Asian-Pacific Field B.

This was the same field previously described as having had an acetic acid concentration of 337 ppm. The temperature history of the piece was provided, and the modeling results are shown along with molar mass results from the sample in Figure 5.12. According to the Figure, molar masses are roughly 5000 g/mole higher than the model predictions. This could be due to changing acetic acid concentration over time, or temperature gradients in the pipe liner.

The remainder of the coupon was cut into mechanical samples as described in Chapter 2, and added, along with fresh unaged PA11, to accelerated ageing tubes at 120°C, 105°C, and 90°C in either 337 ppm acetic acid, 674 ppm acetic acid, or 0 ppm acetic acid. Some of the results of the 105°C experiments were shown in Figure 5.7. Over the course of the ageing experiment, samples were periodically retrieved and mechanical testing was performed. Afterward, the remainder of the mechanical piece was analyzed for molar mass and crystallinity. Figure 5.13 shows the relationship found between percent elongation at break and molar mass for the three temperatures. Each mechanical piece was measured in triplicate over the cross-section of the initial spool.

Asian-Pacific Field B, 337 ppm acetic acid, flange coupon

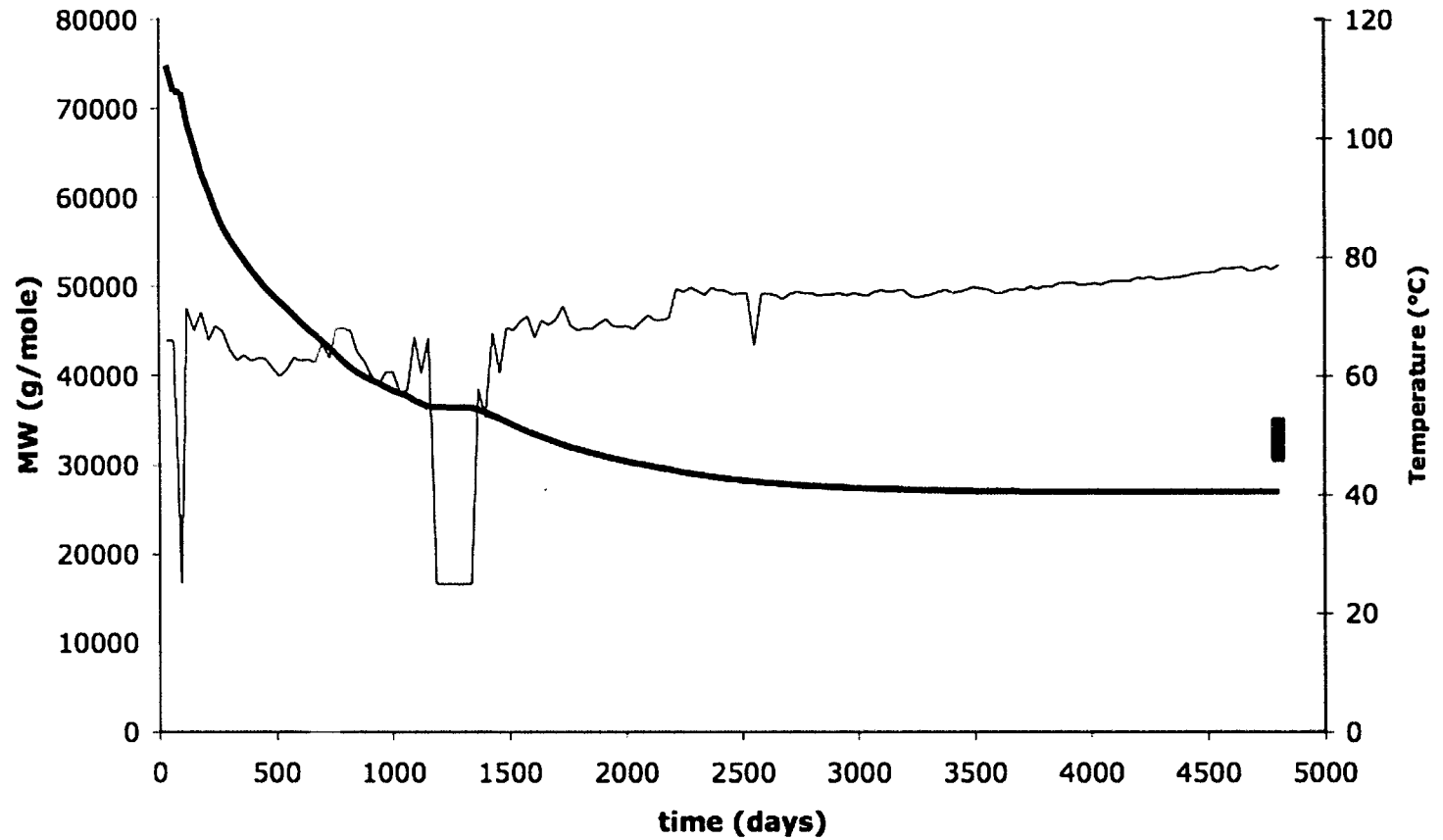


Figure 5.12: Asian-Pacific Field B modeled with 337 ppm acetic acid.

Asian-Pacific Field B, elongation at break vs. molar mass

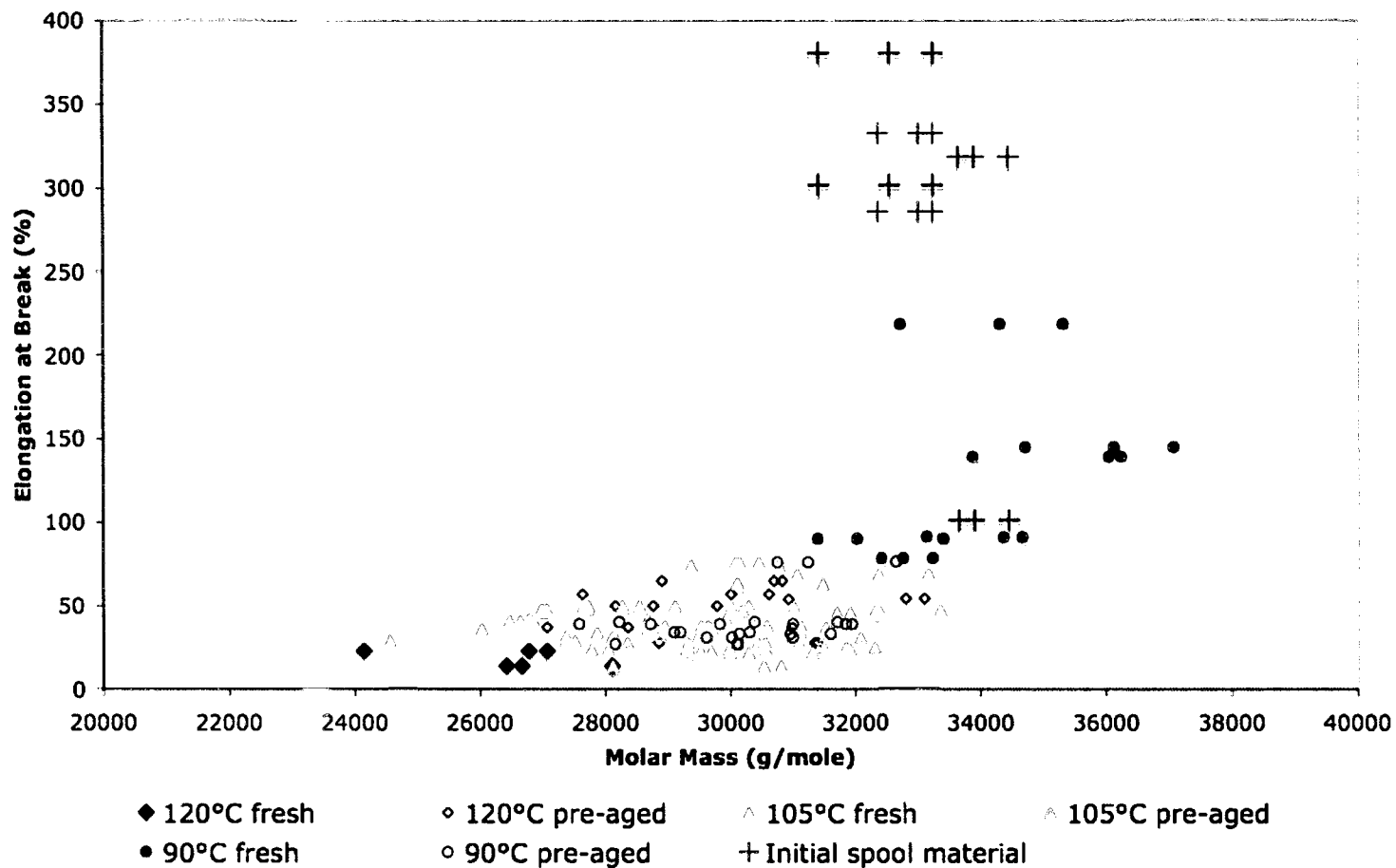


Figure 5.13: Asian-Pacific Field B tensile test results as a function of MW.

Figure 5.13 shows the low molar-mass range of the relationship shown by Meyer et al. in Figure 5.10. Samples under 50% elongation at break are considered unsafe by the offshore oil industry, as their safety margin (probability of failure) is too small. This is seen starting at ~33 000 g/mole, and for all of the samples shown below ~28 000 g/mole. The samples appear to be somewhat separated based on accelerated aging temperature. The 120°C samples have the lowest molar masses, as well as the lowest elongation at break, on average. The 105°C samples are between the 120°C and 90°C samples, yet the elongation at break values are considerably lower than the 90°C samples. The initial spool samples, while not having the highest molar masses, do have the highest elongation at break. They also happen to be the samples aged at the lowest temperature.

Figure 5.14 shows the same mechanical runs in a plot of percent-elongation vs. crystallinity. A clear relationship is shown between the two quantities that is upheld over all temperatures plotted. Samples that have a percent-crystallinity of over 32% have a strong occurrence of failure.

It is impossible to deduce based on Figures 5.14 and 5.13 that the reason for potential failure in any case is due to low molar mass combined with high crystallinity. In the case of the 90°C samples in Figure 5.14, one may see that degree of crystallinity in all samples is below 32%, thus the failures witnessed are likely due to low molar masses. Based on the trends in both plots, it is seen that mechanical failure is a result of both low molar mass and high crystallinity.

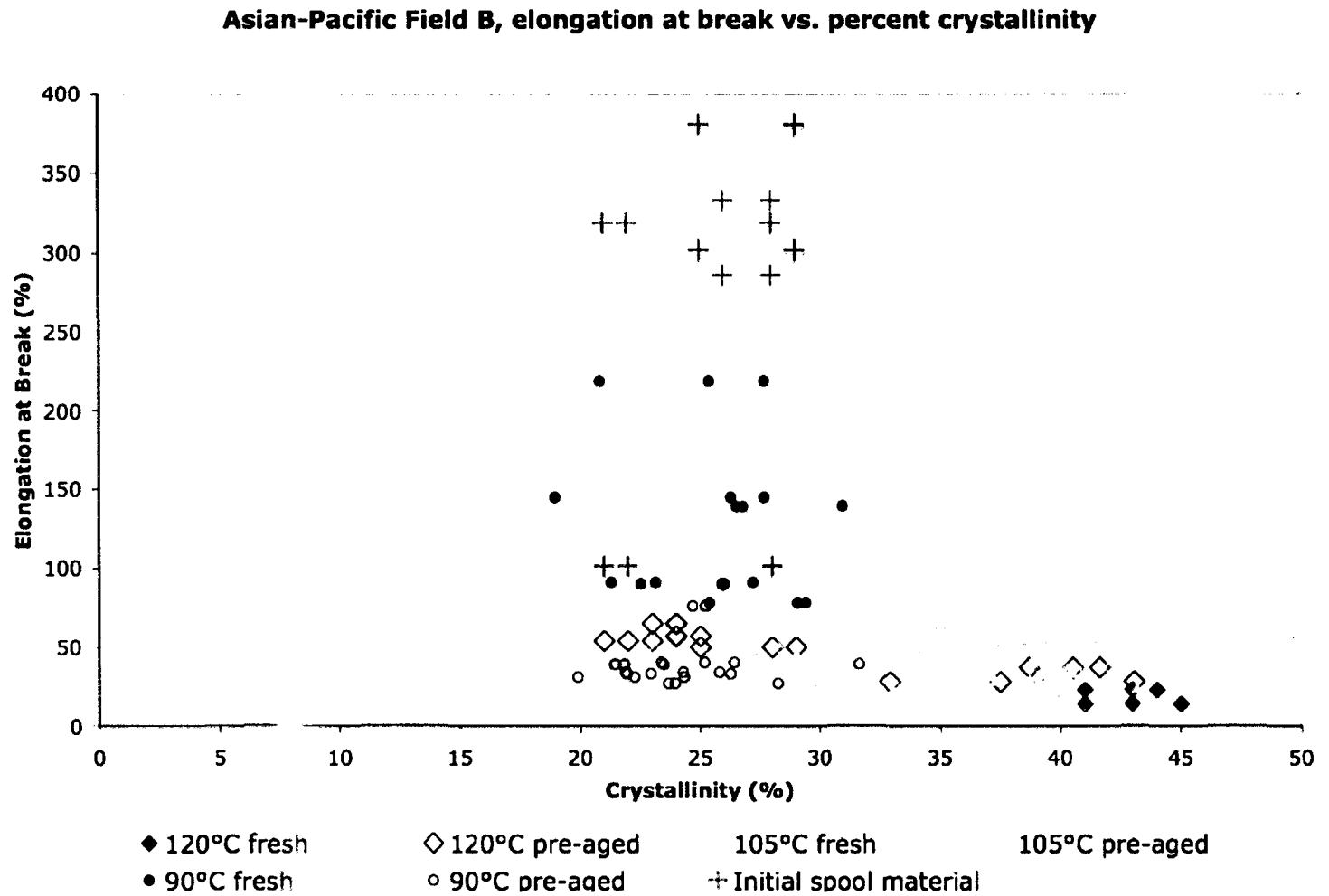


Figure 5.14: Asian-Pacific Field B, tensile test results vs. degree of crystallinity.

Figure 5.15 shows the relationship between crystallinity and aging time for pre-aged and fresh material, at the three temperatures used in the accelerated aging study. The initial spool samples are represented by each respective temperature at day 0. From hand-drawn trendlines, one may deduce that at 120°C, crystallinity increases by 0.11%/day. For 105°C and 90°C, the increases are 0.05%/day and 0.01%/day, respectively. Given a starting crystallinity of 23%, a sample in a 120°C aging study would reach the failure threshold of 32% crystallinity in roughly 100 days, assuming linearity in the increase in crystallinity. By again assuming crystallinity continually increases linearly with time at 105°C and 90°C, one would have 120 and 1000 days, respectively, before a critically high crystallinity is reached.

With this information, one must use accelerated aging wisely when determining mechanical properties of field samples. It should be noted that mechanical results from accelerated aging studies will almost always be pessimistic, giving an overly conservative lifetime estimate; thus the experimenter errs on the side of caution.

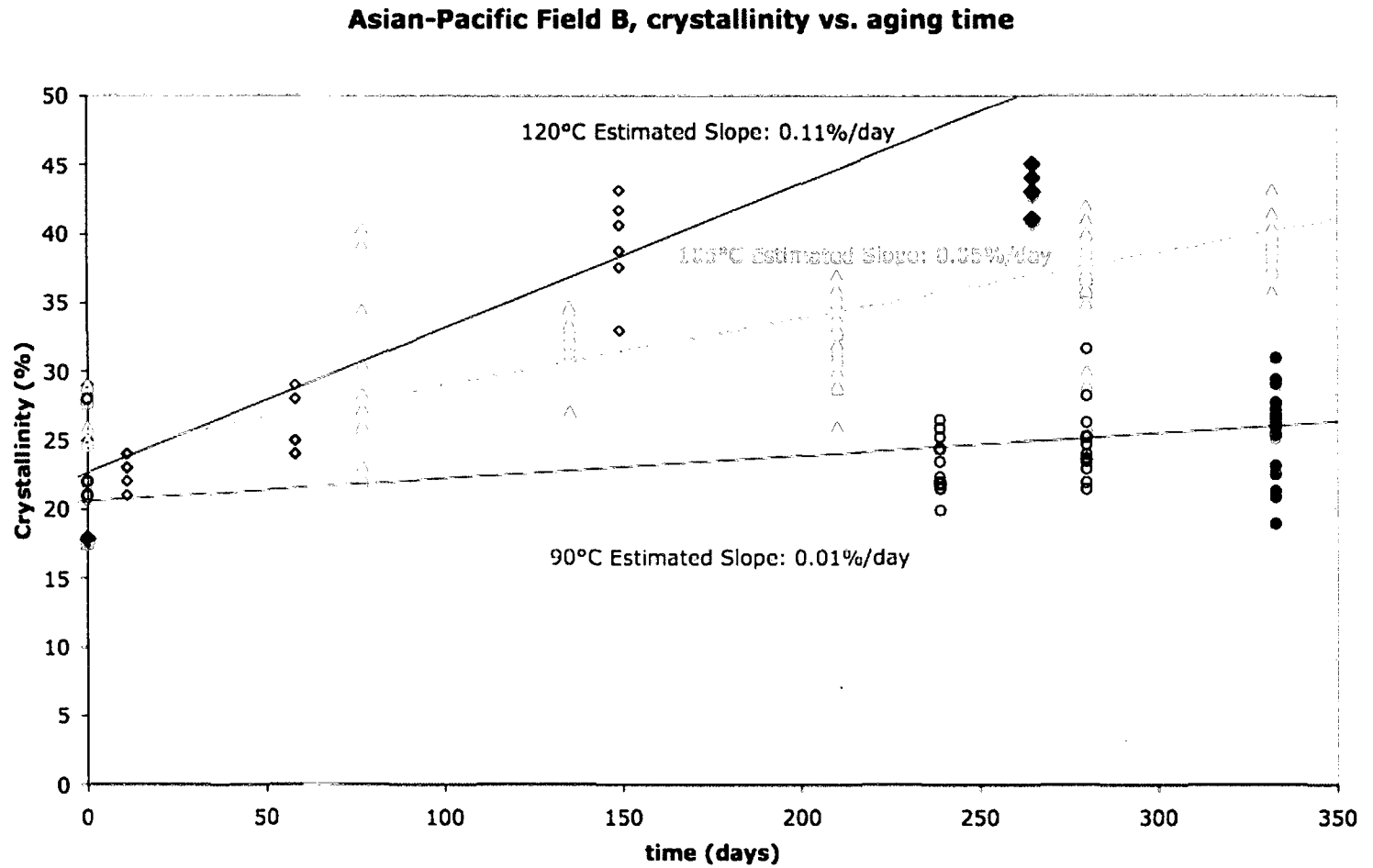


Figure 5.14: Asian-Pacific Field B, crystallinity vs. aging time. Trendlines are hand-drawn and aren't necessarily linear beyond where data collection stops.

Chapter 6: Conclusions

Closing Remarks on this Work

In this work a model of PA11 degradation more scientifically accurate than any published to date has been defined and calibrated based on experimental data. The experimental values of equilibrium molecular weight (MW'_e), rate of hydrolysis (k'_H), and rate of recombination (k'_R) have been determined in various environments and at temperatures found in the field. Based on these experimental values, dependencies on temperature and acetic acid concentration were included in a previously described less exact model that is more suitable for modeling aging in a changing environment.

In Chapter 3, it was shown that degradation by hydrolysis in water is affected by temperature and the presence of small alcohols. According to experimental work detailed in Chapter 3, the highest degree of PA11 degradation in water was seen at 120°C. There, the equilibrium molecular weight (MW) was shown to be 33 000 g/mole. According to the relationship between elongation at break and MW outlined at the end of Chapter 5, the mechanical properties based on this MW would be above 50% elongation at break. An elongation at break above 50% is deemed “safe” by current standards in the offshore oil industry. However, it is then shown in Chapter 5 that the annealing process at such a high temperature would lead to an elongation at break that is below this accepted threshold. With that said, it is imperative that the offshore oil industry assess

the crystallinity of PA11, as well as its molecular weight, when considering the safe use lifetime of pipe liners.

It was also shown in Chapter 3 that the equilibrium MW for a 30% solution of methanol in water at 120°C is 26 000 g/mole. According to Chapter 5, PA11 aged to equilibrium under these conditions would be below the 50% elongation at break threshold. Coupled with the effects of high-temperature annealing, PA11 operated under these conditions is in danger of failure by industry standards.

The 30% ethanol solution at 120°C led to an equilibrium MW of 30 000 g/mole, as shown in Chapter 3. In Chapter 5, samples with this MW had elongation at break values both above and below the 50% elongation at break safety margin. By again considering the effects of annealing, the mechanical properties of this material could fall below this threshold.

Chapter 4 deals with the effects of small organic acid concentration on the rate and degree of PA11 degradation. Acetic acid is shown to have an effect on the rate of hydrolysis, appreciably lowering the equilibrium MW of PA11, especially at high concentrations. The experimental data showed that at 100°C with a 600 ppm concentration of acetic acid, the equilibrium MW of the PA11 was close to 26 000 g/mole. According to Chapter 5, this value would place the PA11 below the 50% elongation at break safety criteria.

According to the temperature-dependent acetic acid aging model established in Chapter 5, with acetic acid concentration at 600 ppm, the operating temperature of the PA11 would need to be below $60^{\circ}\text{C} \pm 3^{\circ}\text{C}$ in order for the equilibrium MW to remain above 33 000 g/mole. In Chapter 5, PA11 at and above this MW was

shown to have elongation at break values above the 50% threshold. Based on the effects of annealing as described in Chapter 5, crystallinity increase should not pose a problem in this environment.

Typically, PA11 liner failure is due to acute stresses. These may occur due to uncontrolled events, such as storms; man made events, such as maintenance; and less-controlled events, such as emergencies. As an example, an abrupt emergency shutdown of oil production would lead to rapidly changing temperatures and pressures experienced by a PA11 liner. The effect of PA11 contracting due to the thermal effects of cooling along with the loss of internal fluid pressure could lead to the failure of the pipe liner under external water pressure forces.

Due to the probabilistic and abrupt nature of this failure mechanism, it is likely that pipe liners may be operated in the “danger zone” with respect to MW and crystallinity without any indication of trouble to the oil producer. It is not until a stress-generating event causes pipe failure does the condition of the PA11 become evident. This is why PA11 monitoring is imperative, *especially* when a producer is operating at temperatures above 90°C, when small acids are present, or when methanol is being used as a hydrate formation inhibitor.

Future Questions for PA11 in the Offshore Oil Industry

With respect to the work presented in this dissertation, there are a number of questions worth pursuing. In Chapter 4, in addition to acetic acid, the effects of 3-cyclopropionic, valeric, and naphthenic acids were studied at two concentrations at 100°C. Their effects on the rate and degree of PA11 degradation were larger than those seen for acetic acid. However, the actual concentrations of these acids in the field are typically below 100 ppm – much less than typical acetic acid concentrations. That being the case, the effects of these acids on the aging of PA11 in the field is likely to be less pronounced than the 600 ppm cases reported in Chapter 4. However, their effects at low concentrations common to field environments warrants future work. Coupled with acetic acid, the effects of these acids on the MW of PA11 could prove to be significant.

It is also worth exploring the roles of small alcohols in conjunction with small carboxylic acids. As was described in Chapter 3, the addition of ethoxide ion to an amide bond under acidic conditions has been proven to accelerate hydrolysis [48]. It is possible that effects of both ethanol and methanol would be exacerbated by the presence of small alcohols. This effect could be in addition to any effect stemming from the acids alone.

The role of oxidative degradation of PA11 has yet to be explored. As discussed in Chapters 3 and 4, experimental steps were taken to remove oxygen to below fifty ppb in the aging environments in order to replicate the anoxic field conditions. However, upon addition of ethanol and methanol to control hydrate formation, oxygen concentration is not well controlled topside on the platform and is likely present at

unknown concentrations in the introduced alcohols. It makes sense that oxidative damage could occur at the methylene portion of PA11, thus removing chain ends from any repolymerization reactions. Oxidative damage is irreversible. Experiments describing the effects of oxidative damage with respect to temperature and concentration are in currently being planned.

New Applications of PA11

PA11 is starting to see use in new applications with regard to the land-based transportation of natural gas. It is becoming favored over polyethylene (PE) due to its higher pressure rating and better resistance to chemical attack [49]. The first installation in the U.S. of PA11 natural gas pipe was reported in October, 2010 and consisted of two installations, one 1.2 miles long, and the other 10.5 miles long. [50] These installations replaced aging steel natural gas pipe and run between Coolidge, TX and Hubbard, TX [51]. As of this point, there is very little published information regarding the effects of aging conditions on the lifetime of PA11 as pertaining to the transportation of natural gas.

The effects of liquefied natural gas at high pressure on PA11 are to this point unknown. Depending on the makeup of the natural gas, it is likely that chemical catalysts for PA11 degradation are scarce. However, the humidity of the natural gas as well as the oxygen concentration in the system could play a role in the degradation of the PA11, and are worth exploring.

As PA11 pipes for natural gas transportation come online, it is important that accurate assessments of the lifetimes of the pipes are performed. As the pipes are typically buried and over time will likely become built upon, the economic impact of replacing the pipes sooner than the currently estimated lifetimes could prove significant. However, more important than the economic aspect of PA11 lifetime is its safety. Should an adequate understanding of the lifetime of PA11 pipe in this application not be had, the results could be deadly. A steel pipe failure in San Bruno, CA in September 2010 led to 4 people killed, twenty injured, and the destruction of 53 homes [52]. The rupture of a PA11 natural gas transport line could lead to a similar catastrophe. Should this occur due to lack of aging studies regarding the suitability of PA11 in this application, given what this work shows, ignorance as an excuse would be unacceptable.

References

- [1] Hays, K. 31 March, 2010. Shell Starts Production at Perdido. *Reuters*. Retrieved Nov. 29, 2010, <http://www.reuters.com/article/idUSN3123683920100331>.
- [2] Product Information, NKT Flexibles. Retrieved Nov. 29, 2010, <http://www.nktflexibles.com/en/Products+and+Solutions/Materials+and+Profiles.Htm>.
- [3] Ross, Peter. 15 June, 2008. "The Night the Sea Caught Fire: Remembering the Piper Alpha." *Scotland on Sunday*. Retrieved 29 Nov. 2010, <http://scotlandonsunday.scotsman.com/spectrum/The-night-the-sea-caught.4184800.jp>.
- [4] Statoil Annual Report 2008. Retrieved 29 Nov. 2010, http://www.statoil.com/AnnualReport2008/en/Sustainability/Environment/Pages/5-3-1-4_InjectedWaterLeakAtTordisAndVisund.aspx.
- [5] Hays, Kristen. 2 July 2008. "High Court Frees Judge to Rule on BP Blast Plea Deal." *The Houston Chronicle*. Retrieved 29 Nov. 2010, <http://www.chron.com/disp/story.mpl/special/05/blast/5867752.html>.
- [6] Tillerson, Rex. "Statement to the National Commission on the BP Deepwater Oil Spill and Offshore Drilling," November 9, 2010, Exxon-Mobil Corporation.
- [7] *2002 API Technical Bulletin TR17RUG, 1st Edition, 2003*, June: American Petroleum Institute.
- [8] IUPAC. *Compendium of Chemical Terminology*, 2nd ed. (the "Gold Book"). Compiled by A. D. McNaught and A. Wilkinson. Blackwell Scientific Publications, Oxford, 1997.
- [9] Allcock, H. and F. Lampe. *Contemporary Polymer Chemistry, 2nd Ed.* New Jersey: Prentice-Hall, Inc.: 1990.
- [10] Showa Denko K.K., Shodex Group, *Shodex Operation Manual No. 840*. Japan.
- [11] Wyatt Technology, Light Scattering University presentation materials, (lecture 111) 17 Jan. 1999.
- [12] P.J. Wyatt, *Anal. Chim. Acta* **1993**, 272, 1-40.

- [13] Carraher, Charles E., Jr., *Polymer Chemistry, 6th Ed.* New York: Marcel Dekker, Inc., 2003.
- [14] MSDS: 1,1,1,3,3,3-hexafluoroisopropan-2-ol, Oakwood Products Inc., West Columbia, SC.
- [15] Chaupart, N.; Serpe, G.; Verdu, J. *Polymer* **1998**, *39*, 1375.
- [16] *2002 API Technical Bulletin TR17RUG, 1st Edition, 2003*, June: American Petroleum Institute.
- [17] Lui, S.; Yu, Y.; Cui, Y.; Zhang, H.; Mo, Z.; *Journal of Applied Polymer Science*. **1998**, *70* 2371-2380.
- [18] Xiao, X.; *Polymer Testing*, **2008**, *27*, 284-295.
- [19] Scott, R. P. W. *Introduction to Analytical Gas Chromatography 2nd Ed.* New York: Marcel Dekker, Inc. 1998. pp. 314-315.
- [20] Aharoni, S. M. *n-Nylons: Their Synthesis, Structure and Properties*. John Wiley & Sons Ltd., **1997**, England, pp. 397-412.
- [21] Brown, R. S.; Bennet, A. J.; Slebocka-Tilk, H. *Acc. Chem. Res.* **1992**, *25*, 481-488.
- [22] Bennet, A. J.; Slebocka-Tilk, H.; Brown, R. S.; Guthrie, J. P.; Jodhan, A. J. *J. Am. Chem. Soc.* **1990**, *112*, 8497-8506.
- [23] McClelland, R. A. *J. Am. Chem. Soc.* **1975**, *97*, 5281-5282.
- [24] Bon, E.; Biggs, D. C. H.; Bertrand, G.; *J. Org. Chem.* **1994**, *59*, 1904-1906.
- [25] Drake, D.; Schowen, R. L.; Jayaraman, H. *J. Am. Chem. Soc.* **1973**, *95*, 454-458.
- [26] Biechler, S.; Taft, R. W. *J. Am. Chem. Soc.* **1957**, *79*, 4927-4935.
- [27] Bender, M. L.; Thomas, R. J. *J. Am. Chem. Soc.* **1961**, *83*, 4183-4189.
- [28] Pollack R.; Bender, M.; *J. Am. Chem. Soc.* **1970**, *92*, 7190-7194.
- [29] Zahn, D.; *Eur. J. Org. Chem.* **2004**, 4020-4023.
- [30] Jacques, B.; Werth, M.; Merdas, I.; ThomINETTE, F.; Verdu, J. *Polymer* **2002**, *43*, 6439-6447.
- [31] Meyer, A.; Jones, N.; Lin, Yao; Kranbuehl, D. *Macromolecules* **2002**, *35*, 2784-2798.

- [32] Sloan, E. D.; Koh, C. A.; **2008**. *Clathrate Hydrates of Natural Gases, 3rd. Ed.* CRC Press, Boca Raton, London, New York.
- [33] Hopper, C.; Schowen, R.; Venkatasubban, K.; Jayaraman, H.; *J. Am. Chem. Soc.* **1973**, *95*, 3280-3283.
- [34] Bobbitt, J.; Scola, D.; *J. Org. Chem.* **1960**, *25*, 560-564.
- [35] Laidler, K.; *Chemical Kinetics, 3rd ed.*, Harper & Row: New York, 1987, pp. 29-31.
- [36] Borgund, A.; Barth, T.; *Org. Geochem.* **1994**, *21*, 943-952.
- [37] Arla, D.; Siquin, A.; Palermo, T.; Hurtevent,; Graciaa, A.; Dicharry, C.; *Energy & Fuels*, **2007**, *21*, 1337-1342.
- [38] Havre, T.; Sjoblom, J.; Vindstad, J.; *J. of Dispersion Science and Technology*, **2003**, *24*, 789-801.
- [39] Ward, K., Jr.; *J. Am. Chem. Soc.* **1938**, *60*, 325-327.
- [40] Bachmann, W.; Carmack, M.; *J. Am. Chem. Soc.* **1941**, *63*, 2494-2499.
- [41] Schowen, R.; Jayaraman, H.; Kershner, L.; *J. Am. Chem. Soc.* **1966**, *88*, 3373-3375.
- [42] Kluger, R.; Chin, J.; *J. Am. Chem. Soc.* **1982**, *104*, 2891-2897.
- [43] Serpe, G. and Chaupart, N., *Polymer* **1997**, *38*, 1911-1917.
- [44] Kawaguchi, S.; Araki, K. *Inorganica Chimica Acta* **2005**, *358*, 947-956.
- [45] Groves, J.; Chambers, R., Jr.; *J. Am. Chem. Soc.* **1984**, *106*, 630-638.
- [46] Wright, D.; Dunk, R.; Bouvart, D.; Autran, M.; *Polymer* **1988**, *29*, 793-796.
- [47] Aharoni, S., *n-Nylons: Their Synthesis, Structure, and Properties*. New Jersey: John Wiley & Sons.: 1997
- [48] Bobbitt, J.; Scola, D.; *J. Org. Chem.*, **1960**, *25*, 560-564.
- [49] "High-pressure plastic lines show promise for gas distribution." *Pipeline & Gas Journal* 1 Dec. **1995**. Print.
- [50] "First Rilsan® PA11 high pressure natural gas pipe installations in the US." Arkema Press Release. 21 Oct. **2010**. Online:
http://www.arkema.com/sites/group/en/press/pr_detail.page?p_filepath=/template

data/Content/Press_Release/data/en/2010/101021_first_rilsan_pa11_high_pressur
e_natural_gas_pipe_installations_in_the_us.xml.

- [51] “Replacing steel, PA-11 gas pipe connects two Texas cities.” *Plastics Today* 11 Oct. 2010. Online: <http://www.plasticstoday.com/mpw/articles/replacing-steel-pa-11-gas-pipe-connects-two-texas-cities>.
- [52] Lagos, M.; Fagan, K.; Cabanatuan, M.; Berton, J.; “San Bruno fire levels neighborhood – gas explosion.” *SFGate* 10 September 2010: Online: http://articles.sfgate.com/2010-09-10/news/23996646_1_gas-line-explosion-wind-whipped-blaze-smoke-inhalation.

Vita

Arthur Jaeton Mitman Glover

Born in Richmond, VA, September 28, 1984, Arthur Jaeton Mitman Glover resided in Tappahannock, VA for the extent of his childhood. Upon graduation from Essex High School in May, 2002, the author moved to Williamsburg, VA to attend The College of William and Mary. Upon receipt of a B.S. in Chemistry, the author stayed on to receive an M.S. in Chemistry in January 2009. Having successfully defended this dissertation in December 2010, the author is scheduled to receive a Ph.D. in Applied Science from The College in January, 2011.

Upon graduation, the author will stay on as a post-doctoral research assistant to further his study of the degradation of PA-11, as well as study Atomic Force Microscopy.

Appendix A: Data Tables from Chapters 3, 4, and 5

Table A.1: Chapter 3 SEC-MALLS data, 120°C.

120°C, 100% DI	
time (days)	MW (g/mole)
0	88850
20	55000
30	37000
41	33450
49	32620
49	32660
49	34790
49	32230
108	33520
129	34660
250	34010

120°C, 30% EtOH	
time (days)	MW (g/mole)
0	88850
3	71660
20	41650
26	42270
30	36170
35	31160
51	33250
96	31050
160	27930

120°C, 10% MeOH	
time (days)	MW (g/mole)
0	88850
12	37360
15	35210
41	32660
49	28080
160	29230
252	27460

120°C, 30% MeOH	
time (days)	MW (g/mole)
0	88850
4	58170
7	47250
12	37013
15	34940
15	41560
20	34820
35	26240
41	30400
41	30230
47	23330
49	25300
49	29550
49	26410
49	24810
49	26490
49	25450
65	22350
65	22980
96	24350
147	27890

Table A.2: Chapter 3 SEC-MALLS data, 100°C.

100°C, 100% DI	
time (days)	MW (g/mole)
0	88850
4	83480
21	66788.4
56	56506.8
77	44920
103	44220
124	42540
151	36270
151	41420
181	36120
187	37240
187	35340
232	38810
232	34920
294	34540
424	33740
631	32710

100°C, 30% EtOH	
time (days)	MW (g/mole)
0	88850
4	86630
21	70340
56	48220
77	42760
103	47310
151	37840
181	39780
187	35870
232	36760
294	30750
294	34940
494	31310

100°C, 10% MeOH	
time (days)	MW (g/mole)
0	88850
4	86630
21	70340
56	48220
77	42760
151	37840
187	35870
294	30750
494	31310

100°C, 30% MeOH	
time (days)	MW (g/mole)
0	88850
21	64440
56	43200
77	31200
103	31550
124	28660
151	28100
181	29830
187	29310
187	27050
232	28370
294	30950
294	29120

Table A.3: Chapter 3 SEC-MALLS data, 90°C.

90°C, 100% DI	
time (days)	MW (g/mole)
0	88850
12	72920
27	68550
44	65330
93	54214
136	50970
149	47586
157	42220
170	39648
189	38110
669	34650
669	35580
674	34410

90°C, 10% MeOH	
time (days)	MW (g/mole)
0	88850
4	88090
5	87010
11	77510
45	60250
95	49630
130	44330
230	35120
293	29310
558	29990
558	28670
866	30280

90°C, 30% EtOH	
time (days)	MW (g/mole)
0	88850
4	88540
5	84890
11	77270
11	75100
45	61560
70	54990
95	53380
105	56140
130	51550
195	38750
230	38700
467	32510

90°C, 30% MeOH	
time (days)	MW (g/mole)
0	88850
4	86660
5	85170
11	78900
11	72450
25	63950
45	48770
70	44150
95	42420
130	37370
230	28030
467	30850
495	25370
558	26010
740	29400
866	23490

Table A.4: Chapter 3 SEC-MALLS data, 70°C.

70°C, 100% DI		70°C, 30% EtOH	
time (days)	MW (g/mole)	time (days)	MW (g/mole)
0	88850	0	88850
11	88560	11	87160
30	84860	30	84090
44	76640	55	83940
90	77860	90	81690
130	76300	216	72000
216	72470	571	54110
571	50670	571	44750
703	49370	728	52180
		999	38520

70°C, 10% MeOH		70°C, 30% MeOH	
time (days)	MW (g/mole)	time (days)	MW (g/mole)
0	88850	0	88850
11	93170	11	85300
30	82910	30	86010
55	80600	90	73640
90	79980	130	67670
130	74470	213	63470
216	66710	571	39930
300	57700	728	40130
728	41560	999	34540

Table A.5: Chapter 4 SEC-MALLS data for 100°C acetic acid. Two concentrations are shown. The oil and water phases were determined to be identical within the error of the measurement, thus were combined for fitting.

100°C, acetic acid, 600ppm oil phase	
time (days)	MW (g/mole)
0	88850
2	80960
12	74910
56	37460
75	37870

100°C, acetic acid, 600ppm water phase	
time (days)	MW (g/mole)
0	88850
2	88330
42	48420
56	40570
75	33860
117	26510
189	26650

100°C, acetic acid, 3600ppm oil phase	
time (days)	MW (g/mole)
0	88850
2	82990
4	81590
8	70960
12	62430
56	31600
75	27170
117	22010
190	16980

100°C, acetic acid, 3600ppm water phase	
time (days)	MW (g/mole)
0	88850
2	79220
4	82050
12	60610
42	42210
56	30890
75	24200
189	16560

Table A.6: Chapter 4 SEC-MALLS data for 100°C valeric acid. Two concentrations are shown. The oil and water phases were determined to be identical within the error of the measurement, thus were combined for fitting.

100°C, valeric acid, 600ppm oil phase	
time (days)	MW (g/mole)
0	88850
2	69580
12	53330
32	36350
42	30690
56	21510
75	18550
117	17550
189	14420

100°C, valeric acid, 600ppm water phase	
time (days)	MW (g/mole)
0	88850
2	87310
12	66940
32	42960
42	37900
56	22830
75	19610
117	15830
189	15520

100°C, valeric acid, 3600ppm oil phase	
time (days)	MW (g/mole)
0	88850
2	78210
4	70120
8	41280
12	32500
21	24500
32	17610
42	15440
56	10960
75	8060
117	6645
190	7882

100°C, valeric acid, 3600ppm water phase	
time (days)	MW (g/mole)
0	88850
2	76790
4	56610
8	34720
12	27450
21	18750
42	11790
56	9336
75	7837
189	7711
189	9342

Table A.7: Chapter 4 SEC-MALLS data for 100°C, 3-cyclopropionic acid. Two concentrations are shown. The oil and water phases were determined to be identical within the error of the measurement, thus were combined for fitting.

100°C, 3-cyclopropionic acid, 600 ppm, oil phase	
time (days)	MW (g/mole)
0	88850
12	63790
32	31740
42	21740
56	13620
75	12440
117	10030

100°C, 3-cyclopropionic acid, 600 ppm, water phase	
time (days)	MW (g/mole)
0	88850
2	79990
32	29200
42	21100
56	14310
75	11610
117	10070
189	9068

100°C, 3-cyclopropionic acid, 3600 ppm, oil phase	
time (days)	MW (g/mole)
0	88850
2	68700
4	69730
8	47440
12	27080
42	11410
56	6984
189	3460

100°C, 3-cyclopropionic acid, 3600 ppm, water phase	
time (days)	MW (g/mole)
0	88850
2	62000
4	69630
8	45630
12	26930
32	11390
42	10510
56	6967
75	6715
117	6328
189	3352

Table A.8: Chapter 4 SEC-MALLS data for 100°C, naphthenic acid. Two concentrations are shown. The oil and water phases were determined to be identical within the error of the measurement, thus were combined for fitting.

100°C, naphthenic acid, 600 ppm, oil phase	
time (days)	MW (g/mole)
0	88850
2	76750
12	61160
42	37210
56	26100
75	20150

100°C, naphthenic acid, 600 ppm, water phase	
time (days)	MW (g/mole)
0	88850
2	77750
42	35880
56	25380
75	25220
189	21200

100°C, naphthenic acid, 3600 ppm, oil phase	
time (days)	MW (g/mole)
0	88850
2	73660
4	76230
8	67780
12	47050
32	29460
42	28480
56	16920
75	13340
117	11380

100°C, naphthenic acid, 3600 ppm, water phase	
time (days)	MW (g/mole)
0	88850
2	68320
4	74880
8	61640
12	48160
42	25830
56	16650
75	14000
189	12420

Table A.9: Chapter 5 SEC-MALLS data for Asian-Pacific Field A, Phase 1 wellhead

Spool Portion	Age (days)	MW (g/mole)
rib	135	38690
rib	135	37340
rib	135	36330
rib	135	35810
core	135	36490
core	135	32950
outside	135	37850
outside	135	35700

Table A.10: Chapter 5 SEC-MALLS data for Asian-Pacific Field A, Phase 1 topside

Time Exposed (days)	Old Formulation MW (g/mole)	New Formulation MW (g/mole)
0	76900	84940
12	77320	83100
33	71480	80110
47	60520	61690
66	59590	63000
89	55000	60500
140	42110	55720
140	53570	58125
140	49790	49190

Table A.11: Chapter 5 SEC-MALLS data for Asian-Pacific Field A, Phase 2 topside. Time exposed is counted from coupon insertion, which occurred on day 168 on Figure 5.4.

Time Exposed (days)	x-axis value (days)	Topside MW (g/mole)	Subsea MW (g/mole)	Fresh MW (g/mole)
0	168	51420	31920	83000
47	215	41830	34520	55700
68	236	40510	31380	47810
97	265	43260	35070	50500
122	290	37750	32540	49060
200	368	35790	32060	50840
200	368	34890	31050	52750
200	368	33170	32690	46020

Table A.12: Chapter 5 SEC-MALLS data for North Sea Field A Riser 1, coupons inserted in 2000. Time exposed is counted from coupon insertion, which occurred on day 0 on Figure 5.5.

Time Exposed (days)	x-axis value (days)	Coupon Core MW (g/mole)	Coupon Surface MW (g/mole)
0	0	61900	61900
828	828	45750	49280
1468	1468	46970	44400
2438	2438	46240	49700
3707	3707	41840	44470

Table A.13: Chapter 5 SEC-MALLS data for North Sea Field A Riser 1, coupons inserted in 2004. Time exposed is counted from coupon insertion, which occurred on day 1468 on Figure 5.5.

Time Exposed (days)	x-axis value (days)	Coupon Core MW (g/mole)	Coupon Surface MW (g/mole)
0	1468	61900	61900
970	2438	57800	58130

Table A.14: Chapter 5 SEC-MALLS data for North Sea Field A Riser 1, coupons inserted in 2006. Time exposed is counted from coupon insertion, which occurred on day 2438 on Figure 5.5.

Time Exposed (days)	x-axis value (days)	Coupon Core MW (g/mole)	Coupon Surface MW (g/mole)
0	2438	61900	61900
658	3096	56200	60150

Table A.15: Chapter 5 SEC-MALLS data for North Sea Field A Riser 5, coupons inserted in 2000. Time exposed is counted from coupon insertion, which occurred on day 0 on Figure 5.6.

Time Exposed (days)	x-axis value (days)	Coupon Core MW (g/mole)	Coupon Surface MW (g/mole)
0	0	61900	61900
828	828	44840	46820
1468	1468	45180	44290
2438	2438	48050	not measured
2438	2438	48790	47880
3707	3707	42360	42190

Table A.16: Chapter 5 SEC-MALLS data for North Sea Field A Riser 5, coupons inserted in 2004. Time exposed is counted from coupon insertion, which occurred on day 1468 on Figure 5.6.

Time Exposed (days)	x-axis value (days)	Coupon Core MW (g/mole)	Coupon Surface MW (g/mole)
0	1468	61900	61900
970	2438	56230	58880

Table A.17: Chapter 5 SEC-MALLS data for North Sea Field A Riser 5, coupons inserted in 2006. Time exposed is counted from coupon insertion, which occurred on day 2438 on Figure 5.6.

Time Exposed (days)	x-axis value (days)	Coupon Core MW (g/mole)	Coupon Surface MW (g/mole)
0	2438	61900	61900
658	3096	49610	51000

Table A.18: Chapter 5 SEC-MALLS data for Asian-Pacific Field B 105°C accelerated lab study. This PA11 was aged in 337 ppm acetic acid.

time (days)	rib MW (g/mole)	core MW (g/mole)	outside MW (g/mole)
0	68000	68000	68000
9		55600	
22		47000	
38		41400	
77		38570	
135		29980	
210	30090	29370	30770
210	32390	31700	31910
210	31470	30090	30120
280		30430	
332	27780	28040	29290
332	28700	27870	29720
332	27730	28270	29110

Table A.19: Chapter 5 SEC-MALLS data for Asian-Pacific Field B 105°C accelerated lab study. This PA11 was aged in 674 ppm acetic acid.

time (days)	rib MW (g/mole)	core MW (g/mole)	outside MW (g/mole)
0	68000	68000	68000
9		51040	
22		44550	
38		37360	
77		32840	
135		29890	
210	30090	30290	31300
210	32390	29340	29690
210	31470	30800	28120
280		27750	
332	27780	27510	24570
332	28700	26980	28270
332	27730	26850	26640

Table A.20: Chapter 5 SEC-MALLS data for Asian-Pacific Field B 105°C accelerated lab study. This pre-aged PA11 was aged in 100% DI water.

time (days)	rib MW (g/mole)	core MW (g/mole)	outside MW (g/mole)
0	33250	32960	32370
22		30900	
38		32520	
77		32320	
135	31090	31460	30550
135	32300	31430	31840
135	29970	31910	30550
210		31770	
280	31490	30110	30170
280	29190	30260	31110
280	30370	30580	31120

Table A.21: Chapter 5 SEC-MALLS data for North Sea Field B, coupons inserted in 2000. Time exposed is counted from coupon insertion, which occurred on day 0 on Figure 5.8.

Time Exposed (days)	x-axis value (days)	Coupon Core MW (g/mole)	Coupon Surface MW (g/mole)
0	0	61900	61900
1483	1483	33000	37620
1483	1483	31010	38410
1483	1483	30650	40870
1483	1483	31930	35570
2418	2418	27070	27070
3103	3103	29020	32030
3103	3103	28510	33150
3103	3103	29140	32360
3707	3707	26970	29820
3707	3707	29870	26240
3707	3707	25610	26560
3707	3707	26610	29920

Table A.22: Chapter 5 SEC-MALLS data for North Sea Field B, coupons inserted in 2005. Time exposed is counted from coupon insertion, which occurred on day 2029 on Figure 5.8.

Time Exposed (days)	x-axis value (days)	Coupon Core MW (g/mole)	Coupon Surface MW (g/mole)
0	2029	61900	61900
1082	3111	38290	41170
1686	3715	39560	46160
1686	3715	38300	42620

Table A.23: Chapter 5 SEC-MALLS data for North Sea Field B, coupons inserted in 2006. Time exposed is counted from coupon insertion, which occurred on day 2424 on Figure 5.8.

Time Exposed (days)	x-axis value (days)	Coupon Core MW (g/mole)	Coupon Surface MW (g/mole)
0	2424	61900	61900
685	3109	41850	44310
685	3109	40220	40740

Table A.24: Chapter 5 SEC-MALLS data for North Sea Field B, coupons inserted in 2008. Time exposed is counted from coupon insertion, which occurred on day 3110 on Figure 5.8.

Time Exposed (days)	x-axis value (days)	Coupon Core MW (g/mole)	Coupon Surface MW (g/mole)
0	3110	61900	61900
604	3714	41860	45540

Table A.25: Chapter 5 SEC-MALLS data for Asian-Pacific Field B flange coupon as shown in Figure 5.12. This PA11 was aged in 337 ppm acetic acid under variable temperatures. These points are from the 12:00 quadrant of the circular round.

time (days)	rib MW (g/mole)	core MW (g/mole)	outside MW (g/mole)
0	68000	68000	68000
4700	34450	33900	33650

Table A.26: Chapter 5 SEC-MALLS data for Asian-Pacific Field B flange coupon as shown in Figure 5.12. This PA11 was aged in 337 ppm acetic acid under variable temperatures. These points are from the 3:00 quadrant of the circular round.

time (days)	rib MW (g/mole)	core MW (g/mole)	outside MW (g/mole)
0	68000	68000	68000
4700	33250	32550	31420

Table A.27: Chapter 5 SEC-MALLS data for Asian-Pacific Field B flange coupon as shown in Figure 5.12. This PA11 was aged in 337 ppm acetic acid under variable temperatures. These points are from the 6:00 quadrant of the circular round.

time (days)	rib MW (g/mole)	core MW (g/mole)	outside MW (g/mole)
0	68000	68000	68000
4700	33250	33010	32370

Table A.28: Chapter 5 120°C SEC-MALLS, tensile test, and crystallinity data for Asian-Pacific Field B accelerated aging study.

sample type	time (days)	acetic acid conc. (ppm)	% elongation (%)	rib portion of cross section		core portion of cross section		outer portion of cross-section	
				MW (g/mole)	% crystallinity (%)	MW (g/mole)	% crystallinity (%)	MW (g/mole)	% crystallinity (%)
fresh	0	-	251	68000	18	68000	18	68000	18
fresh	265	337	14	26660	41	28110	45	26420	43
fresh	265	337	23	24150	43	27070	44	26780	41
pre-aged	0	-	380	33250	29	32550	29	31420	25
pre-aged	0	-	301	33250	29	32550	29	31420	25
pre-aged	11	337	54	30920	23	32800	22	33100	38570
pre-aged	11	337	65	30820	24	30690	24	28900	29980
pre-aged	58	337	57	27630	24	30000	25	30610	38570
pre-aged	58	337	50	28760	28	28160	25	29780	29980
pre-aged	149	337	28	31340	38	28850	43	31380	38570
pre-aged	149	337	37	27070	39	28360	42	30980	29980

Table A.29: Chapter 5 105°C SEC-MALLS, tensile test, and crystallinity data for Asian-Pacific Field B accelerated aging study in 100% DI water and 337 ppm acetic acid.

sample type	time (days)	acetic acid conc. (ppm)	% elongation (%)	rib portion of cross section		core portion of cross section		outer portion of cross-section	
				MW (g/mole)	% crystallinity (%)	MW (g/mole)	% crystallinity (%)	MW (g/mole)	% crystallinity (%)
pre-aged	0	-	332	33250	28	33010	28	32370	26
pre-aged	0	-	285	33250	28	33010	28	32370	26
pre-aged	135	0	28	31090	27	31460	27	30550	34
pre-aged	135	0	25	32300	33	31430	31	31840	35
pre-aged	135	0	24	29970	33	31910	33	30550	32
pre-aged	280	0	-	31490	41	30110	37	30170	40
pre-aged	280	0	34	29190	36	30260	37	31110	40
pre-aged	280	0	38	30370	41	30580	40	31120	42
fresh	0	-	251	68000	18	68000	18	68000	18
fresh	210	337	74	30090	29	29370	30	30770	31
fresh	210	337	46	32390	29	31700	26	31910	34
fresh	210	337	63	31470	30	30090	35	30120	32
fresh	332	337	24	27780	40	28040	40	29290	43
fresh	332	337	34	28700	39	27870	40	29720	39
fresh	332	337	50	27730	41	28270	39	29110	40
pre-aged	0	-	380	33250	29	32550	29	31420	25
pre-aged	0	-	301	33250	29	32550	29	31420	25
pre-aged	77	337	31	29470	27	28100	22	32080	25
pre-aged	77	337	69	31060	26	32370	26	33170	26
pre-aged	77	337	47	32310	27	33360	34	30180	22
pre-aged	280	337	76	30140	36	30450	36	30080	37
pre-aged	280	337	28	28350	30	29320	36	30430	29
pre-aged	280	337	49	27640	38	30010	37	31010	39

Table A.30: Chapter 5 105°C SEC-MALLS, tensile test, and crystallinity data for Asian-Pacific Field B accelerated aging study in 674 ppm acetic acid.

sample type	time (days)	acetic acid conc. (ppm)	% elongation (%)	rib portion of cross section		core portion of cross section		outer portion of cross-section	
				MW (g/mole)	% crystallinity (%)	MW (g/mole)	% crystallinity (%)	MW (g/mole)	% crystallinity (%)
fresh	0	-	251	68000	18	68000	18	68000	18
fresh	210	674	22	29990	36	30290	37	31300	33
fresh	210	674	23	29520	33	29340	31	29690	32
fresh	210	674	14	30530	36	30800	33	28120	31
fresh	332	674	29	27370	37	27510	40	24570	39
fresh	332	674	48	27060	36	26980	38	28270	37
fresh	332	674	41	26470	39	26850	38	26640	39
pre-aged	0	-	380	33250	29	32550	29	31420	25
pre-aged	0	-	301	33250	29	32550	29	31420	25
pre-aged	135	674	42	29920	22	26780	25	28670	39
pre-aged	135	674	50	27710	28	30290	23	28540	25
pre-aged	135	674	37	29670	30	31660	26	31520	40
pre-aged	280	674	38	29630	37	29530	39	28950	37
pre-aged	280	674	32	27370	26	28140	26	28880	24
pre-aged	280	674	36	26030	36	28670	35	28830	38

Table A.31: Chapter 5 90°C SEC-MALLS, tensile test, and crystallinity data for Asian-Pacific Field B accelerated aging study in 337 and 674 ppm acetic acid.

sample type	time (days)	acetic acid conc. (ppm)	% elongation (%)	rib portion of cross section		core portion of cross section		outer portion of cross-section	
				MW (g/mole)	% crystallinity (%)	MW (g/mole)	% crystallinity (%)	MW (g/mole)	% crystallinity (%)
fresh	0	-	251	68000	18	68000	18	68000	18
fresh	333	337	145	36120	26	34710	28	37070	19
fresh	333	337	91	34660	21	34360	27	33140	23
fresh	333	337	139	36230	27	36040	31	33870	27
pre-aged	0	-	101	34450	21	33900	22	33650	28
pre-aged	0	-	318	34450	21	33900	22	33650	28
pre-aged	239	337	39	31840	21	31940	22	31000	22
pre-aged	239	337	40	28220	25	31710	26	30380	23
pre-aged	280	337	76	31240	25	32650	25	30750	25
pre-aged	280	337	33	31600	22	30140	26	30960	23
fresh	0	-	251	68000	18	68000	18	68000	18
fresh	333	674	78	32760	25	33240	29	32420	29
fresh	333	674	218	34310	25	35320	21	32720	28
fresh	333	674	90	32020	26	31390	23	33400	26
pre-aged	0	-	101	34450	21	33900	22	33650	28
pre-aged	0	-	318	34450	21	33900	22	33650	28
pre-aged	239	674	31	31000	24	29620	22	30020	20
pre-aged	239	674	34	29100	26	29200	24	30300	22
pre-aged	280	674	27	28160	28	30120	24	30100	24
pre-aged	280	674	39	27580	32	29830	21	28730	23

Appendix B: Patent Application for Method for Making Polymer Composites Containing Graphene Sheets, Submitted in Final Form June 2010.

Method for Making Polymer Composites Containing Graphene Sheets

Inventors: David Kranbuehl
Sarah Cotts
Hannes C. Schniepp
Mizhen Cai
Arthur Jaeton Glover

METHOD FOR MAKING POLYMER COMPOSITES CONTAINING GRAPHENE SHEETS

Abstract

In one embodiment, a method for producing a graphene-containing composition is provided, the method comprising: (i) mixing a graphene oxide with a medium to form a mixture; and (ii) heating the mixture to a temperature above about 40 °C, whereby a graphene-containing composition is formed from the mixture. Composites of polymers with disperse functionalized graphene sheets and the applications thereof are also described.

Related Applications

[0001] This application claims priority to US Provisional Application Serial No. 61/182,722 filed May 31, 2009, which is hereby incorporated by reference in its entirety.

Background of the Invention

[0002] Polymer nanocomposite materials have been the subject of research in recent years because of their potential for advanced properties and multi-functionality.

Composites using graphene are of particular interest for a wide range of applications, as graphene combines outstanding mechanical, electrical, and barrier properties with a high surface area [1,2].

[0003] The fabrication of macroscopic amounts of single-layer graphene sheets many micrometers in size for large-scale application in nanocomposite materials is challenging. In order to study their electronic, mechanical, and other properties, individual graphene sheets have been produced by mechanical exfoliation at very low yields, but this approach is not well-suited for large-scale applications [6]. A more promising approach for high yields is exfoliation of graphite oxide: graphite is treated with strong acids and oxidizing agents to produce graphite oxide, in which the addition of oxygen-containing functional groups on the surfaces of sheets increases the lamellar spacing between sheets and reduces the van der Waals forces holding the sheets together. This material can be exfoliated either thermally at a very high temperature (e.g., 1050 °C) in a tube furnace in an inert gas [1] or by sonication in solvents [7]. The high demand in energy and time can create challenge in processing. The tube furnace exfoliation simultaneously exfoliates and reduces graphite oxide, thereby removing the vast majority of the functional groups from the oxidized material. These functional groups are released primarily as CO₂ and H₂O gas. The resulting sheets are chemically similar to graphene. Accordingly, they are—like carbon nanotubes—very hydrophobic and thus difficult to handle in liquid processing. As a result, stable dispersions can only be achieved in a small number of relatively exotic solvents.

[0004] This difficulty is avoided when graphite oxide is exfoliated acoustically in solvents, such that the sheets retain a significant amount of their functional surface groups. Consequently, stable dispersions can be achieved in a large range of solvents including water, alcohols, and dimethylformamide. Due to this broad compatibility with

solvent processing, these functionalized graphene sheets (FGS) [7] have been used in composite materials instead of graphene due to its ease of preparation and its compatibility with many polymers. Unfortunately, these more highly functionalized graphene sheets do not have the advantageous mechanical and thermal properties or conductivity as does graphene [8,9]. Thus, it would be desirable to benefit from the unique properties of graphene without sacrificing the ease of preparation of functionalized graphene sheets. Methods of reducing graphene oxide while in aqueous dispersions have been developed [6]. These methods, however, need surfactants to be added in considerable amounts to avoid collapse of the dispersion [7], since the reduction renders the sheets hydrophobic. The presence of such surfactants is not desired in the production of nanocomposites, where the interface between the sheets and the polymer matrix is important to the performance.

[0005] Thus, a need exists to provide a better method of fabricating a graphene-containing composite from graphene oxide.

BRIEF SUMMARY

[0006] One object of the present invention relates to a method of reducing graphene oxide, such that the atomic carbon to oxygen ratios thereof can increase and approach that of pure graphene, thereby producing composites of polymers with dispersed functionalized graphene sheets or nanoparticles. The method can be applicable to reduce any graphene precursor to graphene in a medium, such as a polymer composite. The presently described method allows controlled temperature and process time to optimize particle-polymer interfacial forces, thereby providing optimal macroscopic performance properties of the product without the need for a high temperature, an inert gas

atmosphere, a high energy flash lamp, or additional chemical treatments or surfactants.

Graphene oxide can be mixed with polymers to form polymer composites, which are then reduced by heating at conventional processing temperatures and times to provide the desired increase in the atomic carbon–oxygen ratio in the mixture for the enhancement in performance properties. The method described herein allows for a large-scale production of graphene-containing material with atomic carbon to oxide ratios approaching pure graphene at various concentrations. One advantage of the presently described method over the conventional methods is the much lower temperature and times needed to reduce graphene oxide to graphene in the present method. Potential applications include gas barrier materials, high-strength materials, and electrically conductive materials.

[0007] One embodiment provides a method for producing a graphene-containing composition, the method comprising: (i) mixing graphene oxide with a medium to form a mixture, wherein the medium comprises a solid or a precursor thereof; and (ii) heating the mixture to a temperature above about 40 °C, whereby a graphene-containing composition is formed from the mixture. For example, in one embodiment the energy released during the exothermic reduction process of the graphene oxide to graphene transformation can be further used to heat up the graphene-medium nanocomposite. This method can be used to increase energy efficiency in the processing of the nanocomposites. Furthermore, the heat produced during the reduction can be used to accelerate the melting of the nanocomposite (e.g., for injection molding).

[0008] Another embodiment provides a heat sensor, comprising a graphene oxide and a medium, wherein at least some, such as substantially all, of the graphene oxide is transformed into at least one of (i) graphene and (ii) graphene oxide with a smaller

amount of functional groups when the heat sensor is exposed to an energy source, such as heat.

[0009] An alternative embodiment provides a method of modifying a property of a material, the method comprising: (i) introducing graphene oxide to a material; and then (ii) heating the material at a temperature sufficiently high to promote transformation of at least some, such as substantially all, of the graphene oxide, whereby a property of the material is modified via the formation.

BRIEF DESCRIPTION OF THE DRAWINGS

[0010] Figure B.1 shows an atomic force microscopy (AFM) image with two exfoliated graphene oxide sheets. The sheets have a thickness of approximately 1 nm, corresponding to single-layer sheets with hydroxyl and epoxy functional groups.

[0011] Figure B.2 shows a differential scanning calorimetry (DSC) plot, indicating that the reduction of graphite oxide is an initially endothermic reaction followed by an exothermic reaction. The reduction begins to occur around 110 °C. The majority of the reduction occurs between 150 °C and 250 °C for the shown heating ramp.

[0012] Figure B.3 shows a thermogravimetric analysis (TGA) graph, plotting sample weight as a function of time for a thermal reduction of graphite oxide.

[0013] Figure B.4 shows a TGA graph, plotting sample weight as a function of time for a neat polymer film made from a commercially available polyvinyl pyrrolidone polymer (Plasdone[®] C-17, available from International Specialty Products Inc., Wayne, NJ). As shown in Figure B.4, this polymer has a weight loss at 110 °C of 14.35% due to water but only a weight loss of 0.43% after a hold for 3 hours at 250 °C due to modest degradation.

There is virtually no weight loss during the 110 °C to 250 °C heating ramp.

[0014] Figure B.5 shows a TGA graph, plotting sample weight as a function of time for a Plasdone[®] C-17 polymer composite containing added graphene oxide. Relative to the polymer in Figure B.4, the weight loss due to the loss of water upon heating to 110 °C is comparable. However, in this case, there is significant weight loss of 3.7% upon heating to 250 °C and holding at that temperature for three hours. The majority of this weight loss occurs between 150 °C and 250 °C due to conversion of graphene oxide to graphene.

[0015] Figure B.6 shows a TGA graph, plotting sample weight as a function of time for a neat polymer film made from a commercially available polyvinyl pyrrolidone-vinyl acetate copolymer (Plasdone[®] S-630, available from International Specialty Products Inc., Wayne, NJ). As in Figure B.4, this polymer has a significant weight loss at 110 °C due to loss of water, but has virtually no weight loss upon heating to 220 °C, with significant weight loss thereafter due to polymer degradation.

[0016] Figure B.7 shows a TGA graph, plotting sample weight as a function of time for a Plasdone[®] S-630 polymer composite containing added graphene oxide. Relative to the polymer in Figure B.6, the weight loss due to the loss of water upon heating to 110 °C is comparable. However, in this case, there is significant weight loss of 4.6% upon heating to 220 °C, at which temperature the polymer degrades.

[0017] Figure B.8 shows a TGA graph, plotting sample weight as a function of time for a Plasdone[®] K-120 polymer (a commercially available polyvinyl pyrrolidone-vinyl acetate copolymer available from International Specialty Products Inc., Wayne, NJ, that has a higher molecular weight than Plasdone[®] S-630) composite containing graphene

oxide. When the sample is heated to 110 °C, there is the expected loss in weight due to water evaporation. When the sample is heated in a temperature ramp from 110 °C to 250 °C, there is a weight loss of 1.4%. The majority of this weight loss occurs between 150 °C and 250 °C due to conversion of graphene oxide to graphene and loss of bound water.

[0018] Figure B.9 shows a TGA graph, plotting sample weight as a function of time for a mixture of graphene oxide and graphite oxide (primarily graphene oxide) dispersed in a high performance polyether imide polymer. When the mixture is heated to 110 °C, there is the expected loss in weight due to solvent (dimethyl formamide) evaporation (TGA data). When the sample is heated in a temperature ramp from 110 °C to 250 °C and held for 3 hours, there is a weight loss of 5.2%. The majority of this weight loss occurs between 150 °C and 250 °C due to conversion to graphene and loss of additional solvent.

[0019] Figure B.10 shows an AFM image of several single-layer graphene sheets embedded into a film of polyether imide (PEI)

[0020] Figure B.11 shows an AFM image of graphene nanoparticles that were produced by heat-induced reduction of graphite oxide on a mica surface.

[0021] Figure B.12 shows a schematic of a heat sensor containing graphene oxide in one embodiment.

Detailed Description

[0022] The term “graphite oxide” herein refers to functionalized graphene sheets (FGS) – the oxidized compositions of graphite. These compositions are not defined by a single stoichiometry. Rather, upon oxidation of graphite, oxygen-containing functional groups (e.g., epoxide, carboxyl, and hydroxyl groups) are introduced onto the graphite.

Complete oxidation is not needed. The term “graphite oxide” includes graphene oxide, which is a morphological subset of graphite oxide. In some embodiments described herein, the terms “graphene oxide” and “graphite oxide” are used interchangeably.

[0023] Graphene oxide can refer to a graphene oxide material comprising either single-layer sheets or multiple-layer sheets of graphite oxide. Additionally, in one embodiment, a graphene oxide can refer to a graphene oxide material that contains at least one single layer sheet in a portion thereof and at least one multiple layer sheet in another portion thereof.

[0024] The term “graphene” refers to a one-atom-thick planar sheet of sp²-bonded carbon atoms that are densely packed in a honeycomb crystal lattice. In one embodiment, it refers to a single-layer version of graphite. Functionalized graphene can refer to graphene oxide, where the atomic carbon to oxygen ratio starts at approximately 2. This ratio can be increased in a medium, which can comprise a polymer, a polymer monomer resin or a solvent and approaches pure graphene.

Graphene-Containing Composition

[0025] In one embodiment, a method to produce a graphene-containing composition is provided. The composition can be in any form, such as one comprising a nanoparticle, a

plurality of nanoparticles, a sheet, or a plurality of sheets. The composition can be, for example, a polymer or a composition comprising a polymer. The term “graphene-containing” refers to having pure graphene as a constituent in a mixture/composite or having a molecule resembling pure graphene as a constituent. The resemblance to pure graphene can be delineated via any suitable metrics. For example, the metric can be the hydrophobicity, electrical conductivity, or a combination thereof. A material can also be characterized as graphene-containing, if the atomic carbon to oxygen ratio is sufficiently large as compared to that of a graphene oxide. For example, such a material can be one having an atomic carbon to oxygen ratio approaching pure graphene, but not completely identical to graphene. In one embodiment, the ratio can be at least about 2, 4, 6, 8, 10, 20, 40, 60, 80, 100, at least about 200, or more. The ratio can be an indicator of the degree of surface functionality of the graphene oxide. The atomic ratio of carbon to oxygen of a graphene oxide can be presented as “FGS-#,” wherein the symbol # denotes the ratio. See Table B.1. Note the higher the value of #, the closer in resemblance the material is to pure graphene.

[0026] By controlling the atomic carbon to oxygen ratio, a graphite oxide or graphene oxide containing composition can also be fabricated, such as by Hummers method. For example, the graphite/graphene oxide material can have an atomic carbon to oxygen ratio of about 2. The ratio can be, for example about 2, such as 1.7, 1.8, 1.9, 2.1, 2.2, or 2.3. In another embodiment, a mixture of graphene-containing and graphene oxide containing compositions can be created. The graphene oxide can then undergo the reduction process as described above.

[0027] The method can comprise mixing a graphene oxide with a medium to form a

mixture; and heating the mixture to a pre-defined temperature, whereby a graphene-containing composition is formed from the mixture. The temperature can be any suitable temperature, depending on the application. For example, it can be above about 30 °C, such as above about 40 °C, such as above about 60 °C, such as above about 80 °C, such as above about 100 °C, such as above about 140 °C, such as above about 180 °C, such as above about 200 °C, such as above about 250 °C, such as above 300 °C, such as above about 350 °C, such as above about 400 °C, such as above about 450 °C. The selection of the heating temperature can depend on the materials chosen as the matrix.

[0028] The reduction processing time can be fairly short. For example, it can be less than or equal to 4 hours, such as less than or equal to 2 hours, such as less than or equal to 1 hour, such as less than or equal to 30 minutes, such as less than or equal to 20 minutes, such as less than or equal to 15 minutes, such as less than or equal to 10 minutes. As described above, one advantage of the presently described method is that it needs a much lower temperature and shorter period of heating time to reduce graphene oxide to fabricate graphene-containing material, as compared with conventional methods. Also, it is noted that in conventional methods, when graphene oxide is exposed to a high temperature, such as one that is above the range of the presently described method, the carbon backbone of the resulting products are likely to contain defects, and thus the products do not resemble pure graphene, as in the resultant product of the presently described method.

[0029] Graphene oxide can be mixed with any medium to form a mixture or composite. For example, the medium can comprise an inorganic or organic material, or both. The medium can also be air. In the case of an inorganic medium, the medium can comprise a

metal, such as pure metal, alloy, compound, or combinations thereof, or glass. The medium can be crystalline or amorphous. The medium can comprise a solid or a precursor that can form a solid. For example, the precursor can be in the form of a fluid, such as a liquid, air, or a combination thereof. In the case of an organic medium, the medium can comprise a polymer, a monomer, a precursor to a polymer, or solvent, or combinations thereof, as discussed further below. Graphene oxide can be suitably mixed with polymers using any method known in the art. For example, the polymer can be dissolved in a suitable solvent into which graphene oxide is dispersed. Alternatively, molten polymer can be mixed with graphene oxide. In another embodiment, graphene oxide and a polymer resin could be dry-blended prior to thermal processing. In one embodiment, the graphene oxide in the graphene oxide – medium mixture can be in the form of a sheet that is very flat, or substantially free of wrinkle. After the heating step, the sheet (then has been transformed to be a graphene-containing material or a FGS with a smaller amount of functional groups) can then become wrinkled.

[0030] Polymers, monomers, and solvents, in which graphene oxide can be dispersed, can be used as a medium. They can include: polyethylene, polypropylene and copolymers thereof, polyesters, nylons, polystyrenes, polycarbonates, polycaprolactones, polycaprolactams, fluorinated ethylenes, polyvinyl acetate and its copolymers, polyvinyl chloride, polymethylmethacrylate and acrylate copolymers, high impact polystyrene, styrenic sheet molding compounds, polycaprolactones, polycaprolactams, fluorinated ethylenes, styrene acrylonitriles, polyimides, epoxies, polyurethanes, cellulose esters, or combinations thereof.

[0031] Different solvents can be used. The solvents can be polar or non-polar. Polar

solvents can include water, n-methylpyrrolidone (NMP), dimethylformamide (DMF), tetrahydrofuran (THF), alcohols, glycols such as ethylene glycol, propylene glycol and butylene glycol, aliphatic and aromatic esters, phthalates such as dibutyl phthalate, chlorinated solvents such as methylene chloride, acetic esters, aldehydes, glycol ethers, propionic esters, or combinations thereof. Mixtures with non-polar solvents are also possible.

[0032] In one embodiment, graphene oxide can be compounded into the monomeric precursors of these polymers to effect the polymerization in the presence of the graphene oxide nanoparticles. The graphene oxide in can be in the form of nanoparticles or sheets. For example, the graphene oxide nanoparticles or sheets can be uniformly dispersed in a medium material.

[0033] Graphene oxide can be incorporated into a medium material at a wide variety of concentrations. It is important to control the amount of graphene oxide being incorporated because adding too much graphene oxide could negatively affect the processability and performance of certain polymers. In one embodiment, the graphene oxide can be incorporated into (or mixed with) the medium at a weight ratio of at least about 1 part graphene oxide per 1000 parts medium (i.e., a weight percentage of at least 0.001%), such as at least about 0.01%, such as at least about 0.1%, such as at least about 1%, such as at least about 5% per medium weight.

Reduction to Graphene

[0034] The graphene oxide-medium mixture can be transformed via, for example, reduction of graphene oxide to graphene. The reduction can occur for at least some of

the graphene oxide, such as substantially all or all of the graphene oxide. In one embodiment, reduction of graphene oxide to functionalized graphene in the material matrix can be accomplished by exposing the mixture to a form of energy. The energy source can be, for example, heat, such as an increase in temperature. The heating and reduction step can be carried out in open air. For example, the step can be carried out without the use of a sealed container, such as a sealed autoclave. Rather, the step can be carried out with exposure to ambient air. In one embodiment, the heating can be carried out at any known polymer processing temperatures and times. The reduction reaction can be accelerated by heating at higher temperatures and longer times. The graphene oxide can be reduced in the medium matrix, such as a polymer matrix. The graphene oxide can also be reduced prior to the heating step. In one embodiment, the atomic carbon to oxygen ratio of the graphene oxide is controlled such that it is at a predefined level, such that after the heating step a predefined ratio in the final graphene-containing composition can be reached. In other words, by controlling the atomic carbon to oxygen ratio of the initial graphene oxide, the ratio of the final graphene-containing product can also be controlled.

[0035] The time and temperature can affect the final atomic carbon to oxygen ratio; and alternatively, the time and temperature can be based on the targeted ratio in the final product. Heating can be carried out by any suitable methods known in the art. Heating can be applied globally and uniformly to the entire mixture or can be applied thereto locally, for example, by selective spot treatment with a laser to create at least one localized region having a relative increase in graphene concentration in the mixture (as compared with the non treated region). As a result, in one embodiment, a patterned

conductive element can be easily introduced into the polymer. One result of the reduction of graphene oxide to graphene is the increase in the atomic carbon to oxygen ratio in the material. In one embodiment, the transformation, and thus the change in the atomic carbon to oxygen ratio in graphene oxide, is a continuous process. Specifically, the ratio is continuous increasingly.

[0036] As described previously, the transformation of graphene oxide to graphene can provide improvement of the material properties. Incorporating graphene sheets into polymers can significantly increase mechanical, electrical, and thermal properties of the material, even at graphene concentrations as low as one percent by weight; see [2]. The molecular structure of graphene sheets, a continuous hexagonal network of strongly-linked sp^2 carbon atoms, and the confinement and coupling of conjugated electron and hole states, can give rise to extraordinary mechanical [3,4] and electronic transport [3,5] properties. The in-plane tensile modulus can be, for example, above 1 TPa [4]; the room-temperature carrier mobility can be as high as $10,000 \text{ cm}^2/\text{Vs}$ [5], and the material can sustain currents of greater than $10^8 \text{ A}/\text{cm}^2$ [5]. In one embodiment, graphene sheets can be essentially only a single-atomic layer thick (1 nm or less) and several micrometers across; their aspect ratio is thus very high, and surface areas above $1,000 \text{ m}^2/\text{g}$ can be obtained.

[0037] Not to be bound by any particular theory, but these extreme topological properties can have several advantages with respect to applications in composites. For instance, (1) they have a dramatic effect on the gas barrier properties of a material, creating a tortuous pathway for small molecules [1]; (2) the percolation level can be reached at low concentrations; and (3) strong polymer–graphene interactions can be

possible due to the high surface area. An important property of graphene oxide is its ability to remain completely exfoliated as single nanoparticles in a variety of fluids. However, the ultimate properties of the graphene oxide polymer nanocomposite depend not only on exfoliation but also on interfacial interaction at the nanoparticle-polymer interface. In general, one would like a strong interaction at the polymer-particle interface. Thus, the hydrophilicity, the hydrogen bonding, and the polarity of the particle surface can be tailored to be compatible with the polymer structure. As a result, in addition to the processing temperature and/or time, the type of medium used, such as the chemical structure thereof, can affect the extent of the reduction – i.e., the atomic carbon to oxygen ratio of the final graphene-containing material. Furthermore, the presence of the polymer matrix may facilitate the reduction of graphene oxide within that matrix. In one embodiment wherein the matrix comprises a polymer, the heating can be carried out at a temperature sufficiently high but not high enough to degrade the polymer. Depending on the polymer used, the heating can be carried out at 500 °C or less, such as 450 °C or less, such as 400 °C or less, such as 300 °C or less.

[0038] The transformation can result in improvement in mechanical properties, processing properties, electrical conductivity, diffusion barrier properties, and hydrogen storage capacity. For example, compared to the graphene oxide, graphene can have enhanced modulus, greater load at failure, increased hardness, improved elongation properties, reduced gas permeability, enhanced thermal processing, and enhanced electrical and electromagnetic field properties. For example, the electrical conductivity can be increased as a result of the formation of graphene from graphene oxide because graphene oxide is less electrically conductive than graphene. The terms “increase,”

improved,” and “enhanced” herein denote an increase in the described property. For example, each of these terms can refer to a 20% increase or more, such as 40% increase or more, such as 60% increase or more, such as 80% increase or more, 100% increase or more, such as 150% increase or more, such as 200% increase or more. Similarly, the term “reduced” herein can denote a similar magnitude in reduction to those listed above.

Applications

[0039] Because the transformation of graphene oxide to graphene can improve the material properties of the graphene-oxide mixture (as a result of the superior properties of graphene), such transformation can be used for the purpose of improving a material property. In one embodiment, graphene oxide can be used in a method to modify a property of a material, comprising: (i) introducing graphene oxide to a material to form a mixture/composite; and then (ii) transforming (e.g. reducing) at least some the graphene oxide to graphene to modify at least one property of the functionalized graphene-containing material. The property can be any material property as described above regarding the properties of graphene.

[0040] For example, in one embodiment, the transformation can be used to form a foamed material. The foamed material can be a polymer, an inorganic or metallic material, or combinations thereof. To produce such a material, graphene oxide can be inserted into the material form a mixture/composite, whereupon the mixture is heated to promote the reduction of graphene oxide to graphene. During the reduction, gases, such as CO₂ and/or H₂O gases, can be released from graphene oxide, which gases can then create porosity in the mixture, whereby upon cooling a foamed material can be formed

from the mixture.

[0041] Graphene oxide can also be used as a stabilizer. For example, graphene oxide can be inserted into a material (or medium), and by controlling the carbon and oxygen levels of the graphene oxide to a predefined level, graphene-containing nanoparticles with specific final carbon to oxygen ratio can be created. These nanoparticles can have a tendency to react readily with a gas or chemical in the mixture or ambience, which gas or chemical could otherwise degrade the material. By removing these gases or chemicals by the nanoparticles, the useful life of the material, into which the graphene oxide is initially incorporated, can be extended.

[0042] By targeting specific atomic carbon to oxygen ratio in the initial graphene oxide, graphene-containing or graphite/graphene oxide containing material can be fabricated. The ratio can be controlled at various points during the process. For example, it can be controlled prior to the processing to ensure substantial uniform distribution of the graphene oxide in the medium matrix. For example, the parameters of the Hummers method can be controlled such that the graphene oxide produced thereby can have a predefined carbon to oxygen ratio. The ratio of the final product can also be controlled during or prior to the heating step to attain an FGS-# with the desired properties. The determination of the ideal ratio to be targeted can be an iterative process, taking into account the process parameters of the various process steps involved.

[0043] In one embodiment, graphene oxide, rather than graphene, is relied on to modify a material's property. Depending on the application, graphite oxide or graphene oxide nanoparticles can be incorporated into a material matrix, which can comprise a material

that does not substantially react with the nanoparticles. Because nanoparticles do not substantially interact with the matrix material, these nanoparticles can rise to the surface of the material, thereby forming a protective layer thereover. For example, in one embodiment, a carbon surface layer and/or a gas barrier surface layer can be created over the material.

[0044] In another embodiment, graphene-containing nanoparticles, instead of graphene oxide nanoparticles, can be formed over the material, to provide an electrically conductive surface, which comprises these graphene-containing nanoparticles, over the material. In yet another embodiment, a graphene-containing gas barrier can be produced. Depending on the application, a gas barrier comprising graphene, instead of graphene oxide, can be used. No to be bound by any particular theory, but graphene sheets can be dense enough to create a barrier to gases, even for molecules/atoms as small as hydrogen and helium. Thus, when these impenetrable graphene sheets are added to a polymer, the gas molecules have to go around the sheets and thus take longer to diffuse (i.e., tortuosity effect). In one embodiment, the barrier can be over the material or can be within the material, depending on the location of the barrier.

[0045] The change in electrical conductivity due to the transformation can be utilized. For example, a material that would undergo such a transformation can be used as a thermal or heat sensor. For example, in one embodiment, when a predefined temperature (e.g., exceeding about 140 °C) is reached as a result of exposure to an energy source, such as heat, the transformation of graphene oxide to graphene, and/or into FGS (e.g., graphene oxide) with a smaller amount of functional groups, in the heat sensor can render the device conductive, and the change in conductivity can allow monitoring of thermal

load. A schematic of such a heat sensor is shown in Figure B.12. In Figure B.12, in one embodiment, the sensor 1, containing graphene oxide, can be connected to the heat source 3 and a multi-meter 2.

Non-limiting Working Examples

Materials and Methods

Oxidation of Graphite

[0046] Graphite oxide was prepared by the Hummers method [10]. First, 4 g sodium nitrate was added to 184 mL sulfuric acid and stirred until completely dissolved. Natural flake graphite (Asbury Carbons, Asbury, NJ, grade 3243, 99.5%) was added under vigorous stirring to avoid agglomeration. The solution became dark. After the graphite was well dispersed, 24 g of potassium permanganate were added slowly under stirring. During this process, the temperature can rise rapidly, creating severe effervescence. Potassium permanganate was added slowly enough to keep the temperature below 100 °C. The suspension became thicker, turning into a slurry. The color turned from black to dark brown. After completion of the reaction, the slurry was cooled down. Subsequently, 400 mL of de-ionized water was added to the still very acidic solution, leading to an increase of temperature. After the temperature decreased to room temperature again, 80 mL of 10% hydrochloric acid and 200 mL of 3% hydrogen peroxide were added to the solution to reduce the residual permanganate and manganese dioxide. The graphite oxide slurry was still strongly acidic and was repeatedly washed

using de-ionized water until the pH value of the slurry was above 5. The graphite oxide slurry was then filtered to obtain graphite oxide paste. The dried graphite oxide was obtained by heating the graphite oxide paste to remove residual water.

Exfoliation of Graphite Oxide to Produce Graphene Oxide.

[0047] During oxidation, oxygen-containing functional groups (hydroxyl and epoxy) are intercalated between the graphite layers, increasing the lamellar spacing. Not to be bound by any particular theory, but this reduces the attractive van der Waals forces between the layers and allows exfoliation into single-layer sheets in solvents by ultrasonication. Exfoliation of graphite oxide can be achieved in numerous solvents, including water, dimethylformamide (DMF), and dimethylacetamide (DMAc). In one embodiment, dried graphite oxide was weighed and exfoliated in water, DMF, or DMAc (all at 0.1 wt% of graphite oxide) by ultrasonication (tabletop ultrasonic cleaner FS-30D, Fisher Scientific, Pittsburgh, PA) for 1 hour. This process produced dark, uniform and stable dispersions of single-layer graphite oxide sheets (i.e., graphene oxide) in solvents, which did not precipitate even after several days. When diluted to a concentration of 0.001 wt%, these suspensions were light brown and clear, without any visible particles, indicating stable dispersion of submicron particles. The graphene oxide dispersions became viscous when the sheet concentrations were increased to around 0.5 wt%, because exfoliation produced a large number of single layer sheets.

Preparation of Polymer and Polymer Nanocomposite Samples.

[0048] Films of neat polyvinyl pyrrolidone (PVP) and polyvinyl pyrrolidone/vinyl acetate (PVP/VA; two versions with different molecular weight were used: Plasdone[®] S-630 and Plasdone[®] K-120) were prepared by dissolving the polymers as received in deionized water at concentrations of 10 wt% polymer. Films of neat polyether imide (PEI) were prepared by dissolving the polymer as received in DMF at a concentration of 10 wt% polymer.

[0049] To prepare polymer nanocomposite films containing 1 wt% graphene oxide, PVP and PVP/VA were dissolved in aqueous dispersions of 0.1 wt% graphene oxide, prepared as described above, in concentrations of 10 wt% polymer. PEI nanocomposite films were prepared by dissolving PEI in a DMF-based solution of 0.1% graphene oxide prepared as described above, at a concentration of 10 wt% polymer.

[0050] To cast films, the solutions of polymers or polymer nanocomposites were poured over clean glass plates and placed in a dry box with air flowing through at a temperature of 22 °C and 4% relative humidity. The films were left in the dry box for at least 12 hours, until they were dried through. The resulting films were 0.1—0.3 mm thick.

Characterization of Materials.

[0051] The most direct proof for exfoliation into single-layer sheets is provided by Atomic Force Microscopy (AFM), which was performed as follows. An aqueous

graphene oxide suspension (0.01 wt%) was spin-coated at 2,000 RPM onto a freshly cleaved mica surface. The samples were examined using a NTEGRA Prima AFM (NT-MDT, Russia, Moscow). Contact-mode imaging was performed (BudgetSensors silicon nitride probes, SiNi, force constant 0.27 N/m, tip radius of curvature 15 nm) to measure the thickness of the sheets. The AFM images show that the great majority of the exfoliated sheets have a thickness of around 1 nm, as expected for single-layer graphene with attached functional groups (see Figure B.1).

[0052] Differential Scanning Calorimetry (“DSC”, 2920 Modulated DSC, TA Instruments, New Castle, DE) was performed on a sample of graphite oxide to determine the time and temperature needed for it to be reduced, as shown in Figure B.2. A 5.0 mg sample of graphite oxide was sealed in a hermetic pan (TA Instruments) and heated to 100 °C and held for an hour to remove water. The endothermic peak seen in the first 10 minutes of the DSC plot in Figure B.2 is due to the heat of vaporization of water. When the temperature is increased to 150 °C, there is a large exothermic peak from the reduction of graphite oxide. The majority of the conversion occurs between 150 °C and 250 °C.

[0053] The reduction of graphite oxide involves a weight loss due to the loss of oxygen [1, 11]. This weight change was measured using Thermal Gravimetric Analysis (“TGA”, TA Instruments TGA Q500 V6.3 Build 189). A sample of graphite oxide was heated on a platinum weighing pan under nitrogen, and its weight change was monitored at 0.1 µg precision, as shown in Figure B.3. The sample was heated to 110 °C and held for 2 hours to remove all water. The temperature was increased to 250 °C and held for 3 hours to ensure that all the graphite oxide was reduced. The loss of 30.57% of the sample’s

weight is due to the loss of oxygen when the material is reduced.

Example 1

[0054] Just as bulk graphite oxide can be thermally reduced, it can also be reduced in its exfoliated version—graphene oxide—*in situ* when it is already incorporated into a polymer as disperse single-layer sheets by heating the composite. Using TGA, the weight change of polymer–graphene oxide composites is monitored to verify the reduction occurs within the polymer. In a first step, TGA was performed on a film of the polymer Plasdone[®] C-17 (a polyvinyl pyrrolidone polymer available from International Specialty Products Inc., Wayne, NJ) in the absence of any filler particles (see Figure B.4). The sample was first heated to 110 °C and held for 2 hours. All of the water in the sample, 14.35% by weight, was evaporated in the first few minutes. The sample was then heated to 150 °C, the temperature at which graphene oxide would be reduced. The temperature was held at 150° C for 2 hours, and there was no further weight change. When the temperature was increased to 250 °C and held for three hours, there was a modest additional decrease in weight (0.43%) due to slight degradation of the polymer. The majority of the weight loss was likely due to loss of water, which occurs quickly and at the lower temperature of 100 °C.

[0055] In the second step, TGA was performed on the polymer composite, a dispersion of graphene oxide in Plasdone[®] C-17 polymer. Following the same temperature curve as the neat polymer shown in Figure B.4, the polymer nanocomposite sample was heated to 110 °C and held for 2 hours to ensure that all water has been removed. As shown in Figure B.5, the temperature was then slowly increased to 250 °C and held for three hours.

In contrast to the neat polymer, the sample began to lose weight at 150 °C. Not to be bound by any particular theory, but this can be explained by the presence of the added graphene oxide sheets. Since this is the temperature range for which graphite oxide loses weight due to reduction in one embodiment (see Figure B.3), this recorded weight loss herein verifies that the reduction of graphene oxide occurred while incorporated in the polymer.

Example 2

[0056] The steps of Example 1 were repeated with a different polymer, Plasdone[®] S-630, a polyvinyl pyrrolidone-vinyl acetate copolymer available from International Specialty Products Inc., Wayne, NJ). Figure B.6 shows the TGA of a film of Plasdone[®] S-630 with no added graphene oxide. Again, the water is all lost very quickly, at 110 °C. As the temperature is increased, there is no observed weight change until the temperature reached 225 °C, at which point the polymer began to degrade. The same experiment was performed on a composite of Plasdone[®] S-630 and graphene oxide (see Figure B.7). The water was lost quickly at 110 °C, as was observed with the neat polymer film. In contrast to the results with the neat polymer film, however, the TGA showed a loss of weight for the composite polymer when the temperature was increased to 140 °C; not to be bound by any particularly theory, but this can be attributable to the reduction of graphene oxide to produce graphene. The rate of weight loss slows down until the temperature reaches the degradation temperature 225 °C, at which point the weight dropped more rapidly. The change in weight seen at 140 °C in the composite was not observed in the neat polymer, which demonstrates that graphene oxide was reduced to graphene in the polyvinyl pyrrolidone-vinyl acetate copolymer polymer matrix.

Example 3

[0057] A higher molecular weight polyvinyl pyrrolidone-vinyl acetate copolymer was used in this example. Figure B.8 shows a TGA graph, plotting polymer weight as a function of time for a Plasdone[®] K-120 (a commercially available polyvinyl pyrrolidone-vinyl acetate copolymer available from International Specialty Products Inc., Wayne, NJ, that has a higher molecular weight than Plasdone[®] S-630) polymer composite containing added graphene oxide. The majority of the water was lost in the first few minutes, when the sample was held at 110 °C. When the temperature was increased, the weight began to decrease starting at 140 °C, with a total weight loss of 1.3% due to reduction of graphene oxide and removal of some residual solvent, again demonstrating that graphene oxide was reduced to graphene in the polymer matrix.

Example 4

[0058] A composite of a polyether imide polymer (ULTEM[®], available from the General Electric Company) and graphene oxide was analyzed by TGA as shown in Figure B.9. The solvent used was dimethyl formamide, which has a boiling point of 165 °C and cannot be entirely removed from the sample before the reduction of graphene oxide, which began around 150 °C. The weight loss after 150 °C was likely due to the reduction of graphene oxide and the removal of solvent.

[0059] Figure B.10 shows an AFM image of several single-layer graphene sheets embedded into a film of PEI. The sample was prepared by first spin-coating aqueously dispersed graphene oxide sheets on top of a mica surface. Subsequently, a solution of

PEI in DMF was added on top of the surface. This PEI-graphene oxide film was then heated to 250°C and held for 30 minutes. The AFM image showed significant wrinkling of the sheets, which indicated that the graphene oxide sheets embedded in PEI were reduced during the heating step. Prior to reduction, graphene oxide sheets were very flat (see Figure B.1); during reduction, they usually obtained a significantly wrinkled morphology. For example, Figure B.11 shows an AFM image of graphene nanoparticles that were produced by heat-induced reduction of graphene oxide on a mica surface, and these graphene nanoparticles have a wrinkled appearance.

Example 5

[0060] In this example, the weight fractions of the significant elements in the graphene oxide and graphene in one embodiment were measured via elemental analysis (Galbraith, Knoxville, TN). Table B.1 shows values of the corresponding molar carbon to oxygen ratio over a range of representative polymer processing temperatures for a relatively short time in the presence of air and when the graphite oxide was in a non reactive fluid, dimethyl formamide, along with the atomic carbon to oxygen ratio of two different batches of graphite oxide prepared by the Hummers method. “#” in “FGS-#” denotes the atomic carbon to oxygen ratio in the FGS. The results show that in air or a non reactive medium and at typical polymer processing times and temperatures, the graphene oxide was reduced. The lower portion of Table B.1 shows the results of the samples and their respective reduction conditions with respect to temperature and time. The results show that the value of the atomic carbon oxygen ratio was affected by the processing temperature and time within the range of polymer fabrication procedures generally

known in the art. Specifically, the ratio was substantially increased as a result of the presently described process from about 2 to one that approaches pure graphene.

[0061] All publications, patents, and patent applications cited herein are hereby expressly incorporated by reference in their entirety and for all purposes to the same extent as if each was so individually denoted.

[0062] While specific embodiments of the subject invention have been discussed, the above Specification is illustrative and not restrictive. Many variations of the invention will become apparent to those skilled in the art upon review of this specification. The full scope of the invention should be determined by reference to the claims, along with their full scope of equivalents, and the specification, along with such variations.

[0063] The articles "a" and "an" are used herein to refer to one or to more than one (i.e. to at least one) of the grammatical object of the article. By way of example, "a polymer resin" means one polymer resin or more than one polymer resin. Any ranges cited herein are inclusive. The terms "substantially" and "about" used throughout this Specification are used to describe and account for small fluctuations. For example, they can refer to less than or equal to $\pm 5\%$, such as less than or equal to $\pm 2\%$, such as less than or equal to $\pm 1\%$, such as less than or equal to $\pm 0.5\%$, such as less than or equal to $\pm 0.2\%$, such as less than or equal to $\pm 0.1\%$, such as less than or equal to $\pm 0.05\%$.

What is Claimed:

1. A method for producing a graphene-containing composition, comprising:
 - (i) mixing graphene oxide with a medium to form a mixture, wherein the medium comprises a solid or a precursor thereof; and
 - (ii) heating the mixture to a temperature above about 40 °C, whereby a graphene-containing composition is formed from the mixture.
2. The method of claim 1, wherein the graphene-containing composition comprises a polymer.
3. The method of claim 1, wherein the medium comprises, an organic material, an inorganic material, or combinations thereof.
4. The method of claim 1, wherein step (ii) is carried out in open air.
5. The method of claim 1, wherein the medium comprises a metal, a glass, or a combination thereof.
6. The method of claim 1, wherein step (ii) is carried out for less than or equal to about 4 hours.
7. The method of claim 1, wherein the graphene oxide is in the form of a sheet substantially free of wrinkles before step (ii).
8. The method of claim 1, wherein the graphene oxide is mixed with the medium at a weight ratio of at least about 1 part graphene oxide per 1000 parts medium.

9. The method of claim 1, wherein step (ii) further comprises reducing at least some of the graphene oxide to graphene during the heating.
10. The method of claim 1, wherein step (ii) is selectively applied to the mixture such that at least one localized region having a relative increase in graphene concentration is formed in the mixture.
11. The method of claim 1, wherein compared to the graphene oxide the graphene-containing composition formed after step (ii) has at least one of: enhanced modulus, greater load at failure, increased hardness, improved elongation properties, reduced gas permeability, enhanced thermal processing, and enhanced electrical and electromagnetic field properties.
12. The method of claim 1, wherein compared to the graphene oxide the graphene-containing composition formed after step (ii) has an increased electrical conductivity.
13. The method of claim 1, wherein the atomic carbon to oxygen ratio in the graphene-containing composition is greater than about 4.
14. The method of claim 1, wherein the graphene-containing composition is in the form of at least one nanoparticle.
15. The method of claim 1, wherein step (ii) is carried out at least about 140°C.
16. The method of claim 1, wherein step (ii) is carried out at about 450 °C or less.

17. A heat sensor, comprising a graphene oxide and a medium, wherein at least some of the graphene oxide is transformed into at least one of (i) graphene and (ii) graphene oxide with a smaller amount of functional groups when the heat sensor is exposed to an energy source.
18. The heat sensor of claim 17, wherein the energy is heat.
19. The heat sensor of claim 17, wherein the heat sensor has an increase in electrical conductivity after the exposure to the energy source.
20. The heat sensor of claim 17, wherein the medium comprises a polymer.
21. The heat sensor of claim 17, wherein the graphene oxide is mixed with the medium at a weight ratio of at least about 1 part graphene oxide per 100 parts medium.
22. A method of modifying a property of a material, comprising:
 - (i) introducing graphene oxide to a material; and then
 - (ii) heating the material at a temperature sufficiently high to promote transformation of at least some of the graphene oxide, whereby a property of the material is modified via the transformation.
23. The method of claim 22, further comprising controlling the atomic carbon to oxygen ratio of graphene oxide.
24. The method of claim 22, wherein the material after step (ii) is a foamed material.

25. The method of claim 22, wherein the transformation extends the useful life of the material.
26. The method of claim 22, wherein after the transformation a gas barrier is formed over the material.
27. The method of claim 22, wherein after the transformation a conductive surface is formed over the material.

Table B.1: Results from FGS elemental analysis. Values with an asterisk (*) were inferred based on other elemental content and the theoretical makeup of FGS sheets consisting of carbon, oxygen, and hydrogen.

Hummer Prepared FGS 2					
Sample	% Carbon	% Oxygen	%Hydrogen	%Other	FGS#
1	58.26*	41.74	0*	0*	1.86
2	53.16	36.74	2.12	7.98	1.93
Reduced FGS					
Sample	% Carbon	% Oxygen	% Hydrogen	%Other	FGS#
400C, 10 min	78.59*	21.41	0*	0*	4.89
300C, 10 min	83.8*	16.2	0*	0*	6.89
250C, 10 min	79.95*	20.05	0*	0*	5.31
200C, 10 min	81.22*	18.78	0*	0*	5.76
250C, 4hr, DMF, pressure	73.06	11.84	7.15	7.95	8.22

Figures for Appendix B

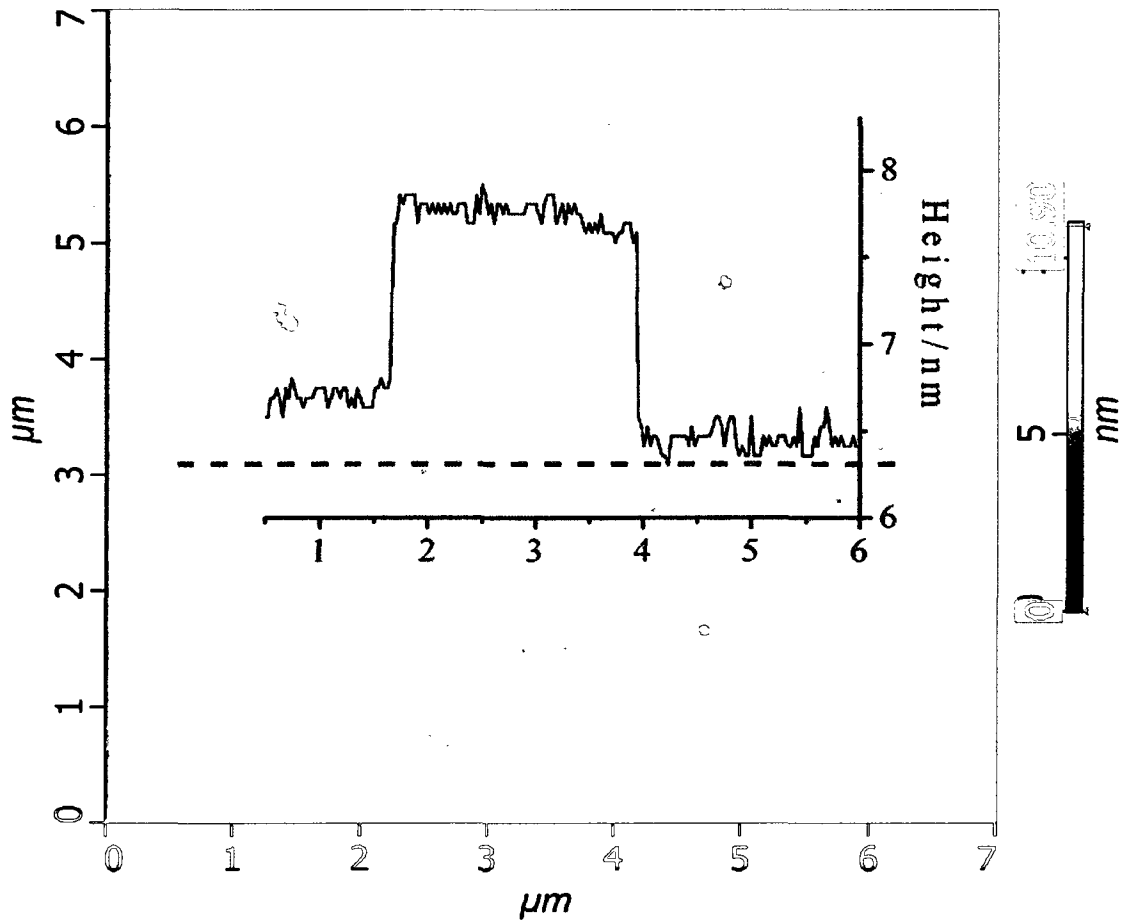


Figure B.1: Atomic force microscopy (AFM) image with two exfoliated graphene oxide sheets. They have a thickness of appx. 1 nm, corresponding to single-layer sheets.

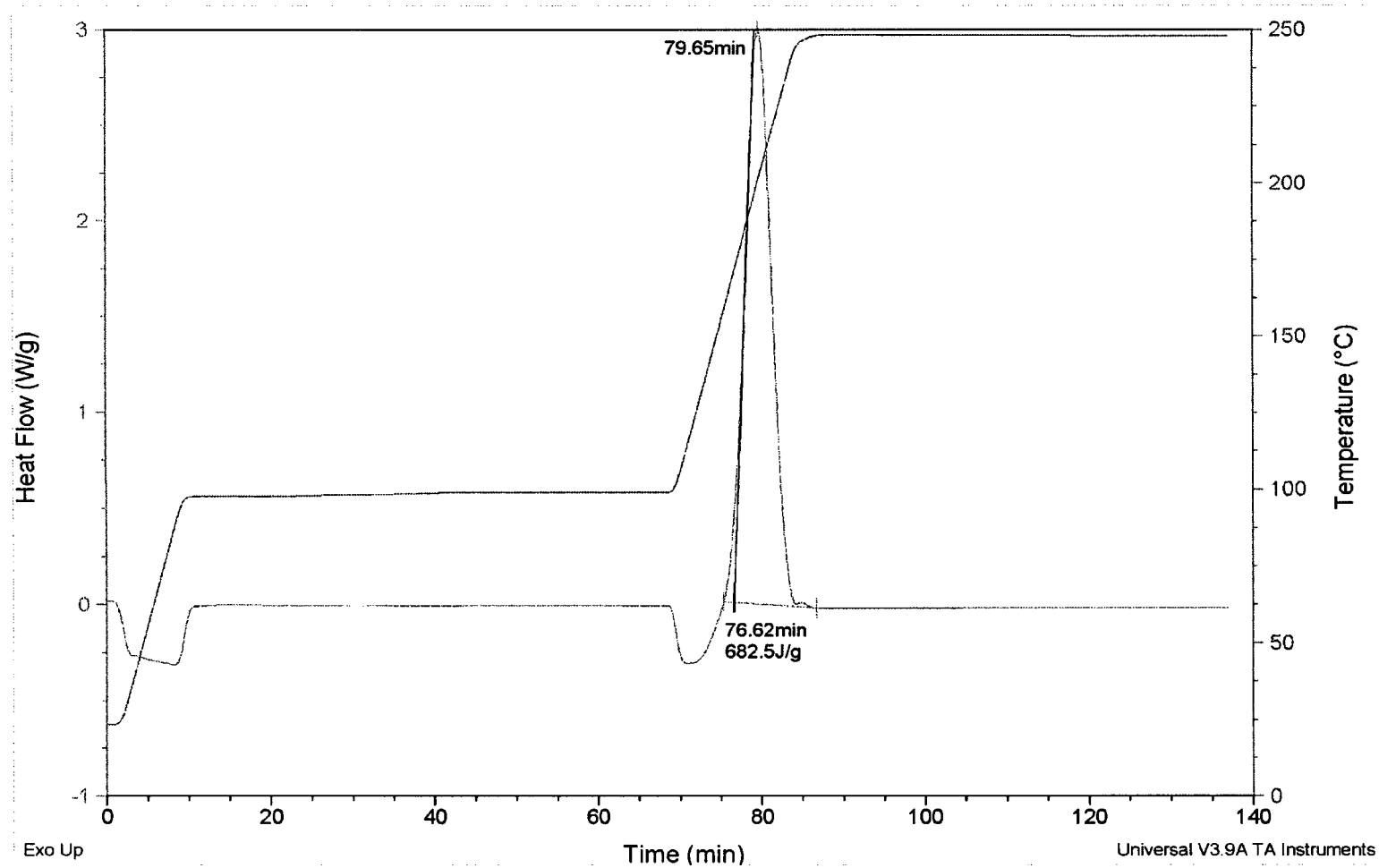


Figure B.2: Differential scanning calorimetry (DSC) plot showing reduction characteristics of graphite oxide.

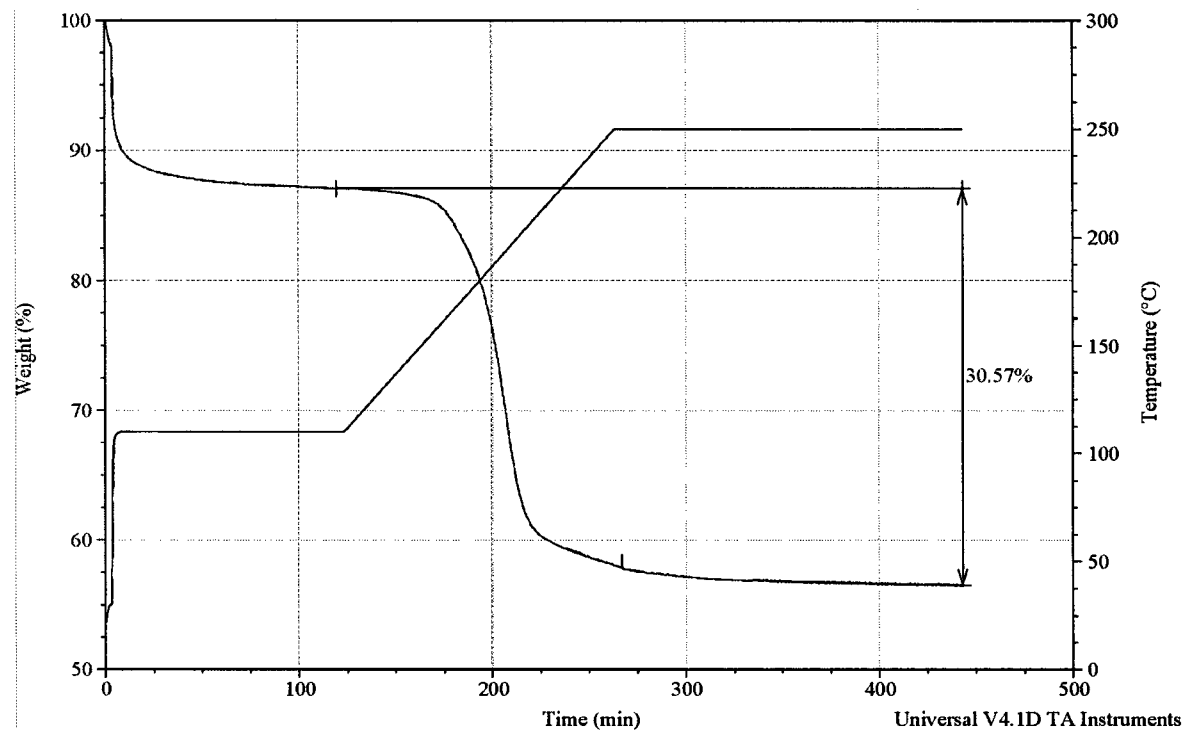


Figure B.3: Thermogravimetric analysis (TGA) plot showing sample weight vs. time for the reduction of graphite oxide.

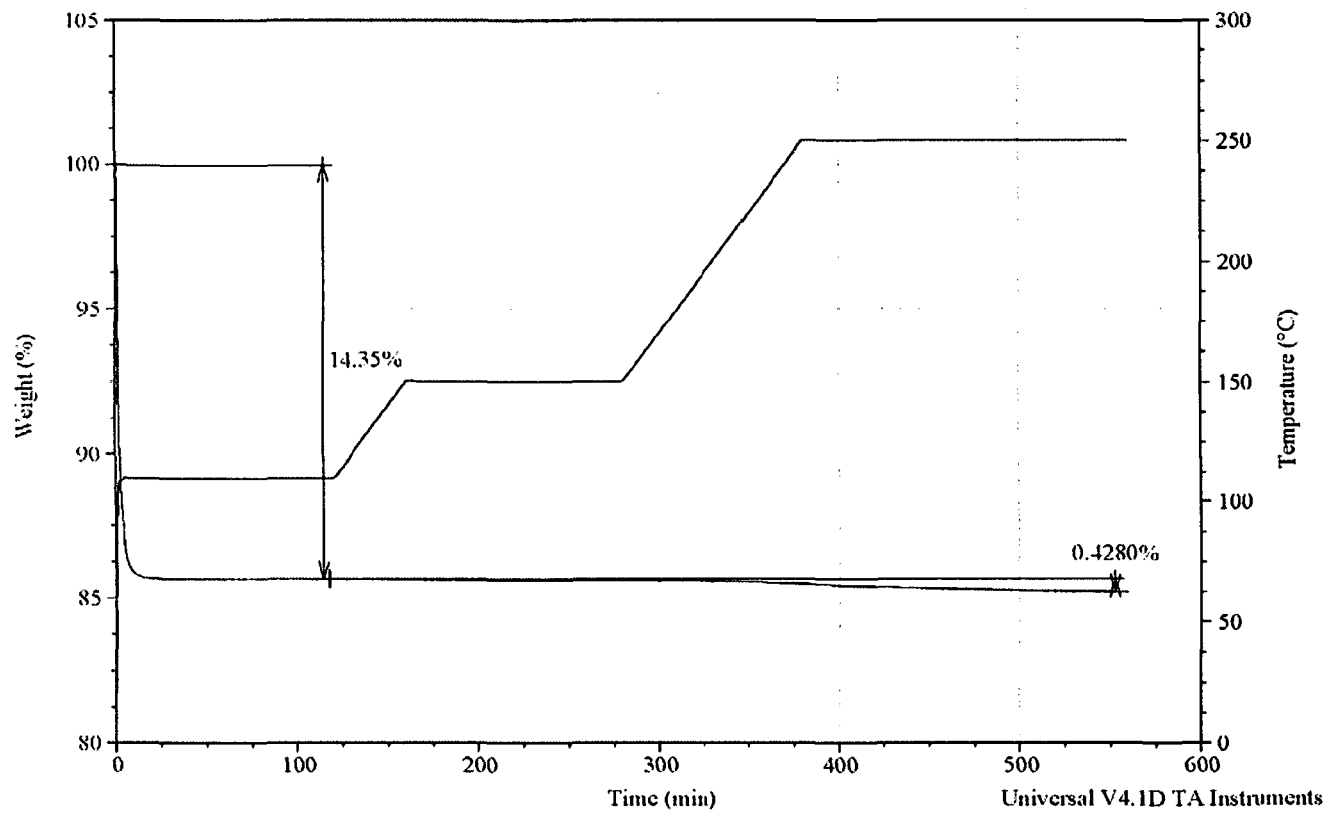


Figure B.4: TGA plot of neat Plasdone® C-17 film.

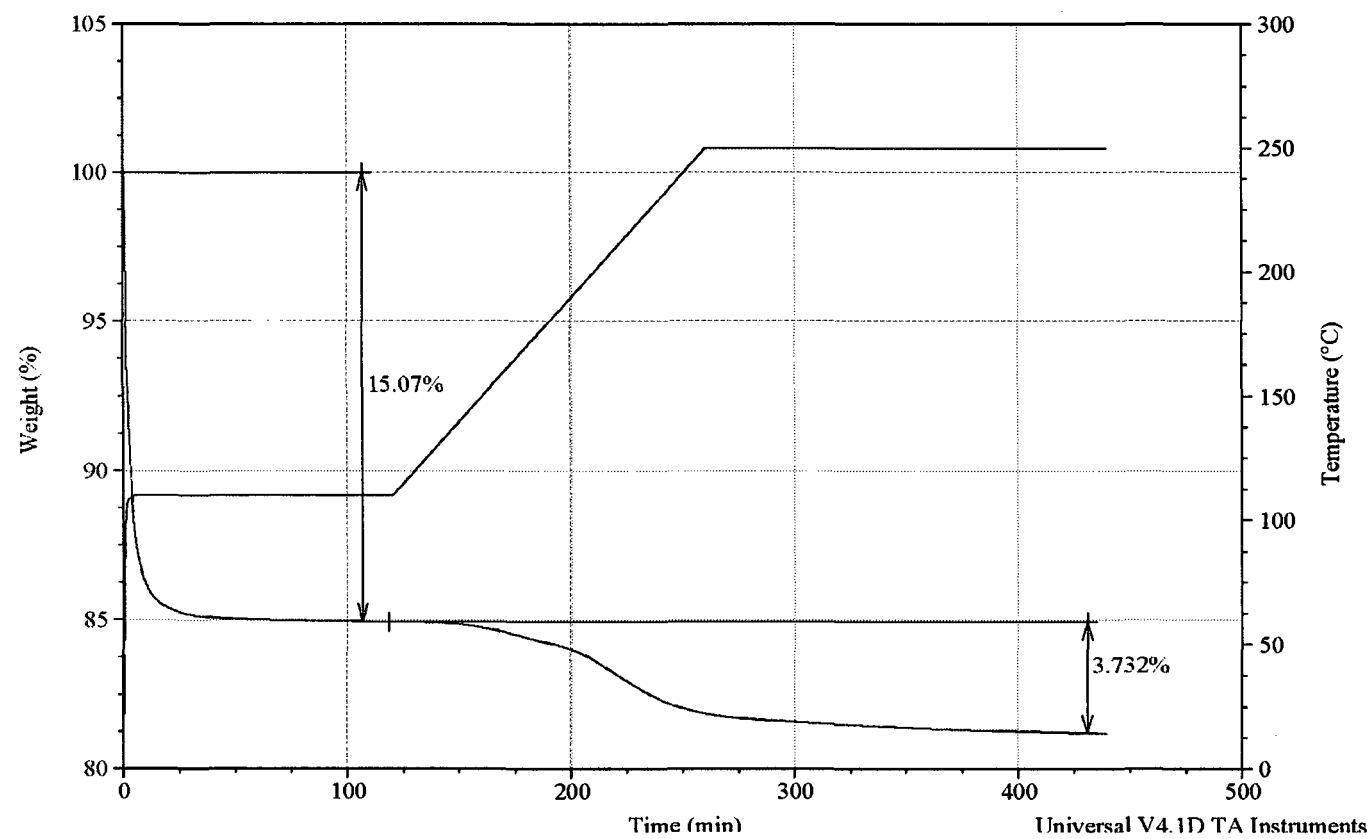


Figure B.5: TGA of Plasdone[®] C-17 loaded with 10% graphene oxide.

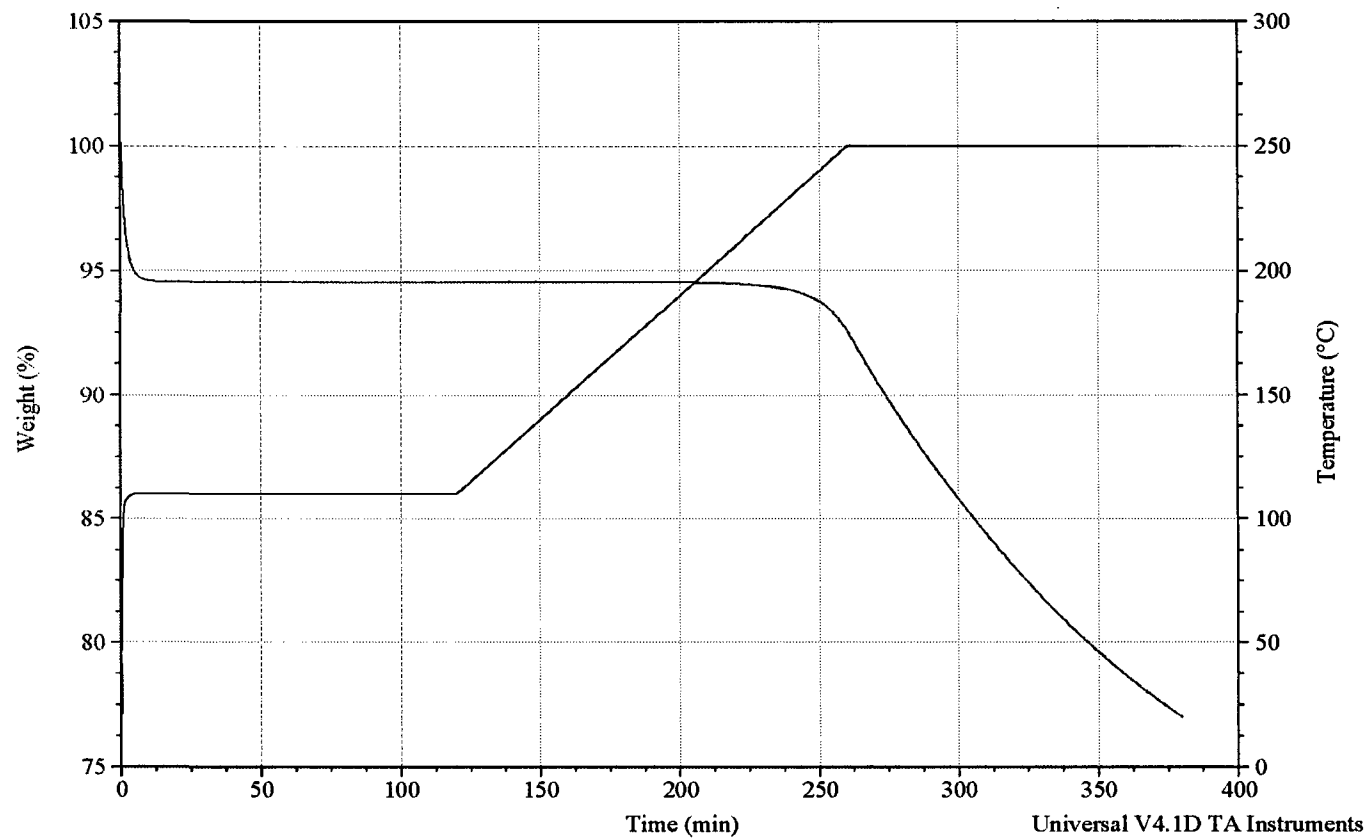


Figure B.6: TGA of neat Plasdane[®] S-630, which is shown to be stable up to almost 220°C.

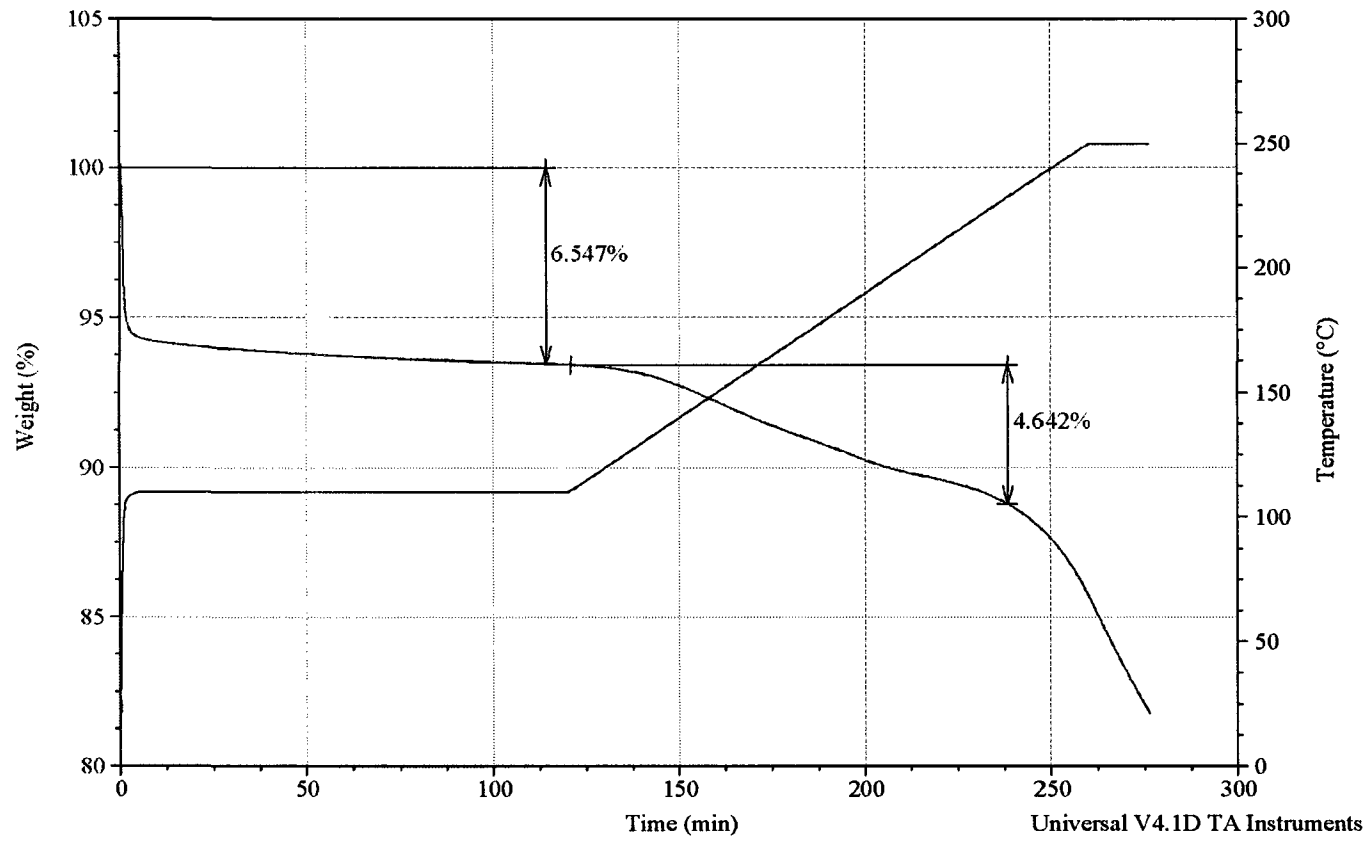


Figure B.7: TGA of Plasdene[®] S-630 which is shown to have 6.55% water. It loses 4.64% of its initial mass as the graphene oxide reduces.

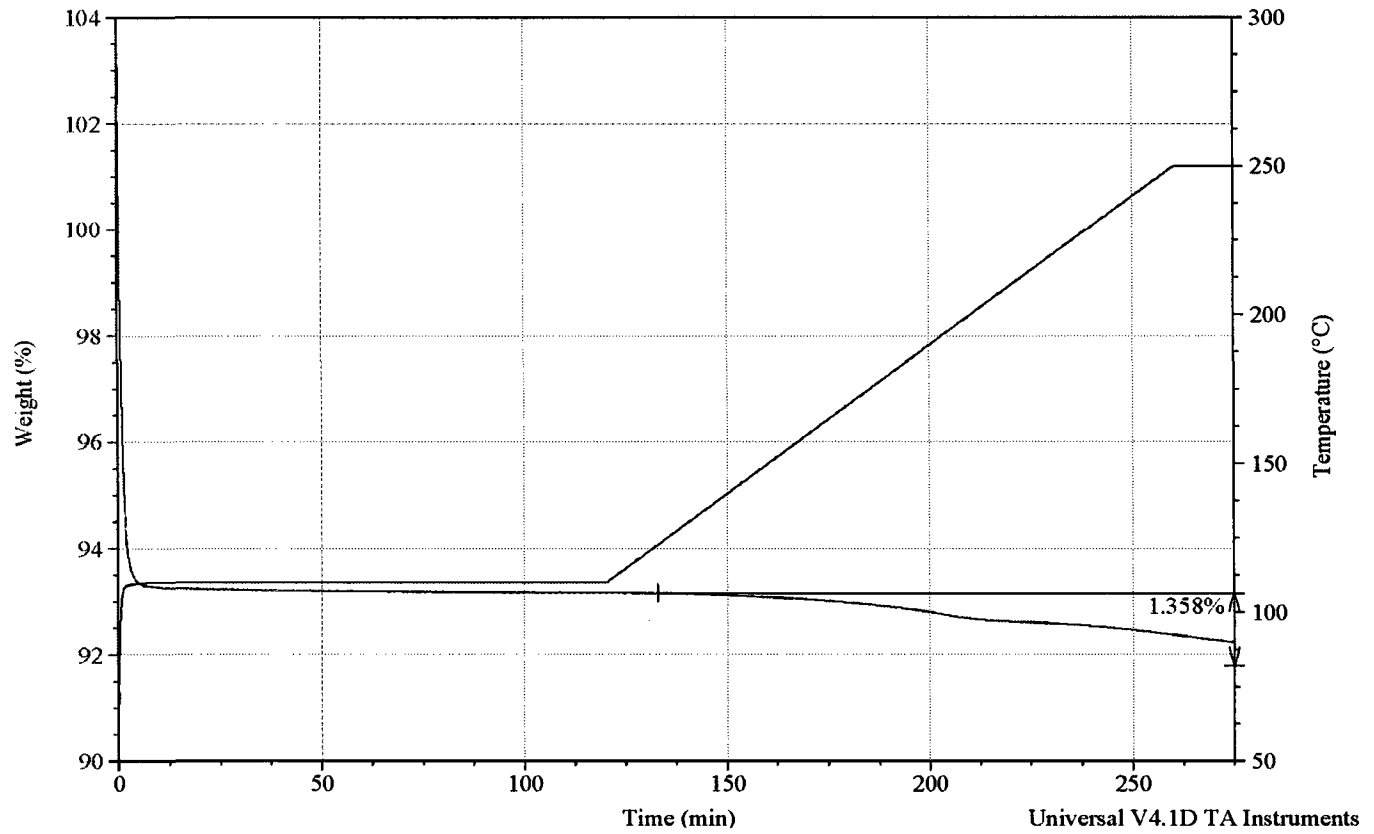


Figure B.8: TGA of Plasdone® K-120 containing 10% graphene oxide. The mass loss of 1.34% is due to thermal reduction of graphene oxide.

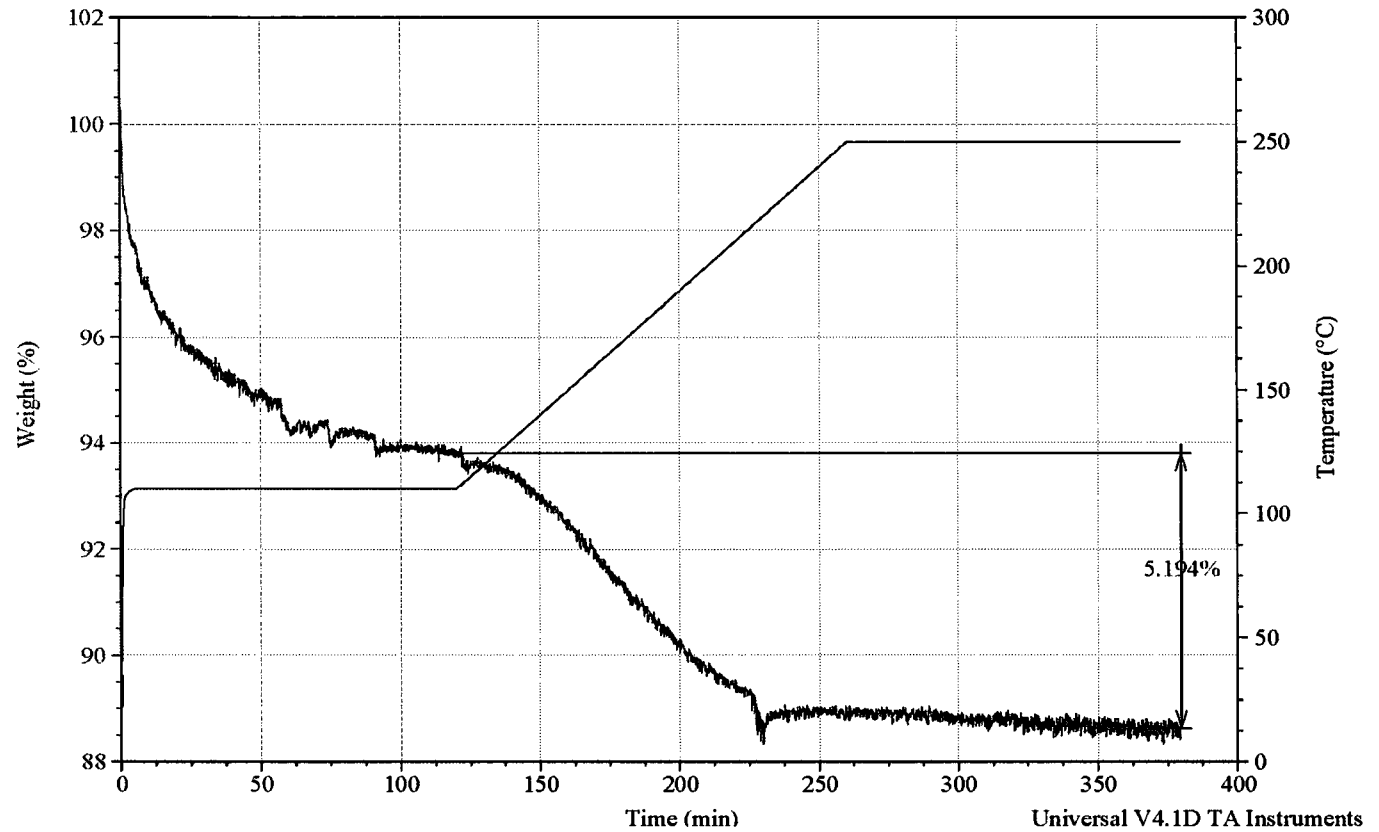


Figure B.9: TGA of Ultem 1000[®], a high-performance polyimide, with 10% graphene oxide sheets. The weight loss corresponds to loss of solvent and reduction of graphene oxide sheets.

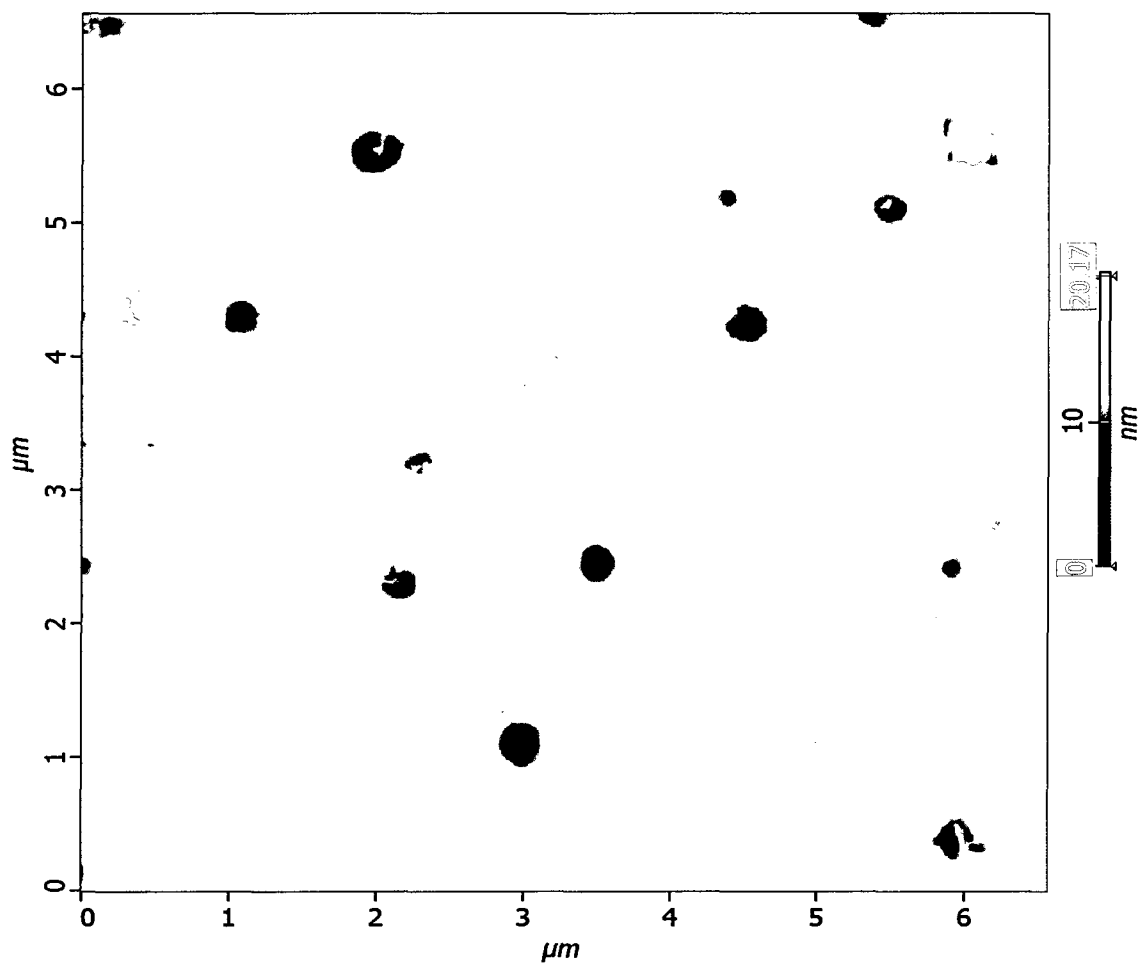


Figure B.10: AFM image of several single-layer graphene sheets within an Ultem 1000® film.

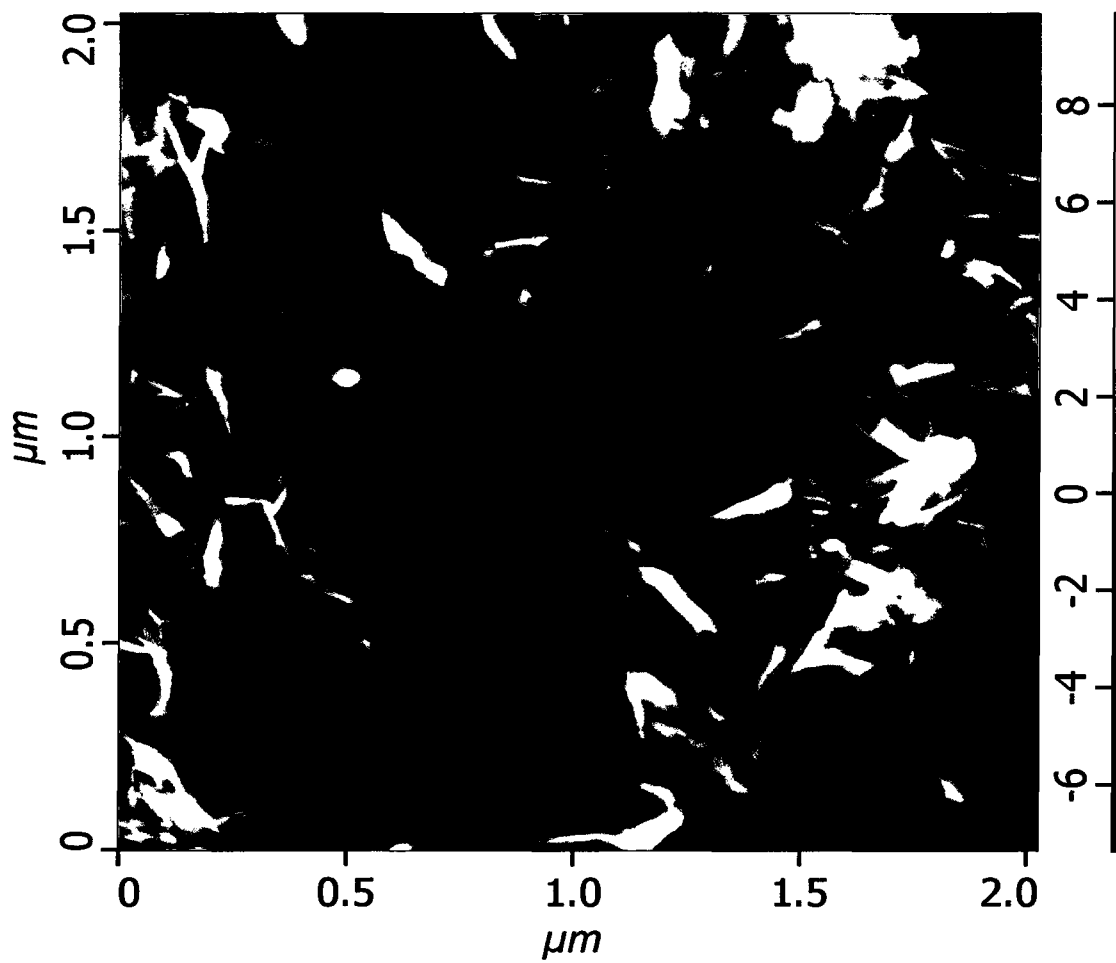


Figure B.11: AFM image of graphene nanoparticles produced by thermal reduction on a mica surface.

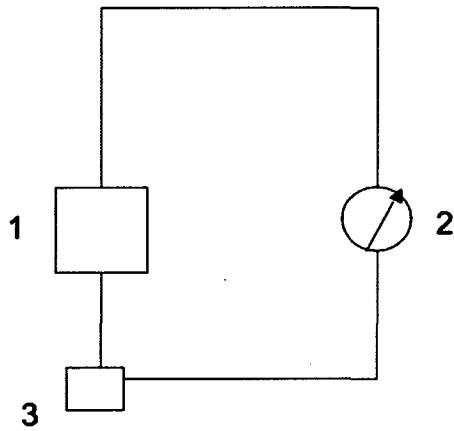


Figure B.12: Schematic of a heat sensor containing graphene oxide in one embodiment.

References for Appendix B

- [1] Schniepp et al. "Functionalized Single Graphene Sheets Derived from Splitting Graphite Oxide." *J. Phys. Chem. B* **110**, 8535–8539 (2006).
- [2] Ramanathan et al. "Graphitic Nanofillers in PMMA Nanocomposites- An Investigation of Particle Size and Dispersion and Their Influence on Nanocomposite Properties." *J. Polym. Sci. B* **45**, 2097–2112 (2007).
- [3] Kelly. "The Physics of Graphite." Applied Science, Essex, England: 1981.
- [4] Blaklee et al. "Elastic Constants of Compression-Annealed Pyrolytic Graphite." *J. Appl. Phys.* **41**, 3373 (1970).
- [5] Novoselov et al. "Electric Field Effect in Atomically Thin Carbon Films." *Science* **306**, 666 (2004).
- [6] Vickery et al. "Fabrication of Graphene-Polymer Nanocomposites with Higher Order Three-Dimensional Architecture." *Adv. Mater.* **21**, 2180 (2009).
- [7] Stankovich et al. "Graphene Based Composite Materials." *Nature* **442**, 282–286 (2006).
- [8] Xu et al. "Thermal Analysis of Polyvinyl Alcohol/Graphite Oxide Intercalated Composites." *Polymer Degradation and Stability* **73**, 29–31 (2001).
- [9] Du et al. "New Method to Prepare Graphite Nanocomposites." *Chem. Mat* **20**, 2066–2068 (2008).
- [10] Hummers et al. "Preparation of Graphite Oxide." *J. Am. Chem. Soc.* **80**, 1339 (1958).
- [11] McAllister et al. "Single Sheet Functionalized Graphene by Oxidation and Thermal Expansion of Graphite." *Chem. Mater.* **19**, 4396 (2007).

Appendix C: A submitted ACS Division of Polymeric Materials: Science and Engineering pre-print that is awaiting publication

Change in the C:O Ratio of Graphene Oxide During Processing

A. Jaeton Glover,^{1,2} Kyle R. Overdeep,¹ Minzhen C. Cai,² David E. Kranbuehl,^{1,2} and Hannes C. Schniepp²

¹*College of William and Mary, Chemistry Department, Williamsburg, VA*

²*College of William and Mary, Department of Applied Science, Williamsburg, VA*

INTRODUCTION

The incorporation of chemically-derived graphene into polymer nanocomposites has become increasingly widespread [1-4], as it is a low-cost material with excellent mechanical properties [5], good electrical conductivity [5], high surface area [6], and gas impermeability [2]. It is produced by conversion of native graphite to graphene oxide (GO), a more easily exfoliated product with a C:O ratio around 2.0, via the Hummers method [7,8]. Subsequent reduction of this product leads to partial restoration of graphene-like properties [6]. In this work we explore the as of yet unknown characteristics of *in situ* thermal GO reduction within polymer nanocomposites and compare them with the time-temperature dependence of GO reduction in air. Whether or not intended, the implications of *in situ* GO reduction at typical polymer processing

temperatures are substantial with regard to the properties of a finished nanocomposite product.

While the thermal reduction process has been described at temperatures ranging from 140°C under vacuum to 1050°C in Ar [9,10], a comprehensive exploration of the time–temperature dependence on the increase of the C:O ratio at low temperatures (150°C–250°C) has yet to be established. The elucidation of this relationship provides a basis for comparison to *in situ* GO reduction. We establish this relationship by measuring the heat evolved during the exothermic reduction of GO in air using Differential Scanning Calorimetry (DSC). We then compare these results with the reduction energies evolved from the *in situ* reduction of GO in GO/polymer nanocomposites made with poly (vinylpyrrolidone/vinyl acetate) (PVP/VA).

We find that the extent of *in situ* reduction within a GO/polymer nanocomposite is dependant on the interactions of the nanoparticles with the composite matrix, i.e. the chemistry of the polymer. By comparing the heats of reduction *in situ* with the heats of reduction in air over the moderate temperature range of 150°C to 250°C, we show that in the case of the GO/PVP nanocomposite the extent of reduction is less than in air, whereas the GO/PVP/VA nanocomposite shows a much higher degree of reduction. We therefore demonstrate that the degree of GO reduction is dependant on the chemistry of the polymer matrix with which it interacts, providing important information regarding the processing of increasingly popular GO nanocomposites.

EXPERIMENTAL

Materials. The GO was produced from graphite powder (Asbury Carbons, Asbury, NJ) using the Hummers' method.

The PVP/VA (S-630), (International Specialty Products, Wayne, NJ,) is a 60:40 by weight PVP:VA copolymer with a published K-value between 30 and 50.

Methods. GO to be used in the nanocomposites was dispersed in water and introduced to PVP or PVP/VA solutions in water to create 9.1% GO (by mass) nanocomposites. The films were cast and left to dry at room temperature in air.

Thermogravimetric analysis (TGA) and DSC experiments were performed using a 1°C/min ramp to 250°C. Elemental analysis was performed by Galbraith Laboratories, Knoxville, TN.

RESULTS

The time-temperature dependence of the reduction of GO in air is shown in Figure C.1. This establishes grounds for comparison in further experiments and demonstrates that there is a time-temperature dependence of the degree of GO reduction in this moderate temperature range.

Figure C.2 is an overlay containing the DSC results of the reduction of GO in air, along with the DSC results of the GO in the S-630 PVP/VA nanocomposite. Note the increase in heat evolved and the increase of peak reduction temperature in the case of this nanocomposite.

Table C.1 shows the *in situ* heat of reduction of the GO in the GO/PVP/VA nanocomposite. Information on reduction of GO in air is included for comparison.

Table C.1. Heat of Reduction and Temperature of Peak Reduction Rate of GO/PVP/VA Nanocomposite as well as GO in Air (Highlighted)

Material	ΔH_{red} (J/g) \pm 20	Peak Reduction Temp. ($^{\circ}\text{C}$) \pm 1$^{\circ}$
GO in Air	830	168
S-630 PVP/VA	1340	190

DISCUSSION

Figure C.1 shows an appreciable increase in C:O ratio of GO in air by elemental analysis at temperatures 175 $^{\circ}\text{C}$ and higher. However, when compared with DSC data on reduction in air in Figure C.2, one sees that by 175 $^{\circ}\text{C}$, the majority of reduction energy has been released. This suggests that the reduction GO and release of oxygen-containing compounds occurs in a series of multiple steps. As the main products of reduction have been shown by McAllister et. al. to be CO_2 and H_2O , it is also possible that the

compounds remain within the unexfoliated GO matrix until temperature-dependant diffusion processes affect their release [11].

Figure C.2 and Table C.1 show that the heat of the *in situ* reduction of the GO in the PVP/VA nanocomposite (1340 J/g) is substantially higher than that of the GO in air (830 J/g). The temperature of peak reduction rate in the GO/PVP/VA nanocomposite (190°C) is higher than in the case of the GO in air (168°C). This suggests that though the reduction occurs at a higher temperature, once started, the PVP/VA polymer matrix facilitates the reduction of the GO, possibly because the VA groups destabilize oxygen-containing functional groups in the GO, catalyzing the reduction.

CONCLUSION

It is shown that the increase in C:O ratio of GO in air occurs with a reproducible time-temperature dependence at temperatures of 175°C–250°C. The fact that the DSC data shows appreciable fraction of the heat of reaction well before 175°C suggests that there are multiple kinetic steps leading to the release of oxygen-containing compounds.

The increased energy released by the *in situ* reduction of the GO in a PVP/VA nanocomposite, when compared to the GO reduction in air, suggests the VA groups facilitate the release of oxygen-containing compounds in the nanocomposite.

These results suggest that in the processing of a GO/polymer nanocomposite, the degree reduction of the GO varies and occurs at temperatures dependant on the chemistry of the polymer in the nanocomposite. This has important implications for the creation of GO nanocomposite systems and subsequent fabrication of GO nanocomposites structures. As one example, the presence of temperature gradients in thicker GO/polymer

nanocomposites may yield GO reduced to different degrees based on depth in the nanocomposite. This can produce differences in the particle-polymer interfacial forces and thereby affect performance properties.

ACKNOWLEDGEMENTS

The authors would like to thank International Specialty Products of Wayne, NJ, particularly Dr. David Hood for providing the polymer used in this work.

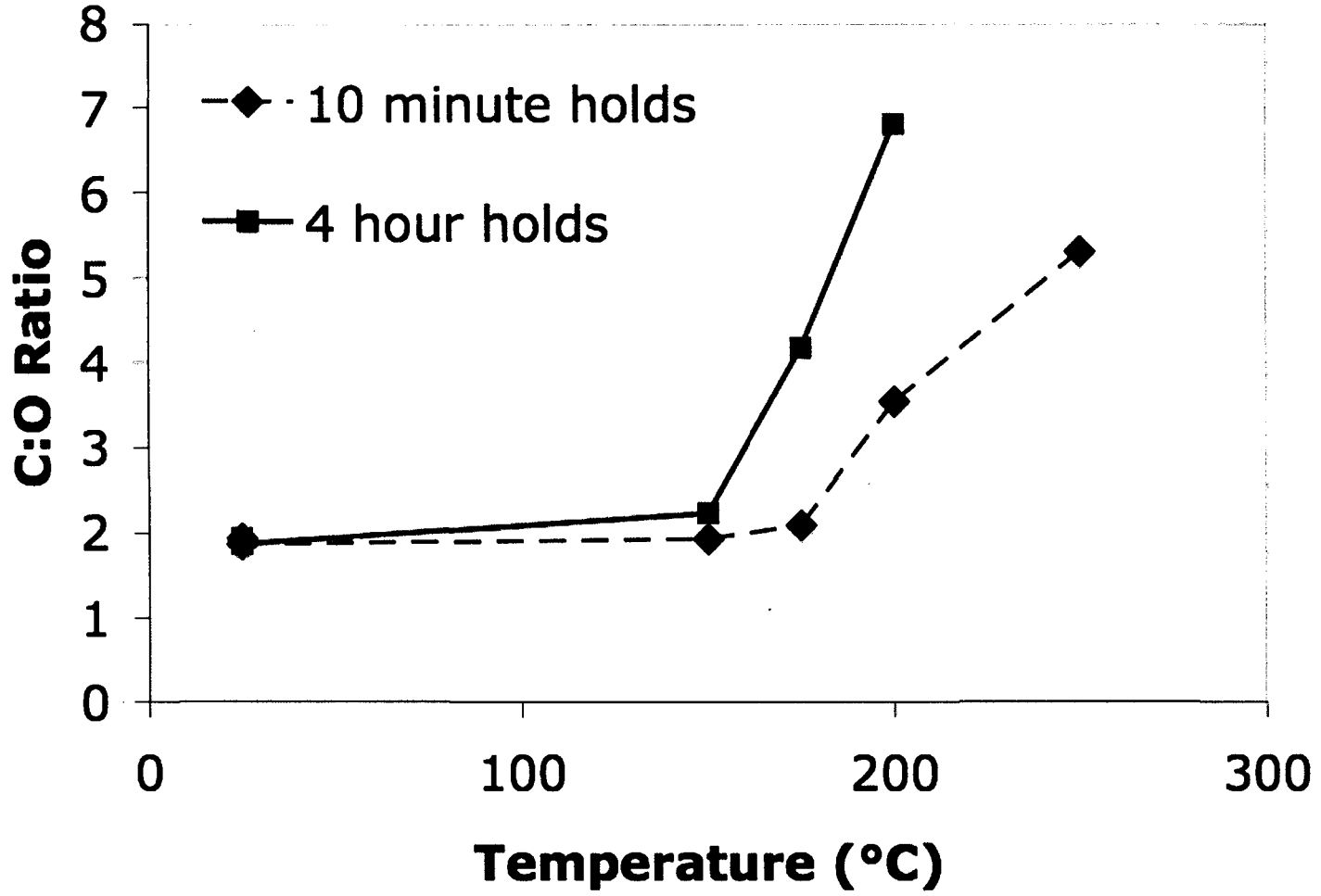


Figure C.1: C:O ratio of GO reduced in air as a function of hold-time and temperature. Features are large due to formatting specifications for pre-prints mandating small in-line figures.

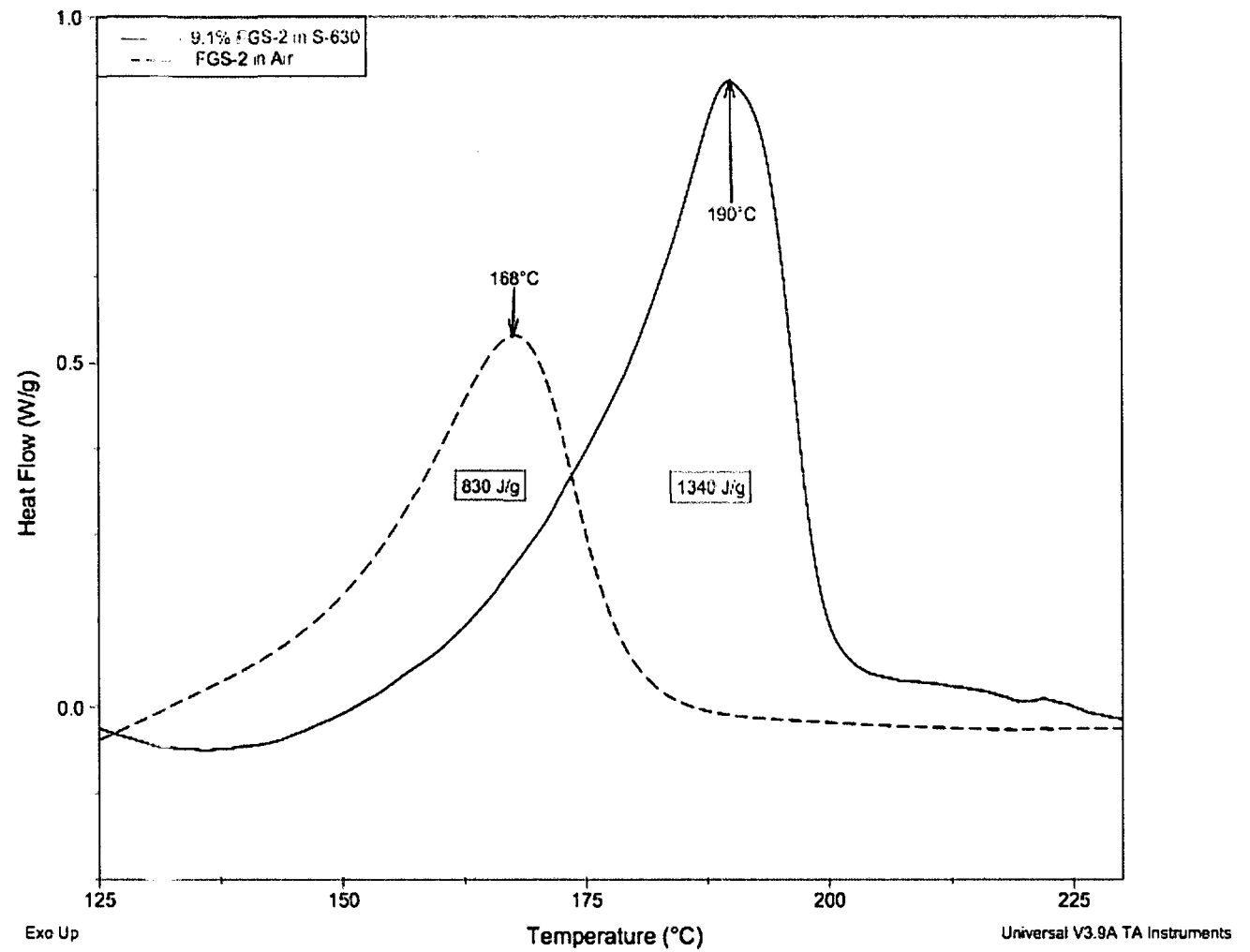


Figure C.2: DSC of GO in air (black, dashed) and 9.1% GO in S-630 nanocomposite (red, solid.)

References for Appendix C

- [1] Kim, H.; Abdala, A. A.; Macosko, C.W. *Macromolecules* **2010**, *43*, 6515.
- [2] Kim, H.; Miura, Y.; Macosko, C. *Chem. Of Mater.* **2010**, *22*, 3441.
- [3] Ramanathan, T.; Abdala, A.; Stankovich, S.; Dikin, D.; Herrera-Alonso, M.; et al *Nature Nano.* **2008**, *3*, 327.
- [4] Stankovich, S.; Dikin, D.; Dommett, G.; Kohlhaas, K.; Zimney, E.; et al. *Nature* **2006**, *442*, 282.
- [5] Sundaram, R.; Gomez-Navarro, C.; Balasubramanian, K.; Burghard, M.; Kern, K. *Advanced Materials* **2008**, *20*, 3050.
- [6] Schniepp, H.; Li, J.; McAllister, M.; Sai, H.; Herrera-Alonso, M.; et al *The Journal of Phys. Chem. B Letters* **2006**, *110*, 8535.
- [7] Hummers Jr., W. S.; Offeman, R. E. J.; *American Chemical Society* **1958**, *80*, 1339.
- [8] Stankovich, S.; Dikin, D. A.; Piner, R. D.; Kohlhaas, K. A.; Kleinhammes, A.; Jia, Y.; Wu, Y.; Nguyen, S. T.; Ruoff, R. S. *Carbon* **2007**, *45*, 1558.
- [9] Jung, I.; Field, D.; Clark, N.; Zhu, Y.; Yang, D.; et al. *J. Phys. Chem. C.* **2009**, *113*, 18480.
- [10] Schniepp, H.; Li, J.; McAllister, M.; Sai, H.; Herrera-Alonso, M; et al. *J. Phys. Chem. Letters B.* **2006**, *110*, 8535.
- [11] McAllister, M.; Li, J.; Adamson, D.; Schniepp, H.; Abdala, A.; et al. *Chem. Mater.* **2007**, *19*, 4396.

Appendix D: *In Situ* Reduction of FGS-2 in Polymer Nanocomposites as a Function of Chemical Structure, Time, and Temperature

Introduction

Interest in the incorporation of chemically derived graphene into polymer nanocomposites has become increasingly widespread [1-7] due to its outstanding mechanical properties [8], good electrical conductivity [8], high surface area [9], impermeability to gases [2], and low cost. A common means of obtaining single-layer graphene is by exfoliating and reducing graphite oxide (GO), which is the product of native graphite treated with the Hummers' method [10,11]. This process is economical in terms of cost and scale.

GO is hydrophilic and readily dispersed in water. The reduction of GO removes oxygen groups allowing for favorable interactions with more hydrophobic solvents, depending on the degree of reduction, facilitating the production of many different polymer-GO nanocomposites. Further, GO reduced to various levels may interact more favorably with the many polymers in nanocomposites. The reduction of GO can also lead to the partial restoration of electrical properties lost in the oxidation process.

Most reduction procedures involve the use of either chemical reducing agents or carefully controlled reduction environments. Reduction by chemical reagents includes exposure to hydrazine [12-21,11], dimethylhydrazine [4], sodium borohydrate [22], hydroquinone [23], alkaline conditions [24], ascorbic acid [25,26],

trioctylphosphine [27], glucose [28], Tyrosine-rich proteins [29], aluminum powder in acidic conditions [30], and gaseous H₂ [31]. Chemical reduction is effective at moderate temperatures (<100°C,) but involves considerable care, multiple steps, and the reagents are sometimes toxic.

The stepwise combination of multiple chemical reduction schemes has also been shown. Si and Samulski have reported stepwise chemical reduction through reduction by NaBH₄ and subsequent hydrazine treatment [32]. Wang et al. demonstrate thermal reduction of GO dispersed in DMF at 180°C and subsequent hydrazine treatment [33].

Less common means of reduction include electrochemistry as demonstrated by Shao et al. via creation of a solution-cast GO electrode and reduction in a three-electrode cell in a 0.1 M Na₂SO₄ solution [34]. Zhou et al. report O:C ratios of less than 6.25% also via electrochemical reduction [35].

Reduction in CH₄/Ar and H₂ plasmas has been shown by Baraket et al. and by Sundaram et al., respectively [36,8].

Thermal reduction is another means of reduction. Schniepp et al. have demonstrated simultaneous reduction and exfoliation in argon via tube furnace at 1050°C [9]. This method was further characterized by McAllister et al., who determined that exfoliation occurs at temperatures of 550°C and above, where production of gaseous products by decomposition of O-containing functional groups out-paces the escape of products by diffusion [37]. Wang et al. reported reduction of GO from 550°C to 1100°C under Ar and H₂ [38]. GO reduction has also been demonstrated under vacuum at temperatures ranging from 140°C-300°C and 600-800°C [39,40]. Li et al. discuss

simultaneous N-doping and thermal reduction at 300°C and above under NH₃ [41].

Localized thermal reduction by a heated AFM probe at no less than 150°C has also been shown [42].

Cote et al. report a photothermal method for GO reduction whereby a Xenon flash generates the heat necessary to catalyze reduction [43]. Electron transfer from TiO₂ irradiated by UV light to suspended GO particles has been shown by Williams et al [44].

Less complex reducing methods involve reduction of GO dispersed in solvent (solvothermal reduction,) as in water, ethanol, butanol, and ethylene glycol in sealed vessels at temperatures ranging from 120°C to 200°C [45]. Maximum reduction is met in all solvents at 16 hours and C:O ratios vary with solvent type from 9 to 19. Solvothermal reduction at atmospheric pressure by refluxing GO in NMP at 205°C for 24 hours yielded a C:O ratio of 5 [46]. Chen and Yan report partial reduction of GO at 150°C, atmospheric pressure, in DMAc/H₂O (10:3 v/v) for one hour and complete reduction at five hours [47]. Similarly, a GO dispersion in 6:1 DMAc/H₂O reduced by 800W microwave led to partial reduction in three minutes and total reduction in ten minutes [48]. Zhou et al. report reduction under pressure of GO dispersed in water at 150°C and more so at 180°C for six hours [49]. GO dispersed in propylene carbonate has been reduced at 150°C for twelve hours [50].

In spite of all the literature available regarding the reduction of GO, the time-temperature dependence on the reduction of GO in air at low temperatures (150°C-250°C) has yet to be defined. The characterization of this process in this paper yields a basis for comparison of the *in situ* reduction of GO in polymer nanocomposites.

We then demonstrate the thermal reduction of GO within polymer nanocomposites. We show that poly (vinylpyrrolidone) (PVP) and poly (vinylpyrrolidone/vinyl acetate) (PVP/VA) as polymer matrix facilitate the reduction of GO *in situ* at temperatures below 250°C. We also report the time-temperature dependence of reduction of GO *in air* at temperatures up to 250°C for a comparison to the *in situ* reduction in a FGS-2/polymer nanocomposite. The C:O ratios of the reduced products are determined by elemental analysis. For the first time, the degree of reduction is shown to be controlled by interactions between the GO and polymer, and quantified through the determination of the heats of reduction by DSC. These results are important to the processing of a polymer-GO nanocomposite as they show that the final C:O ratio depends on the time-temperature processing procedure. The implications of such findings on the processing of polymer-GO nanocomposites are important, as they will likely affect the finished product.

Materials and Methods

GO, now to be referred to as functionalized graphene sheets (FGS) with a C:O ratio of 2 (FGS-2), was produced using the Hummers' method [10]. For the neat FGS-2 TGA and DSC experiments, the product was dispersed in water at 2 mg/mL using a tip sonicator (Microson XL2007, 100W.) The dispersion was dried under vacuum at 45°C for 24 hours prior to use. In order to establish a time/temperature relationship to degree of reduction *in air*, one would ideally use material that had previously been exfoliated, dispersed, and dried – thus allowing byproducts to easily escape so that the C:O ratio could be determined based solely upon the covalently-bonded oxygen. This

would also mirror the condition of the material reduced in solvent and as well-dispersed particles in a nanocomposite.

TGA and DSC experiments were conducted on TA Instruments' models Q-500 and MDSC 2920. 1°C/min temperature ramps were used from room temperature to 250°C.

For the solvothermal reductions, the Hummers' FGS-2 was dispersed in DMF (Sigma-Aldrich, anhydrous, 99.8%) at 2 mg/mL using the tip sonicator. It was reduced in a pressure vessel (Model 452HC, Moline, IL) in a temperature-controlled silicone oil bath. Upon cooling, the material was dried under vacuum at 50°C for 24 hours. All elemental analysis was performed by Galbraith Laboratories, Inc. Knoxville, TN.

The PVP (C-17, K-29/32 and K-120) and PVP/VA (S-630) polymers used were provided by International Specialty Products, Wayne, NJ. Their structures are shown in Figure D.1. The C- and K- designations for the PVP refer to the Fikentscher K-value, a representation of the viscosity of the polymer which increases with average molecular weight. The K-designation represents standard PVP, whereas the C-designation denotes USP-grade material. The S-630 PVP/VA is a 60:40 by weight PVP:VA copolymer with a K-value between 30 and 50.

These materials were dissolved in deionized water at 80-100°C with stirring and cooled to ~50°C prior to addition of the 2 mg/mL FGS-2 in water dispersion. After addition of the FGS-2/water dispersion, films were cast and dried at room temperature in air, later to be used in the TGA and DSC experiments.

Results and Discussion

The DSC and TGA analysis of the pure FGS-2 (GO with C:O ratio of 2) under nitrogen, Figure D.2, establishes a baseline for later comparison with FGS-2 reduced in air, DMF, and in PVP/PVP-VA nanocomposites. The DSC data reveals an exothermic event occurring between 125°C and 220°C. This event reaches a peak at 168°C, and integration of the peak gives a caloric value of 840 J/gram FGS-2. The endothermic event at 120°C is due to vaporization of residual water. The TGA data, also plotted, show a 31% mass loss from the same 125°C to 220°C range, selected to correspond to the exothermic peak. The highest rate of mass loss, indicated by a first derivative maximum, occurred at 171°C. These results agree with work done by McAllister et al. in that both the exothermic event and the peak rate of weight loss occur at approximately the same temperature [37]. However, our results indicate these events occur 30°C prior to temperatures reported in the McAllister paper [37]. As the ramp rates are the same (1°C/min,) this finding is likely due to the prior exfoliation and dispersion in water and subsequent drying under vacuum of our material before testing.

Figure D.3 is a plot of FGS C:O ratio vs. reduction temperature and time in air. Table D.1 tabulates these findings. These data reveal a slight reduction and increase of the C:O ratio up to 150°C. This agrees with the reduction seen in the DSC experiment in Figure D.2. According to the DSC results in Figure D.2, a significant portion of the reduction should be complete at 150°C and most of the exothermic energy is released by 175°C. This is not revealed by elemental analysis data, which shows only a small change in the C:O ratio at 150°C. The 175°C four-hour hold was the first

procedure to show an appreciable change in C:O ratio. This may indicate that the reduction occurs over a series of steps on the reaction pathway toward release of the final gaseous products. This suggests these intermediate products remain within the FGS.

Included on the plot in Figure D.3 is a 200°C and a 250°C/four hour point which was a solvothermal reduction under pressure in DMF. The solvothermal reduction in DMF under pressure at 200°C and 250°C for times comparable to the air reductions is shown to yield similar degrees of reduction. Upon completion of the reduction, the product, FGS-8 was a stable dispersion for more than 72 hours. It agrees with data from the air reduction experiments, but this is likely coincidental, as work by Durbin et al. as well as Nethravathi and Rajamathi demonstrate differences in degree of reduction as a result of solvent type, even at the same temperatures [45,46]. Their findings support the premise of this paper that the medium in which the GO is dispersed defines, along with temperature and time of reduction, the degree of reduction. Thus the dependence of the C:O ratio on the reduction time and reduction temperature in two media at temperatures up to 250°C is quantified.

Figure D.4 shows the TGA data of a 1°C/min ramp under nitrogen to 250°C of the neat K-120 and the K-120/FGS-2 composite loaded at 9.1%. Both materials were dried with a 60-minute isotherm at 100°C and the results were normalized with respect to post-drying masses to counter the effects of different water contents in the materials. As shown in Figure D.4, upon reaching 250°C there is a 1.5% difference in mass loss between the two materials. The neat polymer loses 0.3% of its mass over the range of the experiment, indicating its thermal stability. This mass loss is lower than the 2.7% (31% of the 9.1% FGS-2 present) one would expect from the heating of FGS-2, as

shown in Figure D.1, and is due to the partial *in situ* reduction of the FGS-2, limited by interactions between the FGS-2 and the PVP.

Figure D.5 shows the DSC data for the K-120/FGS-2 nanocomposite reduction at 1°C/min. The published T_g of the neat K-120 is visible at 176°C [50,51]. The onset of the reduction occurs at 165°C and is concluded by 220°C. The peak of the exotherm occurs at 206°C. This higher shift in temperature of both the start of reduction as well as peak reaction temperature is indicative of the thermal stability lent to the FGS-2 by the interaction with the K-120 polymer. This arises from the potential for hydrogen and van der Waals bonding between the K-120 and FGS-2, as well as the overall compatibility of these two materials are shown by their hydrophilic natures. This result when compared to the reduction of FGS-2 in air or in DMF, helps demonstrate the stability lent to the FGS-2 by the K-120 PVP polymer. The shift in the baseline over the course of the reduction event is probably due to the T_g of the nanocomposite. The thermal stability and the T_g of neat K-120 at 176°C, are shown in Figure D.5.

Integration of the reaction energy yields 67.3 J/g of composite, or 740 J/g for FGS-2 *in the K-120 composite*. This is significantly lower than the heat of reduction of pure FGS-2, 840 J/g. While the potential for a small amount of polymer oxidation exists in this scheme, this is unlikely in that the main products released are CO₂ and H₂O [37].

Table D.2 shows similar reaction data for the other molecular weights of PVP: C-17 and K29/32. All heats of reduction for the PVP/FGS-2 composite samples are similarly lower than the heat of reduction of the pure FGS-2, supporting the claim that the reduction is governed by FGS-2/polymer interactions. The heats of reduction appear to

show a trend with the higher molecular weights of the K-120 polymer stabilizing the FGS-2 to a greater degree than the significantly lower molecular weight of the C-17 and K-29/32 polymers. Furthermore, the shift in temperature of the peak reduction increases with the molecular weight of the PVP.

Figure D.6 displays the good thermal stability of the neat PVP/VA copolymer S-630. This copolymer shows a heat of reduction of 1340 J/g for the FGS-2 in the polymer composite. This value is higher than that of the PVP/FGS-2 composites, as well as the neat FGS-2 particles. This suggests a higher degree of FGS reduction is occurring in this polymer than would be seen in its pure form. The peak reduction temperature in this composite, 190°C, is significantly lower than that of the pure FGS-2, indicating this polymer aids reduction of the FGS-2. The increase in the extent of the reduction can be explained by the disruption of hydrogen-bond and van der Waals forces between the FGS-2 and copolymer by the introduction of vinyl acetate, VA, groups in the copolymer. The location of the oxygen in the acetate group in the VA unit may catalyze the release of hydroxyl groups from the FGS-2 by destabilizing the O-H bond, allowing for H to attack and yield H₂O. Again, the chemical structure of the polymer along with time and temperature determines the extent to which FGS-2 is reduced during a fabrication process.

Conclusion

The reduction of previously exfoliated and dried FGS-2 at a 1°C/min ramp rate is an exothermic process shown to occur between 125°C and 220°C, with a peak at 168°C, releasing 840 J/g of energy. A small reduction in the C:O ratio is seen in air for up to four hours at 150°C, a temperature at which more than half of the exothermic energy is released according to DSC. This is likely due to a series of intermediates in the release of the gaseous H₂O and CO₂ final products.

The temperature dependence of the reduction of FGS-2 dispersed in DMF is demonstrated. In the case of DMF specifically, this temperature dependence appears to fall in-line with the air reduction experiments. However, this is not likely to be the case for all solvents, as work by Nethravathi and Rajamathi in other solvents shows differing degrees of reduction [45]. This results suggests that the media which contains the dispersed FGS-2, be it air, solvent, or polymer affects the kinetics and degree of *in situ* reduction.

This idea is verified when FGS-2 is reduced *in situ* in the FGS-2/PVP and PVP/VA nanocomposites. The degree of reduction of FGS-2 in PVP is to a lesser degree than in air, as shown by energy release and mass loss. This shift is proposed to be due to more favorable H-bonding between the polymer and FGS nanoparticle. The case of the FGS-2 in PVP/VA nanocomposite has the opposite result. In the FGS2-PVP/VA nanocomposite the exothermic energy of the reduction reaction increases beyond that observed in air and in DMF. This suggests that the addition of the VA groups in the PVP/VA help destabilize oxygen-containing functional groups and yield a further-reduced carbon:oxygen ratio over the same temperature range.

Tables for Appendix D

Table D.1: Resulting carbon and oxygen content of FGS-2 after reduction under various temperatures and times. Values with an asterisk were reduced under pressure while in a DMF dispersion.

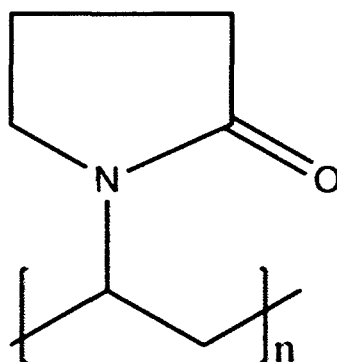
temperature (°C)	hold time (min)	C content (%)	O content (%)	FGS number
25	-	56%	39%	1.9
150	10	56%	39%	1.9
150	240	60%	36%	2.2
175	10	59%	37%	2.1
175	240	73%	23%	4.2
200	10	69%	26%	3.5
200	240	81%	16%	6.8
200*	240*	61%*	12%*	7.01*
250	10	80%	20%	5.3
250*	240*	73%*	12%*	8.2*

Table D.2: Calorimetry data for the pure FGS-2 as well as the FGS-2 nanocomposites. The heats of reduction, which define the degrees to which the FGS-2 reduces, indicate the effects that the different polymer chemistries have on the reactions.

material	polymer type	FGS-2 concentration	onset of red. (°C)	peak of red. (°C)	end of red. (°C)	ΔH_{red} J/g of FGS-2
Pure FGS-2	-	100.0%	125	201	240	830±20
C-17	PVP	9.1%	160	199	225	770±20
K-29/32	PVP	9.1%	165	203	220	780±20
K120	PVP	9.1%	165	206	212	740±20
S-630	PVP/VA	9.1%	135	190	220	1342±20

Figures for Appendix D

Polyvinylpyrrolidone



Poly(1-vinylpyrrolidone-co-vinyl acetate)

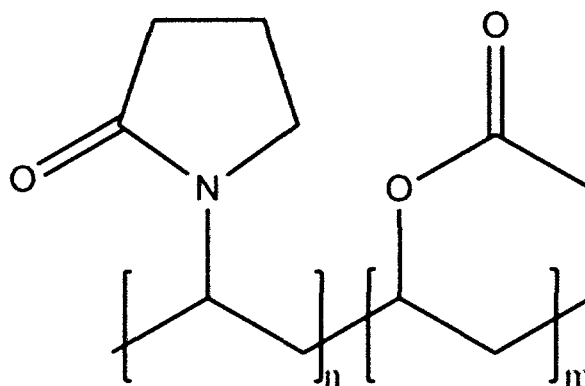


Figure D.1: Chemical structures of PVP and PVP/VA

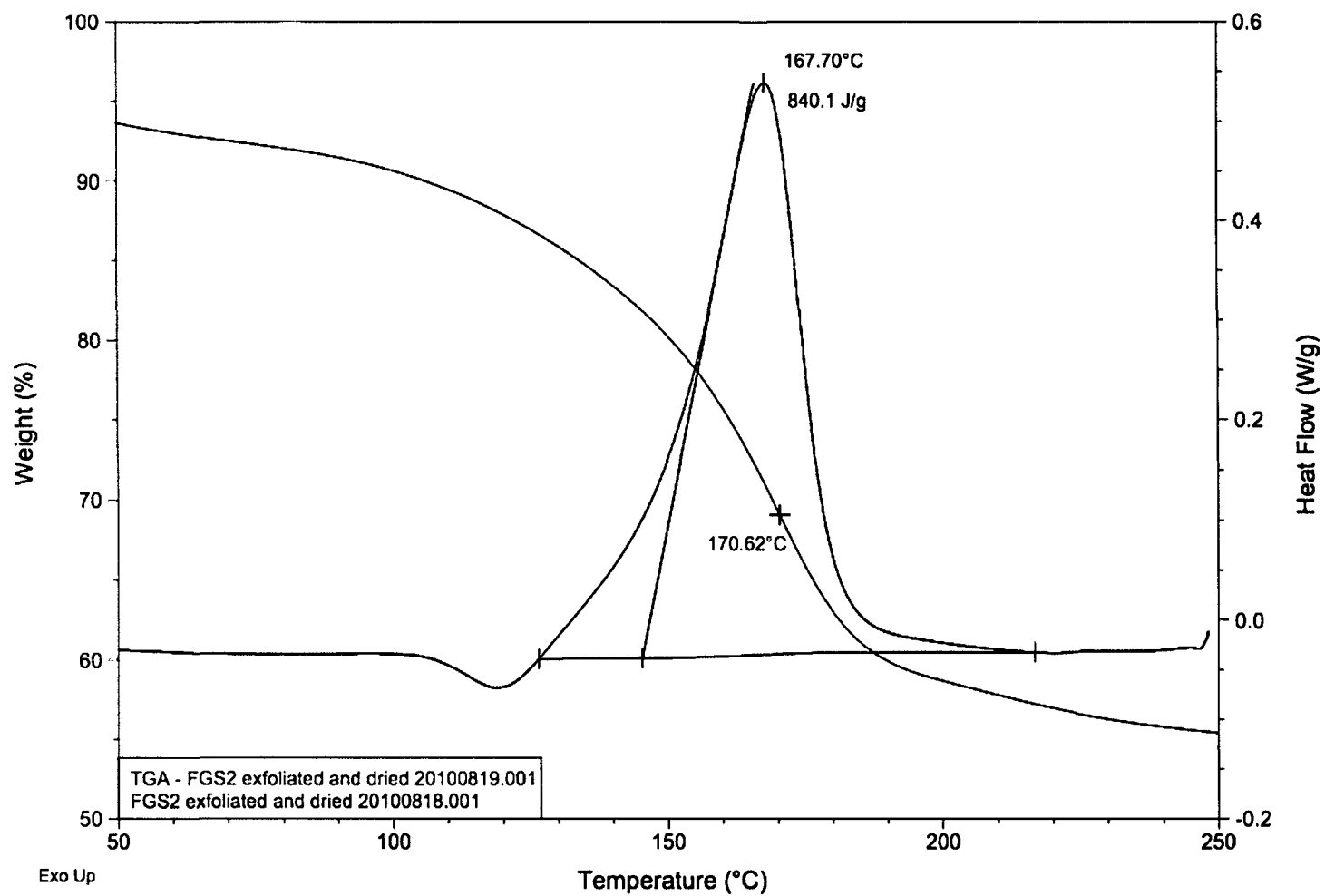


Figure D.2: DSC and TGA of the reduction of FGS-2. Maximum rate of exothermic activity occurs at the same time as maximum rate of mass loss.

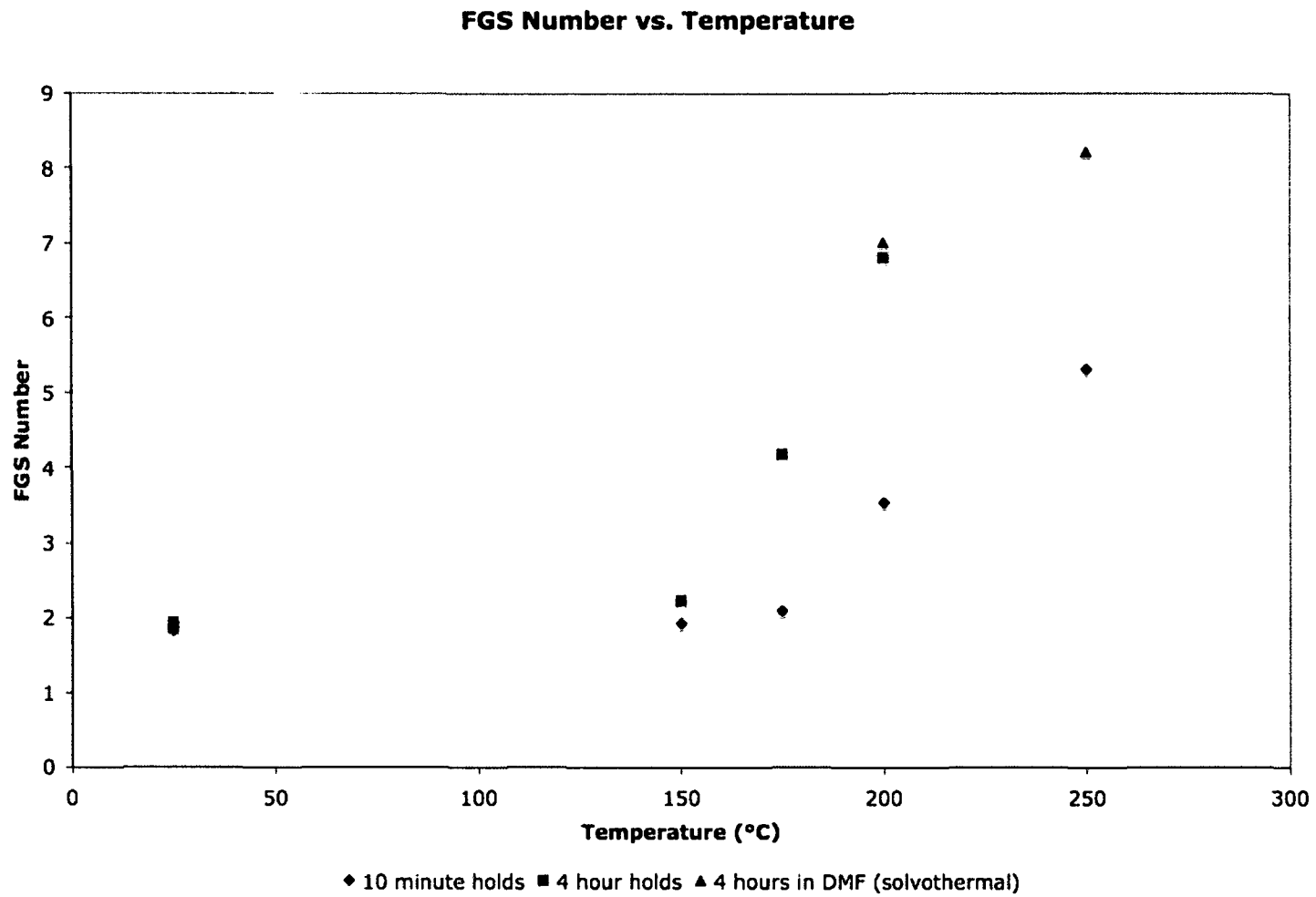


Figure D.3: FGS number (C:O ratio) vs. temperature as a function of reduction time.

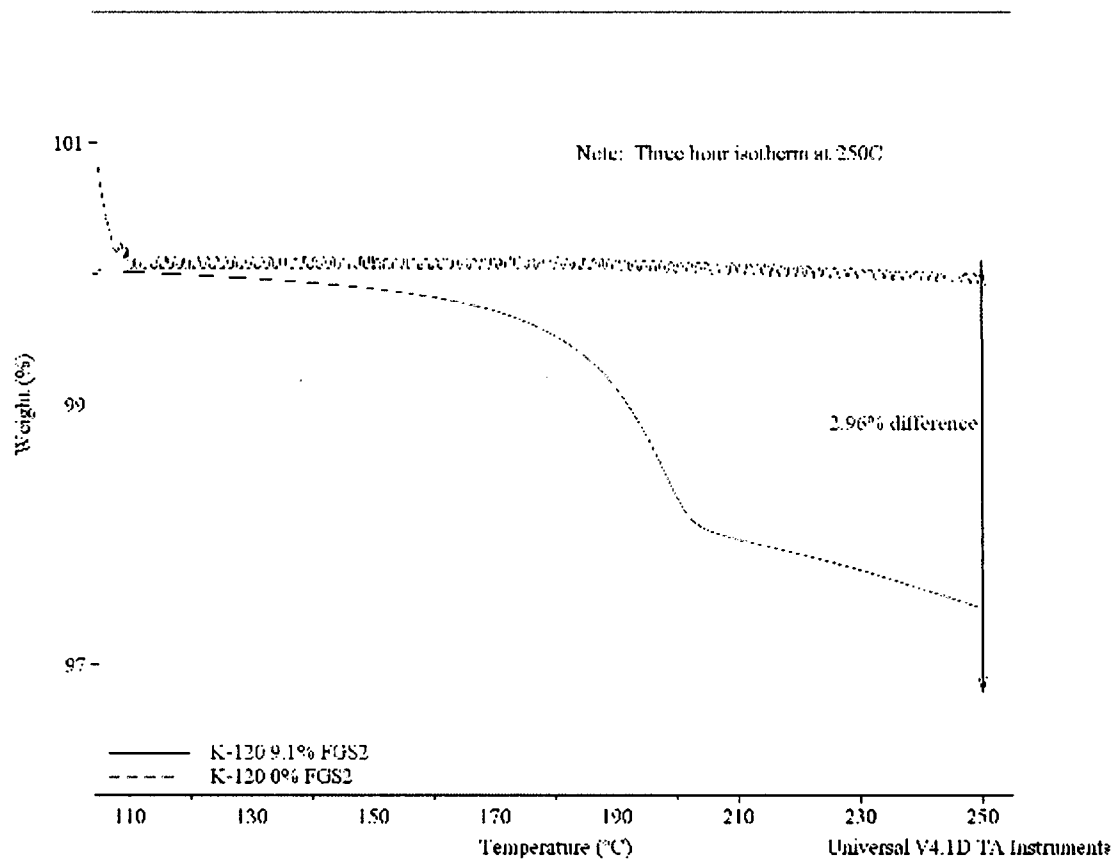


Figure D.4: Neat K-120 and K-120 with 9.1% FGS-2 loading vs. temperature. The thermal stability of the neat K-120 is illustrated, while the mass loss of the nanocomposite is greater than what one would expect in air.

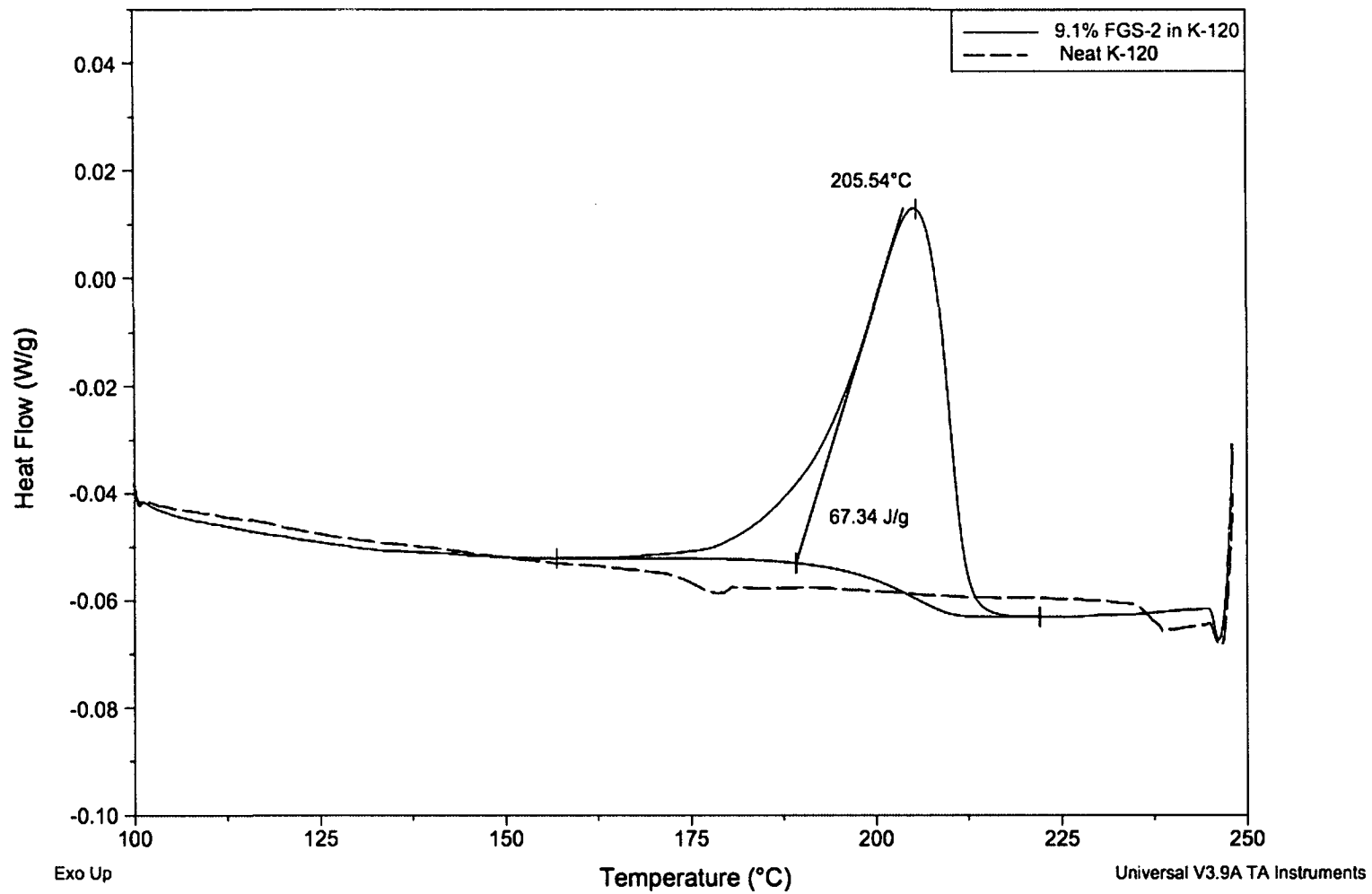


Figure D.5: DSC data for K-120 neat system and the K-120/FGS-2 nanocomposite.

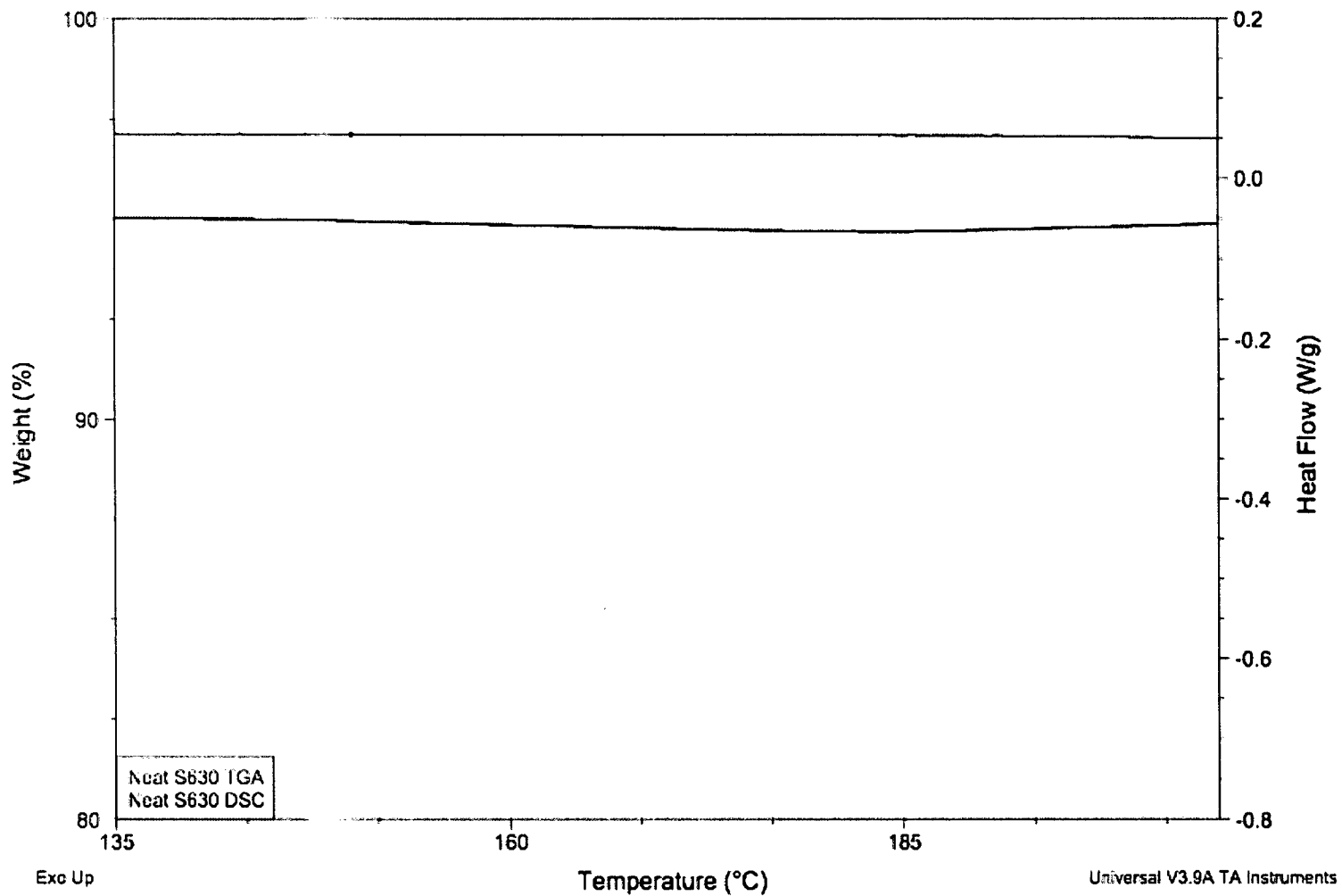


Figure D.6: TGA and DSC experiments on the neat S-630 polymer. Its thermal stability indicates that the large heat of reduction in the S-630 nanocomposite is solely due to the FGS-2 being reduced.